



UiT The Arctic University of Norway

Faculty of Health Sciences

Exploring mitochondrial quality control mechanisms and mitochondria-lipid droplet interactions in cardiac cell models

Gustav Godtliebsen

A dissertation for the degree of Philosophiae Doctor (PhD) – October 2023

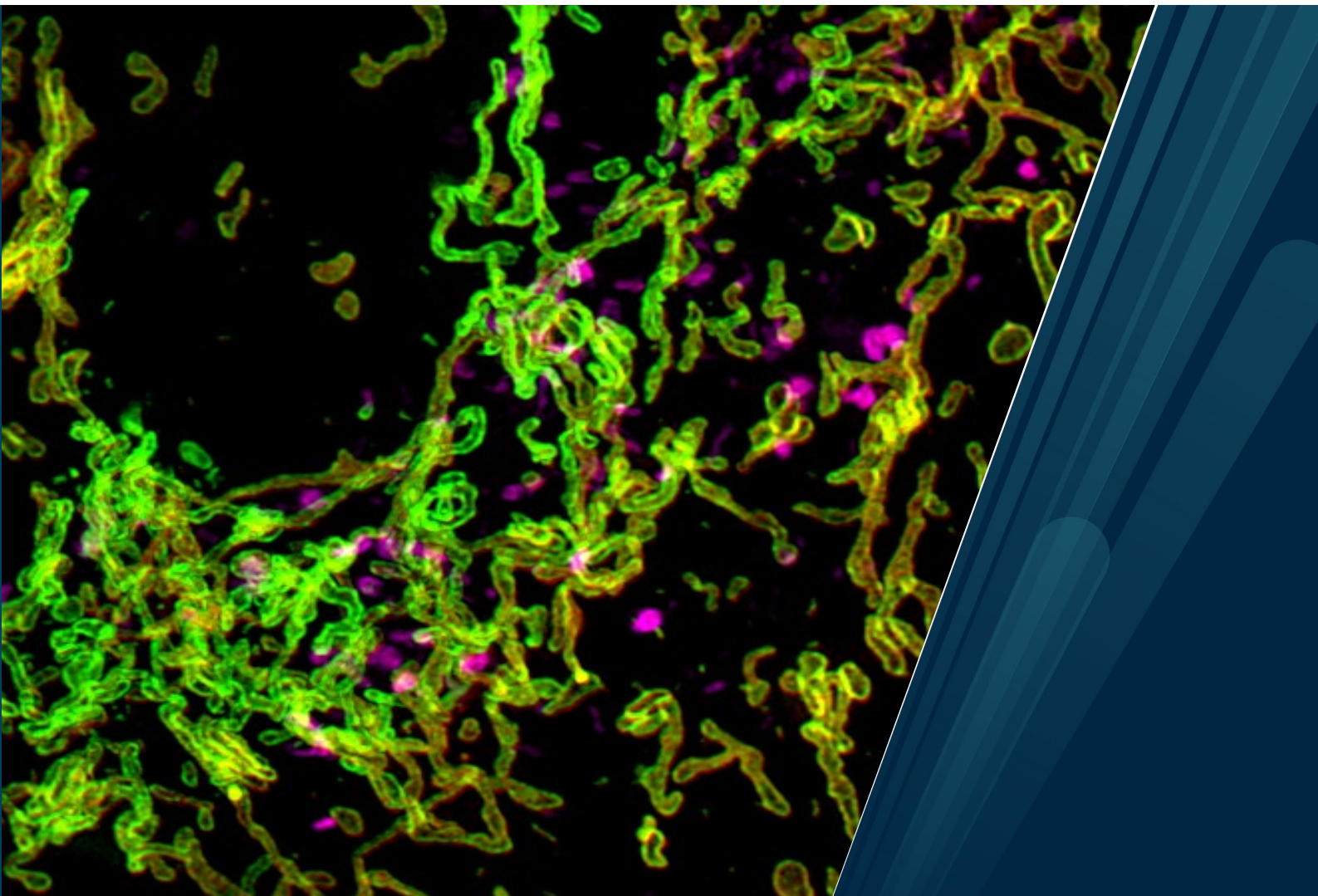


Table of Contents

Abbreviations	IV
List of Papers.....	VI
Summary	VII
Introduction	1
1 Mitochondria	1
1.1 Mitochondrial structure	2
1.1.1 Electron transport chain (ETC)	4
1.1.2 Metabolic pathways.....	6
2 Mitochondrial quality control.....	8
2.1 Regulation of mitochondrial morphology	10
2.1.1 Fusion	11
2.1.2 Fission	11
2.2 Mitophagy.....	13
2.2.1 Mitophagy Pathways	20
2.2.2 Basal Mitophagy	27
2.3 Mitochondrial derived vesicles.....	28
3 Lipid Droplets	31
3.1 Structure of lipid droplets	34
3.2 Lipid droplet turnover.....	34
4 Mitochondria and lipid droplets in the heart	36
Methodological Considerations.....	38
Double-Tag Mitophagy Reporter	38
Microscopy System Selection	39
Conventional Fluorescence Microscopy	40
Super-Resolution Microscopy	41
Corelative Light and Electron Microscopy	42

Mitophagy analysis pipeline.....	43
Summary of results.....	45
Discussion	49
Physiological relevance in biological studies.....	49
Mitophagy – Protecting the host	51
Mitochondrial morphology and mitochondrial dynamics	52
MDVs – an adapted mechanism.....	53
Lipid droplets – controlled use of fatty acids	56
Future Perspectives	60
References	61

Acknowledgements

The work presented in this thesis was carried out at the Cardiovascular Research Group at the Department of Clinical Medicine, Faculty of Health Sciences, University of Tromsø (UiT) – The Arctic University of Norway and was funded by UiT.

I am very grateful for the opportunity to take a PhD with the Cardiovascular Research Group, studying mitochondria and uncovering the intricate complexities of life is a dream come true. There were challenges along the way, most notably a rather disruptive pandemic, nonetheless the journey is now nearing an end heralding a new beginning. I wish to thank all those that supported me over the past 4-5 years.

I would first like to express my sincere and immense gratitude to my supervisor, Åsa Birna Birgisdottir. The guidance and support I have received has allowed me to grow as a person, learn new things and develop an even deeper passion for biomedical research. Thank you for all your help, I could not have asked for a more supportive supervisor. I would also like to express my gratitude to my co-supervisors Truls Myrmel, Zambarlal ‘Pradip’ Bhujabal, and Deanna Wolfson. Your help has been instrumental for my work.

I would also like to thank all past and present members of the Cardiovascular Research Group. This thanks extends to all my co-authors, those I’ve worked alongside over the years, and the members of the Advanced Microscopy Core Facility at UiT. All your help and guidance throughout the years has made my time as a PhD student a fun and interesting journey. I would like to especially express my gratitude to Trine Kalstad for her help and guidance in the cell lab, as well as for keeping a well-stocked candy drawer. Also, Kenneth B. Larsen for his help and guidance in microscopy and image analysis. And a special thanks to Mireia Nager for helping me optimize my quantification methods and reminding me of the importance of a decisive mindset to finish tasks on schedule.

I wish to express my gratitude to my family. No man is an island, and your support has been invaluable. To my father I wish to thank you for always being there when I needed help and providing me guidance and advice, you have helped me reach new heights. To my mother I wish to thank you for all the help and support you have given me, and hurdles you helped me avoid. Finally, my deepest gratitude, thanks and love I give to my wife Musheeshee. You keep me on track and focused, supporting me through the good and bad times of life. Thank you for always being there for me, you are the light of my life and bring golden times into this world.

Abbreviations

3DSIM	three-dimensional structured illumination microscopy
AMPK	adenosine monophosphate activated protein kinase
ATG	autophagy related
ATGL	patatin like phospholipase domain containing 2
ATP	adenosine triphosphate
BafA1	bafilomycin A1
BNIP3	BCL2 interacting protein 3
BNIP3L	BCL2 interacting protein 3 like
CLEM	Corelative Light and Electron Microscopy
CMs	cardiomyocytes
DRP1	dynammin-related protein 1
EM	electron microscopy
ER	endoplasmic reticulum
ETC	electron transport chain
FIP200	FAK family-interacting protein of 200 kDa
FIS1	mitochondrial fission 1 protein
FKBP8	FKBP prolyl isomerase 8
FUNDC1	FUN14 domain containing 1
GABARAP	gamma-aminobutyric acid receptor associated protein
hiPSC-CM	human induced Pluripotent Stem Cell derived cardiomyocytes
IMM	inner mitochondrial membrane
KD	knockdown
KO	knockout
LAL	lysosomal acid lipase
LaLi	Lalistat2
LC3	microtubule-associated proteins 1A/1B light chain 3

LIR	LC3-interacting region
MDV	mitochondria derived vesicle
MFF	mitochondrial fission factor
MUL1	mitochondrial E3 ubiquitin–protein ligase 1
NDP52	calcium-binding and coiled-coil domain 2
OMM	outer mitochondrial membrane
OMP25	Outer Membrane Protein 25
OPA1	optic atrophy 1
OPTN	optineurin
OXPHOS	oxidative phosphorylation
p62	sequestosome 1
PARKIN	parkin RBR E3 ubiquitin protein ligase
PE	phosphatidylethanolamine
PI3P	phosphatidylinositol-3-phosphate
PINK1	PTEN-induced putative kinase 1
PLIN	perilipin
PtdIns3K	phosphatidylinositol 3-kinase
RAB9A	RAB9A member RAS oncogene family
ROS	reactive oxygen species
SIM	structured illumination microscopy
SLR	sequestosome-like receptor
SRM	super-resolution microscopy
TAG	triacylglycerol
TBK1	TANK-binding kinase 1
TCA	tricarboxylic acid
ULK1	unc-51 like autophagy activating kinase 1
UPR	unfolded protein response

List of Papers

Paper I

High-resolution visualization and assessment of basal and OXPHOS-induced mitophagy in H9c2 cardiomyoblasts

Godtlielsen, G., Larsen, K. B., Bhujabal, Z., Opstad, I. S., Nager, M., Punnakkal, A. R., Kalstad, T. B., Olsen, R., Lund, T., Prasad, D. K., Agarwal, K., Myrnel, T., and Birgisdottir, A. B. (2023).

Autophagy. PMID: 37405374.

Paper II

Mitochondrial dynamics and quantification of mitochondria-derived vesicles in cardiomyoblasts using structured illumination microscopy

Opstad, I. S., Godtlielsen, G., Ahluwalia, B. S., Myrnel, T., Agarwal, K., Birgisdottir, A. B. (2022).

J Biophotonics. PMID: 34766731.

Paper III

A study of mitochondria and lipid droplet interplay in H9c2 rat cardiomyoblasts and hiPSC derived cardiomyocytes

Godtlielsen, G., Larsen, K. B., Bhujabal, Z., Nager, M., Kalstad, T. B., Olsen, R., Myrnel, T., and Birgisdottir, A. B. (2023).

Manuscript

List of papers not included in the thesis:

Punnakkal, A. R., **Godtlielsen, G.**, Somani, A., Andres Acuna Maldonado, S., Birna Birgisdottir, Á., Prasad, D. K., Horsch, A., & Agarwal, K. (2023). Analyzing Mitochondrial Morphology Through Simulation Supervised Learning. *Journal of visualized experiments : JoVE*, (193), 10.3791/64880. <https://doi.org/10.3791/64880>

Sekh, A.A., Opstad, I.S., **Godtlielsen, G.** et al. Physics-based machine learning for subcellular segmentation in living cells. *Nat Mach Intell* 3, 1071–1080 (2021). <https://doi.org/10.1038/s42256-021-00420-0>

Summary

The complexity of eukaryotic cells is facilitated by the energetic capacity provided by mitochondria. In cells with high energy demands such as those in cardiac tissue the cells require efficiently functioning mitochondria and metabolic substrates to meet their energy needs. To maintain a pool of efficiently functioning mitochondria mitophagy, a form for selective autophagy, allows cells to remove dysfunctional and excess mitochondria. Individual mitochondria can also release mitochondrial derived vesicles as a housekeeping mechanism to clear damaged mitochondrial components. The metabolic substrate preferentially utilized by cardiac mitochondria to meet the energy needs of their host cell is fatty acids, which cells store within cytosolic lipid droplets and transfer to mitochondria in a controlled manner.

In paper I, mitophagy was investigated in H9c2 cardiomyoblasts expressing a stable mCherry-EGFP-SYNJ2B-TM double-tag mitochondrial reporter. The pH-sensitive mitochondrial reporter allowed detection of lysosomal mitochondrial degradation. This was exploited to assess the level of mitophagy under basal growth conditions and in response to elevated mitochondrial respiration (OXPHOS) induced by galactose adaptation. OXPHOS induction resulted in a higher level of lysosomal degradation of mitochondria. Results from super-resolution imaging and correlative light and electron microscopy (CLEM) revealed mitochondrial fragments or remnants within lysosomes. Both canonical and alternative autophagy mediators were involved in OXPHOS induced mitophagy.

In paper II, mitochondrial derived vesicles (MDVs) were visualized through utilization of the advanced optical super-resolution technique three-dimensional structured illumination microscopy in the H9c2 cardiomyoblasts expressing a fluorescent outer mitochondrial membrane reporter. Ranging in size from 70 to 150 nm, these small vesicles were imaged in live and fixed cells, with live cell microscopy capturing the high-speed movements of the small vesicles and the formation of dynamic mitochondrial tubules. Quantifications were also performed, displaying an increase in mitochondrial derived vesicles in galactose adapted cells.

In paper III, lipid droplet accumulation, turnover, and crosstalk with mitochondria was visualized and assessed. Two cell models, rat H9c2 cardiomyoblasts and human inducible pluripotent stem cell derived cardiomyocytes were utilized and treated with excess fatty acids. Galactose adaption resulted in decreased accumulation of lipid droplets. Lipid droplet turnover and mitochondrial crosstalk was investigated under basal growth conditions.

Introduction

The high energy demand placed on cardiomyocytes in cardiac tissue requires efficiently functioning mitochondria, whose quality is maintained by multiple quality control mechanisms. The continued function of these mechanisms allows the heart to sustain efficient contractions and our lives to continue without disruption. The preferred substrates consumed by the heart for this ceaseless beating are fatty acids, converted to energy by the mitochondria. Fatty acids can be stored within cells in lipid droplets and the role of lipid droplets in heart function has not been fully characterized. This thesis explores mitochondrial quality control mechanisms and mitochondria-lipid droplet interplay in cardiac cell models. The different topics covered below serve as a framework for the papers included in the thesis.

1 Mitochondria

For most eukaryotic cells the mitochondria are crucial subcellular organelles, with their main prominent role being energy production in the form of adenosine triphosphate (ATP). They also take part in multiple other cellular functions, such as reactive oxygen species (ROS) production, signaling, calcium homeostasis, thermogenesis, synthesis of different metabolites and programmed cell death (apoptosis) (Bowser et al., 1998; McBride et al., 2006; Ricquier, 2006). The study of many of these processes are at the cutting edge of modern science with hopes that deeper understanding will allow for medical breakthroughs. The origin of mitochondria according to the theory of endosymbiosis was a critical step for the development of eukaryotic cells, with heterotrophic anaerobes consuming and forming a symbiotic relationship with aerobic prokaryotic microbes (protomitochondria) (Sagan, 1967; Wallin, 1927). This is supported by the existence of mitochondrial DNA (mtDNA) within mitochondria capable of replicating, transcribing, and translating encoded molecules (Wang et al., 2021). The selective pressure that favored this union is presumed to be the atmospheric transition that occurred early in the history of Earth, the new highly oxidizing environment being favorable to organisms with respiratory capacity (Castresana & Saraste, 1995; Lyons et al., 2014). With such a critical role in the function and theorized development of eukaryotic cells it is no wonder that mitochondria as organelles are of intense interest. The scientific interest in these organelles now spans more than 165 years, from the initial discovery in 1857 by Swiss physiologist Rudolf Albrecht von Kölliker who labeled them as “sarcosomes”. Then in 1890 Richard Altmann proposed in a

transformative early histological description that they were intracellular parasites with metabolic and genetic functions in the cell and named them “bioblasts”. Finally in 1898 the term “mitochondrion” was coined by Carl Brenda from the Greek term for thread “mitos” and granule “khondros”, the plural term being “mitochondria” (Nair et al., 2022; O'Rourke, 2010). The interest in this fascinating organelle has only increased since then alongside our understanding of its importance. Furthermore, the development of new imaging techniques has revealed the highly dynamic nature of mitochondria and provided detailed structural information.

1.1 Mitochondrial structure

Mitochondria are separated from the cytosol by two phospholipid membranes called the outer mitochondrial membrane (OMM) and the inner mitochondrial membrane (IMM), which separate the interior of the mitochondria into compartments known as the matrix and the intermembrane space (IMS) (Figure 1A). The OMM, separated by the IMS, encapsulates the IMM and serves to isolate the workings of the mitochondria from the cytosol. The OMM of a mitochondrion can engage in direct contact interactions with other organelles in the cell including the endoplasmic reticulum (ER), lipid droplets, lysosomes, and other mitochondria (Audano et al., 2020; Ma et al., 2021). These contacts are facilitated by the motility granted mitochondria through their interactions with the motor proteins on microtubules and actin filaments of the cellular cytoskeleton (Kruppa & Buss, 2021; Moore & Holzbaur, 2018). The OMM does not have a maintained membrane potential (see below) relative to the cytosol and its pore-forming membrane proteins (porins) allow for free traversal of ions and small uncharged molecules. Larger molecules such as proteins are imported through the OMM by special translocases. The IMM on the other hand works as a tight diffusion barrier, preventing the passage of all ions and molecules, except by the utilization of selective membrane transport proteins that only allow the passage of a particular ion or molecule. The ion selectivity of the IMM allows for its electrochemical membrane potential. It is the process of oxidative phosphorylation (OXPHOS) taking place at the IMM through membrane bound complexes that creates the electrochemical gradient between the matrix and IMS, which is utilized for the synthesis of ATP (Kuhlbrandt, 2015).

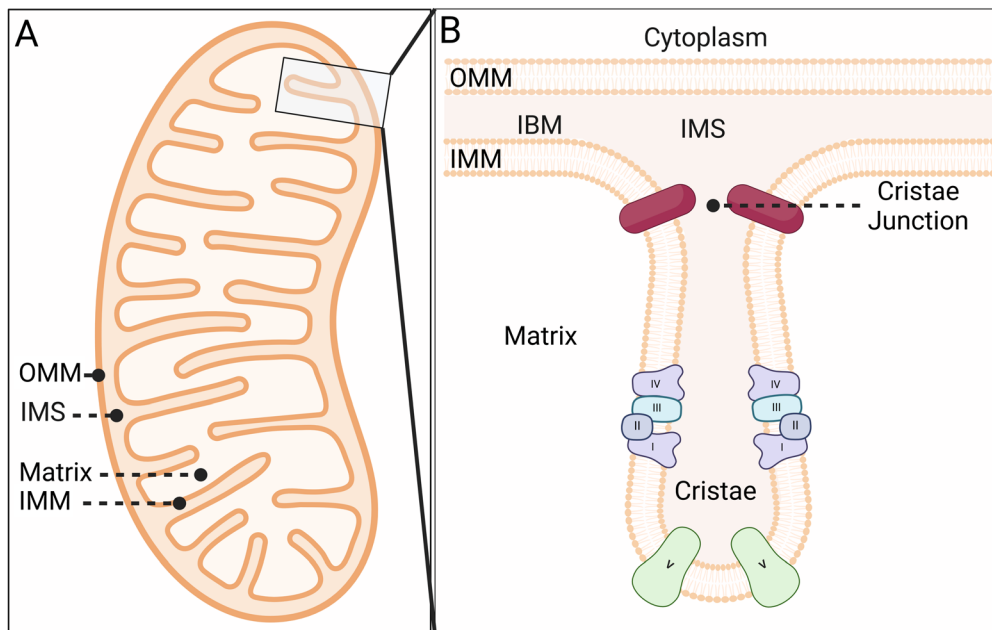


Figure 1: Overview of the structure of mitochondria. (A) An illustration of a mitochondrion with mitochondrial compartments indicated. (B) A schematic overview of the structure of mitochondrial cristae. Cristae junctions function as boundaries for the cristae. The invagination of the IMM into cristae greatly increase the IMM surface area and is important for the mitochondrial production of ATP through the electron transport chain (ETC). ETC complexes I-IV as well as complex V (ATP synthase) are indicated. Abbreviations: Inner boundary membrane (IBM); Inner mitochondrial membrane (IMM); Intermembrane space (IMS); Outer mitochondrial membrane (OMM). Image created with BioRender.com.

The IMM is organized into two morphologically distinct domains, the first of these domains is the inner boundary membrane (IBM) which is juxtaposed to the OMM creating the IMS, a ~20 nm gap between the membranes (Kuhlbrandt, 2015; Perkins et al., 1997). The IMS contains only 5% of the mitochondrial proteome but possesses the greatest variety of mechanisms for protein import. Mitochondrial proteins are imported into the organelle with numerous and varied protein translocases and import complexes that guide each protein to its intended compartment in a process governed by internal targeting sequences. Due to 99% of mitochondrial proteins being nuclear-encoded their import is crucial for mitochondrial function (Edwards et al., 2021; Rath et al., 2021).

The second IMM domain is the cristae, which is the name for the invaginations of the IMM connected to the IBM by narrow, tubular structures known as crista junctions (Figure 1B). The crista junctions function as diffusion barriers for membrane and soluble proteins, metabolites and even for protons (Kondadi et al., 2020). The junctions serve as a boundary for the cristae lumen and are important for the cristae-bound biochemical process of ATP production (Raven,

2021). The cristae take the form of multiple invaginations into the mitochondrial matrix with tubular or lamellar forms and account for most of the surface area of the IMM (Kuhlbrandt, 2015). It is within the cristae that the vast majority of electron transport chain (ETC) protein complexes necessary for ATP synthesis in the IMM operate. The cristae were for many years thought to be mostly static structures, only observed in a fixed state through electron microscopy (EM) (Gilkerson et al., 2003; Vogel et al., 2006). Recently, advanced super-resolution techniques have enabled demonstrating the highly dynamic nature of cristae and their ability to remodel on a timescale of seconds (Huang et al., 2018). These advances are promising for the continued study of the modulation of mitochondrial structure to meet the functional needs of various cell types with vastly different metabolic needs (Glancy et al., 2020).

The innermost compartment of the mitochondria, located within the confines of the IMM is the mitochondrial matrix. This is where the mitochondria perform their mitochondrial DNA replication, transcription, protein biosynthesis and a multitude of different enzymatic reactions. The pH of the mitochondrial matrix is higher than in the cytosol, between 7.9 to 8, constituting the trans-membrane electrochemical gradient necessary for ATP synthesis and the uptake of ions and metabolites into the matrix (Llopis et al., 1998; Zorova et al., 2018).

1.1.1 Electron transport chain (ETC)

The ETC consists of the transmembrane protein complexes I-IV and the two freely mobile electron transporters ubiquinone and cytochrome c. In conjunction with complex V, also known as ATP synthase, the ETC is responsible for mitochondrial energy production in the form of ATP generation by OXPHOS of tricarboxylic acid (TCA) cycle intermediates (Figure 2). Within the ETC there are two substrate specific pathways for electron transport that are supported by the TCA cycle, with NADH processed by complex I/III/IV and succinate processed by complex II/III/IV. The electron transport of these pathways is used to generate the proton gradient of the IMM that is utilized by ATP synthase (complex V) to produce ATP (Nolfi-Donagan et al., 2020; Zhao et al., 2019).

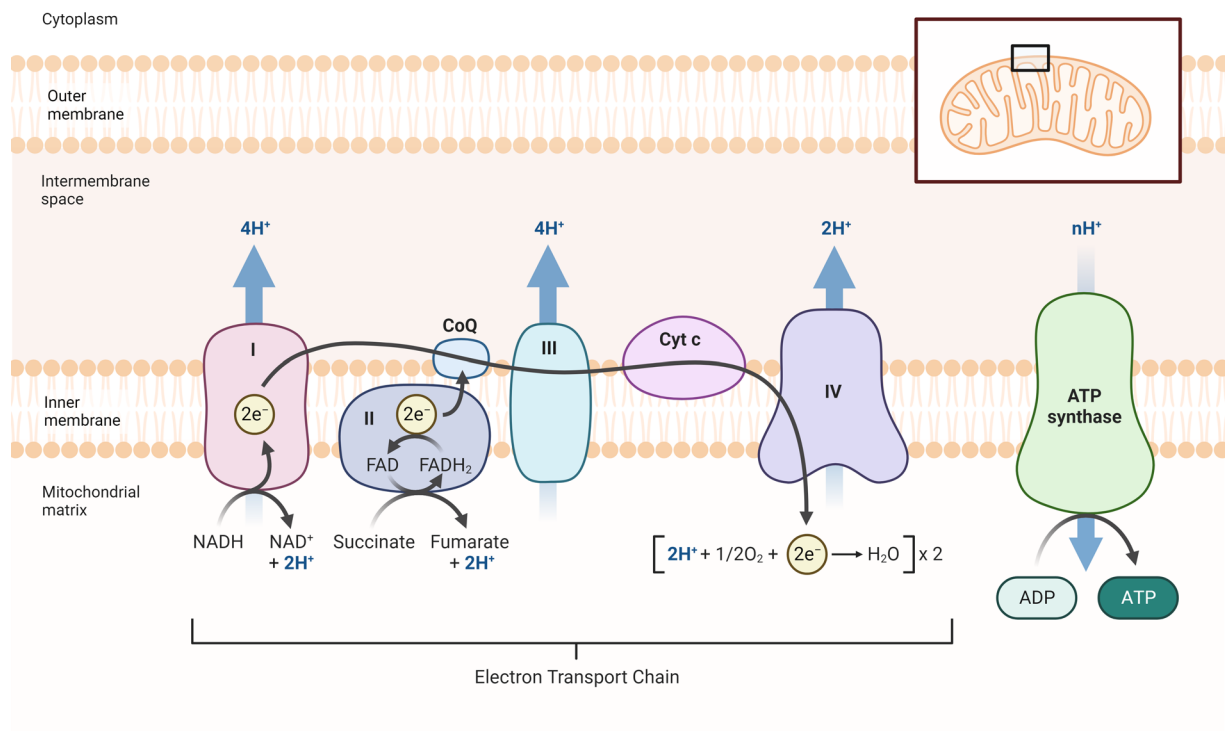


Figure 2: Schematic overview of the electron transport chain (ETC) of the mitochondria. The electron (e^-) flow used to pump protons (H^+) for ATP production is initiated by either NADH binding complex I or succinate binding complex II. The proton gradient created by pumping protons out of the matrix is exploited by ATP synthase to produce ATP. Image created with biorender.com.

The activity of the ETC produces mitochondrial ROS as a byproduct. The primary source of cellular ROS is the mitochondria, with a small portion of electrons passing through the ETC leaking out and interacting with oxygen to produce ROS instead of completing the electron transfer of the ETC (Turrens, 2003; Zhao et al., 2019). Excessive ROS can have detrimental cellular effects, but ROS can also function as an important second messenger which participates in multiple different intracellular pathways (Brand, 2016; D'Autreaux & Toledano, 2007). In its role as a signaling molecule, ROS is important in the process of hypoxia adaptation, cell proliferation, and cell fate determination. ROS is beneficial or damaging to the cellular environment dependent on the amount generated (Zhao et al., 2019). Excessive levels of ROS can cause irreversible mitochondrial impairment, disruption of ATP generation, DNA damage, protein oxidation, lipid peroxidation, and may ultimately lead to cell death through apoptosis (Orrenius et al., 2007). Given the crucial role of the ETC for cells, especially those with high energy needs, it is important that the necessary metabolic compounds are available for this process to operate.

1.1.2 Metabolic pathways

The metabolic substrates that can be processed as carbon sources by cells to take part in the TCA cycle are carbohydrates, fatty acids, and amino acids. Through their conversion into intermediate metabolites these metabolic substrates are incorporated into the TCA cycle where carbon molecules are oxidized into CO₂ and water to produce energy through the ETC. Most metabolites incorporate into the TCA cycle through acetyl coenzyme A (Acetyl-CoA) via specific pathways (Bagheri et al., 2020). The metabolic processing of carbohydrates for the TCA cycle involves the process of glycolysis in the cytosol to convert glucose into pyruvate, which is then subsequently imported into the mitochondrial matrix where it is converted to Acetyl-CoA (Arnold & Finley, 2023; Chandel, 2021b). Another carbohydrate, galactose, can also be converted into pyruvate through glycolysis, but must first be converted into the glycolysis intermediary glucose 1-phosphate through the Leloir pathway (Frey, 1996; Williams, 2003). A key difference between these two carbohydrates is that the production of pyruvate through glycolysis with glucose results in 2 net ATP being generated, while producing pyruvate through glycolysis with galactose results in no net ATP generation. This lack of ATP generation through pyruvate production with galactose adapted cells forces a heavier reliance on OXPHOS for energy production (Aguer et al., 2011). Galactose conversion to glucose 6-phosphate through the Leloir pathway is however performed at a slower rate compared to the conversion of glucose into glucose 6-phosphate. Another restriction on galactose as an energy source is that when galactose is used to replace glucose in proliferating cells the galactose will preferentially be used for the Pentose Phosphate Pathway (PPP) to provide ribose 5-phosphate which is important for cell proliferation (Chandel, 2021a). Thus, the cells instead gain ATP through OXPHOS of other metabolic substrates such as fatty acids and amino acids. For fatty acids to take part in the TCA cycle they must be imported into the mitochondria as long-chain fatty acids through the mitochondrial carnitine system. This process involves carnitine palmitoyltransferase I (CPT I) located in the OMM, carnitine-acylcarnitine translocase on the IMM, and carnitine palmitoyltransferase II (CPT II) located on the matrix side of the IMM and results in long-chain fatty acyl-CoA entering the matrix (Kerner & Hoppel, 2000). Upon β -oxidation, these long-chain fatty acyl-CoA are metabolized in multiple stages with each stage producing an acetyl-CoA which can then take part in the TCA cycle (Adeva-Andany et al., 2019). The metabolism of amino acids for the TCA cycle requires the catabolism of glutamine to produce glutamate, which can subsequently become α -ketoglutarate, a key intermediate in the TCA cycle (Wu et al., 2016).

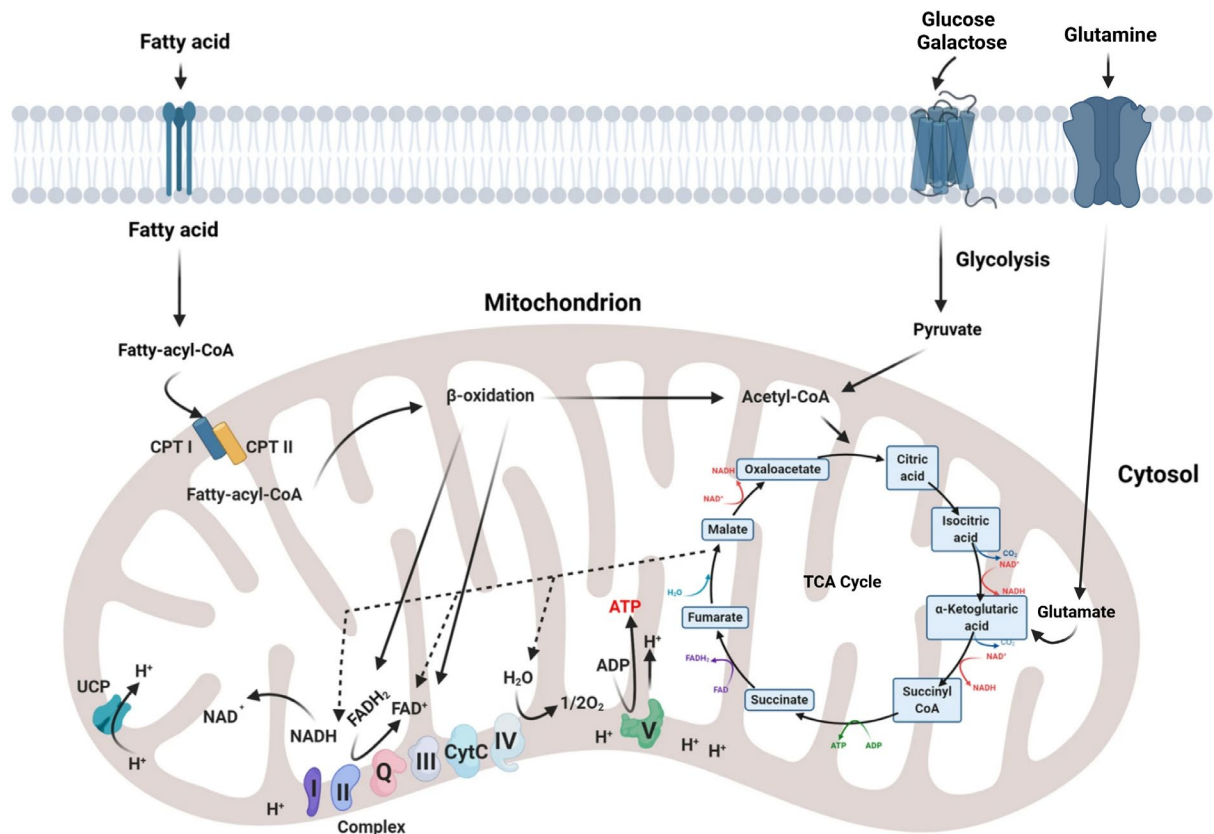


Figure 3: Overview of mitochondrial metabolic pathways. Through their involvement in the production of ATP and molecular biosynthesis, the metabolic pathways of mitochondria have a crucial role in cellular metabolism. Within mitochondria electrons are directed to the ETC (complex I-IV) through oxidation of pyruvate, fatty acids, and amino acids (glutamine). The placement of illustrated ETC components is not representative of their actual localization in mitochondria. Abbreviations: Carnitine palmitoyltransferase I, II (CPT1, CPT2), Cytochrome c (CytC), Flavin adenine dinucleotide (FADH), Nicotinamide adenine dinucleotide (NADH), and Uncoupling proteins (UCPs). Figure adapted from (Bagheri et al., 2020) using BioRender. Used with permission according to Creative Commons Attribution 4.0 International License (<http://creativecommons.org/licenses/by/4.0/>).

In addition to its role in generating energy for the cell through ATP production, the TCA cycle serves an important role in biosynthesis with several of its intermediate products serving as critical precursors for macromolecule biosynthesis. An example of this is α -ketoglutarate which can be converted to glutamate and diverted from the TCA cycle to take part in synthesis of amino acids and nucleotides (Arnold & Finley, 2023). To meet their metabolic needs, cells require a carbon source, both as an energy source and for biosynthesis (Kurniawan et al., 2021). Cultured mammalian cells often utilize glucose as their primary carbon source, and this causes many cell lines to become highly glycolytic and less reliant on OXPHOS for energy production. Using galactose as a primary carbon source forces cells to rely on OXPHOS for energy production. Increasing mitochondrial activity by OXPHOS induction enhances their

susceptibility to damage and facilitates the study of mitochondrial dysfunction (Aguer et al., 2011; Hossler et al., 2017).

2 Mitochondrial quality control

The crucial nature of mitochondria for the health of the individual cell and organism has resulted in the evolution of interconnected quality control mechanisms that ensure their function (Figure 4). For mitochondria there are three mechanisms that serve as protein quality control checkpoints (Figure 4, A-C); the ubiquitin (Ub)-proteasome system (UPS), precursor-associated degradation, and the mitochondrial proteases. The mitochondria can also initiate a nuclear transcriptional response (Figure 4, D) through the signaling cascade of the mitochondrial unfolded protein response (UPR) which induces chaperone and protease gene expression to reduce the mitochondrial protein burden in response to accumulation of aberrant proteins. The mitochondrial organellar quality control checkpoints (Figure 4, E-G) encompass mitochondrial fusion/fission, mitophagy, and mitochondria derived vesicles (Ng et al., 2021).

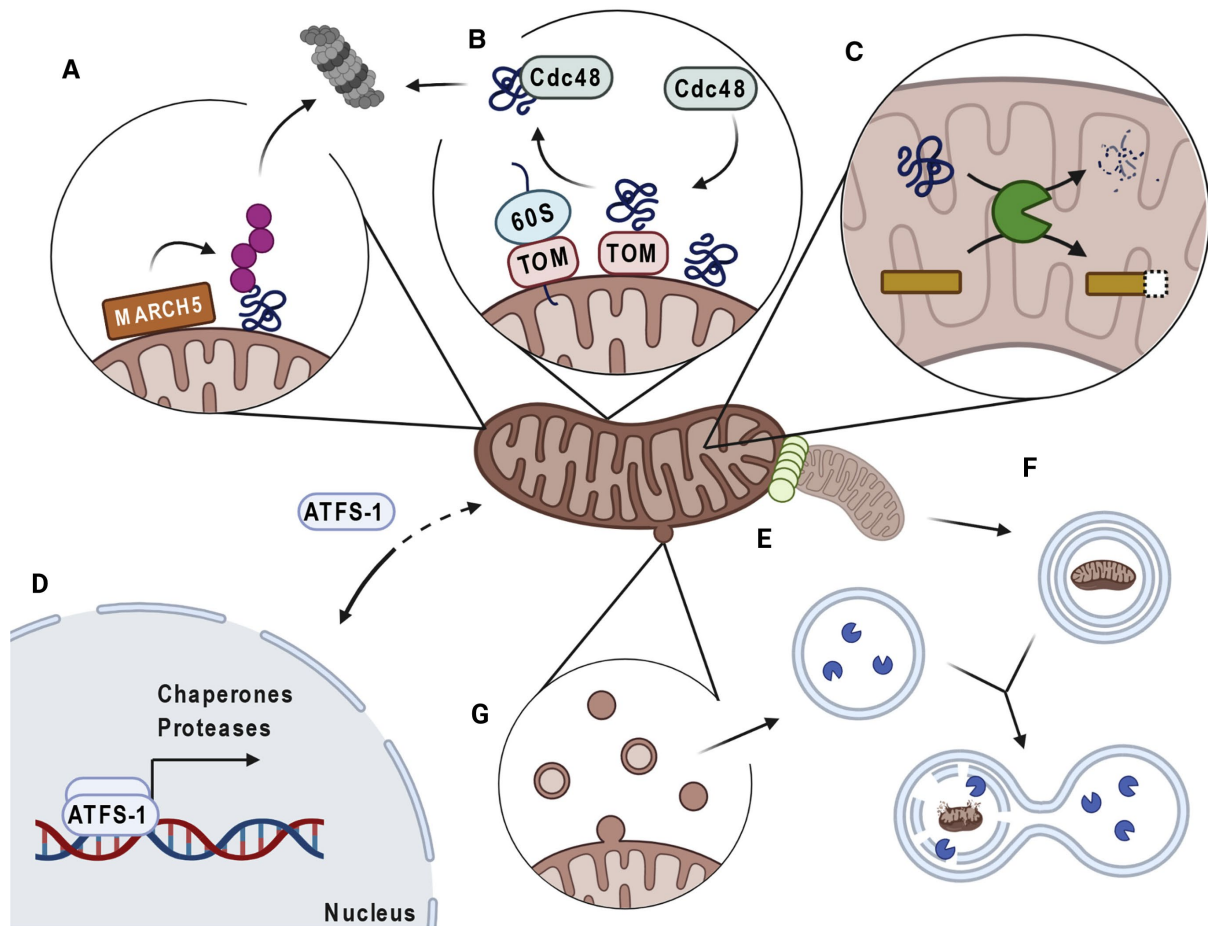


Figure 4: Mitochondrial protein and organelle quality control mechanisms. (A) The Ubiquitin proteasome system (UPS) uses E3 ubiquitin ligases (such as MARCH5) to conjugate mitochondrial proteins with polyubiquitin chains (purple) that target those to degradation by the proteasome. (B) Aberrant proteins on the OMM are removed and delivered for proteasomal degradation. (C) The proteases of the mitochondria are involved in regulatory functions and quality control within the mitochondrial compartments. (D) Transcription factors, such as ATFS-1, can be activated by mitochondrial UPR as a response to mitochondrial stress for the induction of chaperone and protease gene expression. (E) Fusion and fission (green dots) events regulate mitochondrial morphology. (F) The process of mitophagy involves engulfment of mitochondrial fragments targeted for degradation into autophagosomes which subsequently fuse with lysosomes to degrade their cargo. (G) Mitochondria derived vesicles can form from the OMM, or the OMM and IMM, and contain selected mitochondrial cargo targeted to lysosomes for degradation or to other organelles for different purposes. Abbreviations: Stress activated transcription factor *atfs-1* (ATFS-1). Adapted from (Ng et al., 2021) with permission.

Due to the importance of mitochondrial quality control mechanisms for maintaining a healthy pool of mitochondria there can be severe consequences for the organism when these mechanisms are dysfunctional. The focus below will be on the organellar quality control checkpoints, with the primary focus on mitophagy.

2.1 Regulation of mitochondrial morphology

The morphology of mitochondria is highly dynamic and varies greatly between different cell types, reflecting the metabolic demands of the cell type or tissue. The inter-connected nature of the functions and dynamics of mitochondria is reflected by morphology changes resulting from activity such as ongoing mitochondrial respiration or the induction of apoptosis. The effects of mitochondrial dynamics play an important role in the ability of cells to respond and adapt to physiological changes (Serasinghe & Chipuk, 2017; Vafai & Mootha, 2012). Changes in mitochondrial morphology occur when there is a shift in the balance between the two highly regulated and opposing processes of mitochondrial fission and fusion (Figure 5A). Fission refers to a process where a mitochondrion is divided into two mitochondria, and fusion implicates two mitochondria merging to form a single mitochondrion. These two processes and the ability of mitochondria to move throughout the cell is collectively referred to as mitochondrial dynamics (Serasinghe & Chipuk, 2017). The dynamic nature of mitochondrial morphology is further highlighted by another means of mitochondria-to-mitochondria communication called mitochondrial nanotunnels. These thin tubular structures have a diameter between 40 and 200 nm and can extend in length up to 30 μm from a mitochondrion, allowing connections to be formed with other mitochondria. The process involves both the IMM and OMM and contributes to the transfer of mitochondrial matrix contents (Lavorato et al., 2017; Vincent et al., 2017). Interestingly, dynamic mitochondrial tubules with similarities to nanotunnels have been reported in several cell lines (Qin et al., 2020; Wang et al., 2015).

Fusion and fission events also allow for the exchange and mixing of both mtDNA and mitochondrial proteins. Removal of damaged mitochondria components through degradation by mitophagy (see below) is often preceded by fission of the damaged components from the rest of the mitochondria network. The biogenesis of mitochondria, as well as their distribution to daughter cells when cells undergo cell division, is also tied to mitochondrial fission. Abnormalities and disruptions to the coordination of mitochondrial dynamics can negatively affect cellular functions and stress responses and act as a key element in the manifestation of diseases such as cancer, cardiomyopathies, metabolic disorders and neuro-degenerative diseases (Serasinghe & Chipuk, 2017).

2.1.1 Fusion

The process of mitochondrial fusion is coordinated by the three large dynamin-related GTPases, termed mitofusin 1 (Mfn1), mitofusin 2 (Mfn2) and optic atrophy 1 (OPA1) (Figure 5B). Mitochondrial fusion proceeds through the activation of these proteins in three stages (Yu et al., 2020). The first stage of this process is the tethering of two mitochondria with guanosine triphosphate (GTP) hydrolysis acting as the driving force of the conformational change that brings the two membranes into contact. Cycles of GTP hydrolysis induce positioning of a linear arrangement of proteins referred to as a docking ring around the contact point where the OMM of the two mitochondria meet. During the second stage the two membranes are fused together from the periphery of their contact point, triggered by further GTP hydrolysis of Mfn1/Mfn2 (Brandt et al., 2016). In the final stage, fusion of the IMM is mediated by OPA1 (Yu et al., 2020). Cells suffering from a deficiency or loss of fusion proteins have increased mitochondrial fragmentation (Ichishita et al., 2008).

2.1.2 Fission

The process of mitochondrial fission can be divided into two types, midzone and periphery, with distinct functions and molecular machineries for each. Midzone fission, where a fission event occurs in the middle of a mitochondrion which is defined as corresponding to a central point within 50% of its total length, is associated with mitochondrial proliferation. Conversely, periphery fission is a fission event that occurs at a point that is less than 25% by length from the tip of a mitochondrion and is associated with mitochondrial degradation. Both types of fission are mediated by dynamin-related protein 1 (DRP1) (Kleele et al., 2021). DRP1 recruitment to the mitochondria is aided by the mitochondria-bound proteins mitochondrial fission factor (MFF) and mitochondrial dynamics protein 49 and 51 kDa (MiD49 and MiD51, respectively), some of which have overlapping functions (Loson et al., 2013). The specific mechanisms determining if a mitochondrial fission event will be midzone or periphery are not fully known but there are distinct differences. Midzone mitochondrial fission in the human osteosarcoma cell line (U2OS) begins with the fission site having contacts with the ER and coordinated actin polymerization (Korobova et al., 2013), the location where this occurs is also the site of concurrent mtDNA replication in the matrix (Lewis et al., 2016). The recruitment of actin filaments at the fission site is linked to DRP1 accumulation (Ji et al., 2015), which begins after constriction of the OMM initiates. In African green monkey Cos-7 cells and mouse

cardiomyocytes the adaptor protein MFF is primarily associated with midzone mitochondrial fission, accumulating at sites for midzone constriction (Kleele et al., 2021).

In most periphery mitochondrial fission events, before the recruitment of DRP1, an internal gradient within the mitochondria forms. There is a decrease in membrane potential and proton motive force alongside an increase in ROS and Ca^{2+} levels constituting the gradient towards the tip of the mitochondrion. This is speculated to function as a positioning cue for the fission event, allowing labeling of a division site without the mitochondria interacting with other organelles. There are also lysosomal contacts with the OMM in the area preceding the fission event, but in most cases, there are no ER contacts and no actin polymerization. The OMM protein fission mitochondrial 1 (FIS1) appears to play a still elusive regulatory role in periphery mitochondrial fission. FIS1 does not accumulate at fission sites but is rather evenly distributed on mitochondria, with the smaller daughter mitochondria resulting from periphery fission enriched with FIS1 (Kleele et al., 2021). The above findings reveal the complex mechanisms and regulatory events involved in mitochondrial fusion and fission events. These intricate mechanisms also impact on the degradation of dysfunctional mitochondria by mitophagy.

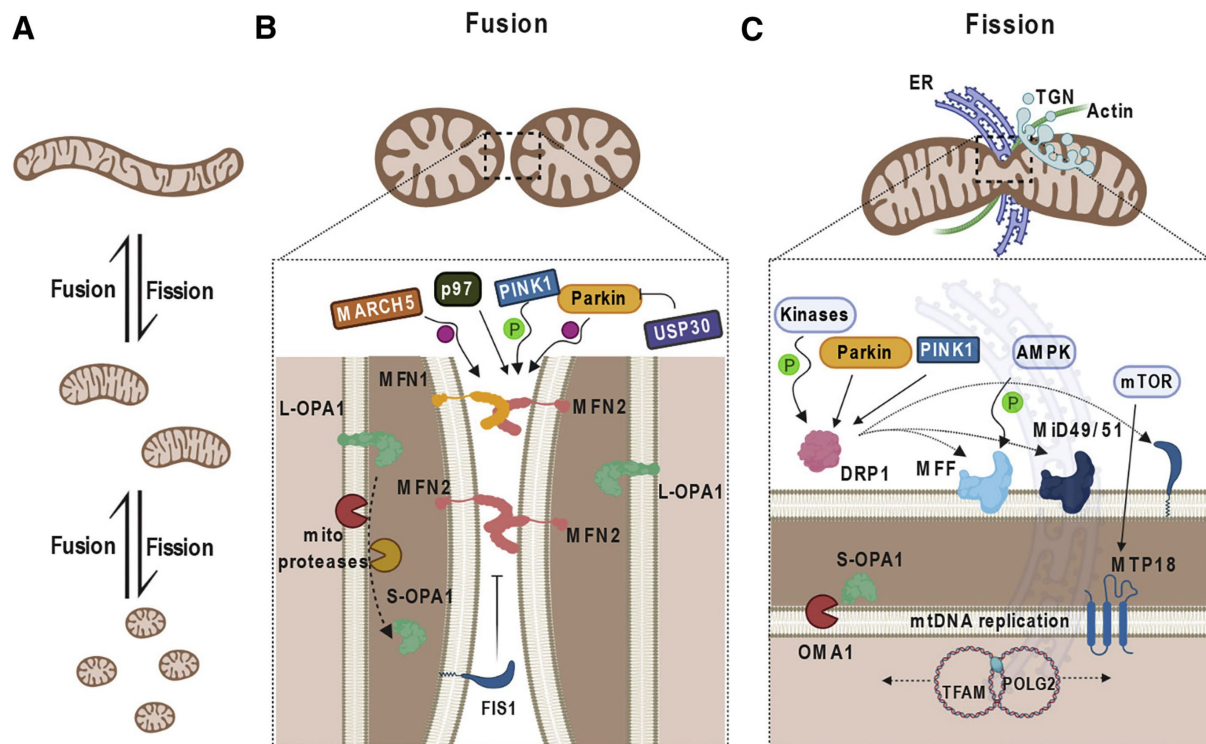


Figure 5: Regulation of mitochondrial morphology. (A) Shifts in the balance between fusion and fission events in response to stimuli results in dynamic changes to mitochondrial morphology. (B) Schematic overview of mitochondrial fusion. OMM and IMM fusion is mediated by the dynamin-like GTPases MFN1/2 and L-OPA1, respectively. Mitochondrial fusion is regulated by ubiquitination, undergoing post-translational modification (MARCH5, p97, PARKIN), deubiquitination by USP30, or phosphorylation by PINK1. The mitoproteases OMA1 and YME1L can also take part in regulation through proteolytic cleavage. OMM fusion is inhibited by FIS1. (C) Schematic overview of mitochondrial fission. Where the OMM is in contact with the ER and actin, DRP1 binds to MFF or MiD49/51. Downstream of DRP1 the *Trans*-Golgi network (TGN) completes mitochondrial fission. As part of IMM fission TFAM and POLG2 mediate mtDNA replication. OMA1 generates an accumulation of S-OPA1 which accelerates fission. Abbreviations: mitochondrial fission process 1 (MTP18), DNA polymerase gamma 2 accessory subunit (POLG2), valosin containing protein (p97), transcription factor A mitochondrial (TFAM), trans-Golgi network (TGN), short isoform OPA1 (S-OPA1), long isoform OPA1 (L-OPA1). Adapted from (Ng et al., 2021) with permission.

2.2 Mitophagy

The process of selective degradation of mitochondria by autophagy is termed mitophagy. It serves as the mechanism of mitochondrial quality control where dysfunctional or surplus mitochondria undergo lysosomal degradation. Despite the many quality control measures available to cells for maintaining the health of their mitochondrial population, the mitochondria gradually develop dysfunction (Ashrafi & Schwarz, 2013). Conditions of cellular stress

affecting the mitochondria, such as oxidative stress or starvation, increase the prevalence of dysfunctional mitochondria (De Gaetano et al., 2021). The initiation of mitophagy is regulated with complex mechanisms that designate persistently dysfunctional mitochondria or parts of mitochondria to proceed with the process and undergo lysosomal degradation (Ashrafi & Schwarz, 2013). Their degradation avoids the accumulation of damaged mitochondria and protects the cell from pro-apoptotic signaling (Kubli & Gustafsson, 2012). The components of the dysfunctional organelle also get recycled through the acidic hydrolase enzymes of the lysosome resulting in e.g. amino acids and fatty acids available for the cell to reuse (Kriegenburg et al., 2018).

Macroautophagy, henceforth referred to simply as autophagy, is a highly conserved cellular process that serves to degrade organelles and cellular components in lysosomes and recycles their macromolecules. This is accomplished through sequestration by double-membrane vesicles called autophagosomes that subsequently deliver their cargo to lysosomes. There are various types of autophagy, and autophagy can be categorized as nonselective or selective. Nonselective autophagy is an engulfment of random portions of the cytoplasm into autophagosomes and their subsequent degradation. Selective autophagy differs in that it targets and sequesters a specific cargo, such as a protein complex, an organelle, or an invasive microbe. The double membrane sequestering compartment that arises during the engulfment process is referred to as a phagophore which then expands and closes into an autophagosome (Jin et al., 2013). Autophagy serves as a method to relieve various forms for cellular stress and plays a key role in many processes, including cellular development and differentiation (Yang & Klionsky, 2009).

The study of autophagy has advanced significantly since Christian de Duve's 1963 use of the term autophagy with its current definition of self-eating damaged or redundant cellular components within a cell, eight years after de Duve's discovery of the lysosome in 1955 (Klionsky, 2008). Work by Yoshinori Ohsumi and others resulting in the identification of autophagy genes in yeast during nitrogen starvation in the 1990s serves as a breakthrough (Mizushima et al., 1998; Tsukada & Ohsumi, 1993) that functions as a foundation for autophagy research to this day (Mizushima, 2018; Ohsumi, 2014). This breakthrough led to the identification of the mammalian counterparts to the yeast autophagy genes, which are now known to encode core autophagy machinery. This includes the core autophagy protein identified as ATG1 in yeast, with the mammalian ortholog later being identified as unc-51 like autophagy activating kinase 1 (ULK1) (Chan et al., 2007). ULK1 forms a complex with

ATG13, ATG101 and FAK family-interacting protein of 200 kDa (FIP200), termed the ULK1 complex (Figure 6A), which plays a central role in initiating the autophagy process and integrating signals for starvation-induced autophagy (Jung et al., 2009). Upstream signals are transduced by the ULK1 complex from sensors such as mammalian target of rapamycin (mTOR) and adenosine monophosphate activated protein kinase (AMPK) to regulate the autophagy pathway (Kim et al., 2011). When the ULK1 complex is activated and translocated to the phagophore formation sites at the ER it recruits ATG9, a lipid scramblase essential for phagophore growth, and the phosphatidylinositol 3-kinase (PtdIns3K) complex (Brier et al., 2019; van Vliet et al., 2022). The autophagy specific Complex I (C1) variant of the PtdIns3K (Figure 6B) consists of kinase subunit vacuolar protein sorting 34 (VPS34), phosphoinositide-3-kinase regulatory subunit 4 (PIK3R4, also known as VPS15), Beclin-1 and ATG14L. PtdIns3K-C1 is involved in the nucleation of the phagophore through inducing production of phosphatidylinositol-3-phosphate (PI3P) at the phagophore formation site, which is critical for autophagosome biogenesis and maturation (Choi et al., 2018; Mizushima et al., 2011). The phagophore membranes are elongated in this process and further formation of the autophagosome involves the ATG8 proteins and is dependent on two ubiquitin-like conjugation processes. The first involves ATG12-conjugation to ATG5, resulting in the ATG12-ATG5:ATG16L complex (Figure 6C). The second involves ATG8 conjugation to phosphatidylethanolamine (PE) dependent on protease cleavage of ATG8 (Figure 6D and 6E) (Choi et al., 2018; Tanida et al., 2004). The ATG8 protein family are ubiquitin-like proteins with seven functional ATG8 genes in the human genome further divided into two subfamilies; microtubule-associated proteins 1A/1B light chain 3 (LC3) subfamily (LC3A, LC3B, LC3B2, LC3C) and the gamma-aminobutyric acid receptor associated protein (GABARAP) subfamily (GABARAP, GABARAPL1, and GABARAPL2) (Shpilka et al., 2011). Unlike ubiquitin which conjugates to a target protein's lysine residue, ATG8 proteins conjugate to the membrane lipid headgroup of PE. This process, termed ATG8-lipidation, is a major hallmark of the autophagy process and has important roles in phagophore elongation and both cargo selection and recruitment (Ichimura et al., 2000; Martens & Fracchiolla, 2020). The ATG12-ATG5:ATG16L1 complex enables conjugation of ATG8 family proteins to PE, incorporating them into the growing phagophore membrane (Bento et al., 2016). The ATG8-protein has to undergo cleavage by protease (ATG4) to attach to PE and both ATG12-conjugation and ATG8-processing work in tandem to mediate ATG8 conjugation to PE (Figure 6E) (Tanida et al., 2004). PE-conjugated LC3 plays a critical role in autophagic membrane expansion and lysosomal fusion through its oligomerization and ability to tether membranes (Choi et al., 2018;

Nakatogawa et al., 2009). An important member of the autophagy machinery taking part in both the ATG12-conjugation and ATG-8 conjugation pathways is ATG7, an E1 activating enzyme (Lystad & Simonsen, 2019). Further autophagy-related functions of ATG7 involve membrane trafficking events dependent on ATG8 lipidation (Collier et al., 2021). Cargo selection and recruitment to autophagosomes involves ubiquitinated substrates being recognized by autophagy receptors such as sequestosome 1 (SQSTM1, also known as p62) (Figure 6F) which can bind to PE-conjugated LC3. Finally, autophagosome maturation and lysosomal fusion involves the Complex II (C2) variant of the PtdIns3K (Figure 6G), which contains VPS34, VPS15, Beclin-1, and UV radiation resistance-associated gene product (UVRAG) (Luo et al., 2020).

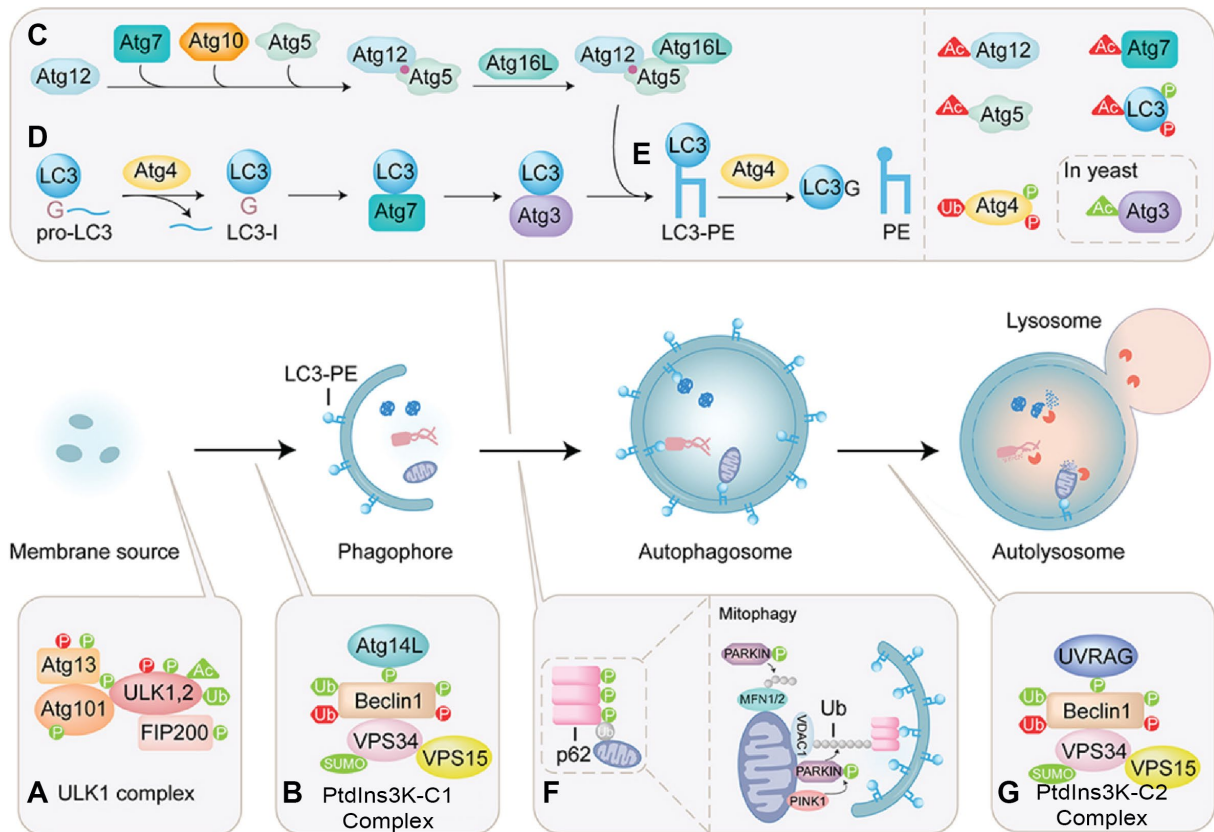


Figure 6: Overview of autophagosome formation process. (A) The ULK1 complex initiates induction of autophagy and activates (B) the PtdIns3K-C1 complex resulting in the formation of the phagophore. The elongation and closure of the autophagosome is mediated by the two ubiquitin-like conjugation systems (C-E). Cargo selection and recruitment (F) involves autophagy receptors such as p62 that recognize ubiquitinated substrates. (G) The PtdIns3K-C2 complex then mediates autophagosome maturation and lysosomal fusion. Post-translational modifications applied to ATG proteins are also displayed, green for positive regulation of the autophagy process and red for inhibition of the autophagy process. Abbreviations for post-translational modifications are phosphorylation (P), acetylation (Ac), ubiquitination (Ub), and sumoylation (SUMO). Figure adapted from (Luo et al., 2020). Used with permission according to Creative Commons Attribution 4.0 International License (<http://creativecommons.org/licenses/by/4.0/>).

The term mitophagy was first defined as a selective form of autophagy targeting mitochondria by Lemasters in 2005 (Lemasters, 2005), after first being used in 1998 (Scott & Klionsky, 1998) and has since become a research subject of great interest. Its implication in ageing and human pathologies, such as neurodegenerative disorders, cardiovascular diseases, and cancer, are the reason mitophagy is studied with an eye toward potential long-term advances in medicine. Current research focuses on uncovering the specific pathways regulating mitophagy, cell type

variations, potential therapeutic approaches, and the specifics of its initiation under different physiological conditions (Chen et al., 2020; Palikaras et al., 2018).

Based on the physiological context mitophagy can be subdivided into three categories as basal, stress-induced, and programmed mitophagy (Palikaras et al., 2018). The first of these, basal mitophagy, is the mitophagy cells undergo under normal conditions. It is a continuous process, sometimes called mitochondrial housekeeping, that ensures a healthy mitochondrial population through the recycling of damaged and old organelles (McWilliams et al., 2016; Sun et al., 2015). Basal mitophagy will be discussed in greater depth in a separate section below. The second category is stress-induced mitophagy, occurring when extracellular stress affects the mitochondrial physiology. If this extracellular stress places significant strain on the mitochondria to the point where first in line quality control mechanisms are insufficient, the induction of stress-induced mitophagy allows for enhanced mitochondrial clearance. This enhanced process is crucial for adjusting the cell's metabolic state to meet external challenges. Stress-induced mitophagy is the most studied form of mitophagy. Elevated mitophagy produced through induction of cellular stress is a key methodology for studying mitochondria degradation and imperative to past and present investigations (Palikaras et al., 2018). Sources of stimuli that cause stress-induced mitophagy include oxidative stress, hypoxia, nutrient starvation, and loss of mitochondrial membrane potential (Panigrahi et al., 2020). These forms for stimuli can be induced through controlled treatments in a laboratory setting. Oxidative stress can be induced through a metabolic switch forcing cells to rely on OXPHOS for their ATP production (Allen et al., 2013). Oxidative stress will also be induced as a byproduct of other forms of stress such as hypoxia, nutrient availability, and changes to mitochondrial membrane potential (Kowalczyk et al., 2021). Hypoxia-like conditions can be induced through oxygen deprivation, causing the stabilization of the protein hypoxia-inducible factor 1-alpha (HIF1 α) which drives the transcriptional response for low oxygen adaption. Loss of iron through iron chelator deferiprone (DFP) treatment almost abolishes oxygen consumption within 24 hours and stabilizes the HIF1 α protein through disruption of its degradation (Allen et al., 2013; Bellot et al., 2009; Pugh, 2016). Nutrient starvation is induced by placing cells in a nutrient deprived environment, forcing their reliance on non-selective autophagy as a source of essential amino acids and nutrients as well as inducing selective autophagy for damaged or excessive organelles (Ding & Yin, 2012). Finally, inducing loss of mitochondrial membrane potential can be done chemically with substances such as carbonyl cyanide m-chlorophenyl hydrazine (CCCP) which opens the permeability transition pore in the IMM (Miyazono et al., 2018) or Antimycin A which inhibits

complex III of the ETC (Hytti et al., 2019). The third category is programmed mitophagy which different cell types activate during their development (Palikaras et al., 2018). Examples of this include erythrocytes, which completely remove their mitochondria during maturation (Sandoval et al., 2008), and the fertilization triggered degradation of sperm-derived mitochondria in oocytes (Sato & Sato, 2011). Also cardiomyocyte maturation involves programmed mitophagy. During cardiomyocyte maturation, fetal mitochondria using glucose as their primary energy source for ATP production are removed by mitophagy and replaced with new reformed mitochondria that preferentially use fatty acids for their energy needs. This process allows for a functional and morphological transition that enables the cardiomyocytes to meet the adult heart's energy demands (Gong et al., 2015). Programmed mitophagy also plays a key part in the metabolic rewiring necessary for induced pluripotent stem cell generation by somatic cell reprogramming and subsequent cellular differentiation (Xiang et al., 2017; Yang et al., 2022). Advances in human pluripotent stem cell generation and differentiation, with their great potential for therapeutic use, have boosted interest in programmed mitophagy (Cairns et al., 2020; Krantz et al., 2021; Mostafavi et al., 2021).

New microscopy assays allow for both *in vitro* and *in vivo* visualization of mitophagy by different means, facilitating live cell experiments and observations (Kobayashi et al., 2020a; Sun et al., 2017). Central to one of these mitophagy assays is mt-Keima, which works by utilizing the expression of a pH-dependent dual-excitation ratiometric fluorescence protein located to the mitochondrial matrix. The dual-excitation predominantly favors the shorter of its two wavelengths at physiological pH and will gradually shift to the longer wavelength when exposed to the lower pH of an acidic environment such as within a lysosome. However, due to its pH-dependent nature the protein is limited to use in live cells and fresh tissues as an acidic environment is required to maintain its longer wavelength state (Sun et al., 2017). Another approach is characterized by the application of two tandem fluorescent tags to a target protein, with one tag being sensitive and the other insensitive to pH changes. The use of a fused enhanced green fluorescent protein (EGFP) and mCherry tag is one method for this, with the pH-sensitive EGFP tag being quenched in acidic environments and the mCherry tag remaining fluorescent. This enables a clear distinction for the target protein's localization between acidic and non-acidic environments (Hundeshagen et al., 2011; Shaner et al., 2005). The most prominent double-tag reporters in use for mitophagy assays are Mito-QC and mt-Rosella, used to assess both *in vivo* and *in vitro* mitophagy (Fang et al., 2017; Palikaras & Tavernarakis, 2017; Rosignol et al., 2020). Mito-QC utilizes the above described mCherry-EGFP model to detect

mitochondrial degradation through the expression of a functionally inert mitochondrial targeting sequence of the OMM protein FIS1 with a fused fluorescent double-tag (McWilliams et al., 2016). Meanwhile, mt-Rosella consists of the pH-insensitive DsRed fused with the pH-sensitive GFP, locating to the mitochondrial matrix when used with its mitochondrial targeting sequence (Kobayashi et al., 2020a). The double-tag reporters are usable with both live and fixed cells, giving the approach greatly increased flexibility with experimental planning and quantitative imaging (Hobro & Smith, 2017) compared to mt-Keima.

2.2.1 Mitophagy Pathways

Through multiple signaling cascades activated by different promoting stimuli in distinct cellular contexts, mitophagy can be initiated through multiple mechanisms (Palikaras et al., 2017). Mitophagy regulatory pathways engage in complex crosstalk to meet the needs of the cell encountering different sources of mitochondrial stress (Pickles et al., 2018). Our still limited mechanistic knowledge of mitophagy complicates the process of separating distinct pathways. However, there exists distinctions by which they may be categorized, with one such distinction being if initiation of mitophagy requires the soluble sequestosome-like receptor (SLR) proteins or the OMM localized mitophagy receptors (Ganley & Simonsen, 2022). The best characterized mitophagy pathway is the SLR-dependent PINK1-PARKIN pathway (Iorio et al., 2021). There are however other SLR-dependent pathways that are independent of PINK1-PARKIN which will be presented separately below. The SLR-independent pathways will then be presented before finally looking at the still largely unknown, ATG8-lipidation independent, alternative mitophagy pathway.

2.2.1.1 SLR-dependent mitophagy – PINK1-PARKIN dependent

In healthy mitochondria PTEN-induced putative kinase 1 (PINK1) is imported and cleaved by mitochondrial proteases before undergoing proteasomal degradation (Figure 7A). This process is dependent on the membrane potential of the mitochondria, as upon depolarization PINK1 accumulates on the OMM (Greene et al., 2012; Jin et al., 2010; Yamano & Youle, 2013). The PINK1 accumulating on the OMM is in a stabilized form that mediates phosphorylation of ubiquitin conjugated to OMM proteins, leading to parkin RBR E3 ubiquitin protein ligase (PRKN, also known as PARKIN) recruitment and activation (Figure 7B) (Ganley & Simonsen,

2022; Wauer et al., 2015). Polyubiquitylation of OMM proteins is then primarily performed by PARKIN, with several other E3 ubiquitin ligases also able to contribute with polyubiquitylation of OMM proteins. This includes membrane-associated ring-CH-type finger 5 (MARCF5) which is proposed to assist PARKIN recruitment and activation by performing protein ubiquitylation prior to phosphorylation by PINK1 (Koyano et al., 2019).

Ubiquitylated OMM proteins can then interact with SLR receptors through specific ubiquitin-binding domains within the SLRs. By binding to ubiquitin and ATG8s the SLRs connect polyubiquitylated mitochondria to the phagophore membrane (Ganley & Simonsen, 2022). Members of this family of proteins implicated in mitophagy include SQSTM1/p62, calcium-binding and coiled-coil domain 2 (CALCOCO2; also known as NDP52), and optineurin (OPTN) (Dikic & Elazar, 2018). The first of these, p62, has been shown to be involved in mitophagy in leukemia cells and macrophages (Nguyen et al., 2019; Zhong et al., 2016). The two others, NDP52 and OPTN, are recruited by PINK1 in HeLa cells as autophagy receptors for PINK1-PARKIN dependent mitophagy, where they recruit autophagy factors including ULK1 (Lazarou et al., 2015). The ability of these SLRs to interact with ATG8 proteins on autophagosome membranes is facilitated by their LC3-interacting region (LIR) (Johansen & Lamark, 2020). LIR motifs, a conserved feature of the autophagy pathway, are short peptide motifs which interact with LC3/GABARAB through hydrophobic interactions (Farnung et al., 2023). Through phosphorylation of residues surrounding and within the LIR motif their interactions can be modulated, as is the case with OPTN which is regulated in this manner by ULK1 and TANK-binding kinase 1 (TBK1) for PARKIN-dependent mitophagy (Harding et al., 2021). The process of binding to ubiquitylated OMM proteins on damaged mitochondria can further modulate autophagy receptors and take part in their recruitment. This includes externalized matrix proteins in depolarized mitochondria such as 4-Nitrophenylphosphatase domain and non-neuronal SNAP25-like protein homolog 1 (NIPSNAP1) and NIPSNAP2. These externalized matrix proteins stabilize on the OMM where they serve as degradation signals and are involved in the recruitment of p62 and NDP52 (as well as other SLRs) (Princely Abudu et al., 2019).

For dysfunctional or damaged mitochondria, the coordinated actions of SLRs and ATG8s in their complex interactions with mitochondrial membrane proteins and lipids underlie the resulting mitophagosome membrane biogenesis around the organelle (Ganley & Simonsen, 2022). However as shown in HeLa cells by Nguyen in 2016, PINK1-PARKIN dependent mitophagy is not vitally dependent on ATG8s for cargo selection and autophagosome

formation, although they are needed for fusion between the autophagosome and lysosome (Figure 7C). The complete loss of the ATG8s did however result in both a reduction in autophagosome formation rate and the resulting autophagosomes were smaller (Nguyen et al., 2016). Another finding indicates that ATG8s form a ATG8-dependent positive feedback loop through their recruitment of the SLRs OPTN and NDP52. By recruiting these SLRs via their LIR motifs to growing phagophore membranes in a ubiquitin-independent manner, autophagosome growth is increased and it enhances selective autophagy following autophagosome initiation. This enhancement is accomplished in part by the SLRs recruiting additional ULK1 complexes which further amplify autophagosome biogenesis and mitophagy (Padman et al., 2019). Another connection between NDP52 and ULK1 is seen during PINK1-PARKIN dependent mitophagy where the ULK1 complex has enhanced membrane binding triggered through the promotion of FIP200 recruitment to the mitochondrial membrane by NDP52 (Shi et al., 2020; Vargas et al., 2019). The SLR's recruitment of the ULK1 kinase complex shows their involvement in *de novo* biogenesis of phagophore membranes, expanding their known roles in autophagy (Ravenhill et al., 2019; Turco et al., 2019; Vargas et al., 2019).

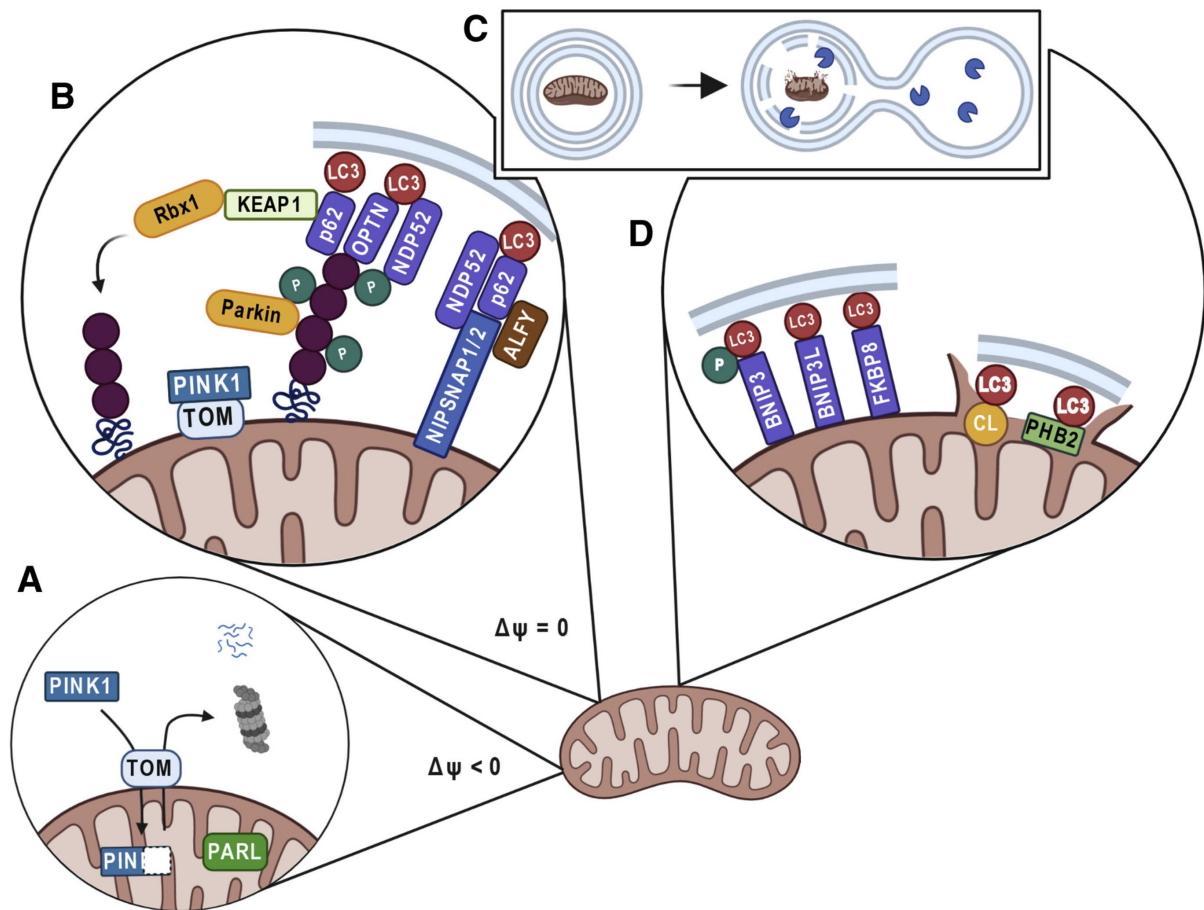


Figure 7: Overview of mitophagy pathways. (A) Healthy mitochondria import PINK1, it is cleaved by mitochondrial proteases, released to the cytosol, and undergoes proteasomal degradation. (B) SLR-dependent PINK1-PARKIN dependent mitophagy. (C) Engulfment of mitochondria in double-membrane autophagosomes precede lysosomal fusion and mitochondrial degradation. (D) SLR-independent mitophagy. Abbreviations: WD repeat and FYVE domain containing 3 (ALFY), BCL2 interacting protein 3 (BNIP3), BCL2 interacting protein 3 like (BNIP3L), cardiolipin (CL), FKBP prolyl isomerase 8 (FKBP8), kelch like ECH associated protein 1 (KEAP1), presenilin associated rhomboid like (PARL), prohibitin 2 (PHB2), ring-box 1 (RBX1). Adapted from (Ng et al., 2021) with permission.

2.2.1.2 SLR-dependent mitophagy – PINK1-PARKIN-independent

SLR-dependent mitophagy appears to have redundancies in the form of several E3 ubiquitin–protein ligases with similar function to PARKIN. Included among these is mitochondrial E3 ubiquitin–protein ligase 1 (MUL1) which is anchored to the OMM and together with PINK1 synergistically promotes mitophagy (Calle et al., 2022). MUL1 is shown in *Drosophila* to help maintain mitochondrial integrity and quality by suppressing PINK1 or PARKIN loss of function mutant-phenotypes and also to be important for the elimination of paternal mitochondria in mice (Rojansky et al., 2016; Yun et al., 2014). The ariadne RBR E3 ubiquitin–

protein ligase 1 (ARIH1) is identified as a trigger for mitophagy in cancer cells and potential promoter of therapeutic resistance (Villa et al., 2017). There is also the E3 ubiquitin ligase Tumor necrosis factor Receptor-Associated Factor 2 (TRAF2), which in neonatal rat cardiomyocytes colocalizes with ubiquitin, the SLR p62, and mitochondria in autophagosomes decorated with the ATG8 protein LC3. TRAF2 both colocalizes and interacts with PARKIN, and the expression of exogenous TRAF2 can partially restore mitophagy with a PARKIN knockdown (KD). In addition, KD of TRAF2 results in accumulation of depolarized mitochondria under stress-induction by mitochondrial depolarization agents. Together these results indicate that TRAF2 has a role as a mitophagy effector in joint action with PARKIN (Yang et al., 2015). HEK-293 cells with mitophagy induction, using the mitochondrial fragmentation inducing anti-parasitic compound lactone ivermectin, display two other E3 ubiquitin ligases involved in PINK1-PARKIN-independent mitophagy, cIAP1 and cIAP2, which function with TRAF2 in a pathway involving the SLR OPTN (Zachari et al., 2019). There is also the α isoform of tripartite motif-containing protein 5 (TRIM5 α) which is involved in recruitment of autophagy regulators to damaged mitochondria in mitophagy pathways both dependent and independent of PARKIN (Saha et al., 2022). TRIM5 α is known to interact with the SLR p62 and mitochondria associated ATG8 proteins (Mandell et al., 2014). Together these E3 ubiquitin ligases hint at the variety and complexity of SLR-dependent mitophagy pathways.

2.2.1.3 SLR-independent mitophagy

In response to cellular or environmental sources of stress such as iron depletion or hypoxia, the pathways used for initiating mitophagy appear to not rely on SLRs or OMM protein ubiquitylation. These pathways are complex and there remain unknowns in their interplay. However, direct interaction between ATG8 proteins of the phagophore membrane and mitochondrial proteins containing a LIR motif does appear to be required. These mitochondrial proteins function as mitophagy receptors and are normally located on the OMM facing the cytosol (Figure 7D) (Ganley & Simonsen, 2022).

The mitophagy receptors known to take part in SLR-independent mitophagy in humans include BCL2 interacting protein 3 (BNIP3) (Quinsay et al., 2010), BCL2 interacting protein 3 like (BNIP3L, also known as NIX) (Novak et al., 2010; Sandoval et al., 2008; Schwarten et al., 2009), FUN14 domain containing 1 (FUNDC1) (Liu et al., 2012), FKBP prolyl isomerase 8 (FKBP8) (Bhujabal et al., 2017), Bcl-2-like 13 (Bcl2-L-13) (Murakawa et al., 2015), and NLR

family member X1 (NLRX1) (Zhang et al., 2019). BNIP3 and BNIP3L are highly homologous to each other, and both belong to the Bcl-2 protein family (Wang et al., 2023). BNIP3 is a OMM protein which in the absence of cellular-stress signals such as those produced by hypoxia is an inactive monomer. For stabilization, BNIP3 undergoes homodimerization (Hanna et al., 2012) and the disruption of this dimer formation results in defective mitophagy, indicating it is crucial for BNIP3 mediated mitophagy (Chinnadurai et al., 2008; Wang et al., 2023). Regulation of BNIP3-mediated mitophagy levels is achieved through stabilization and destabilization of BNIP3 through the ubiquitin-proteasome pathway (He et al., 2022; Poole et al., 2021). The phosphorylation of specific amino acids enclosing the LIR motif of BNIP3 are essential for its binding to ATG8 proteins and positive regulation of mitophagy (Zhu et al., 2013). BNIP3L is also a OMM protein, which serves as a mitophagy receptor (Li et al., 2021). It mediates mitophagy which can be categorized as programmed mitophagy, including the mitochondrial clearance from reticulocytes in their transition to mature erythrocytes (Sandoval et al., 2008; Zhang et al., 2012). It is also involved in the differentiation of retinal ganglion cells and the induction of pluripotent stem cells through somatic cell reprogramming (Esteban-Martinez & Boya, 2018; Esteban-Martinez et al., 2017). Clearance of mitochondria by mitophagy through this pathway involves ATG7 but is not totally dependent on it as BNIP3L mediated mitophagy is reduced but not completely blocked in the absence of ATG7 (Zhang et al., 2009). This indicates the existence of a LC3-independent pathway of BNIP3L-mediated mitophagy (Wang et al., 2023). Phosphorylation of specific residues in the LIR motif of BNIP3L amplifies its affinity for LC3A and thereby increases autophagosome recruitment (Rogov et al., 2017). BNIP3L-mediated mitophagy is also associated with a variety of diseases, including cancer, cardiovascular, neurological, and metabolic disorders (Li et al., 2021). While both BNIP3 and BNIP3L are involved in eliminating mitochondria in response to hypoxia or iron depletion they do not appear to be important for the removal of depolarized mitochondria, unlike PARKIN (He et al., 2022; Leermakers et al., 2020; Wang et al., 2023). The complex interplay between mitophagy pathways can be observed here as BNIP3 and BNIP3L can both improve PARKIN-mediated mitophagy and help cells compensate for a lack of functional PARKIN (Y. Lee et al., 2011).

FUNDC1 is a ubiquitously expressed OMM protein which interacts with LC3B with its LIR motif to initiate mitophagy. The absence of the FUNDC1 LIR motif impairs mitophagy, with this mitophagy pathway appearing to be dependent on ATG5 (Liu et al., 2012; Lv et al., 2017). FUNDC1-mediated mitophagy is regulated through conformational changes induced on

FUNDC1 by phosphorylation and dephosphorylation which control its interplay with LC3B (Kuang et al., 2016; Lv et al., 2017; Wu et al., 2014). Different residues of FUNDC1 are phosphorylated by different kinases, with ULK1 phosphorylation promoting the FUNDC1-LC3B interaction and phosphorylation by Src kinase disrupting it (Kuang et al., 2016; Lv et al., 2017). Dephosphorylation is also involved in enhancing the FUNDC1-LC3B binding affinity, with PGAM family member 5 (PGAM5) positively regulating this while phosphorylation of the same residue by casein kinase 2 completely blocks their interaction (Chen et al., 2014). Another interacting partner of FUNDC1 during hypoxic stress is the OMM protein and mitophagy receptor FKBP8, although the function of this interaction is yet to be elucidated (Wang et al., 2023). As a mitophagy receptor FKBP8 promotes Parkin-independent mitophagy through its LIR motif which recruits lipidated LC3A to damaged mitochondria. Interestingly the interactions of FKBP8 with LC3A are not regulated by the LIR motif undergoing phosphorylation or dephosphorylation. The sources of cellular stress that can induce FKBP8-mediated mitophagy include depolarization, hypoxia, and iron depletion (Bhujabal et al., 2017). FKBP8 avoids being degraded by the autophagosomes through translocating to the ER from the mitochondria after its recruitment of LC3A (Bhujabal et al., 2017; Saita et al., 2013). The mitophagy receptor Bcl2-L-13, a homologue of ATG32, is capable of binding to LC3 with its LIR motif and participates in the induction of PARKIN-independent mitophagy (Murakawa et al., 2015). In addition, there is NLRX1, which is the only protein with a mitochondrial targeting sequence in the Nod-like receptor (NLR) family. This mitophagy receptor uses its LIR motif to interact with LC3 and is essential for a variant of mitophagy induced by the pathogen *L. monocytogenes* to enhance its survivability in macrophages by reducing the production of ROS (Zhang et al., 2019). Finally, the inner mitochondrial protein Prohibitin 2 (PHB2) can function as a receptor during Parkin-dependent mitophagy. Here rupture of the outer membrane allows LC3 on a phagophore to bind PHB2 resulting in mitophagy (Wei et al., 2017).

In addition to these mitophagy receptor proteins, membrane lipids can serve a similar role, with a prominent example being the lipid cardiolipin which is primarily located in the IMM of healthy mitochondria. This lipid, upon mitochondrial depolarization, is translocated from the IMM and externalized upon the OMM increasing the OMM cardiolipin content substantially (Chu et al., 2013; de la Ballina et al., 2020; Kagan et al., 2016). This externalized cardiolipin is then able to bind both LC3A and LC3B through electrostatic interaction, giving rise to cardiolipin mediated mitophagy (de la Ballina et al., 2020; Iriondo et al., 2022).

2.2.1.4 Alternative mitophagy

Both SLR-dependent and SLR-independent mitophagy rely on the ubiquitin-like ATG8 conjugation system critical for conventional macroautophagy, yet mitophagy is possible in cells where ATG5 or ATG7 is lost. This alternative form for mitophagy is less comprehensively characterized than conventional mitophagy but is known to involve ULK1 and the PtdIns3K-complex in its regulation. The generation of autophagosomes for this form of autophagy is dependent on the small GTPase RAB9A member RAS oncogene family (RAB9A) and fusion of isolation membranes with late endosomes and vesicles originating from the trans-Golgi network (Nishida et al., 2009). Signaling pathways involving mitogen-activated protein kinase 1 (MAPK1) and mitogen-activated protein kinase 14 (MAPK14) have also been identified as important for alternative mitophagy (Hirota et al., 2015). In terms of which forms of cellular stress this mitophagy pathway is known to apply to there are certain types of physiological and pathophysiological conditions such as reticulocyte development (Honda et al., 2014; Nishida et al., 2009) and ischemic stress in the heart (Saito et al., 2019).

2.2.2 Basal Mitophagy

The three categories of mitophagy serve different purposes in the cell, as described briefly above. Basal mitophagy is the least studied among these categories due to technical challenges. These include the low activity level of basal mitophagy relative to stress-induced mitophagy, the difficulties in measuring low level mitophagy and the substantial variation that can occur in basal mitophagy levels which can mask the effects of tested experimental parameters (Klionsky et al., 2021). The creation of two transgenic mouse models, one expressing the Mito-QC double-tag mitochondrial reporter and the other expressing mt-Keima targeting the mitochondria, enabled assessment of basal mitophagy *in vivo*. This revealed that most cell types perform basal mitophagy as part of their mitochondrial quality control (McWilliams et al., 2016; Sun et al., 2015). Basal mitophagy operates in most cell types at a low intensity, with the spleen and thymus having relatively lower levels of basal mitophagy compared with the elevated levels seen in tissues including the heart, nervous system, skeletal muscle, hepatic and renal tissue (Palikaras et al., 2018; Sun et al., 2015).

While still much is unknown about the specific mechanisms of basal mitophagy there are indications that its regulation is tissue-specific, with variable expression patterns of regulatory factors (Glick et al., 2012; Palikaras et al., 2018; Yasuda et al., 1999). A major finding is that

metabolically active tissues undergo PINK1-independent basal mitophagy (McWilliams et al., 2018), further confirmed by studies showing the non-essential role of the PINK1-PARKIN pathway for basal mitophagy in both *Drosophila* and mammalian cells (Le Guerroue et al., 2017; Lee et al., 2018). With the best characterized mitophagy pathway, PINK1-PARKIN, found dispensable for basal mitophagy in some cell types the importance of PINK1-PARKIN-independent pathways during basal mitophagy is highlighted. The SLR-dependent but PINK1-PARKIN-independent pathways and the SLR-independent pathways are prime candidates for investigations into the molecular mechanisms of basal mitophagy. This also includes proteins such as MUL1, which appears to function in a parallel pathway to PINK1-PARKIN mediated mitophagy (Yun et al., 2014). There are still many unanswered questions regarding the molecular mechanisms of basal mitophagy. However, KD of the phosphatase USP30 induces basal mitophagy in U2OS and RPE-1 cells (Marcassa et al., 2018), knockout (KO) of the protein kinase leucine-rich repeat kinase 2 (LRRK2) leads to increased basal mitophagy in mice (Singh et al., 2021) and depletion of the mitochondrial protein TMEM11 increases BNIP3/BNIP3L-mediated basal mitophagy in HeLa and U2OS cells (Gok et al., 2023). Conversely, KD of the small GTPase Rheb reduces basal mitophagy in HeLa cells (Melser et al., 2013). Furthermore, the inactivation of FUNDC1-mediated mitophagy in HeLa cells under physiological conditions indicates that FUNDC1 does not engage in basal mitophagy (Liu et al., 2012). Meanwhile, the observation that there is a dramatic reduction in basal mitophagy in the embryonic brains of mice lacking ATG7 indicates a dependence on LC3 (Sun et al., 2015). The reports on the role of FBXL4 in negative regulation of basal mitophagy through mediating proteasomal turnover of the SLR-independent autophagy receptors BNIP3 and BNIP3L showcase the cellular mechanisms for maintaining an optimal mitochondrial pool (Nguyen-Dien et al., 2023). A comprehensive understanding of basal mitophagy is still distant, however the past decade has brought findings that promise an even deeper understanding with further research.

2.3 Mitochondrial derived vesicles

First observed by electron microscopy, mitochondrial derived vesicles (MDVs) have a diameter of 70 to 150 nm and are produced from mitochondria during both basal and stress-related conditions (Soubannier et al., 2012a). MDVs consist of either a single or double membrane, depending on if they formed from just the OMM or the IMM and the OMM. The ability of mitochondria to form vesicles loaded with selective content is an evolutionary conserved

process integral to many of their functions (Andrade-Navarro et al., 2009). Their most prominent role is in quality control of mitochondria, as a baseline first layer of defense for removal of damaged mitochondrial components destined for degradation in peroxisomes or lysosomes. This hinders the accumulation of damaged mitochondrial components that eventually would cause dysfunction and necessitate the degradation of the whole organelle through mitophagy (Cadete et al., 2016; Lv et al., 2020). Turnover of damaged mitochondrial components, including fully assembled protein complexes, by MDVs ensures mitochondrial integrity. Other roles ascribed to MDVs are inter-organellar communication, mitochondrial antigen presentation, peroxisome biogenesis and antimicrobial defense. MDVs target to lysosomes, peroxisomes, bacterial phagosomes, or extracellular vesicles based on different cellular stimuli (Popov, 2022).

The formation of an MDV visually appears as a budding off a mitochondrion and was first observed in a cell in 2008 (Neuspiel et al., 2008). The initiation of MDV formation involves thin membrane protrusions being pulled in a microtubule-mediated process dependent on ras homolog family member T1/2 (RHOT1/2, also known as MIRO1/2). The second step of their formation involves the assembly of a small foci of DRP1 near the tip of the membrane protrusion. Recruitment of DRP1 is mediated by MID49, MID51, and MFF which are redundant DRP1 receptors. The MDV formation is finalized through DRP1 mediated scission, subsequently the MDVs undergo transport to their targeted destinations. The exact mechanisms of MDV transport are not known but may involve transport along the cytoskeleton with MIRO-motor complexes or other transport machinery (König et al., 2021).

The role of DRP1 in MDV formation has been a subject of dispute, first found to be non-essential through siRNA and dominant negative mutant experiments (McLelland et al., 2014; Neuspiel et al., 2008; Soubannier et al., 2012a). However, more recent work utilizing CRISPR–Cas9 for KO of DRP1 or all its receptors (MID49, MID51, and MFF) showed complete loss of MDV formation (König et al., 2021). The recent findings on the membrane-constricting and -severing capabilities of DRP1 for mediating efficient scission of membrane tubules with a thickness between 25 nm to 250 nm (Kamerkar et al., 2018) further support its capacity to be involved in scission of MDVs as well as taking part in organellar division processes (König et al., 2021).

The heterogenous nature of the MDV population and the cargo is an interesting recent finding (Ryan & Tumbarello, 2021). For MDVs destined for lysosomal degradation the cargo can be

divided into two categories based on if the MDV is a single or double membrane. As the generation of vesicles is compartment specific the single membrane MDVs round up OMM proteins including the translocase of the outer membrane 20 (TOM20) and β -Barrel proteins (König et al., 2021; Ryan et al., 2020). MDVs with a double membrane are formed from the OMM and IMM and can therefore contain proteins from both membranes as well as matrix proteins. IMM components that have been found in MDVs include the OXPHOS complexes II, III and IV, but not complexes I and V. Cargo identified from the matrix include pyruvate dehydrogenase (Soubannier et al., 2012b), proteins from the TCA cycle and fatty acid β -oxidation (Vasam et al., 2021), and mtDNA (Picca et al., 2020).

The regulation of MDVs appears to be different for the continuous production of basal steady-state MDVs and those induced through heightened cellular stress. This indicates the presence of multiple mechanisms providing different levels of specificity in the signaling for vesicle generation. Showcasing this is PARKIN, which does not appear to have a role in the generation of basal steady-state MDVs (König et al., 2021). However, for a subset of MDVs induced by oxidative stress, PINK1 and PARKIN are documented to function as positive regulators (McLelland et al., 2014). Furthermore, PINK1/PARKIN negatively regulates mitochondrial antigen presentation from inflammation induced MDVs (Matheoud et al., 2016).

As a mitochondrial quality control pathway, MDVs contribute significantly to mitochondrial protein turnover with a cargo specific turnover rate per hour of 1-4% (Soubannier et al., 2012b), comparable to mitochondrial proteases in yeast which have a turnover rate of 6-12% per hour (Augustin et al., 2005). Alongside the findings that MDVs form in a manner independent of the autophagy machinery (König et al., 2021; McLelland et al., 2014) the role of MDVs as a mitochondrial quality control pathway emerges. MDVs act as a selective means to remove fully assembled protein complexes and thus provide cells with another protective layer of mitochondrial quality control.

3 Lipid Droplets

Fatty acids and other lipids serve vital roles in many cellular processes. Fatty acids are crucial for energy metabolism as discussed previously but also serve as a form for energy storage within cells. Identified roles include membrane biosynthesis, signaling mediators, and regulation of gene transcription (de Carvalho & Caramujo, 2018; Jump et al., 2013). These crucial molecules and their interactions with other cellular constituents must be regulated as excess free fatty acids beyond the anabolic and catabolic needs of a cell cause lipotoxicity, a variant of cellular toxicity caused by lipid overload (Schaffer, 2003). This can result in the activation of the UPR, with excessive or prolonged activation culminating in apoptosis (Han & Kaufman, 2016). A primary method in regulating lipids such as fatty acids and their interactions is through their storage in the form of lipid droplets. Any excess fatty acids can undergo esterification and be stored as neutral lipids such as triacylglycerol (TAG) and sterol esters within lipid droplets, isolating the contained neutral lipids and restricting them to regulated interactions (Figure 8) (Schaffer, 2003; Zadoorian et al., 2023).

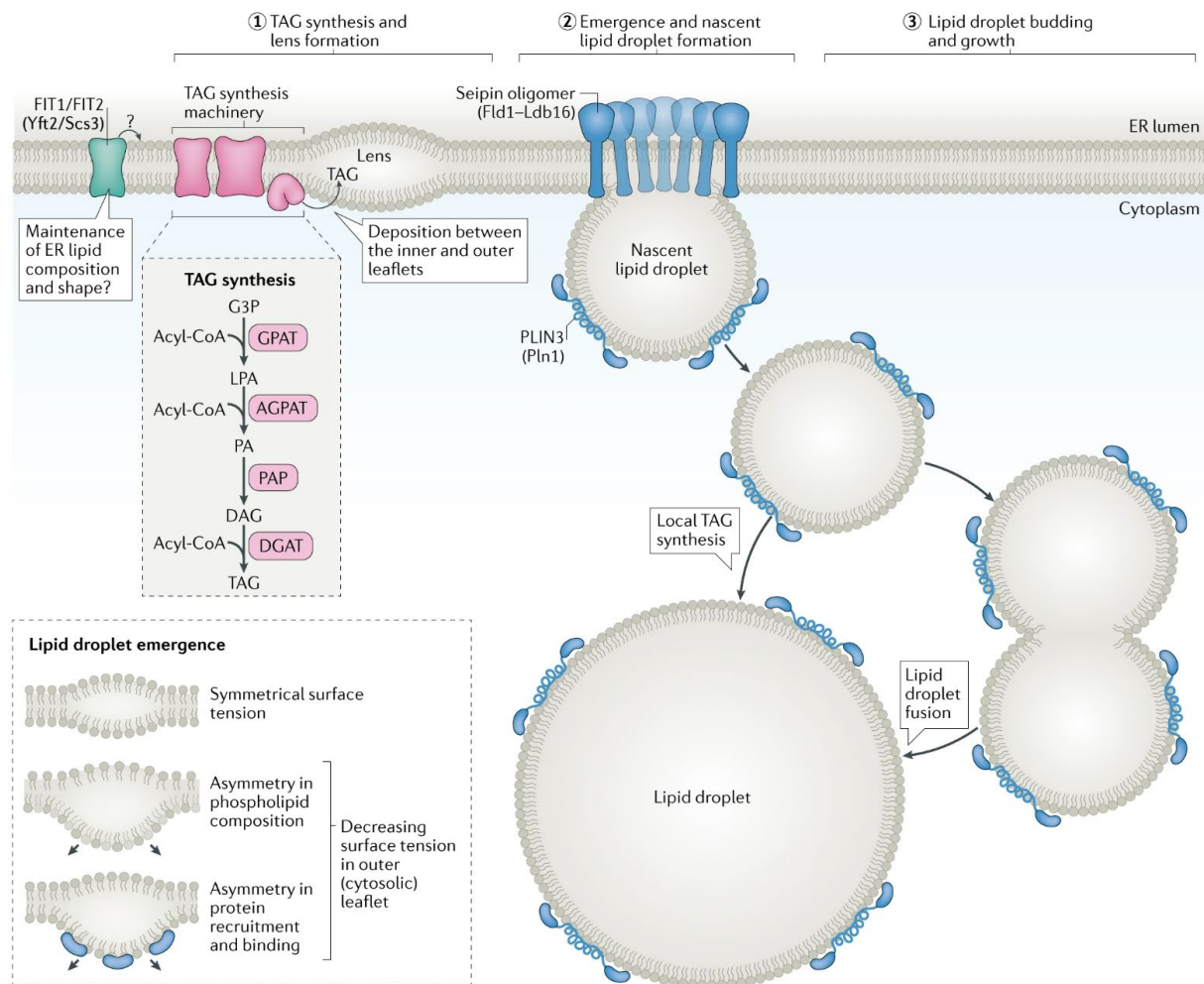


Figure 8: Overview of Lipid Droplet Biogenesis. A schematic overview of the process of lipid droplet formation and the structure of lipid droplets. The first step of lipid droplet biogenesis is neutral lipids being deposited between the ER bilayer leaflets by enzymes that synthesize TAG and cholesterol esters. At sufficient concentration these coalesce into a neutral lipid lens. The second step involves recruitment of lipid droplet biogenesis factors, such as seipin, to the lens structure where they participate in growing the nascent lipid droplet. The third step is lipid droplet budding and growth. Lipid droplets in some mammalian cells grow through fusion with other lipid droplets or through local lipid synthesis. Abbreviations: fat storage inducing transmembrane protein 1/2 (FIT1/FIT2). Adapted from (Olzmann & Carvalho, 2019) with permission.

Lipid droplets serve central roles in lipid homeostasis and energy metabolism. In most mammalian cells lipid droplets are pervasive with variations depending on the cell type. For instance, in adipocytes their major function is lipid storage while in cardiomyocytes they are more involved with energy metabolism and lipid homeostasis (Fujimoto & Parton, 2011; Wang et al., 2013). Being tightly tied to cellular metabolism and nutrient availability, lipid droplets dynamically switch between growth and depletion reflecting cellular needs. The neutral lipids

within lipid droplets can be utilized by the cell through the process of lipolysis or the selective variant of autophagy termed lipophagy (Olzmann & Carvalho, 2019).

As lipid repositories involved in interactions with different organelles, lipid droplet dysfunction can disrupt their cellular functions and be a contributing factor to disease (Gandotra et al., 2011; Greenberg et al., 2011). The molecular basis for many of their interactions with other organelles is still poorly understood. Their spatial positioning relative to other organelles is however thought to be a key factor for their interactions, many of which involve tethering or membrane fusion between the interacting organelles (Olzmann & Carvalho, 2019). Lipid droplets associate with numerous organelles including the ER, Golgi, lysosomes, mitochondria, and peroxisomes depending on the nutrient status of the cell (Valm et al., 2017). Among these organelle interactions, the most crucial interaction is with the ER, as this is the site of lipid droplet biogenesis. The ER also plays a key role in lipid droplet expansion by transferring the neutral lipid TAG through ER membrane bridges, one of three known methods of lipid droplet expansion. The other two methods of lipid droplet expansion include fusion of lipid droplets (Olzmann & Carvalho, 2019), and TAG synthesis on the lipid droplet surface dependent on the necessary proteins relocating from the ER to the lipid droplet (Wilfling et al., 2013).

Mitochondria and their interactions with lipid droplets are crucial for both lipid droplet function in energy metabolism and lipid homeostasis. For energy metabolism the supply of fatty acids to mitochondria is carefully regulated. The lipid droplets store the fatty acids fueling the mitochondria for β -oxidation depending on the nutrient status of the cell. The balance must be carefully maintained as too much fatty acid availability will disrupt lipid homeostasis in the mitochondria and cause lipotoxicity. Failure to sequester fatty acids in lipid droplets results in acylcarnitine accumulation within the mitochondria (Nguyen et al., 2017). This fatty acid intermediate is catalyzed at the OMM for transport into the mitochondria (K. Lee et al., 2011) through the mitochondrial membranes and into the matrix (Murthy & Pande, 1984) for the purpose of β -oxidation (Tarasenko et al., 2018). Acylcarnitine accumulation is proposed to take part in disrupting mitochondria membrane composition thereby reducing its effectiveness as a tight diffusion barrier. The failing mitochondrial membrane potential then causes an increase in cell death (Nguyen et al., 2017).

3.1 Structure of lipid droplets

The functions of lipid droplets are dictated by their structure, including membrane lipid and protein composition. Lipid droplets have a unique structure consisting of a phospholipid monolayer with specific proteins surrounding a hydrophobic core of neutral lipids. In this phospholipid monolayer the cytosol encounters the phospholipid polar head groups while the acyl chains are in contact with the internal store of neutral lipids. While the structural organization of all lipid droplets is similar there is a morphological diversity among lipid droplets. Variations in lipid droplet morphology can exist between cells and within a cell as a reflection of their metabolic status. Thus, the number of lipid droplets within a cell, their size and their composition are all dependent on the metabolic state of the cell (Olzmann & Carvalho, 2019).

The lipid droplet proteome is composed of a variable number of integral and peripheral proteins, differing between cell types. There are currently 100-150 known lipid droplet associated proteins in a typical mammalian cell (Bersuker et al., 2018). Proteins with functions such as membrane trafficking and protein degradation have a significant representation in the lipid droplet proteome. The predominant members of the lipid droplet proteome are however, regardless of cell type, enzymes involved in lipid metabolism including representatives of the perilipin (PLIN) family (Olzmann & Carvalho, 2019). The PLIN proteins take part in sequestering lipids through their protection of lipid droplets from lipase action. Different cell types have variations in the relative expression of PLINs, with their protective capability adapted to balance the need of the cell type between lipid storage and utilization. For most cell types PLIN 2 and 3 are predominantly expressed on the surface of lipid droplets, while cells specialized in lipid-storage usually have larger lipid droplets expressing PLIN 1, 4, and/or 5 (Sztalryd & Brasaemle, 2017). For lipid droplet-mitochondria interactions, which facilitate fatty acid trafficking, PLIN5 is of particular importance as it takes part in tethering lipid droplets to mitochondria (Miner et al., 2023).

3.2 Lipid droplet turnover

The key enzymes taking part in intracellular lipolysis to release free fatty acids during lipid droplet turnover are called lipases. The process of lipolysis can be divided into neutral and acid lipolysis based on if the lipases function at a physiological or acidic pH. Neutral lipolysis occurs in the cytosol by patatin like phospholipase domain containing 2 (PNPLA2, also known as

ATGL), hormone-sensitive lipase, and monoacylglycerol lipase (Zechner et al., 2017). In the heart ATGL mediated neutral lipolysis is crucial, as shown with *Atgl*-KO mice which display excessive lipid droplet accumulation and a severe functional decline with mitochondrial defects, abnormal heart function and premature death (Haemmerle et al., 2011). Acid lipolysis occurs in the lysosome by lysosomal acid lipase (LAL), which facilitates lipophagy (Zechner et al., 2017). Lipophagy is a form of selective autophagy for the lysosomal degradation of cytosolic lipid droplets, including their components such as lipid droplet associated proteins or TAG (Zhang et al., 2022). Until the discovery of lipophagy in 2009, neutral and acid lipolysis were considered distinct pathways that did not have much functional overlap (Singh et al., 2009). Acid lipolysis was previously only known to take part in the catabolism of endocytosed lipo-proteins. Thus, its involvement in hydrolysis of TAG stored in cytosolic lipid droplets expanded its known roles as this was previously thought to be the exclusive domain of neutral lipolysis. It remains unknown what the overall contribution of each of these lipolytic pathways is to lipid catabolism and it may be highly variable between cell types.

During lipophagy, lipid droplets can be degraded in their entirety or in smaller fragments. This capability to degrade smaller lipid droplet fragments is important as some lipid droplets can reach sizes which impede their recruitment to the autophagosomes. Subsequent fusion with late endosomes or lysosomes degrade the lipid droplet containing autophagosomes (Zechner et al., 2017). Lipophagy can provide a release valve for lipid droplet accumulation as through its lysosomal processing of lipid droplets it can produce an extracellular efflux of fatty acids by lysosomal fusion with the plasma membrane. These expelled fatty acids may be taken up anew by the cell or undergo extracellular trafficking (Cui et al., 2021). Much remains unknown of the molecular mechanisms involved in selection of lipid droplets for lipophagy, however oxysterol binding protein like 8 (OSBPL8, also known as ORP8) and spartin have both been identified as lipophagy receptors which interact with members of the core autophagy machinery (Chung et al., 2023; Pu et al., 2023). In HeLa cells the lipid transfer protein ORP8, independent of its lipid transporter activity, has greater localization to lipid droplets during lipophagy induction and gains increased affinity for the phagophore-anchored ATG8 proteins LC3/GABARAPs with its LIR motifs. Phosphorylation by AMPK bestows this increased affinity and mediates lipid droplet encapsulation by autophagosomal membranes (Pu et al., 2023). In SUM159 and HEK293T cells, a protein termed spartin localized to lipid droplets and is required for delivering lipid droplets to lysosomes. Spartin interacts with the ATG8 proteins LC3A and LC3C through its LIR motif. In humans, loss of function mutation to the gene

encoding spartin causes the nervous system disorder Troyer syndrome. Accumulation of lipid droplets and TAG has been demonstrated in cultured human neurons and murine brain neurons if the function of spartin is disrupted (Chung et al., 2023). With lipid droplets serving as important organelles affecting health from the cellular to whole organism level there has been significant efforts directed towards their study.

4 Mitochondria and lipid droplets in the heart

The importance of the mitochondria for energy generation is greatly enhanced in tissues with high energy demands. Cardiac tissue is an excellent example of this, requiring a ceaseless supply of energy to maintain its specialized cellular processes such as ion transport, intracellular Ca^{2+} homeostasis and sarcomere function (Huss & Kelly, 2005). All of this is required to keep operating the healthy adult human heart as a highly efficient pump which will under resting conditions pump around 5 liters of blood per minute. Over the course of a day this will exceed 7000 liters, which adds up to more than 2.6 million liters per year (Taegtmeyer, 2004). The heart will beat from its early stage as an embryonic heart throughout the entirety of a human life (Manner, 2022). The cardiomyocytes of the heart perform the contractions necessary for this continuous pumping and thus have high energy needs met by their mitochondria which take up more than 30% of the cell by volume (Saks et al., 2001). The mitochondria produce 90% of the cells adenosine triphosphate (ATP), with the heart containing approximately 0.7 grams of ATP. This may not sound particularly remarkable until one takes into consideration that maintaining normal cardiac function and workload uses around 6000 grams of ATP per day. The low storage of ATP relative to daily consumption speaks to the truly tremendous workload and throughput of the mitochondria in cardiac cells and helps explain why disruptions and failures in this energy producing machinery can cause disease (Ingwall, 2002).

More than 50% of mitochondrial ATP production in the adult heart is derived from the oxidation of fatty acids (Lopaschuk et al., 2010) and altered fatty acid metabolism can contribute to cardiac pathology. Lipid droplets have been primarily studied in adipose tissue and the liver. Less work has focused on their role in the heart and cardiovascular disease, despite lipid droplet overabundance in cardiac cells during hyperlipidemic conditions such as obesity and diabetes (Goldberg et al., 2018). The continued study of lipid droplets in cardiac cells could

shed light on their role in pathogenesis as well as give deeper insights into their role in energy generation and storage in the heart.

The crucial function of the heart means that any disease affecting it can have severe effects on lifespan and quality of life. Disease that affects the heart is a form for cardiovascular disease (CVD), with this categorization including any disease of the cardiovascular system. CVD is the leading cause of disease burden in the world, it is a major contributor to disability and globally the leading cause of mortality. For 2019 the number of deaths attributed to CVD globally was approximately 18.6 million and of these about 49% were caused by ischemic heart disease (~9.14 million). It is a growing problem globally with the number of cases of CVD nearly doubling from 1990 to 2019, increasing from 271 million to 523 million (Roth et al., 2020). There is no single solution that will remove CVD as a threat to humanity, but rather a myriad of them that need to be implemented. This includes preventative measures to avoid the development of CVD and improved treatment options. Many such solutions are already known but not universally implemented, there is however still much that is unknown. The many varied diseases that are categorized as CVD are not yet fully understood and further basic research is required to better understand the conditions and reveal new treatment options. Mitochondrial dysfunction plays a key role in numerous CVD types (Poznyak et al., 2020).

Improving our understanding of the mechanisms involved in pathological developments at a cellular level promises the possibility of target-based drug design aimed at halting the pathological progression of CVD and even reversing the process. The use of human induced pluripotent stem cell derived cardiomyocytes as a model for these purposes is a promising opportunity to further advance such studies. Mitochondria and lipid droplets are involved in many human pathologies and a comprehensive understanding of these organelles may serve as a gateway to greatly improved human health.

Methodological Considerations

Numerous molecular biology methods were utilized for the work in the papers of this thesis, the specifics of which are detailed in the paper's respective materials and methods sections. As microscopy and image analysis served as principal tools of investigation for the papers of this thesis a selection of imaging related methodological considerations will be discussed in greater depth below.

Double-Tag Mitophagy Reporter

Stable cell lines with a fluorescent mitochondrial reporter are a versatile tool for mitochondrial studies and were utilized in all the papers included in this thesis. Their use presents opportunities for live cell imaging and greatly simplifies sample preparation for fluorescent microscopy. The capability to observe labeled mitochondria in both live and fixed cells through fluorescent microscopy allows for great flexibility in experimental planning. The double-tag reporter utilizes an acid stable and an acid sensitive fluorescent tag to visualize the labeled target and differentiate its localization between acidic environments where the acid sensitive fluorescence is quenched and non-acidic environments where both fluorescence tags are functional. The mitophagy reporter mt-Keima meanwhile shifts fluorescence with changes in pH and is therefore only functional in live cells. Creating large datasets involving numerous time-sensitive conditions is greatly complicated if working with live cells. The double-tag reporter circumvents this issue due to the properties of its fluorophores enabling a functional post-fixation mitophagy assay, allowing imaging to take place when convenient. In our double-tag mitophagy reporter, mCherry-EGFP is fused to the transmembrane domain of mitochondrial outer membrane protein SYNJ2B and thus there is no loss or gain of function for the SYNJ2B protein itself.

However, the double-tag reporter will under some circumstances require adapting protocols to overcome complications that arise with its use. One notable limitation experienced during the work with the double-tag reporter is related to its detection. During analysis it must be determined if a signal from the reporter places it in an acidic or non-acidic environment. We accomplished this by setting an intensity based empirically derived threshold for how much higher the mCherry (acid stable) signal had to be than the EGFP (non-acid stable) signal for the signal to be determined to be in an acidic environment. However, if there are confounding

factors such as high background signal in the EGFP channel this will artificially inflate the threshold the mCherry signal must exceed to be counted as acidic. This issue was especially problematic for early attempts at using siRNA KD to investigate the mechanisms of observed mitophagy. Detecting differences in mitophagy under physiologically relevant levels of cellular stress is difficult as the induced differences are small compared with the induced mitophagy of highly elevated levels of cellular stress. Our solution to this problem was two-pronged, the first was taking steps to reduce the high background signal in the EGFP channel. Halting use of a mounting media containing DAPI, which caused high and inconsistent levels of background in the EGFP channel, reduced the unwanted background signal greatly. The second step was utilization of protease inhibitors to allow for mitophagy flux measurements, the details of which are covered in the materials and methods section of paper I.

A second limitation in regard to fluorescence microscopy and the double-tag reporters is the use of two bands of wavelength to label mitochondria. Studies which may benefit from using a double-tag reporter may find it to not be feasible if they wish to also use additional fluorescence markers which would interfere with each other. EGFP and mCherry together occupy the fluorescence bands for numerous other fluorescent tags, limiting the selection of available fluorescent labels. In cases where the only labeled structure is mitochondria and one channel is sufficient for imaging purposes the double-tag reporter can still be used. In such cases only one tag needs to be utilized as was the case for the high-speed three-dimensional structured illumination microscopy (3DSIM) imaging performed in paper II for quantification of MDVs and observation of the highly dynamic mitochondrial tubules.

Microscopy System Selection

A central tool utilized for all the papers in this thesis is advanced microscopy. Finding the right tool for the task at hand is crucial and there are numerous considerations which come into play when choosing a microscope. The most fundamental aspect to consider is what resolution is necessary. All samples investigated for the purposes of the papers of this thesis are thin monolayers of cells grown *in vitro*, so thick samples were not a relevant consideration for microscope choice.

Conventional Fluorescence Microscopy

For the quantification of red-only structures in paper I the widefield Cell Discoverer 7 microscope with a Plan-Apochromat 50x objective with a numerical aperture (NA) of 1.2 was utilized as described in the methods section. The microscope was unable to detect some of the smallest red-only structures observable with a confocal microscope. Selecting this microscope came down to its ability to produce large datasets of sufficient quality both quickly and reliably. Using a confocal microscope instead would have provided some benefits, namely its narrow focal depth would have helped somewhat compensate for the problem with high background signal in the EGFP channel described above but that issue was ultimately resolved by other means. Another advantage would have been the possibility of the inclusion of the smallest red-only structures more clearly demonstrating mitophagy trends induced by experimental treatments, a possibility which is yet to be fully explored. The greatest issue with using a confocal microscope compared with our chosen widefield microscope and the reason it was deemed non-optimal for our intended use was the much larger time-investment necessary for imaging a dataset for analysis. To gain more data from a confocal microscope would require greater magnification to make use of its enhanced resolution. This greater magnification results in smaller fields-of-view and thereby fewer cells per frame, necessitating capturing more images. The acquisition time per image is much greater, resulting in greatly increased imaging time.

For the work requiring a higher resolution in paper I and III, confocal microscopes were utilized. In paper I this was most notably for co-localization of the double-tag reporter with other mitochondrial proteins in acidic and non-acidic environments as large datasets were not required, and as the confocal microscope more clearly demonstrated the co-localization it was chosen for this task. For paper III the imaging of lipid droplets stained with neutral lipid stains did warrant use of a confocal microscope. Benefits included the higher resolution allowing individual lipid droplets to be better distinguished from one another when clustered and the narrow focal depths helping determine their localization in the z-plane. The correlative light portion of CLEM, described below, also utilized a confocal microscope.

Super-Resolution Microscopy

All three papers included in this thesis made use of super-resolution microscopy (SRM) techniques. Within microscopy, the resolution of even the most powerful conventional microscope is restricted by the diffraction limit to around 200 nm. The diffraction limit is defined as $\lambda/2NA$ where λ is the utilized wavelength of light and NA is the numerical aperture of the microscope's objective. Functionally this serves as a barrier to the observation of cellular events and interactions which are too small to be distinguished as separate using such a microscope. To circumvent this inconvenience imposed upon us by the laws of physics, numerous microscopy techniques have been developed that utilize the attributes of light to allow for varying degrees of increased resolution. The SRM techniques utilized in the papers constituting this thesis are structured illumination microscopy (SIM) and Airyscan.

SIM

Both paper I and II utilized SIM for SRM of both fixed and live samples. The selection of this methodology was because of the high resolution achievable using the structured illumination patterns of this technique. As samples prepared for conventional fluorescence microscopy can be used with this microscopy technique, the ease of sample preparation with our double-tagged mitochondria H9c2 cell line was another benefit. Furthermore, the live cell imaging performed with 3DSIM allowed for a high resolution in the z-axis making it possible to a greater degree to discern if observed objects in the z-axis were separate or co-localizing. A significant drawback to SIM is its susceptibility to reconstruction artifacts during the computational image reconstruction from the structured illumination pattern which requires specialized training to detect (Heintzmann & Huser, 2017). Our coauthor who handled the SIM microscopy is highly skilled with SIM and performed the image reconstructions. Another issue with SIM which had to be considered is the significant photobleaching which occurs because of the multiple images that need to be taken to reconstruct a final single image. The photobleaching is not a significant issue for single images of fixed cells, however during live cell imaging using 3DSIM the high number of images taken in quick succession results in very rapid photobleaching. Due to this the technique was found to be best suited for low duration high resolution live cell imaging. A final issue with live imaging using 3DSIM is that the high number of images required per channel results in increased time delay between channels being imaged. This may result in fast moving objects having shifted location in the time between one channel being imaged and the next, which complicates the observation of multi-channel fast moving objects. This complicated identification of red-only structures in live SIM images.

Airyscan

The second SRM technique, Airyscan, was utilized through the Zeiss Airyscan add-on module to a LSM880 diffraction-limited, point scanning confocal microscope. This technique makes use of a specialized 32-channel Airyscan detector which replaces the confocal microscopes adjustable pinhole. Airyscan images must be processed to maximize their resolution gain, with the final image having increased resolution along each axis (x, y, and z). The technique also gives greatly enhanced signal strength relative to that attained using the equivalent excitation power on a conventional confocal image acquisition, furthermore there is also a reduction in the images background noise. Airyscan images have their resolution improved two-fold and signal-to-noise ratio eight-fold relative to a conventional confocal microscope (Wu & Hammer, 2021). The microscope also retains its capacity to function as a conventional confocal microscope, allowing significant flexibility in its utilization for imaging datasets.

Both paper I and III made use of the FAST mode of Airyscan which provides a four-fold increase to imaging speed with a small loss to resolution, field of view and sensitivity (Huff, 2016). FAST mode was utilized for high-speed imaging of live cells using low laser intensity for extended time periods to observe dynamic cellular events over time. There was little photobleaching when utilizing Airyscan FAST, which in paper I allowed the interactions of red-only structures with the mitochondrial network to be followed over time with LysoView 650 staining labeling all acidic structures. For paper III lipid droplets labeled with a neutral lipid dye were observed in their dynamic interactions with the mitochondrial network. The highly dynamic and often brief nature of the observed events made the high resolution and quick imaging speed of Airyscan FAST the best tool available for our purposes. The ease of use and lack of photobleaching comparative to SIM is also a significant benefit for imaging over extended time periods.

Corelative Light and Electron Microscopy

For paper I and III Corelative Light and Electron Microscopy (CLEM) was utilized for the verification of features and events observed by fluorescent microscopy. EM is the gold standard for visualization of cellular ultrastructure (Chun Chung et al., 2022), making it the optimal tool to confirm observations from fluorescence microscopy. CLEM allows information obtained from light microscopy and EM to be directly correlated. The methods section of paper I and III describes the protocol used for CLEM but does not elaborate on how the confocal imaging was

carried out to facilitate sample preparation for EM and correlation of selected cells. To identify cells of interest for sectioning, grided dishes with grid labels were used as mentioned in their respective methods section. Each circular dish was divided into four quadrants and one cell containing features of interest was selected for each quadrant so that each condition per dataset had redundant samples. For the actual confocal imaging an overview image was first taken with the cell of interest placed centrally and labeled while the brightfield channel would contain orienting features of the labeled grid. A zoomed in high resolution image would then be taken of only the cell of interest, followed by a 3x3 overview tile-scan image to clearly identify the labeled grid the cell of interest was located in. The selection of cells of interest away from grid lines and taking high quality confocal images greatly facilitates both the sectioning of the selected specific cell for EM and the eventual correlation of the fluorescence and EM images.

Mitophagy analysis pipeline

The assessment of mitophagy in H9c2 cardiomyoblasts in paper I exploited the double-tag reporter to identify lysosomal degradation of mitochondria. For an event to be registered as a mitochondrial structure undergoing lysosomal degradation an empirical threshold was set at 50% greater mCherry signal intensity relative to EGFP. This threshold was of sufficient size that a large intensity difference was necessary to register as a “red-only” event and mitigated for small differences in the signal intensity of the channels. To effectively process and quantify mitophagy in imaging datasets an image processing “pipeline” was developed and continuously optimized for efficiency and processing capacity. The basics of this quantification are covered in the methods section of paper I, however several key aspects and details of the analysis are not.

The Imaris XTension “Channel Arithmetics” which is mentioned in the methods section of paper I was used to create a new channel that labels red-only mitochondria, which then functions as a mask for further analysis. The way this XTension function works is by allowing the intensity values for each individual pixel value to be used for arithmetic calculations between signal channels to create a new channel. For the creation of the mask channel, the intensity values of the pixels of EGFP values were multiplied by 1.5 before being subtracted from the mCherry intensity values, providing a new channel exclusive for signals meeting the “red-only” criteria. The Imaris Spots function was then utilized to identify these signals in the new channel. However, to avoid false positives from the background, areas between cells,

where signal values are very low, a minimum intensity cut-off was set for mCherry signal intensity in identified red-only mitochondria.

The Spots function was also used to count cell nuclei per frame while excluding any within 1 μm of the frame edge. The quantification sought the number of red-only structures per cell in cells containing red-only structures, which was averaged per frame. By excluding cells that did not fully have their nuclei within frame, the manual removal of Spots associated with excluded cells was simplified during visual inspection. The use of DAPI to label nuclei, while not strictly required to use the analysis pipeline, greatly increased quantification speed and simplified the process of determining cell borders from mitochondria distribution.

Visual inspection and verification of labeling was crucial to remove false positives and outliers from datasets, even after exclusion of out-of-focus images. Apoptotic cells and chromatic aberrations were the most common source of false positives, while outliers that were removed were usually cells that contained highly abnormal numbers of red-only structures. To verify that unintended researcher bias was not impacting quantifications during visual inspection and verification, multiple datasets were analyzed with both known experimental conditions and blind. For blind analysis each image frame was given a randomized filename to conceal its identity. There were only minor differences in the quantifications when comparing blind and non-blind analysis and all statistically significant relationships were maintained, showing that observed relationships were not the result of researcher bias.

Summary of results

Paper I

High-resolution visualization and assessment of basal and OXPHOS-induced mitophagy in H9c2 cardiomyoblasts

Godtliebsen, G., Larsen, K. B., Bhujabal, Z., Opstad, I. S., Nager, M., Punnakkal, A. R., Kalstad, T. B., Olsen, R., Lund, T., Prasad, D. K., Agarwal, K., Myrmel, T., and Birgisdottir, A. B. (2023).

Autophagy. PMID: 37405374.

In Paper I, mitophagy was visualized and assessed in H9c2 cardiomyoblasts under basal conditions and during OXPHOS induction by galactose adaption. The utilized cell line has a stable expression of a pH-sensitive double-fluorescent tag functioning as a mitochondrial reporter. This enables distinction between mitochondria or mitochondrial fragments within a non-acidic and an acidic compartment. Utilization of advanced imaging techniques and analysis tools allowed assessment of mitophagy. A machine-learning based approach was used to evaluate mitochondrial morphology.

Main findings

- Basal mitophagy and OXPHOS induced mitophagy could be monitored in H9c2 cardiomyoblasts using the mCherry-EGFP-SYNJ2B-TM double-tag mitochondrial reporter.
- A metabolic shift to OXPHOS dependent metabolism in H9c2 cells resulted in elevated mitophagy and a more fragmented mitochondrial morphology where mitochondria appeared shorter and less in network than under basal conditions.
- Super-resolution live cell imaging of H9c2 cells with the mitochondrial reporter and labeled lysosomes allowed monitoring of highly dynamic interactions between mitochondria and lysosomes. Mitochondrial contents were observed to rapidly (within a few minutes) undergo lysosomal engulfment.
- CLEM revealed the ultrastructure information of mCherry-EGFP and mCherry-only (red-only) mitochondria in the H9c2 cell line in basal conditions and during OXPHOS induction, with and without cathepsin inhibitor treatment. Mitochondria with mCherry-EGFP signal had tubular shapes and cristae, while mCherry-only mitochondria were

electron dense structures with features typical of autophagic vacuoles of varying size and content.

- Utilizing siRNA KD of ULK1, ATG7, or RAB9A, showed that each of these proteins plays a significant role in OXPHOS induced mitophagy displayed as perturbed mitophagic flux (revealed by use of lysosomal inhibitors).

Paper II

Mitochondrial dynamics and quantification of mitochondria-derived vesicles in cardiomyoblasts using structured illumination microscopy

Opstad, I. S., Godtliebsen, G., Ahluwalia, B. S., Myrnes, T., Agarwal, K., Birgisdottir, A. B. (2022).

J Biophotonics. PMID: 34766731.

In Paper II, the optical super-resolution technique 3DSIM was utilized to image H9c2 cells with a stable expression of outer mitochondrial membrane fluorescent tags to visualize MDVs. As MDVs are small and fast-moving objects they are not easily captured by imaging. Through optimization of the 3DSIM imaging protocol for imaging both live and fixed cells, high-resolution images of MDVs and mitochondrial dynamics were captured. Image analysis for quantification of MDVs was performed to investigate the effect of metabolic perturbation, through galactose adaptation, on MDV abundance. Interestingly, dynamic and often long mitochondrial tubules extending from the mitochondria were also observed. To our knowledge, our study is the first to report such mitochondrial tubules as well as high-resolution based quantification of MDVs in H9c2 cardiomyoblasts.

Main findings

- A greater number of MDVs was observed in galactose adapted cells when assessed both with live and fixed imaging.
- The number of MDVs observed per cell exceeded that of previous studies relying on immunofluorescent staining of TOMM20 or PDH positive MDVs in fixed cells.
- First demonstration of dynamic mitochondrial tubules in H9c2 cardiomyoblasts, including observations of tubules fusing with other mitochondria to form temporary membrane bridges.
- Super-resolution microscopy techniques utilized with fixed cells depend on appropriate fixation method to preserve structures from fixation artifacts.

Paper III

A study of mitochondria and lipid droplet interplay in H9c2 rat cardiomyoblasts and hiPSC derived cardiomyocytes

Godtliebsen, G., Larsen, K. B., Bhujabal, Z., Nager, M., Kalstad, T. B., Olsen, R., Myrmed, T., and Birgisdottir, A. B. (2023).

Manuscript

In Paper III, lipid droplet accumulation, turnover, and crosstalk with mitochondria was visualized and assessed in H9c2 cardiomyoblasts with fluorescent mitochondria (EGFP-SYNJ2B-TM) and in human inducible pluripotent stem cell (hiPSC) derived cardiomyocytes (CMs). The cells were treated with excess fatty acids and assessments of lipid droplet accumulation was performed under basal growth conditions and during OXPHOS induction by galactose adaption. Lipid droplet turnover and crosstalk with mitochondria was investigated under basal growth conditions. Advanced imaging and analysis techniques allowed quantification and monitoring of lipid droplets visualized with neutral lipid stains in both fixed and live cells.

Main findings

- OXPHOS induction by galactose adaptation resulted in reduced lipid droplet abundance in both cell models. The effect was more pronounced in the hiPSC-CMs.
- Lipid loading resulted in a significant increase in lipid droplet size in glucose containing conditions while the size of lipid droplets was smaller in OXPHOS reliant cells.
- Lipid droplet turnover was perturbed in both cell types by inhibition of lysosomal lipase with Lalistat2. The inhibition of lysosomal vacuolar type H⁺-ATPase (V-ATPase) with BafA1 meanwhile only caused reduction of lipid droplet degradation in H9c2 cells.
- SRM live imaging allowed observation of lipid droplet interactions with the mitochondrial network, with interaction dynamics appearing similar for both cell lines.
- CLEM revealed the ultrastructure of close contact sites between lipid droplets and mitochondria in hiPSC-CMs.

Discussion

The past century has seen humanity take great strides forward in our knowledge of cells and how their complex interplays can affect health and disease. Mitochondria have in this time been subject to numerous studies and there have been many significant findings revealing new insights into their function. The unique evolutionary origin of mitochondria as primordially independent organisms sets them apart from other organelles in mammalian cells (Youle, 2019). When mitochondria are perceived with their symbiotic origin in mind interesting possibilities regarding the origin of current mitochondrial functions become apparent. In the past their symbiotic origin led to the mistaken belief that mitochondria were essential energy generating organelles that operated as independent functional components of cells. This perception changed with findings that showed the increasingly complex and interconnected nature of mitochondria as well as their multitude of functions within cells (McBride et al., 2006). While mitochondria do perform energy generation in most mammalian cell types as part of their functions and are critical for cells with high energy needs, such as cardiomyocytes (CMs), this is not their only function (Casanova et al., 2023). Other important functions of mitochondria include ROS production, apoptosis regulation and biosynthesis. However, as the role of mitochondria in energy generation is a central theme throughout the papers of this thesis it remains an important aspect for the discussion.

The growing knowledge of mitochondria, their functions and interactions with other organelles such as lipid droplets, is part of the greater efforts within biological research to reveal the secrets of life. From a biomedical perspective, the source of organelle dysfunction is also a potential therapeutic target. To develop a pharmacological intervention to treat a particular mitochondrial or lipid droplet dysfunction causing, or contributing to, a pathological condition it is greatly beneficial to have a comprehensive understanding how the process should operate under normal conditions.

Physiological relevance in biological studies

It is not currently possible to perform *in vitro* studies that perfectly mimic the physiological conditions cells would experience *in vivo* with routinely used cell culture media composed to ensure optimal cell growth of cultured cells. These media formulations contain a supraphysiological dose of nutrients, which reduces the physiological relevance and biomedical

applicability of findings from *in vitro* experiments (Allen et al., 2023; Arora, 2013). Investigations must seek to find an optimal balance between *in vitro* growth conditions, physiological relevance, and experimental considerations. A central aspect of our studies in paper I and II is performing investigations under physiologically relevant settings. This includes normal H9c2 growth conditions (basal level) and galactose adaptation. These growth conditions were chosen as they are closer to that which cells may experience in a physiological environment compared to that experienced with experimental treatments that induce high cellular stress, e.g. mitochondrial uncouplers. The effects induced by mitochondrial uncouplers do usually not occur in a physiological environment. Despite this it is common to employ mitochondrial uncouplers such as FCCP and CCCP to elicit highly elevated mitochondrial dysfunction and induce mitochondrial clearance (Demine et al., 2019).

For our purposes of investigating mitophagy (paper I) and MDVs (paper II) in H9c2 cells, the induction of OXPHOS by galactose adaptation allowed increased cellular reliance on the mitochondria for energy generation. Most likely this led to elevated mitochondrial turnover displayed by induced mitophagy and higher numbers of MDVs. Adult cardiomyocytes rely heavily on their mitochondria for energy production. Thus increasing the H9c2 cells reliance on their mitochondria approximates these conditions and is a physiologically relevant condition requiring increased mitochondrial quality control activity. However, investigating quality control mechanisms such as mitophagy under basal and near-basal conditions poses a challenge. There is not a high mitophagy activity present in these cells, relative to cells exposed to e.g. mitochondrial uncouplers. Detecting small changes to the rate of mitophagy in conditions with low mitochondrial turnover is exceedingly difficult due to high inter-cell variability (Klionsky et al., 2021). Furthermore, for the study of any quality control pathway there is the possibility of cells having redundant mechanisms to compensate for any loss-of-function, such as that induced by an experimental treatment. This could obscure treatment effects as the mechanisms involved are not pushed to their maximal capacity under basal and near-basal conditions. Despite these challenges, performing investigations in as physiologically relevant settings as possible is the path to produce results more beneficial for biomedical applications.

The lipid loading performed as part of the experimental procedures for paper III using oleic acid or a fatty acid analog would not have occurred in a physiological environment. However, it does allow inducing the accumulation of lipid droplets, a condition associated with cardiomyopathy in patients with metabolic diseases such as obesity and diabetes mellitus (Borradaile & Schaffer, 2005). This was necessary to investigate how cells adapted to different

metabolic substrates would handle the inflow of fatty acids and accumulation of lipid droplets to counteract lipotoxicity. Studies seeking to investigate specific cellular functions in near physiological conditions are limited by available methodologies and the attributes of their cell model. For studying lipid droplets in H9c2 cells and hiPSC-CMs the low number of lipid droplets present without lipid loading, under both basal growth conditions and in galactose adapted cells, necessitated inducing lipid droplet accumulation. Investigations seeking to reveal new insights into specific cellular functions cannot always take into account physiological conditions until the investigated cellular functions are better characterized.

Mitophagy – Protecting the host

The first paper of this thesis focused on investigating degradation of mitochondria through mitophagy as a mitochondrial quality control mechanism under basal conditions and during OXPHOS induction in H9c2 rat cardiomyoblasts. Mitochondrial quality control is multi-layered in nature and there appears to be numerous redundant processes. This is reflected by the many different mitophagy pathways that have so far been identified (Ganley & Simonsen, 2022; Ng et al., 2021). Within organisms, the presence of redundant mechanisms is a strong indicator that a particular process is of crucial importance for survival (Krakauer & Plotkin, 2002; Lavi, 2015), something which is of particular interest when considering the endosymbiotic past of mitochondria. The current role of mitophagy may have evolved as a responsive control mechanism. Protecting the host from these foreign organelles in a signal dependent manner such as by excessive mitochondrial ROS production or loss of mitochondrial membrane potential. As an early form for selective autophagy for endosymbiont control within the host this mechanism may have worked in parallel with xenophagy, which targets intracellular pathogens, as both share common molecular actors such as TBK1 (Singh et al., 2018). By ensuring a healthy mitochondrial population through the removal of damaged mitochondria, mitophagy could initially have served as an evolutionary favorable method to maintain the intracellular environment.

The work in paper I points toward avenues for further characterization of mitophagy. After a metabolic shift to OXPHOS there appears to be multiple active mitophagy pathways that may have redundant functions and thus compensate if one pathway is blocked. With siRNA KD of either ATG7 or RAB9A, only flux measurements allowed an impairment of mitophagy to be observed. This indicates that during OXPHOS induced lysosomal degradation of mitochondria,

both canonical and alternative mitophagy pathways can take part in mitochondrial clearance and redundant pathways may be compensating for the siRNA induced loss-of-function. In an attempt to further investigate the involved mitophagy regulators, we performed a siRNA KD of ULK1, which acts upstream of both ATG7 and RAB9A. Unexpectedly, we found that the reduction in mitophagy was similar to that of KDs of ATG7 or RAB9A with the observable reduction in mitophagy only apparent using flux measurements. This implies the activation of ULK1-independent mitophagy to compensate for the reduced rate of ULK1-dependent mitophagy. It is also possible that other mitochondrial quality control mechanisms may have increased activity, but this was not investigated. There are several potential mechanisms that have been shown for ULK1-independent autophagy which may be involved in ULK1-independent mitophagy. This includes an interaction taking place between FIP200 and ATG16L1 which can determine if autophagy is ULK1-dependent or -independent (Gammoh et al., 2013). There is also deacetylation of VPS34 by inactivation of acetyltransferase p300, inducing PI3P production and autophagy even in ULK1^{-/-} cells (Su et al., 2017).

Further work characterizing the pathways involved in OXPHOS induced mitophagy should expand the screen of protein KDs to attempt to find further key proteins which have a detectable effect on the rate of mitophagy, with or without flux measurements. Of particular interest for KD studies are mitophagy receptors, as they were not investigated as part of paper I. The step beyond KD studies is attempting to create KO cell lines for already identified key mitophagy proteins. KO cell lines would ensure complete absence of the KO protein and could be combined with further siRNA KDs to attempt to elucidate compensatory mechanisms. The H9c2 cells are difficult to create KO cell lines with (Zhao et al., 2020) and our previous attempt at creating FKBP8- and BNIP3-KO cell lines was unsuccessful. However, a different cell line could be used instead for such investigations if creating H9c2 KO cell lines proves infeasible.

Mitochondrial morphology and mitochondrial dynamics

Mitochondrial morphology varies greatly between cell types and the H9c2 cardiomyoblasts have mitochondria with high motility and tubular appearance which brings to mind their ancient endosymbiotic origin. While such mitochondrial morphologies may at a glance resemble their bacterial ancestors, mitochondria have evolved alongside different eukaryotic lineages in diverse pathways. The bulk of the mitochondrial proteome has its evolutionary origin outside their ancestral *Alphaproteobacteria* (Gray, 2012). This is very much reflected and observable in

H9c2 cells with the dynamic nature of their mitochondria, undergoing rapid fusion/fission in response to complex cellular needs and signals yet to be elucidated, behaviors not seen in bacteria. As part of our investigations for paper I into the impact of OXPHOS induction on mitochondria, the change in mitochondrial morphology, while subtle, was noticeable by eye in microscopy images. Quantifying this observable change in morphology however proved difficult but was resolved by using a machine-learning based approach for segmentation and quantification as described in the methods section of paper I.

In galactose adapted cells, the mitochondria were on average shorter with the mitochondrial population as a whole being more fragmented e.g. contained less networked mitochondria. A shift in the balance of fusion and fission is in line with the known mitochondrial behavior of adapting their form to a fragmented or fused shape in response to stress (Zemirli et al., 2018). Fragmentation of mitochondrial morphology to mitigate strain on the mitochondria during galactose adaption has been previously demonstrated in BT25 cells and human skin fibroblasts (Kamradt et al., 2021; Tronstad et al., 2014). The greater fragmentation of the mitochondrial population aligns with our observations of increased mitophagy in galactose adapted cells, as mitochondrial fission allows separation of dysfunctional parts of mitochondria for mitophagy (Kobayashi et al., 2020b). The machine learning based methodology used for our analysis and quantification of mitochondrial morphology through fluorescent microscopy images greatly reduces the workload necessary for performing such a quantitative analysis (Punnakkal et al., 2023). However, a persistent challenge with two-dimensional morphological quantifications of three-dimensional data is overestimation of networked mitochondria. Despite this being a challenge facing any such analysis, the machine learning approach managed to quantify the observed shift in morphology. Machine learning approaches such as the one utilized for paper I are highly promising as analysis tools for the future of biomedical research. With further development they may greatly simplify and streamline many analysis tasks currently requiring significant time investments from researchers.

MDVs – an adapted mechanism

Many of the functions of mitochondria appear to be tied to their endosymbiotic origin, however MDVs stand out as special among these adapted mechanisms due to potentially playing a key role in eukaryogenesis. As eukaryotes are thought to be the result of a symbiosis between archaea and bacteria (Dey et al., 2016), there remains the question of the origin of the

endomembrane system and the membrane transition from an archaea-type membrane based on isoprene ether lipids to a bacterial-type membrane based on fatty acid esters (Jain et al., 2014). Both archaea and bacteria can secrete outer membrane vesicles (OMVs). If a protomitochondrion hosted in the cytosol of an archaea host cell were to release OMVs it could have potentially been responsible for generating the endomembrane systems first vesicles. The fusion of these vesicles with each other could have generated the membrane compartments within the cytosol. Furthermore, through fusion of these OMVs with the host archaea plasma membrane, the chemical composition the membrane could have been shifted. If hosting a protomitochondrion was what allowed an archaea to form an endomembrane system this is a potential explanation for why eukaryotic cells have mitochondria. Given this scenario, these ancient endosymbiotic bacteria played a major role in eukaryogenesis (Gould et al., 2016). The present-day mitochondria retain their ability to generate vesicles, producing both single- and double-membrane MDVs.

The work in paper II focused on MDVs, applying the advanced super-resolution microscopy technique 3DSIM. This approach allowed high-resolution imaging and quantification of MDVs in both live and fixed cells, something that to our knowledge had not been done previously. In the galactose adapted H9c2 cells undergoing OXPHOS induction we observed an increased number of MDVs relative to cells in basal growth conditions. This could represent an increased production of MDVs as a quality control response to the increased respiration activity by the mitochondria, similar to the observed increase in rate of mitophagy observed in galactose adapted cells in paper I. This quantified increase in MDVs support its suggested role as a first-line of defense mitochondrial quality control mechanism that can be upregulated in response to cellular stress (Cadete et al., 2016). One important consideration is that the roles of detected and quantified MDVs cannot be ascertained. Hence, an unknown ratio of observed MDVs could be involved in activities not related to mitochondrial quality control. However, given that the mitochondria are under substantial respiration induced strain when cultured in galactose media, as seen from the increased rate of mitophagy and fragmentation of the mitochondrial network, it is likely that the observed increase can be attributed to quality control efforts. A future continuation of this work could attempt to identify the distribution of MDVs assigned to their different ascribed roles. This would most likely be restricted to analysis of fixed cells, as immunofluorescent staining would allow labeling specific proteins associated with known MDV roles or targets, such as the MDVs containing MUL1 as cargo which target peroxisomes (Neuspiel et al., 2008). Dedicated cell lines, with fluorescent tags labeling the OMM and a

targeted protein for a designated MDV role, would likely be a superior option and would allow live cell imaging.

Another finding in paper II is the importance of utilizing appropriate sample preparation techniques that preserve cellular structures in conjunction with super-resolution techniques that facilitate studying objects below the diffraction limit of conventional microscopy. Previous studies made use of a conventional fixation procedures of 5% paraformaldehyde and permeabilization to allow for immunofluorescent staining of fixed H9c2 cells (Cadete et al., 2016; Li et al., 2020). As paper II demonstrated, paraformaldehyde fixation causes fragmentation and disruption of the mitochondrial network which would hinder MDV quantification, although at conventional resolutions the fragmentation of the mitochondrial network would not be as apparent. To optimally preserve cellular structures different fixation methods must be used such as the inclusion of glutaraldehyde in the fixation buffer, cues for this strategy taken from chemical fixation for EM (Hayat, 1986). The use of permeabilization is also likely detrimental to studying MDVs. Permeabilization induces a substantial loss of cellular mass density due to the destruction of membrane integrity (Cheng et al., 2019) and this could also include loss of MDVs. Furthermore, the limited resolution of conventional confocal microscopes meant that the apparent size of observed MDVs was around 300 nm with the actual size of MDVs estimated to be around 50 nm. MDVs in these previous studies were identified by being positive for either TOMM20 or PDH immunofluorescent staining, but not both as to discriminate them from mitochondria (Cadete et al., 2016). By utilizing a SRM technique with sufficient resolution to distinguish MDVs by their diameter of 70-150 nm, and a cell line with a fluorescent mitochondrial outer membrane marker, MDVs can be visualized clearly and quantified with greater accuracy. Previous studies in H9c2 cells detected less than 10 MDVs per cell under basal conditions (Li et al., 2020) and approximately 30 MDVs per cell under OXPHOS induction by galactose adaption (Cadete et al., 2016). This contrasts strongly with the utilization of 3DSIM and our cell line which assessed an average of 127 MDVs per frame in fixed cells, with each frame not even encompassing a single entire cell. The importance of visualizing these highly dynamic and very small structures in living cells is further highlighted by the number of MDVs observed per μm^2 being 84% higher in live cells relative to fixed. This difference may in part be due to selection of imaging site but could also be caused by the fixation procedure. If MDVs are lost during fixation than permeabilizing the cells would most likely exacerbate loss of MDVs. The importance of selecting appropriate methodologies for

MDV imaging studies cannot be understated and SRM should be considered a routine technique and necessary tool for studying MDVs by imaging.

For further avenues of study beyond determining the distribution of roles within an MDV population there are numerous possibilities. Of particular interest may be investigating MDV formation, which has been found to involve mitochondrial tubules, similar to those we observed. The mechanism for this process was elucidated in a study by König et al. published in late 2021, shortly after our article was accepted for publication (König et al., 2021). As we can directly observe the mitochondrial tubules through the SRM technique 3DSIM we could in an siRNA KD study of key molecular players identified by König et al. observe the effects of KDs on both the mitochondrial tubules themselves and the MDV population in living cells. Another possibility is an in-depth quantification study to determine MDV generation rate based on different types of cellular stress, which could shed light on their role as a mitochondrial quality control response. It is unknown if quality control MDVs are released equally in response to all forms of cellular stress, or if they are a mitochondrial response for a selected array of stress inducing conditions. This could also be combined with a siRNA KD screen of key proteins to evaluate the effects of induced loss of function on MDV release to elucidate new molecular actors with regulatory functions. As the study of MDVs is still an emerging field within mitochondrial quality control there are many discoveries yet to be made. While there were no significant new mechanistic findings in paper II, the methods employed for the study can serve as a guideline for future studies seeking to visualize and potentially quantify MDVs through light microscopy as part of their investigations.

Lipid droplets – controlled use of fatty acids

The evolutionary advantage protomitochondria provided to their archaean host cells was the bioenergetic capacity necessary to achieve eukaryotic cell complexity (Martin et al., 2015). The metabolic pathways present in mammalian cells have multiple substrates (carbohydrates, fatty acids, and amino acids) that fuel the bioenergetic activity of mitochondria. From an evolutionary perspective, having the capability to generate energy from different metabolic substrates is advantageous for cell survivability. The cell becomes less vulnerable to a reduction in a particular substrate availability. Among metabolic substrates, fatty acids are a standout, having the highest energy density among all known energy substrates and, in vertebrates, providing the most efficient energy production (Zechner et al., 2017). However, an

overabundance of fatty acids is not beneficial to cells. High concentrations of fatty acids cause lipotoxicity which can cause cellular dysfunction and cell death (Unger, 2002). Storing fatty acids as neutral lipids within lipid droplets allows cells to safely segregate these crucial metabolic compounds and access them as needed through lipolysis or lipophagy. Cells must balance the processes of lipid storage in lipid droplets with lipid utilization. Thus, an imbalance favoring lipid storage results in aberrant accumulation of lipid droplets. This is a pathological feature of compromised cardiac function associated with hyperlipidemia-related metabolic diseases such as obesity and diabetes mellitus (Lopaschuk et al., 2010; Schott et al., 2019).

The work in paper III investigated lipid droplets in H9c2 cells and hiPSC-CMs. We focused on determining the feasibility of studying lipid droplet accumulation, degradation, and interactions with mitochondria in these cell models. As part of this we employed OXPHOS induction by galactose adaption to observe the impact of elevated OXPHOS on lipid droplet accumulation. Our findings showed that the lipid droplet population present in both cell models was significantly lower, both before and after lipid loading, in cells having undergone OXPHOS induction by galactose adaption relative to those grown in the presence of glucose. This may indicate that the cells which have undergone galactose adaption have a higher utilization of fatty acids in their metabolism. This would counteract their increased uptake of fatty acids during lipid loading resulting in less lipid droplet accumulation. The cells in glucose containing growth media meanwhile utilize glucose for glycolysis and therefore have less use for fatty acids in their energy metabolism. The effect of different growth medias being more pronounced in the hiPSC-CMs may be due to their differentiated status and the additional energy required for the cells rhythmical beating. A further factor potentially exacerbating the pronounced difference is that galactose adaption of the hiPSC-CMs may accelerate their maturation into more adult-like CMs with higher oxidative metabolism (Correia et al., 2017).

The significantly lower lipid droplet population in galactose adapted cells posed challenges for quantification. Low and highly variable signal-to-noise ratios complicated detection, and low lipid droplet populations gave enhanced statistical weight to outlier cells with large lipid reserves. For the investigation of lipid droplet turnover we therefore kept the cells in their normal glucose containing conditions for the lipid loading treatment and the subsequent withdrawal period. In the H9c2 cells the lipid droplet area per cell was reduced to less than 20% after oleic acid withdrawal, a significant and very steep decline. The perturbed lipid droplet degradation with lysosomal lipase inhibitor Lalistat2 (LaLi) or lysosomal inhibitor bafilomycin A1 (BafA1) indicates that acid lipolysis and lipophagy are part of an important pathway which

can resolve lipid droplet overabundance. We have yet to determine the fate of the lipid droplets lost during the withdrawal. Lysosomal exocytosis may be involved in the rapid reduction of lipid droplets in H9c2 cells. Lysosomal exocytosis, where the lysosome fuses with the plasma membrane to expel its contents, is identified as a route for the efflux of fatty acids derived from lipophagy (Cui et al., 2021). The peripheral localization of the lipid droplets in H9c2 cells after oleic acid loading and after lysosomal inhibition further supports this. The involvement of lysosomal exocytosis in clearing the cells of lipids could be investigated by mucolipin TRP cation channel 1 (MCOLN1) siRNA KD to inhibit lysosome-plasma membrane fusion.

Our results from the lipid droplet turnover quantification in the hiPSC-CMs revealed a different trend, showcasing high variability in lipid handling between cell types. We observed a much lower but still significant post-withdrawal decline for lipid droplet area per cell, a 17% reduction relative to pre-withdrawal levels. Furthermore, the effects of LaLi and BafA1 also differed with the LaLi treated cells having a significant increase (36%) in post-withdrawal lipid droplet area per cell relative to pre-withdrawal while BafA1 treated cells had no significant effect. The differentiated hiPSC-CMs could have a higher threshold for how much lipids are considered beneficial before the risk of lipotoxicity outweighs potential metabolic benefits. The greatly reduced rate of lipid droplet turnover found in the hiPSC-CMs relative to the H9c2 cells supports the need for attempting a longer duration withdrawal as it may demonstrate lipid droplet turnover trends more clearly. A longer duration withdrawal may thus help determine if lipophagy is merely of reduced importance or entirely uninvolved in the lipid droplet turnover post-lipid loading. The lack of significant effect of BafA1 supports a central role of the neutral lipases in hiPSC-CM lipid droplet turnover. ATGL has a crucial role in neutral lipolysis in mice hearts (Haemmerle et al., 2011) and hiPSC-CMs could have different ATGL expression levels than H9c2 cells or a higher minimum neutral lipase efficiency required to maintain normal function. Investigations to the relative contributions of neutral lipolysis and lipophagy should also consider changes to lipid droplet morphology. In hepatocytes, inhibition of either or both mechanisms did not significantly change overall lipid droplet content, however lipid droplet morphology was dramatically impacted. Inhibiting ATGL or both neutral lipolysis and lipophagy simultaneously resulted in enlarged lipid droplets, while inhibiting only lipophagy by lysosomal inhibition resulted in accumulation of numerous small lipid droplets (Schott et al., 2019). Investigating if lipid droplets are targeted by lipolysis as a prerequisite for lipophagy in cardiac cells, similar to in hepatocytes, would reveal if this aspect of lipid droplet catabolism is cell type specific or a common pathway.

Lipid droplet-mitochondria interplay was investigated by SRM in both H9c2 cells and hiPSC-CMs revealing similarly frequent interactions and extended periods of close contact between the two organelles. While mitochondria were observed to be highly mobile, independent of lipid droplet presence, the movements of lipid droplets appeared to be more oscillating with a limited range of movement unless they were in close contact with mitochondria. Interactions between the ER and lipid droplets were not investigated but are a potential avenue for further characterizing lipid droplet motility. The oscillating movements of the lipid droplets may have been caused by ongoing ER-lipid droplet contacts, given previous findings in COS-7 cells where the ER is most frequently in contact with lipid droplets (Valm et al., 2017). Our CLEM images of the hiPSC-CMs confirmed the proximity of lipid droplets and mitochondria. The revealed ultrastructure of the close contacts between lipid droplets and mitochondria indicates these as means of material (e.g. fatty acid) transfer between lipid droplets and mitochondria in cardiomyocytes. These defined contacts also fit with the reported ability of lipid droplets to clear the OMM of pro- and anti-apoptotic proteins (Bischof et al., 2017).

We utilized neutral lipid stains to label lipid droplets in our cell models, however as neutral lipids are not limited to lipid droplets, other organelles such as late endosomes and lysosomes may also be affected by the stain (Henne, 2019). Furthermore, in conditions with few lipid droplets the signal-to-noise ratio becomes insufficient to perform accurate quantifications. An improvement on the current methodologies employed would be a technique which specifically labels only lipid droplets and provides a higher intensity signal. One approach to accomplish this would be creating stable cell lines with a fluorescent label attached to a lipid droplet specific protein. A good candidate for this is PLIN5 as it is lipid droplet specific and tethers lipid droplets to mitochondria through an interaction with solute carrier family 27 member 4 (SLC27A4, also known as FATP4) in the OMM (Miner et al., 2023). The work in paper III forms a foundation upon which new insights into lipid droplet accumulation, turnover and mitochondrial interactions can be elucidated in cardiac cells.

Future Perspectives

Human health is an exceedingly complex balance of cellular processes that are both highly robust and sensitive to disruption. Our studies of mitophagy, MDVs and lipid droplets all seek to further our understanding of these specific aspects of cellular biology for the advancement of human health. As many cellular processes are regulated differently between different cell and tissue types, the cell model used for an investigation is important. Choosing to perform investigations in cardiac cell models allows our findings, derived insights, and continued research to be more relevant for cardiovascular disease, the leading global disease burden.

The findings from our studies alongside the tools and expertise developed form a foundation upon which future research can continue. For mitophagy and MDVs the further characterization of these mechanisms under more physiologically relevant conditions is a challenge but promises to give a more comprehensive understanding of how mitochondrial quality control operates under normal conditions. In regards to lipid droplets, studies have focused on adipocytes and hepatocytes, yet the crucial functions of lipid droplets are not limited to these cell types. Furthermore, as their different roles in the cellular environment are still elusive, studying lipid droplets in different cell types may uncover new insights into this intriguing organelle and even yield avenues for therapeutic intervention. The path from basic science to therapeutic application is typically a long multi-decade process, however that may not always be the case. In our rapidly changing world with ceaseless technological advancements and our continued efforts to delve into the unknown, we may experience and benefit from faster-than-expected breakthroughs yielding better health for all. A small finding today may be a steppingstone for tomorrow's breakthrough.

References

- Adeva-Andany, M. M., Carneiro-Freire, N., Seco-Filgueira, M., Fernandez-Fernandez, C., & Mourino-Bayolo, D. (2019). Mitochondrial beta-oxidation of saturated fatty acids in humans. *Mitochondrion*, 46, 73-90. <https://doi.org/10.1016/j.mito.2018.02.009>
- Aguer, C., Gambarotta, D., Mailloux, R. J., Moffat, C., Dent, R., McPherson, R., & Harper, M. E. (2011). Galactose enhances oxidative metabolism and reveals mitochondrial dysfunction in human primary muscle cells. *PLoS One*, 6(12), e28536. <https://doi.org/10.1371/journal.pone.0028536>
- Allen, G. F., Toth, R., James, J., & Ganley, I. G. (2013). Loss of iron triggers PINK1/Parkin-independent mitophagy. *EMBO Rep*, 14(12), 1127-1135. <https://doi.org/10.1038/embor.2013.168>
- Allen, S. L., Elliott, B. T., Carson, B. P., & Breen, L. (2023). Improving physiological relevance of cell culture: the possibilities, considerations, and future directions of the ex vivo coculture model. *Am J Physiol Cell Physiol*, 324(2), C420-C427. <https://doi.org/10.1152/ajpcell.00473.2022>
- Andrade-Navarro, M. A., Sanchez-Pulido, L., & McBride, H. M. (2009). Mitochondrial vesicles: an ancient process providing new links to peroxisomes. *Curr Opin Cell Biol*, 21(4), 560-567. <https://doi.org/10.1016/j.ceb.2009.04.005>
- Arnold, P. K., & Finley, L. W. S. (2023). Regulation and function of the mammalian tricarboxylic acid cycle. *J Biol Chem*, 299(2), 102838. <https://doi.org/10.1016/j.jbc.2022.102838>
- Arora, M. (2013). Cell culture media: a review. *Mater methods*, 3(175), 24.
- Ashrafi, G., & Schwarz, T. L. (2013). The pathways of mitophagy for quality control and clearance of mitochondria. *Cell Death Differ*, 20(1), 31-42. <https://doi.org/10.1038/cdd.2012.81>
- Audano, M., Pedretti, S., Ligorio, S., Crestani, M., Caruso, D., De Fabiani, E., & Mitro, N. (2020). "The Loss of Golden Touch": Mitochondria-Organelle Interactions, Metabolism, and Cancer. *Cells*, 9(11). <https://doi.org/10.3390/cells9112519>
- Augustin, S., Nolden, M., Muller, S., Hardt, O., Arnold, I., & Langer, T. (2005). Characterization of peptides released from mitochondria: evidence for constant proteolysis and peptide efflux. *J Biol Chem*, 280(4), 2691-2699. <https://doi.org/10.1074/jbc.M410609200>
- Bagheri, H. S., Bani, F., Tasoglu, S., Zarebkohan, A., Rahbarghazi, R., & Sokullu, E. (2020). Mitochondrial donation in translational medicine; from imagination to reality. *J Transl Med*, 18(1), 367. <https://doi.org/10.1186/s12967-020-02529-z>
- Bellot, G., Garcia-Medina, R., Gounon, P., Chiche, J., Roux, D., Pouyssegur, J., & Mazure, N. M. (2009). Hypoxia-induced autophagy is mediated through hypoxia-inducible factor induction of BNIP3 and BNIP3L via their BH3 domains. *Mol Cell Biol*, 29(10), 2570-2581. <https://doi.org/10.1128/MCB.00166-09>
- Bento, C. F., Renna, M., Ghislat, G., Puri, C., Ashkenazi, A., Vicinanza, M., Menzies, F. M., & Rubinsztein, D. C. (2016). Mammalian Autophagy: How Does It Work? *Annu Rev Biochem*, 85, 685-713. <https://doi.org/10.1146/annurev-biochem-060815-014556>
- Bersuker, K., Peterson, C. W. H., To, M., Sahl, S. J., Savikhin, V., Grossman, E. A., Nomura, D. K., & Olzmann, J. A. (2018). A Proximity Labeling Strategy Provides Insights into the Composition and Dynamics of Lipid Droplet Proteomes. *Dev Cell*, 44(1), 97-112 e117. <https://doi.org/10.1016/j.devcel.2017.11.020>
- Bhujabal, Z., Birgisdottir, A. B., Sjøttem, E., Brenne, H. B., Overvatn, A., Habisov, S., Kirkin, V., Lamark, T., & Johansen, T. (2017). FKBP8 recruits LC3A to mediate Parkin-independent mitophagy. *EMBO Rep*, 18(6), 947-961. <https://doi.org/10.15252/embr.201643147>
- Bischof, J., Salzmann, M., Streubel, M. K., Hasek, J., Geltinger, F., Duschl, J., Bresgen, N., Briza, P., Haskova, D., Lejskova, R., Sopjani, M., Richter, K., & Rinnerthaler, M. (2017). Clearing the outer mitochondrial membrane from harmful proteins via lipid droplets. *Cell Death Discov*, 3, 17016. <https://doi.org/10.1038/cddiscovery.2017.16>
- Borradaile, N. M., & Schaffer, J. E. (2005). Lipotoxicity in the heart. *Curr Hypertens Rep*, 7(6), 412-417. <https://doi.org/10.1007/s11906-005-0035-y>
- Bowser, D. N., Minamikawa, T., Nagley, P., & Williams, D. A. (1998). Role of mitochondria in calcium regulation of spontaneously contracting cardiac muscle cells. *Biophys J*, 75(4), 2004-2014. [https://doi.org/10.1016/S0006-3495\(98\)77642-8](https://doi.org/10.1016/S0006-3495(98)77642-8)

- Brand, M. D. (2016). Mitochondrial generation of superoxide and hydrogen peroxide as the source of mitochondrial redox signaling. *Free Radic Biol Med*, 100, 14-31. <https://doi.org/10.1016/j.freeradbiomed.2016.04.001>
- Brandt, T., Cavellini, L., Kuhlbrandt, W., & Cohen, M. M. (2016). A mitofusin-dependent docking ring complex triggers mitochondrial fusion in vitro. *Elife*, 5. <https://doi.org/10.7554/eLife.14618>
- Brier, L. W., Ge, L., Stjepanovic, G., Thelen, A. M., Hurley, J. H., & Schekman, R. (2019). Regulation of LC3 lipidation by the autophagy-specific class III phosphatidylinositol-3 kinase complex. *Mol Biol Cell*, 30(9), 1098-1107. <https://doi.org/10.1091/mbc.E18-11-0743>
- Cadete, V. J., Deschenes, S., Cuillerier, A., Brisebois, F., Sugiura, A., Vincent, A., Turnbull, D., Picard, M., McBride, H. M., & Burelle, Y. (2016). Formation of mitochondrial-derived vesicles is an active and physiologically relevant mitochondrial quality control process in the cardiac system. *J Physiol*, 594(18), 5343-5362. <https://doi.org/10.1113/JP272703>
- Cairns, G., Thumiah-Mootoo, M., Burelle, Y., & Khacho, M. (2020). Mitophagy: A New Player in Stem Cell Biology. *Biology (Basel)*, 9(12). <https://doi.org/10.3390/biology9120481>
- Calle, X., Garrido-Moreno, V., Lopez-Gallardo, E., Norambuena-Soto, I., Martinez, D., Penalzoza-Otarola, A., Troncossi, A., Guerrero-Moncayo, A., Ortega, A., Maracaja-Coutinho, V., Parra, V., Chiong, M., & Lavandero, S. (2022). Mitochondrial E3 ubiquitin ligase 1 (MUL1) as a novel therapeutic target for diseases associated with mitochondrial dysfunction. *IUBMB Life*, 74(9), 850-865. <https://doi.org/10.1002/iub.2657>
- Casanova, A., Wevers, A., Navarro-Ledesma, S., & Pruijboom, L. (2023). Mitochondria: It is all about energy. *Front Physiol*, 14, 1114231. <https://doi.org/10.3389/fphys.2023.1114231>
- Castresana, J., & Saraste, M. (1995). Evolution of energetic metabolism: the respiration-early hypothesis. *Trends Biochem Sci*, 20(11), 443-448. [https://doi.org/10.1016/s0968-0004\(00\)89098-2](https://doi.org/10.1016/s0968-0004(00)89098-2)
- Chan, E. Y., Kir, S., & Tooze, S. A. (2007). siRNA screening of the kinome identifies ULK1 as a multidomain modulator of autophagy. *J Biol Chem*, 282(35), 25464-25474. <https://doi.org/10.1074/jbc.M703663200>
- Chandel, N. S. (2021a). Carbohydrate Metabolism. *Cold Spring Harb Perspect Biol*, 13(1). <https://doi.org/10.1101/cshperspect.a040568>
- Chandel, N. S. (2021b). Glycolysis. *Cold Spring Harb Perspect Biol*, 13(5). <https://doi.org/10.1101/cshperspect.a040535>
- Chen, G., Han, Z., Feng, D., Chen, Y., Chen, L., Wu, H., Huang, L., Zhou, C., Cai, X., Fu, C., Duan, L., Wang, X., Liu, L., Liu, X., Shen, Y., Zhu, Y., & Chen, Q. (2014). A regulatory signaling loop comprising the PGAM5 phosphatase and CK2 controls receptor-mediated mitophagy. *Mol Cell*, 54(3), 362-377. <https://doi.org/10.1016/j.molcel.2014.02.034>
- Chen, G., Kroemer, G., & Kepp, O. (2020). Mitophagy: An Emerging Role in Aging and Age-Associated Diseases. *Front Cell Dev Biol*, 8, 200. <https://doi.org/10.3389/fcell.2020.00200>
- Cheng, R., Zhang, F., Li, M., Wo, X., Su, Y. W., & Wang, W. (2019). Influence of Fixation and Permeabilization on the Mass Density of Single Cells: A Surface Plasmon Resonance Imaging Study. *Front Chem*, 7, 588. <https://doi.org/10.3389/fchem.2019.00588>
- Chinnadurai, G., Vijayalingam, S., & Gibson, S. B. (2008). BNIP3 subfamily BH3-only proteins: mitochondrial stress sensors in normal and pathological functions. *Oncogene*, 27 Suppl 1(Suppl 1), S114-127. <https://doi.org/10.1038/onc.2009.49>
- Choi, S., Houdek, X., & Anderson, R. A. (2018). Phosphoinositide 3-kinase pathways and autophagy require phosphatidylinositol phosphate kinases. *Adv Biol Regul*, 68, 31-38. <https://doi.org/10.1016/j.jbior.2018.02.003>
- Chu, C. T., Ji, J., Dagda, R. K., Jiang, J. F., Tyurina, Y. Y., Kapralov, A. A., Tyurin, V. A., Yanamala, N., Shrivastava, I. H., Mohammadyani, D., Wang, K. Z. Q., Zhu, J., Klein-Seetharaman, J., Balasubramanian, K., Amoscato, A. A., Borisenko, G., Huang, Z., Gusdon, A. M., Cheikhi, A., . . . Kagan, V. E. (2013). Cardiolipin externalization to the outer mitochondrial membrane acts as an elimination signal for mitophagy in neuronal cells. *Nat Cell Biol*, 15(10), 1197-1205. <https://doi.org/10.1038/ncb2837>
- Chun Chung, G. H., Gissen, P., Stefan, C. J., & Burden, J. J. (2022). Three-dimensional Characterization of Interorganelle Contact Sites in Hepatocytes using Serial Section Electron Microscopy. *J Vis Exp*(184). <https://doi.org/10.3791/63496>

- Chung, J., Park, J., Lai, Z. W., Lambert, T. J., Richards, R. C., Zhang, J., Walther, T. C., & Farese, R. V., Jr. (2023). The Troyer syndrome protein spartin mediates selective autophagy of lipid droplets. *Nat Cell Biol*, 25(8), 1101-1110. <https://doi.org/10.1038/s41556-023-01178-w>
- Collier, J. J., Suomi, F., Olahova, M., McWilliams, T. G., & Taylor, R. W. (2021). Emerging roles of ATG7 in human health and disease. *EMBO Mol Med*, 13(12), e14824. <https://doi.org/10.15252/emmm.202114824>
- Correia, C., Koshkin, A., Duarte, P., Hu, D., Teixeira, A., Domian, I., Serra, M., & Alves, P. M. (2017). Distinct carbon sources affect structural and functional maturation of cardiomyocytes derived from human pluripotent stem cells. *Sci Rep*, 7(1), 8590. <https://doi.org/10.1038/s41598-017-08713-4>
- Cui, W., Sathyanarayan, A., Lopresti, M., Aghajan, M., Chen, C., & Mashek, D. G. (2021). Lipophagy-derived fatty acids undergo extracellular efflux via lysosomal exocytosis. *Autophagy*, 17(3), 690-705. <https://doi.org/10.1080/15548627.2020.1728097>
- D'Autreaux, B., & Toledano, M. B. (2007). ROS as signalling molecules: mechanisms that generate specificity in ROS homeostasis. *Nat Rev Mol Cell Biol*, 8(10), 813-824. <https://doi.org/10.1038/nrm2256>
- de Carvalho, C., & Caramujo, M. J. (2018). The Various Roles of Fatty Acids. *Molecules*, 23(10). <https://doi.org/10.3390/molecules23102583>
- De Gaetano, A., Gibellini, L., Zanini, G., Nasi, M., Cossarizza, A., & Pinti, M. (2021). Mitophagy and Oxidative Stress: The Role of Aging. *Antioxidants (Basel)*, 10(5). <https://doi.org/10.3390/antiox10050794>
- de la Ballina, L. R., Munson, M. J., & Simonsen, A. (2020). Lipids and Lipid-Binding Proteins in Selective Autophagy. *J Mol Biol*, 432(1), 135-159. <https://doi.org/10.1016/j.jmb.2019.05.051>
- Demine, S., Renard, P., & Arnould, T. (2019). Mitochondrial Uncoupling: A Key Controller of Biological Processes in Physiology and Diseases. *Cells*, 8(8). <https://doi.org/10.3390/cells8080795>
- Dey, G., Thattai, M., & Baum, B. (2016). On the Archaeal Origins of Eukaryotes and the Challenges of Inferring Phenotype from Genotype. *Trends Cell Biol*, 26(7), 476-485. <https://doi.org/10.1016/j.tcb.2016.03.009>
- Dikic, I., & Elazar, Z. (2018). Mechanism and medical implications of mammalian autophagy. *Nat Rev Mol Cell Biol*, 19(6), 349-364. <https://doi.org/10.1038/s41580-018-0003-4>
- Ding, W. X., & Yin, X. M. (2012). Mitophagy: mechanisms, pathophysiological roles, and analysis. *Biol Chem*, 393(7), 547-564. <https://doi.org/10.1515/hsz-2012-0119>
- Edwards, R., Eaglesfield, R., & Tokatlidis, K. (2021). The mitochondrial intermembrane space: the most constricted mitochondrial sub-compartment with the largest variety of protein import pathways. *Open Biol*, 11(3), 210002. <https://doi.org/10.1098/rsob.210002>
- Esteban-Martinez, L., & Boya, P. (2018). BNIP3L/NIX-dependent mitophagy regulates cell differentiation via metabolic reprogramming. *Autophagy*, 14(5), 915-917. <https://doi.org/10.1080/15548627.2017.1332567>
- Esteban-Martinez, L., Sierra-Filardi, E., McGreal, R. S., Salazar-Roa, M., Marino, G., Seco, E., Durand, S., Enot, D., Grana, O., Malumbres, M., Cvekl, A., Cuervo, A. M., Kroemer, G., & Boya, P. (2017). Programmed mitophagy is essential for the glycolytic switch during cell differentiation. *EMBO J*, 36(12), 1688-1706. <https://doi.org/10.15252/emboj.201695916>
- Fang, E. F., Palikaras, K., Sun, N., Fivenson, E. M., Spangler, R. D., Kerr, J. S., Cordonnier, S. A., Hou, Y., Dombi, E., Kassahun, H., Tavernarakis, N., Poulton, J., Nilsen, H., & Bohr, V. A. (2017). In Vitro and In Vivo Detection of Mitophagy in Human Cells, C. Elegans, and Mice. *J Vis Exp*(129). <https://doi.org/10.3791/56301>
- Farnung, J., Muhar, M., Liang, J. R., Tolmachova, K. A., Benoit, R. M., Corn, J. E., & Bode, J. W. (2023). Semisynthetic LC3 Probes for Autophagy Pathways Reveal a Noncanonical LC3 Interacting Region Motif Crucial for the Enzymatic Activity of Human ATG3. *ACS Cent Sci*, 9(5), 1025-1034. <https://doi.org/10.1021/acscentsci.3c00009>
- Frey, P. A. (1996). The Leloir pathway: a mechanistic imperative for three enzymes to change the stereochemical configuration of a single carbon in galactose. *FASEB J*, 10(4), 461-470. <https://www.ncbi.nlm.nih.gov/pubmed/8647345>

- Fujimoto, T., & Parton, R. G. (2011). Not just fat: the structure and function of the lipid droplet. *Cold Spring Harb Perspect Biol*, 3(3). <https://doi.org/10.1101/cshperspect.a004838>
- Gammoh, N., Florey, O., Overholtzer, M., & Jiang, X. (2013). Interaction between FIP200 and ATG16L1 distinguishes ULK1 complex-dependent and -independent autophagy. *Nat Struct Mol Biol*, 20(2), 144-149. <https://doi.org/10.1038/nsmb.2475>
- Gandotra, S., Le Dour, C., Bottomley, W., Cervera, P., Giral, P., Reznik, Y., Charpentier, G., Auclair, M., Delepine, M., Barroso, I., Semple, R. K., Lathrop, M., Lascols, O., Capeau, J., O'Rahilly, S., Magre, J., Savage, D. B., & Vigouroux, C. (2011). Perilipin deficiency and autosomal dominant partial lipodystrophy. *N Engl J Med*, 364(8), 740-748. <https://doi.org/10.1056/NEJMoa1007487>
- Ganley, I. G., & Simonsen, A. (2022). Diversity of mitophagy pathways at a glance. *J Cell Sci*, 135(23). <https://doi.org/10.1242/jcs.259748>
- Gilkerson, R. W., Selker, J. M., & Capaldi, R. A. (2003). The cristal membrane of mitochondria is the principal site of oxidative phosphorylation. *FEBS Lett*, 546(2-3), 355-358. [https://doi.org/10.1016/s0014-5793\(03\)00633-1](https://doi.org/10.1016/s0014-5793(03)00633-1)
- Glancy, B., Kim, Y., Katti, P., & Willingham, T. B. (2020). The Functional Impact of Mitochondrial Structure Across Subcellular Scales. *Front Physiol*, 11, 541040. <https://doi.org/10.3389/fphys.2020.541040>
- Glick, D., Zhang, W., Beaton, M., Marsboom, G., Gruber, M., Simon, M. C., Hart, J., Dorn, G. W., 2nd, Brady, M. J., & Macleod, K. F. (2012). BNip3 regulates mitochondrial function and lipid metabolism in the liver. *Mol Cell Biol*, 32(13), 2570-2584. <https://doi.org/10.1128/MCB.00167-12>
- Gok, M. O., Connor, O. M., Wang, X., Menezes, C. J., Llamas, C. B., Mishra, P., & Friedman, J. R. (2023). The outer mitochondrial membrane protein TMEM11 demarcates spatially restricted BNIP3/BNIP3L-mediated mitophagy. *J Cell Biol*, 222(4). <https://doi.org/10.1083/jcb.202204021>
- Goldberg, I. J., Reue, K., Abumrad, N. A., Bickel, P. E., Cohen, S., Fisher, E. A., Galis, Z. S., Granneman, J. G., Lewandowski, E. D., Murphy, R., Olive, M., Schaffer, J. E., Schwartz-Longacre, L., Shulman, G. I., Walther, T. C., & Chen, J. (2018). Deciphering the Role of Lipid Droplets in Cardiovascular Disease: A Report From the 2017 National Heart, Lung, and Blood Institute Workshop. *Circulation*, 138(3), 305-315. <https://doi.org/10.1161/CIRCULATIONAHA.118.033704>
- Gong, G., Song, M., Csordas, G., Kelly, D. P., Matkovich, S. J., & Dorn, G. W., 2nd. (2015). Parkin-mediated mitophagy directs perinatal cardiac metabolic maturation in mice. *Science*, 350(6265), aad2459. <https://doi.org/10.1126/science.aad2459>
- Gould, S. B., Garg, S. G., & Martin, W. F. (2016). Bacterial Vesicle Secretion and the Evolutionary Origin of the Eukaryotic Endomembrane System. *Trends Microbiol*, 24(7), 525-534. <https://doi.org/10.1016/j.tim.2016.03.005>
- Gray, M. W. (2012). Mitochondrial evolution. *Cold Spring Harb Perspect Biol*, 4(9), a011403. <https://doi.org/10.1101/cshperspect.a011403>
- Greenberg, A. S., Coleman, R. A., Kraemer, F. B., McManaman, J. L., Obin, M. S., Puri, V., Yan, Q. W., Miyoshi, H., & Mashek, D. G. (2011). The role of lipid droplets in metabolic disease in rodents and humans. *J Clin Invest*, 121(6), 2102-2110. <https://doi.org/10.1172/JCI46069>
- Greene, A. W., Grenier, K., Aguileta, M. A., Muise, S., Farazifard, R., Haque, M. E., McBride, H. M., Park, D. S., & Fon, E. A. (2012). Mitochondrial processing peptidase regulates PINK1 processing, import and Parkin recruitment. *EMBO Rep*, 13(4), 378-385. <https://doi.org/10.1038/embor.2012.14>
- Haemmerle, G., Moustafa, T., Woelkart, G., Buttner, S., Schmidt, A., van de Weijer, T., Hesselink, M., Jaeger, D., Kienesberger, P. C., Zierler, K., Schreiber, R., Eichmann, T., Kolb, D., Kotzbeck, P., Schweiger, M., Kumari, M., Eder, S., Schoiswohl, G., Wongsiriroj, N., . . . Zechner, R. (2011). ATGL-mediated fat catabolism regulates cardiac mitochondrial function via PPAR-alpha and PGC-1. *Nat Med*, 17(9), 1076-1085. <https://doi.org/10.1038/nm.2439>
- Han, J., & Kaufman, R. J. (2016). The role of ER stress in lipid metabolism and lipotoxicity. *J Lipid Res*, 57(8), 1329-1338. <https://doi.org/10.1194/jlr.R067595>

- Hanna, R. A., Quinsay, M. N., Orogo, A. M., Giang, K., Rikka, S., & Gustafsson, A. B. (2012). Microtubule-associated protein 1 light chain 3 (LC3) interacts with Bnip3 protein to selectively remove endoplasmic reticulum and mitochondria via autophagy. *J Biol Chem*, 287(23), 19094-19104. <https://doi.org/10.1074/jbc.M111.322933>
- Harding, O., Evans, C. S., Ye, J., Cheung, J., Maniatis, T., & Holzbaur, E. L. F. (2021). ALS- and FTD-associated missense mutations in TBK1 differentially disrupt mitophagy. *Proc Natl Acad Sci U S A*, 118(24). <https://doi.org/10.1073/pnas.2025053118>
- Hayat, M. A. (1986). Glutaraldehyde: Role in electron microscopy. *Micron and Microscopica Acta*, 17(2), 115-135. [https://doi.org/https://doi.org/10.1016/0739-6260\(86\)90042-0](https://doi.org/https://doi.org/10.1016/0739-6260(86)90042-0)
- He, Y. L., Li, J., Gong, S. H., Cheng, X., Zhao, M., Cao, Y., Zhao, T., Zhao, Y. Q., Fan, M., Wu, H. T., Zhu, L. L., & Wu, L. Y. (2022). BNIP3 phosphorylation by JNK1/2 promotes mitophagy via enhancing its stability under hypoxia. *Cell Death Dis*, 13(11), 966. <https://doi.org/10.1038/s41419-022-05418-z>
- Heintzmann, R., & Huser, T. (2017). Super-Resolution Structured Illumination Microscopy. *Chem Rev*, 117(23), 13890-13908. <https://doi.org/10.1021/acs.chemrev.7b00218>
- Henne, M. (2019). And three's a party: lysosomes, lipid droplets, and the ER in lipid trafficking and cell homeostasis. *Curr Opin Cell Biol*, 59, 40-49. <https://doi.org/10.1016/j.ceb.2019.02.011>
- Hirota, Y., Yamashita, S., Kurihara, Y., Jin, X., Aihara, M., Saigusa, T., Kang, D., & Kanki, T. (2015). Mitophagy is primarily due to alternative autophagy and requires the MAPK1 and MAPK14 signaling pathways. *Autophagy*, 11(2), 332-343. <https://doi.org/10.1080/15548627.2015.1023047>
- Hobro, A. J., & Smith, N. I. (2017). An evaluation of fixation methods: Spatial and compositional cellular changes observed by Raman imaging. *Vibrational Spectroscopy*, 91, 31-45. <https://doi.org/https://doi.org/10.1016/j.vibspec.2016.10.012>
- Honda, S., Arakawa, S., Nishida, Y., Yamaguchi, H., Ishii, E., & Shimizu, S. (2014). Ulk1-mediated Atg5-independent macroautophagy mediates elimination of mitochondria from embryonic reticulocytes. *Nat Commun*, 5, 4004. <https://doi.org/10.1038/ncomms5004>
- Hossler, P., Racicot, C., Chumsae, C., McDermott, S., & Cochran, K. (2017). Cell culture media supplementation of infrequently used sugars for the targeted shifting of protein glycosylation profiles. *Biotechnol Prog*, 33(2), 511-522. <https://doi.org/10.1002/btpr.2429>
- Huang, X., Fan, J., Li, L., Liu, H., Wu, R., Wu, Y., Wei, L., Mao, H., Lal, A., Xi, P., Tang, L., Zhang, Y., Liu, Y., Tan, S., & Chen, L. (2018). Fast, long-term, super-resolution imaging with Hessian structured illumination microscopy. *Nat Biotechnol*, 36(5), 451-459. <https://doi.org/10.1038/nbt.4115>
- Huff, J. (2016). The Fast mode for ZEISS LSM 880 with Airyscan: high-speed confocal imaging with super-resolution and improved signal-to-noise ratio. *Nature Methods*, 13(11), i-ii. <https://doi.org/10.1038/nmeth.f.398>
- Hundeshagen, P., Hamacher-Brady, A., Eils, R., & Brady, N. R. (2011). Concurrent detection of autolysosome formation and lysosomal degradation by flow cytometry in a high-content screen for inducers of autophagy. *BMC Biol*, 9, 38. <https://doi.org/10.1186/1741-7007-9-38>
- Huss, J. M., & Kelly, D. P. (2005). Mitochondrial energy metabolism in heart failure: a question of balance. *J Clin Invest*, 115(3), 547-555. <https://doi.org/10.1172/JCI24405>
- Hytti, M., Korhonen, E., Hyttinen, J. M. T., Roehrich, H., Kaarniranta, K., Ferrington, D. A., & Kauppinen, A. (2019). Antimycin A-Induced Mitochondrial Damage Causes Human RPE Cell Death despite Activation of Autophagy. *Oxid Med Cell Longev*, 2019, 1583656. <https://doi.org/10.1155/2019/1583656>
- Ichimura, Y., Kirisako, T., Takao, T., Satomi, Y., Shimonishi, Y., Ishihara, N., Mizushima, N., Tanida, I., Kominami, E., Ohsumi, M., Noda, T., & Ohsumi, Y. (2000). A ubiquitin-like system mediates protein lipidation. *Nature*, 408(6811), 488-492. <https://doi.org/10.1038/35044114>
- Ichishita, R., Tanaka, K., Sugiura, Y., Sayano, T., Mihara, K., & Oka, T. (2008). An RNAi screen for mitochondrial proteins required to maintain the morphology of the organelle in *Caenorhabditis elegans*. *J Biochem*, 143(4), 449-454. <https://doi.org/10.1093/jb/mvm245>
- Ingwall, J. S. (2002). *ATP and the Heart* (Vol. 11). Springer Science & Business Media.

- Iorio, R., Celenza, G., & Petricca, S. (2021). Mitophagy: Molecular Mechanisms, New Concepts on Parkin Activation and the Emerging Role of AMPK/ULK1 Axis. *Cells*, *11*(1). <https://doi.org/10.3390/cells11010030>
- Iriondo, M. N., Etxaniz, A., Varela, Y. R., Ballesteros, U., Hervás, J. H., Montes, L. R., Goni, F. M., & Alonso, A. (2022). LC3 subfamily in cardiolipin-mediated mitophagy: a comparison of the LC3A, LC3B and LC3C homologs. *Autophagy*, *18*(12), 2985-3003. <https://doi.org/10.1080/15548627.2022.2062111>
- Jain, S., Caforio, A., & Driessen, A. J. (2014). Biosynthesis of archaeal membrane ether lipids. *Front Microbiol*, *5*, 641. <https://doi.org/10.3389/fmicb.2014.00641>
- Ji, W. K., Hatch, A. L., Merrill, R. A., Strack, S., & Higgs, H. N. (2015). Actin filaments target the oligomeric maturation of the dynamin GTPase Drp1 to mitochondrial fission sites. *Elife*, *4*, e11553. <https://doi.org/10.7554/eLife.11553>
- Jin, M., Liu, X., & Klionsky, D. J. (2013). SnapShot: Selective autophagy. *Cell*, *152*(1-2), 368-368 e362. <https://doi.org/10.1016/j.cell.2013.01.004>
- Jin, S. M., Lazarou, M., Wang, C., Kane, L. A., Narendra, D. P., & Youle, R. J. (2010). Mitochondrial membrane potential regulates PINK1 import and proteolytic destabilization by PARL. *J Cell Biol*, *191*(5), 933-942. <https://doi.org/10.1083/jcb.201008084>
- Johansen, T., & Lamark, T. (2020). Selective Autophagy: ATG8 Family Proteins, LIR Motifs and Cargo Receptors. *J Mol Biol*, *432*(1), 80-103. <https://doi.org/10.1016/j.jmb.2019.07.016>
- Jump, D. B., Tripathy, S., & Depner, C. M. (2013). Fatty acid-regulated transcription factors in the liver. *Annu Rev Nutr*, *33*, 249-269. <https://doi.org/10.1146/annurev-nutr-071812-161139>
- Jung, C. H., Jun, C. B., Ro, S. H., Kim, Y. M., Otto, N. M., Cao, J., Kundu, M., & Kim, D. H. (2009). ULK-Atg13-FIP200 complexes mediate mTOR signaling to the autophagy machinery. *Mol Biol Cell*, *20*(7), 1992-2003. <https://doi.org/10.1091/mbc.e08-12-1249>
- Kagan, V. E., Jiang, J., Huang, Z., Tyurina, Y. Y., Desbordes, C., Cottet-Rousselle, C., Dar, H. H., Verma, M., Tyurin, V. A., Kapralov, A. A., Cheikhi, A., Mao, G., Stolz, D., St Croix, C. M., Watkins, S., Shen, Z., Li, Y., Greenberg, M. L., Tokarska-Schlattner, M., . . . Schlattner, U. (2016). NDPK-D (NM23-H4)-mediated externalization of cardiolipin enables elimination of depolarized mitochondria by mitophagy. *Cell Death Differ*, *23*(7), 1140-1151. <https://doi.org/10.1038/cdd.2015.160>
- Kamerkar, S. C., Kraus, F., Sharpe, A. J., Pucadyil, T. J., & Ryan, M. T. (2018). Dynamin-related protein 1 has membrane constricting and severing abilities sufficient for mitochondrial and peroxisomal fission. *Nat Commun*, *9*(1), 5239. <https://doi.org/10.1038/s41467-018-07543-w>
- Kamradt, M. L., Jung, J. U., Pflug, K. M., Lee, D. W., Fanniel, V., & Sitcheran, R. (2021). NIK promotes metabolic adaptation of glioblastoma cells to bioenergetic stress. *Cell Death Dis*, *12*(3), 271. <https://doi.org/10.1038/s41419-020-03383-z>
- Kerner, J., & Hoppel, C. (2000). Fatty acid import into mitochondria. *Biochim Biophys Acta*, *1486*(1), 1-17. [https://doi.org/10.1016/s1388-1981\(00\)00044-5](https://doi.org/10.1016/s1388-1981(00)00044-5)
- Kim, J., Kundu, M., Viollet, B., & Guan, K. L. (2011). AMPK and mTOR regulate autophagy through direct phosphorylation of Ulk1. *Nat Cell Biol*, *13*(2), 132-141. <https://doi.org/10.1038/ncb2152>
- Kleele, T., Rey, T., Winter, J., Zaganelli, S., Mahecic, D., Perreten Lambert, H., Ruberto, F. P., Nemir, M., Wai, T., Pedrazzini, T., & Manley, S. (2021). Distinct fission signatures predict mitochondrial degradation or biogenesis. *Nature*, *593*(7859), 435-439. <https://doi.org/10.1038/s41586-021-03510-6>
- Klionsky, D. J. (2008). Autophagy revisited: a conversation with Christian de Duve. *Autophagy*, *4*(6), 740-743. <https://doi.org/10.4161/auto.6398>
- Klionsky, D. J., Abdel-Aziz, A. K., Abdelfatah, S., Abdellatif, M., Abdoli, A., Abel, S., Abeliovich, H., Abildgaard, M. H., Abudu, Y. P., Acevedo-Arozena, A., Adamopoulos, I. E., Adeli, K., Adolph, T. E., Adornetto, A., Aflaki, E., Agam, G., Agarwal, A., Aggarwal, B. B., Agnello, M., . . . Tong, C. K. (2021). Guidelines for the use and interpretation of assays for monitoring autophagy (4th edition)(1). *Autophagy*, *17*(1), 1-382. <https://doi.org/10.1080/15548627.2020.1797280>
- Kobayashi, S., Patel, J., Zhao, F., Huang, Y., Kobayashi, T., & Liang, Q. (2020a). Novel Dual-Fluorescent Mitophagy Reporter Reveals a Reduced Mitophagy Flux in Type 1 Diabetic Mouse Heart. *J Am Osteopath Assoc*, *120*(7), 446-455. <https://doi.org/10.7556/jaoa.2020.072>

- Kobayashi, S., Zhao, F., Zhang, Z., Kobayashi, T., Huang, Y., Shi, B., Wu, W., & Liang, Q. (2020b). Mitochondrial Fission and Mitophagy Coordinately Restrict High Glucose Toxicity in Cardiomyocytes. *Front Physiol*, *11*, 604069. <https://doi.org/10.3389/fphys.2020.604069>
- Kondadi, A. K., Anand, R., & Reichert, A. S. (2020). Cristae Membrane Dynamics - A Paradigm Change. *Trends Cell Biol*, *30*(12), 923-936. <https://doi.org/10.1016/j.tcb.2020.08.008>
- Korobova, F., Ramabhadran, V., & Higgs, H. N. (2013). An actin-dependent step in mitochondrial fission mediated by the ER-associated formin INF2. *Science*, *339*(6118), 464-467. <https://doi.org/10.1126/science.1228360>
- Kowalczyk, P., Sulejczak, D., Kleczkowska, P., Bukowska-Osko, I., Kucia, M., Popiel, M., Wietrak, E., Kramkowski, K., Wrzosek, K., & Kaczynska, K. (2021). Mitochondrial Oxidative Stress-A Causative Factor and Therapeutic Target in Many Diseases. *Int J Mol Sci*, *22*(24). <https://doi.org/10.3390/ijms222413384>
- Koyano, F., Yamano, K., Kosako, H., Tanaka, K., & Matsuda, N. (2019). Parkin recruitment to impaired mitochondria for nonselective ubiquitylation is facilitated by MITOL. *J Biol Chem*, *294*(26), 10300-10314. <https://doi.org/10.1074/jbc.RA118.006302>
- Krakauer, D. C., & Plotkin, J. B. (2002). Redundancy, antiredundancy, and the robustness of genomes. *Proc Natl Acad Sci U S A*, *99*(3), 1405-1409. <https://doi.org/10.1073/pnas.032668599>
- Krantz, S., Kim, Y. M., Srivastava, S., Leasure, J. W., Toth, P. T., Marsboom, G., & Rehman, J. (2021). Mitophagy mediates metabolic reprogramming of induced pluripotent stem cells undergoing endothelial differentiation. *J Biol Chem*, *297*(6), 101410. <https://doi.org/10.1016/j.jbc.2021.101410>
- Kriegenburg, F., Ungermann, C., & Reggiori, F. (2018). Coordination of Autophagosome-Lysosome Fusion by Atg8 Family Members. *Curr Biol*, *28*(8), R512-R518. <https://doi.org/10.1016/j.cub.2018.02.034>
- Kruppa, A. J., & Buss, F. (2021). Motor proteins at the mitochondria-cytoskeleton interface. *J Cell Sci*, *134*(7). <https://doi.org/10.1242/jcs.226084>
- Kuang, Y., Ma, K., Zhou, C., Ding, P., Zhu, Y., Chen, Q., & Xia, B. (2016). Structural basis for the phosphorylation of FUNDC1 LIR as a molecular switch of mitophagy. *Autophagy*, *12*(12), 2363-2373. <https://doi.org/10.1080/15548627.2016.1238552>
- Kubli, D. A., & Gustafsson, A. B. (2012). Mitochondria and mitophagy: the yin and yang of cell death control. *Circ Res*, *111*(9), 1208-1221. <https://doi.org/10.1161/CIRCRESAHA.112.265819>
- Kuhlbrandt, W. (2015). Structure and function of mitochondrial membrane protein complexes. *BMC Biol*, *13*, 89. <https://doi.org/10.1186/s12915-015-0201-x>
- Kurniawan, H., Kobayashi, T., & Brenner, D. (2021). The emerging role of one-carbon metabolism in T cells. *Curr Opin Biotechnol*, *68*, 193-201. <https://doi.org/10.1016/j.copbio.2020.12.001>
- König, T., Nolte, H., Aaltonen, M. J., Tatsuta, T., Krols, M., Stroh, T., Langer, T., & McBride, H. M. (2021). MIROs and DRP1 drive mitochondrial-derived vesicle biogenesis and promote quality control. *Nat Cell Biol*, *23*(12), 1271-1286. <https://doi.org/10.1038/s41556-021-00798-4>
- Lavi, O. (2015). Redundancy: a critical obstacle to improving cancer therapy. *Cancer Res*, *75*(5), 808-812. <https://doi.org/10.1158/0008-5472.CAN-14-3256>
- Lavorato, M., Iyer, V. R., Dewight, W., Cupo, R. R., Debattisti, V., Gomez, L., De la Fuente, S., Zhao, Y. T., Valdivia, H. H., Hajnoczky, G., & Franzini-Armstrong, C. (2017). Increased mitochondrial nanotunneling activity, induced by calcium imbalance, affects intermitochondrial matrix exchanges. *Proc Natl Acad Sci U S A*, *114*(5), E849-E858. <https://doi.org/10.1073/pnas.1617788113>
- Lazarou, M., Sliter, D. A., Kane, L. A., Sarraf, S. A., Wang, C., Burman, J. L., Sideris, D. P., Fogel, A. I., & Youle, R. J. (2015). The ubiquitin kinase PINK1 recruits autophagy receptors to induce mitophagy. *Nature*, *524*(7565), 309-314. <https://doi.org/10.1038/nature14893>
- Le Guerroue, F., Eck, F., Jung, J., Starzetz, T., Mittelbronn, M., Kaulich, M., & Behrends, C. (2017). Autophagosomal Content Profiling Reveals an LC3C-Dependent Piecemeal Mitophagy Pathway. *Mol Cell*, *68*(4), 786-796 e786. <https://doi.org/10.1016/j.molcel.2017.10.029>
- Lee, J. J., Sanchez-Martinez, A., Martinez Zarate, A., Beninca, C., Mayor, U., Clague, M. J., & Whitworth, A. J. (2018). Basal mitophagy is widespread in Drosophila but minimally affected by loss of Pink1 or parkin. *J Cell Biol*, *217*(5), 1613-1622. <https://doi.org/10.1083/jcb.201801044>

- Lee, K., Kerner, J., & Hoppel, C. L. (2011). Mitochondrial carnitine palmitoyltransferase 1a (CPT1a) is part of an outer membrane fatty acid transfer complex. *J Biol Chem*, 286(29), 25655-25662. <https://doi.org/10.1074/jbc.M111.228692>
- Lee, Y., Lee, H. Y., Hanna, R. A., & Gustafsson, A. B. (2011). Mitochondrial autophagy by Bnip3 involves Drp1-mediated mitochondrial fission and recruitment of Parkin in cardiac myocytes. *Am J Physiol Heart Circ Physiol*, 301(5), H1924-1931. <https://doi.org/10.1152/ajpheart.00368.2011>
- Leermakers, P. A., Remels, A. H. V., Zonneveld, M. I., Rouschop, K. M. A., Schols, A., & Gosker, H. R. (2020). Iron deficiency-induced loss of skeletal muscle mitochondrial proteins and respiratory capacity; the role of mitophagy and secretion of mitochondria-containing vesicles. *FASEB J*, 34(5), 6703-6717. <https://doi.org/10.1096/fj.201901815R>
- Lemasters, J. J. (2005). Selective mitochondrial autophagy, or mitophagy, as a targeted defense against oxidative stress, mitochondrial dysfunction, and aging. *Rejuvenation Res*, 8(1), 3-5. <https://doi.org/10.1089/rej.2005.8.3>
- Lewis, S. C., Uchiyama, L. F., & Nunnari, J. (2016). ER-mitochondria contacts couple mtDNA synthesis with mitochondrial division in human cells. *Science*, 353(6296), aaf5549. <https://doi.org/10.1126/science.aaf5549>
- Li, B., Zhao, H., Wu, Y., Zhu, Y., Zhang, J., Yang, G., Yan, Q., Li, J., Li, T., & Liu, L. (2020). Mitochondrial-Derived Vesicles Protect Cardiomyocytes Against Hypoxic Damage. *Front Cell Dev Biol*, 8, 214. <https://doi.org/10.3389/fcell.2020.00214>
- Li, Y., Zheng, W., Lu, Y., Zheng, Y., Pan, L., Wu, X., Yuan, Y., Shen, Z., Ma, S., Zhang, X., Wu, J., Chen, Z., & Zhang, X. (2021). BNIP3L/NIX-mediated mitophagy: molecular mechanisms and implications for human disease. *Cell Death Dis*, 13(1), 14. <https://doi.org/10.1038/s41419-021-04469-y>
- Liu, L., Feng, D., Chen, G., Chen, M., Zheng, Q., Song, P., Ma, Q., Zhu, C., Wang, R., Qi, W., Huang, L., Xue, P., Li, B., Wang, X., Jin, H., Wang, J., Yang, F., Liu, P., Zhu, Y., . . . Chen, Q. (2012). Mitochondrial outer-membrane protein FUNDC1 mediates hypoxia-induced mitophagy in mammalian cells. *Nat Cell Biol*, 14(2), 177-185. <https://doi.org/10.1038/ncb2422>
- Llopis, J., McCaffery, J. M., Miyawaki, A., Farquhar, M. G., & Tsien, R. Y. (1998). Measurement of cytosolic, mitochondrial, and Golgi pH in single living cells with green fluorescent proteins. *Proc Natl Acad Sci U S A*, 95(12), 6803-6808. <https://doi.org/10.1073/pnas.95.12.6803>
- Lopaschuk, G. D., Ussher, J. R., Folmes, C. D., Jaswal, J. S., & Stanley, W. C. (2010). Myocardial fatty acid metabolism in health and disease. *Physiol Rev*, 90(1), 207-258. <https://doi.org/10.1152/physrev.00015.2009>
- Loson, O. C., Song, Z., Chen, H., & Chan, D. C. (2013). Fis1, Mff, MiD49, and MiD51 mediate Drp1 recruitment in mitochondrial fission. *Mol Biol Cell*, 24(5), 659-667. <https://doi.org/10.1091/mbc.E12-10-0721>
- Luo, Y., Jiang, C., Yu, L., & Yang, A. (2020). Chemical Biology of Autophagy-Related Proteins With Posttranslational Modifications: From Chemical Synthesis to Biological Applications. *Front Chem*, 8, 233. <https://doi.org/10.3389/fchem.2020.00233>
- Lv, J., Guan, W., You, Q., Deng, L., Zhu, Y., Guo, K., Gao, X., Kong, J., & Yang, C. (2020). RIPC provides neuroprotection against ischemic stroke by suppressing apoptosis via the mitochondrial pathway. *Sci Rep*, 10(1), 5361. <https://doi.org/10.1038/s41598-020-62336-w>
- Lv, M., Wang, C., Li, F., Peng, J., Wen, B., Gong, Q., Shi, Y., & Tang, Y. (2017). Structural insights into the recognition of phosphorylated FUNDC1 by LC3B in mitophagy. *Protein Cell*, 8(1), 25-38. <https://doi.org/10.1007/s13238-016-0328-8>
- Lyons, T. W., Reinhard, C. T., & Planavsky, N. J. (2014). The rise of oxygen in Earth's early ocean and atmosphere. *Nature*, 506(7488), 307-315. <https://doi.org/10.1038/nature13068>
- Lystad, A. H., & Simonsen, A. (2019). Mechanisms and Pathophysiological Roles of the ATG8 Conjugation Machinery. *Cells*, 8(9). <https://doi.org/10.3390/cells8090973>
- Ma, X., Qian, H., Chen, A., Ni, H. M., & Ding, W. X. (2021). Perspectives on Mitochondria-ER and Mitochondria-Lipid Droplet Contact in Hepatocytes and Hepatic Lipid Metabolism. *Cells*, 10(9). <https://doi.org/10.3390/cells10092273>
- Mandell, M. A., Jain, A., Arko-Mensah, J., Chauhan, S., Kimura, T., Dinkins, C., Silvestri, G., Munch, J., Kirchhoff, F., Simonsen, A., Wei, Y., Levine, B., Johansen, T., & Deretic, V. (2014). TRIM

- proteins regulate autophagy and can target autophagic substrates by direct recognition. *Dev Cell*, 30(4), 394-409. <https://doi.org/10.1016/j.devcel.2014.06.013>
- Manner, J. (2022). When Does the Human Embryonic Heart Start Beating? A Review of Contemporary and Historical Sources of Knowledge about the Onset of Blood Circulation in Man. *J Cardiovasc Dev Dis*, 9(6). <https://doi.org/10.3390/jcdd9060187>
- Marcassa, E., Kallinos, A., Jardine, J., Rusilowicz-Jones, E. V., Martinez, A., Kuehl, S., Islinger, M., Clague, M. J., & Urbe, S. (2018). Dual role of USP30 in controlling basal pexophagy and mitophagy. *EMBO Rep*, 19(7). <https://doi.org/10.15252/embr.201745595>
- Martens, S., & Fracchiolla, D. (2020). Activation and targeting of ATG8 protein lipidation. *Cell Discov*, 6, 23. <https://doi.org/10.1038/s41421-020-0155-1>
- Martin, W. F., Garg, S., & Zimorski, V. (2015). Endosymbiotic theories for eukaryote origin. *Philos Trans R Soc Lond B Biol Sci*, 370(1678), 20140330. <https://doi.org/10.1098/rstb.2014.0330>
- Matheoud, D., Sugiura, A., Bellemare-Pelletier, A., Laplante, A., Rondeau, C., Chemali, M., Fazel, A., Bergeron, J. J., Trudeau, L. E., Burelle, Y., Gagnon, E., McBride, H. M., & Desjardins, M. (2016). Parkinson's Disease-Related Proteins PINK1 and Parkin Repress Mitochondrial Antigen Presentation. *Cell*, 166(2), 314-327. <https://doi.org/10.1016/j.cell.2016.05.039>
- McBride, H. M., Neuspiel, M., & Wasiak, S. (2006). Mitochondria: more than just a powerhouse. *Curr Biol*, 16(14), R551-560. <https://doi.org/10.1016/j.cub.2006.06.054>
- McLelland, G. L., Soubannier, V., Chen, C. X., McBride, H. M., & Fon, E. A. (2014). Parkin and PINK1 function in a vesicular trafficking pathway regulating mitochondrial quality control. *EMBO J*, 33(4), 282-295. <https://doi.org/10.1002/emboj.201385902>
- McWilliams, T. G., Prescott, A. R., Allen, G. F., Tamjar, J., Munson, M. J., Thomson, C., Muqit, M. M., & Ganley, I. G. (2016). mito-QC illuminates mitophagy and mitochondrial architecture in vivo. *J Cell Biol*, 214(3), 333-345. <https://doi.org/10.1083/jcb.201603039>
- McWilliams, T. G., Prescott, A. R., Montava-Garriga, L., Ball, G., Singh, F., Barini, E., Muqit, M. M. K., Brooks, S. P., & Ganley, I. G. (2018). Basal Mitophagy Occurs Independently of PINK1 in Mouse Tissues of High Metabolic Demand. *Cell Metab*, 27(2), 439-449 e435. <https://doi.org/10.1016/j.cmet.2017.12.008>
- Melser, S., Chatelain, E. H., Lavie, J., Mahfouf, W., Jose, C., Obre, E., Goorden, S., Priault, M., Elgersma, Y., Rezvani, H. R., Rossignol, R., & Benard, G. (2013). Rheb regulates mitophagy induced by mitochondrial energetic status. *Cell Metab*, 17(5), 719-730. <https://doi.org/10.1016/j.cmet.2013.03.014>
- Miner, G. E., So, C. M., Edwards, W., Ragusa, J. V., Wine, J. T., Wong Gutierrez, D., Airola, M. V., Herring, L. E., Coleman, R. A., Klett, E. L., & Cohen, S. (2023). PLIN5 interacts with FATP4 at membrane contact sites to promote lipid droplet-to-mitochondria fatty acid transport. *Dev Cell*, 58(14), 1250-1265 e1256. <https://doi.org/10.1016/j.devcel.2023.05.006>
- Miyazono, Y., Hirashima, S., Ishihara, N., Kusakawa, J., Nakamura, K. I., & Ohta, K. (2018). Uncoupled mitochondria quickly shorten along their long axis to form indented spheroids, instead of rings, in a fission-independent manner. *Sci Rep*, 8(1), 350. <https://doi.org/10.1038/s41598-017-18582-6>
- Mizushima, N. (2018). A brief history of autophagy from cell biology to physiology and disease. *Nat Cell Biol*, 20(5), 521-527. <https://doi.org/10.1038/s41556-018-0092-5>
- Mizushima, N., Noda, T., Yoshimori, T., Tanaka, Y., Ishii, T., George, M. D., Klionsky, D. J., Ohsumi, M., & Ohsumi, Y. (1998). A protein conjugation system essential for autophagy. *Nature*, 395(6700), 395-398. <https://doi.org/10.1038/26506>
- Mizushima, N., Yoshimori, T., & Ohsumi, Y. (2011). The role of Atg proteins in autophagosome formation. *Annu Rev Cell Dev Biol*, 27, 107-132. <https://doi.org/10.1146/annurev-cellbio-092910-154005>
- Moore, A. S., & Holzbaur, E. L. F. (2018). Mitochondrial-cytoskeletal interactions: dynamic associations that facilitate network function and remodeling. *Curr Opin Physiol*, 3, 94-100. <https://doi.org/10.1016/j.cophys.2018.03.003>
- Mostafavi, S., Balafkan, N., Pettersen, I. K. N., Nido, G. S., Siller, R., Tzoulis, C., Sullivan, G. J., & Bindoff, L. A. (2021). Distinct Mitochondrial Remodeling During Mesoderm Differentiation in a Human-Based Stem Cell Model. *Front Cell Dev Biol*, 9, 744777. <https://doi.org/10.3389/fcell.2021.744777>

- Murakawa, T., Yamaguchi, O., Hashimoto, A., Hikoso, S., Takeda, T., Oka, T., Yasui, H., Ueda, H., Akazawa, Y., Nakayama, H., Taneike, M., Misaka, T., Omiya, S., Shah, A. M., Yamamoto, A., Nishida, K., Ohsumi, Y., Okamoto, K., Sakata, Y., & Otsu, K. (2015). Bcl-2-like protein 13 is a mammalian Atg32 homologue that mediates mitophagy and mitochondrial fragmentation. *Nat Commun*, *6*, 7527. <https://doi.org/10.1038/ncomms8527>
- Murthy, M. S., & Pande, S. V. (1984). Mechanism of carnitine acylcarnitine translocase-catalyzed import of acylcarnitines into mitochondria. *J Biol Chem*, *259*(14), 9082-9089. <https://www.ncbi.nlm.nih.gov/pubmed/6430896>
- Nair, R., Gupta, P., & Shanmugam, M. (2022). Mitochondrial metabolic determinants of multiple myeloma growth, survival, and therapy efficacy. *Front Oncol*, *12*, 1000106. <https://doi.org/10.3389/fonc.2022.1000106>
- Nakatogawa, H., Suzuki, K., Kamada, Y., & Ohsumi, Y. (2009). Dynamics and diversity in autophagy mechanisms: lessons from yeast. *Nat Rev Mol Cell Biol*, *10*(7), 458-467. <https://doi.org/10.1038/nrm2708>
- Neuspiel, M., Schauss, A. C., Braschi, E., Zunino, R., Rippstein, P., Rachubinski, R. A., Andrade-Navarro, M. A., & McBride, H. M. (2008). Cargo-selected transport from the mitochondria to peroxisomes is mediated by vesicular carriers. *Curr Biol*, *18*(2), 102-108. <https://doi.org/10.1016/j.cub.2007.12.038>
- Ng, M. Y. W., Wai, T., & Simonsen, A. (2021). Quality control of the mitochondrion. *Dev Cell*, *56*(7), 881-905. <https://doi.org/10.1016/j.devcel.2021.02.009>
- Nguyen-Dien, G. T., Kozul, K. L., Cui, Y., Townsend, B., Kulkarni, P. G., Ooi, S. S., Marzio, A., Carroddus, N., Zuryn, S., Pagano, M., Parton, R. G., Lazarou, M., Millard, S. S., Taylor, R. W., Collins, B. M., Jones, M. J., & Pagan, J. K. (2023). FBXL4 suppresses mitophagy by restricting the accumulation of NIX and BNIP3 mitophagy receptors. *EMBO J*, *42*(13), e112767. <https://doi.org/10.15252/emboj.2022112767>
- Nguyen, T. B., Louie, S. M., Daniele, J. R., Tran, Q., Dillin, A., Zoncu, R., Nomura, D. K., & Olzmann, J. A. (2017). DGAT1-Dependent Lipid Droplet Biogenesis Protects Mitochondrial Function during Starvation-Induced Autophagy. *Dev Cell*, *42*(1), 9-21 e25. <https://doi.org/10.1016/j.devcel.2017.06.003>
- Nguyen, T. D., Shaid, S., Vakhrusheva, O., Koschade, S. E., Klann, K., Tholken, M., Baker, F., Zhang, J., Oellerich, T., Surun, D., Derlet, A., Haberbosch, I., Eimer, S., Osiewacz, H. D., Behrends, C., Munch, C., Dikic, I., & Brandts, C. H. (2019). Loss of the selective autophagy receptor p62 impairs murine myeloid leukemia progression and mitophagy. *Blood*, *133*(2), 168-179. <https://doi.org/10.1182/blood-2018-02-833475>
- Nguyen, T. N., Padman, B. S., Usher, J., Oorschot, V., Ramm, G., & Lazarou, M. (2016). Atg8 family LC3/GABARAP proteins are crucial for autophagosome-lysosome fusion but not autophagosome formation during PINK1/Parkin mitophagy and starvation. *J Cell Biol*, *215*(6), 857-874. <https://doi.org/10.1083/jcb.201607039>
- Nishida, Y., Arakawa, S., Fujitani, K., Yamaguchi, H., Mizuta, T., Kanaseki, T., Komatsu, M., Otsu, K., Tsujimoto, Y., & Shimizu, S. (2009). Discovery of Atg5/Atg7-independent alternative macroautophagy. *Nature*, *461*(7264), 654-658. <https://doi.org/10.1038/nature08455>
- Nolfi-Donagan, D., Braganza, A., & Shiva, S. (2020). Mitochondrial electron transport chain: Oxidative phosphorylation, oxidant production, and methods of measurement. *Redox Biol*, *37*, 101674. <https://doi.org/10.1016/j.redox.2020.101674>
- Novak, I., Kirkin, V., McEwan, D. G., Zhang, J., Wild, P., Rozenknop, A., Rogov, V., Lohr, F., Popovic, D., Occhipinti, A., Reichert, A. S., Terzic, J., Dotsch, V., Ney, P. A., & Dikic, I. (2010). Nix is a selective autophagy receptor for mitochondrial clearance. *EMBO Rep*, *11*(1), 45-51. <https://doi.org/10.1038/embor.2009.256>
- O'Rourke, B. (2010). From bioblasts to mitochondria: ever expanding roles of mitochondria in cell physiology. *Front Physiol*, *1*, 7. <https://doi.org/10.3389/fphys.2010.00007>
- Ohsumi, Y. (2014). Historical landmarks of autophagy research. *Cell Res*, *24*(1), 9-23. <https://doi.org/10.1038/cr.2013.169>
- Olzmann, J. A., & Carvalho, P. (2019). Dynamics and functions of lipid droplets. *Nat Rev Mol Cell Biol*, *20*(3), 137-155. <https://doi.org/10.1038/s41580-018-0085-z>

- Orrenius, S., Gogvadze, V., & Zhivotovsky, B. (2007). Mitochondrial oxidative stress: implications for cell death. *Annu Rev Pharmacol Toxicol*, 47, 143-183. <https://doi.org/10.1146/annurev.pharmtox.47.120505.105122>
- Padman, B. S., Nguyen, T. N., Uoselis, L., Skulsuppaisarn, M., Nguyen, L. K., & Lazarou, M. (2019). LC3/GABARAPs drive ubiquitin-independent recruitment of Optineurin and NDP52 to amplify mitophagy. *Nat Commun*, 10(1), 408. <https://doi.org/10.1038/s41467-019-08335-6>
- Palikaras, K., Daskalaki, I., Markaki, M., & Tavernarakis, N. (2017). Mitophagy and age-related pathologies: Development of new therapeutics by targeting mitochondrial turnover. *Pharmacol Ther*, 178, 157-174. <https://doi.org/10.1016/j.pharmthera.2017.04.005>
- Palikaras, K., Lionaki, E., & Tavernarakis, N. (2018). Mechanisms of mitophagy in cellular homeostasis, physiology and pathology. *Nat Cell Biol*, 20(9), 1013-1022. <https://doi.org/10.1038/s41556-018-0176-2>
- Palikaras, K., & Tavernarakis, N. (2017). In vivo Mitophagy Monitoring in *Caenorhabditis elegans* to Determine Mitochondrial Homeostasis. *Bio Protoc*, 7(7). <https://doi.org/10.21769/BioProtoc.2215>
- Panigrahi, D. P., Praharaj, P. P., Bhol, C. S., Mahapatra, K. K., Patra, S., Behera, B. P., Mishra, S. R., & Bhutia, S. K. (2020). The emerging, multifaceted role of mitophagy in cancer and cancer therapeutics. *Semin Cancer Biol*, 66, 45-58. <https://doi.org/10.1016/j.semcancer.2019.07.015>
- Perkins, G., Renken, C., Martone, M. E., Young, S. J., Ellisman, M., & Frey, T. (1997). Electron tomography of neuronal mitochondria: three-dimensional structure and organization of cristae and membrane contacts. *J Struct Biol*, 119(3), 260-272. <https://doi.org/10.1006/jsbi.1997.3885>
- Picca, A., Beli, R., Calvani, R., Coelho-Junior, H. J., Landi, F., Bernabei, R., Bucci, C., Guerra, F., & Marzetti, E. (2020). Older Adults with Physical Frailty and Sarcopenia Show Increased Levels of Circulating Small Extracellular Vesicles with a Specific Mitochondrial Signature. *Cells*, 9(4). <https://doi.org/10.3390/cells9040973>
- Pickles, S., Vigie, P., & Youle, R. J. (2018). Mitophagy and Quality Control Mechanisms in Mitochondrial Maintenance. *Curr Biol*, 28(4), R170-R185. <https://doi.org/10.1016/j.cub.2018.01.004>
- Poole, L. P., Bock-Hughes, A., Berardi, D. E., & Macleod, K. F. (2021). ULK1 promotes mitophagy via phosphorylation and stabilization of BNIP3. *Sci Rep*, 11(1), 20526. <https://doi.org/10.1038/s41598-021-00170-4>
- Popov, L. D. (2022). Mitochondrial-derived vesicles: Recent insights. *J Cell Mol Med*, 26(12), 3323-3328. <https://doi.org/10.1111/jcmm.17391>
- Poznyak, A. V., Ivanova, E. A., Sobenin, I. A., Yet, S. F., & Orekhov, A. N. (2020). The Role of Mitochondria in Cardiovascular Diseases. *Biology (Basel)*, 9(6). <https://doi.org/10.3390/biology9060137>
- Princely Abudu, Y., Pankiv, S., Mathai, B. J., Hakon Lystad, A., Bindesboll, C., Brenne, H. B., Yoke Wui Ng, M., Thiede, B., Yamamoto, A., Mutugi Nthiga, T., Lamark, T., Esguerra, C. V., Johansen, T., & Simonsen, A. (2019). NIPSNAP1 and NIPSNAP2 Act as "Eat Me" Signals for Mitophagy. *Dev Cell*, 49(4), 509-525 e512. <https://doi.org/10.1016/j.devcel.2019.03.013>
- Pu, M., Zheng, W., Zhang, H., Wan, W., Peng, C., Chen, X., Liu, X., Xu, Z., Zhou, T., Sun, Q., Neculai, D., & Liu, W. (2023). ORP8 acts as a lipophagy receptor to mediate lipid droplet turnover. *Protein Cell*, 14(9), 653-667. <https://doi.org/10.1093/procel/pwac063>
- Pugh, C. W. (2016). Modulation of the Hypoxic Response. *Adv Exp Med Biol*, 903, 259-271. https://doi.org/10.1007/978-1-4899-7678-9_18
- Punnakkal, A. R., Godtliebsen, G., Somani, A., Andres Acuna Maldonado, S., Birna Birgisdottir, A., Prasad, D. K., Horsch, A., & Agarwal, K. (2023). Analyzing Mitochondrial Morphology Through Simulation Supervised Learning. *J Vis Exp*(193). <https://doi.org/10.3791/64880>
- Qin, J., Guo, Y., Xue, B., Shi, P., Chen, Y., Su, Q. P., Hao, H., Zhao, S., Wu, C., Yu, L., Li, D., & Sun, Y. (2020). ER-mitochondria contacts promote mtDNA nucleoids active transportation via mitochondrial dynamic tubulation. *Nat Commun*, 11(1), 4471. <https://doi.org/10.1038/s41467-020-18202-4>
- Quinsay, M. N., Thomas, R. L., Lee, Y., & Gustafsson, A. B. (2010). Bnip3-mediated mitochondrial autophagy is independent of the mitochondrial permeability transition pore. *Autophagy*, 6(7), 855-862. <https://doi.org/10.4161/auto.6.7.13005>

- Rath, S., Sharma, R., Gupta, R., Ast, T., Chan, C., Durham, T. J., Goodman, R. P., Grabarek, Z., Haas, M. E., Hung, W. H. W., Joshi, P. R., Jourdain, A. A., Kim, S. H., Kotrys, A. V., Lam, S. S., McCoy, J. G., Meisel, J. D., Miranda, M., Panda, A., . . . Mootha, V. K. (2021). MitoCarta3.0: an updated mitochondrial proteome now with sub-organelle localization and pathway annotations. *Nucleic Acids Res*, 49(D1), D1541-D1547. <https://doi.org/10.1093/nar/gkaa1011>
- Raven, J. A. (2021). Determinants, and implications, of the shape and size of thylakoids and cristae. *J Plant Physiol*, 257, 153342. <https://doi.org/10.1016/j.jplph.2020.153342>
- Ravenhill, B. J., Boyle, K. B., von Muhlinen, N., Ellison, C. J., Masson, G. R., Otten, E. G., Foeglein, A., Williams, R., & Randow, F. (2019). The Cargo Receptor NDP52 Initiates Selective Autophagy by Recruiting the ULK Complex to Cytosol-Invasive Bacteria. *Mol Cell*, 74(2), 320-329 e326. <https://doi.org/10.1016/j.molcel.2019.01.041>
- Ricquier, D. (2006). Fundamental mechanisms of thermogenesis. *C R Biol*, 329(8), 578-586; discussion 653-575. <https://doi.org/10.1016/j.crv.2005.10.010>
- Rogov, V. V., Suzuki, H., Marinkovic, M., Lang, V., Kato, R., Kawasaki, M., Buljubasic, M., Sprung, M., Rogova, N., Wakatsuki, S., Hamacher-Brady, A., Dotsch, V., Dikic, I., Brady, N. R., & Novak, I. (2017). Phosphorylation of the mitochondrial autophagy receptor Nix enhances its interaction with LC3 proteins. *Sci Rep*, 7(1), 1131. <https://doi.org/10.1038/s41598-017-01258-6>
- Rojansky, R., Cha, M. Y., & Chan, D. C. (2016). Elimination of paternal mitochondria in mouse embryos occurs through autophagic degradation dependent on PARKIN and MUL1. *Elife*, 5. <https://doi.org/10.7554/eLife.17896>
- Rosignol, I., Villarejo-Zori, B., Teresak, P., Sierra-Filardi, E., Pereiro, X., Rodriguez-Muela, N., Vecino, E., Vieira, H. L. A., Bell, K., & Boya, P. (2020). The mito-QC Reporter for Quantitative Mitophagy Assessment in Primary Retinal Ganglion Cells and Experimental Glaucoma Models. *Int J Mol Sci*, 21(5). <https://doi.org/10.3390/ijms21051882>
- Roth, G. A., Mensah, G. A., Johnson, C. O., Addolorato, G., Ammirati, E., Baddour, L. M., Barengo, N. C., Beaton, A. Z., Benjamin, E. J., Benziger, C. P., Bonny, A., Brauer, M., Brodmann, M., Cahill, T. J., Carapetis, J., Catapano, A. L., Chugh, S. S., Cooper, L. T., Coresh, J., . . . Group, G.-N.-J. G. B. o. C. D. W. (2020). Global Burden of Cardiovascular Diseases and Risk Factors, 1990-2019: Update From the GBD 2019 Study. *J Am Coll Cardiol*, 76(25), 2982-3021. <https://doi.org/10.1016/j.jacc.2020.11.010>
- Ryan, T. A., Phillips, E. O., Collier, C. L., Jb Robinson, A., Routledge, D., Wood, R. E., Assar, E. A., & Tumbarello, D. A. (2020). Tollip coordinates Parkin-dependent trafficking of mitochondrial-derived vesicles. *EMBO J*, 39(11), e102539. <https://doi.org/10.15252/embj.2019102539>
- Ryan, T. A., & Tumbarello, D. A. (2021). A central role for mitochondrial-derived vesicles in the innate immune response: implications for Parkinson's disease. *Neural Regen Res*, 16(9), 1779-1780. <https://doi.org/10.4103/1673-5374.306074>
- Sagan, L. (1967). On the origin of mitosing cells. *J Theor Biol*, 14(3), 255-274. [https://doi.org/10.1016/0022-5193\(67\)90079-3](https://doi.org/10.1016/0022-5193(67)90079-3)
- Saha, B., Salemi, M., Williams, G. L., Oh, S., Paffett, M. L., Phinney, B., & Mandell, M. A. (2022). Interatomic analysis reveals a homeostatic role for the HIV restriction factor TRIM5alpha in mitophagy. *Cell Rep*, 39(6), 110797. <https://doi.org/10.1016/j.celrep.2022.110797>
- Saita, S., Shirane, M., & Nakayama, K. I. (2013). Selective escape of proteins from the mitochondria during mitophagy. *Nat Commun*, 4, 1410. <https://doi.org/10.1038/ncomms2400>
- Saito, T., Nah, J., Oka, S. I., Mukai, R., Monden, Y., Maejima, Y., Ikeda, Y., Sciarretta, S., Liu, T., Li, H., Baljinnyam, E., Fraidenraich, D., Fritzky, L., Zhai, P., Ichinose, S., Isobe, M., Hsu, C. P., Kundu, M., & Sadoshima, J. (2019). An alternative mitophagy pathway mediated by Rab9 protects the heart against ischemia. *J Clin Invest*, 129(2), 802-819. <https://doi.org/10.1172/JCI122035>
- Saks, V. A., Kaambre, T., Sikk, P., Eimre, M., Orlova, E., Paju, K., Piirsoo, A., Appaix, F., Kay, L., Regitz-zagrosek, V., Fleck, E., & Seppet, E. (2001). Intracellular energetic units in red muscle cells. *Biochemical Journal*, 356(2), 643-657. <https://doi.org/10.1042/bj3560643>
- Sandoval, H., Thiagarajan, P., Dasgupta, S. K., Schumacher, A., Prechal, J. T., Chen, M., & Wang, J. (2008). Essential role for Nix in autophagic maturation of erythroid cells. *Nature*, 454(7201), 232-235. <https://doi.org/10.1038/nature07006>

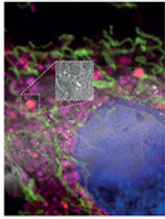
- Sato, M., & Sato, K. (2011). Degradation of paternal mitochondria by fertilization-triggered autophagy in *C. elegans* embryos. *Science*, 334(6059), 1141-1144. <https://doi.org/10.1126/science.1210333>
- Schaffer, J. E. (2003). Lipotoxicity: when tissues overeat. *Curr Opin Lipidol*, 14(3), 281-287. <https://doi.org/10.1097/00041433-200306000-00008>
- Schott, M. B., Weller, S. G., Schulze, R. J., Krueger, E. W., Drizyte-Miller, K., Casey, C. A., & McNiven, M. A. (2019). Lipid droplet size directs lipolysis and lipophagy catabolism in hepatocytes. *J Cell Biol*, 218(10), 3320-3335. <https://doi.org/10.1083/jcb.201803153>
- Schwarten, M., Mohrluder, J., Ma, P., Stoldt, M., Thielmann, Y., Stangler, T., Hersch, N., Hoffmann, B., Merkel, R., & Willbold, D. (2009). Nix directly binds to GABARAP: a possible crosstalk between apoptosis and autophagy. *Autophagy*, 5(5), 690-698. <https://doi.org/10.4161/autophagy.5.5.8494>
- Scott, S. V., & Klionsky, D. J. (1998). Delivery of proteins and organelles to the vacuole from the cytoplasm. *Curr Opin Cell Biol*, 10(4), 523-529. [https://doi.org/10.1016/s0955-0674\(98\)80068-9](https://doi.org/10.1016/s0955-0674(98)80068-9)
- Serasinghe, M. N., & Chipuk, J. E. (2017). Mitochondrial Fission in Human Diseases. *Handb Exp Pharmacol*, 240, 159-188. https://doi.org/10.1007/164_2016_38
- Shaner, N. C., Steinbach, P. A., & Tsien, R. Y. (2005). A guide to choosing fluorescent proteins. *Nat Methods*, 2(12), 905-909. <https://doi.org/10.1038/nmeth819>
- Shi, X., Chang, C., Yokom, A. L., Jensen, L. E., & Hurley, J. H. (2020). The autophagy adaptor NDP52 and the FIP200 coiled-coil allosterically activate ULK1 complex membrane recruitment. *Elife*, 9. <https://doi.org/10.7554/eLife.59099>
- Shpilka, T., Weidberg, H., Pietrokovski, S., & Elazar, Z. (2011). Atg8: an autophagy-related ubiquitin-like protein family. *Genome Biol*, 12(7), 226. <https://doi.org/10.1186/gb-2011-12-7-226>
- Singh, A., Kendall, S. L., & Campanella, M. (2018). Common Traits Spark the Mitophagy/Xenophagy Interplay. *Front Physiol*, 9, 1172. <https://doi.org/10.3389/fphys.2018.01172>
- Singh, F., Prescott, A. R., Rosewell, P., Ball, G., Reith, A. D., & Ganley, I. G. (2021). Pharmacological rescue of impaired mitophagy in Parkinson's disease-related LRRK2 G2019S knock-in mice. *Elife*, 10. <https://doi.org/10.7554/eLife.67604>
- Singh, R., Kaushik, S., Wang, Y., Xiang, Y., Novak, I., Komatsu, M., Tanaka, K., Cuervo, A. M., & Czaja, M. J. (2009). Autophagy regulates lipid metabolism. *Nature*, 458(7242), 1131-1135. <https://doi.org/10.1038/nature07976>
- Soubannier, V., McLelland, G. L., Zunino, R., Braschi, E., Rippstein, P., Fon, E. A., & McBride, H. M. (2012a). A vesicular transport pathway shuttles cargo from mitochondria to lysosomes. *Curr Biol*, 22(2), 135-141. <https://doi.org/10.1016/j.cub.2011.11.057>
- Soubannier, V., Rippstein, P., Kaufman, B. A., Shoubridge, E. A., & McBride, H. M. (2012b). Reconstitution of mitochondria derived vesicle formation demonstrates selective enrichment of oxidized cargo. *PLoS One*, 7(12), e52830. <https://doi.org/10.1371/journal.pone.0052830>
- Su, H., Yang, F., Wang, Q., Shen, Q., Huang, J., Peng, C., Zhang, Y., Wan, W., Wong, C. C. L., Sun, Q., Wang, F., Zhou, T., & Liu, W. (2017). VPS34 Acetylation Controls Its Lipid Kinase Activity and the Initiation of Canonical and Non-canonical Autophagy. *Mol Cell*, 67(6), 907-921 e907. <https://doi.org/10.1016/j.molcel.2017.07.024>
- Sun, N., Malide, D., Liu, J., Rovira, II, Combs, C. A., & Finkel, T. (2017). A fluorescence-based imaging method to measure in vitro and in vivo mitophagy using mt-Keima. *Nat Protoc*, 12(8), 1576-1587. <https://doi.org/10.1038/nprot.2017.060>
- Sun, N., Yun, J., Liu, J., Malide, D., Liu, C., Rovira, II, Holmstrom, K. M., Fergusson, M. M., Yoo, Y. H., Combs, C. A., & Finkel, T. (2015). Measuring In Vivo Mitophagy. *Mol Cell*, 60(4), 685-696. <https://doi.org/10.1016/j.molcel.2015.10.009>
- Sztalryd, C., & Brasaemle, D. L. (2017). The perilipin family of lipid droplet proteins: Gatekeepers of intracellular lipolysis. *Biochim Biophys Acta Mol Cell Biol Lipids*, 1862(10 Pt B), 1221-1232. <https://doi.org/10.1016/j.bbalip.2017.07.009>
- Taegtmeyer, H. (2004). Cardiac metabolism as a target for the treatment of heart failure. *Circulation*, 110(8), 894-896. <https://doi.org/10.1161/01.CIR.0000139340.88769.D5>
- Tanida, I., Ueno, T., & Kominami, E. (2004). LC3 conjugation system in mammalian autophagy. *Int J Biochem Cell Biol*, 36(12), 2503-2518. <https://doi.org/10.1016/j.biocel.2004.05.009>

- Tarasenko, T. N., Cusmano-Ozog, K., & McGuire, P. J. (2018). Tissue acylcarnitine status in a mouse model of mitochondrial beta-oxidation deficiency during metabolic decompensation due to influenza virus infection. *Mol Genet Metab*, 125(1-2), 144-152. <https://doi.org/10.1016/j.ymgme.2018.06.012>
- Tronstad, K. J., Nooteboom, M., Nilsson, L. I., Nikolaisen, J., Sokolewicz, M., Grefte, S., Pettersen, I. K., Dyrstad, S., Hoel, F., Willems, P. H., & Koopman, W. J. (2014). Regulation and quantification of cellular mitochondrial morphology and content. *Curr Pharm Des*, 20(35), 5634-5652. <https://doi.org/10.2174/1381612820666140305230546>
- Tsukada, M., & Ohsumi, Y. (1993). Isolation and characterization of autophagy-defective mutants of *Saccharomyces cerevisiae*. *FEBS Lett*, 333(1-2), 169-174. [https://doi.org/10.1016/0014-5793\(93\)80398-e](https://doi.org/10.1016/0014-5793(93)80398-e)
- Turco, E., Witt, M., Abert, C., Bock-Bierbaum, T., Su, M. Y., Trapannone, R., Sztacho, M., Danieli, A., Shi, X., Zaffagnini, G., Gamper, A., Schuschnig, M., Fracchiolla, D., Bernklau, D., Romanov, J., Hartl, M., Hurley, J. H., Daumke, O., & Martens, S. (2019). FIP200 Claw Domain Binding to p62 Promotes Autophagosome Formation at Ubiquitin Condensates. *Mol Cell*, 74(2), 330-346 e311. <https://doi.org/10.1016/j.molcel.2019.01.035>
- Turrens, J. F. (2003). Mitochondrial formation of reactive oxygen species. *J Physiol*, 552(Pt 2), 335-344. <https://doi.org/10.1113/jphysiol.2003.049478>
- Unger, R. H. (2002). Lipotoxic diseases. *Annu Rev Med*, 53, 319-336. <https://doi.org/10.1146/annurev.med.53.082901.104057>
- Vafai, S. B., & Mootha, V. K. (2012). Mitochondrial disorders as windows into an ancient organelle. *Nature*, 491(7424), 374-383. <https://doi.org/10.1038/nature11707>
- Valm, A. M., Cohen, S., Legant, W. R., Melunis, J., Hershberg, U., Wait, E., Cohen, A. R., Davidson, M. W., Betzig, E., & Lippincott-Schwartz, J. (2017). Applying systems-level spectral imaging and analysis to reveal the organelle interactome. *Nature*, 546(7656), 162-167. <https://doi.org/10.1038/nature22369>
- van Vliet, A. R., Chiduzza, G. N., Maslen, S. L., Pye, V. E., Joshi, D., De Tito, S., Jefferies, H. B. J., Christodoulou, E., Roustan, C., Punch, E., Hervas, J. H., O'Reilly, N., Skehel, J. M., Cherepanov, P., & Tooze, S. A. (2022). ATG9A and ATG2A form a heteromeric complex essential for autophagosome formation. *Mol Cell*, 82(22), 4324-4339 e4328. <https://doi.org/10.1016/j.molcel.2022.10.017>
- Vargas, J. N. S., Wang, C., Bunker, E., Hao, L., Maric, D., Schiavo, G., Randow, F., & Youle, R. J. (2019). Spatiotemporal Control of ULK1 Activation by NDP52 and TBK1 during Selective Autophagy. *Mol Cell*, 74(2), 347-362 e346. <https://doi.org/10.1016/j.molcel.2019.02.010>
- Vasam, G., Nadeau, R., Cadete, V. J. J., Lavalley-Adam, M., Menzies, K. J., & Burrelle, Y. (2021). Proteomics characterization of mitochondrial-derived vesicles under oxidative stress. *FASEB J*, 35(4), e21278. <https://doi.org/10.1096/fj.202002151R>
- Villa, E., Proics, E., Rubio-Patino, C., Obba, S., Zunino, B., Bossowski, J. P., Rozier, R. M., Chiche, J., Mondragon, L., Riley, J. S., Marchetti, S., Verhoeyen, E., Tait, S. W. G., & Ricci, J. E. (2017). Parkin-Independent Mitophagy Controls Chemotherapeutic Response in Cancer Cells. *Cell Rep*, 20(12), 2846-2859. <https://doi.org/10.1016/j.celrep.2017.08.087>
- Vincent, A. E., Turnbull, D. M., Eisner, V., Hajnoczky, G., & Picard, M. (2017). Mitochondrial Nanotunnels. *Trends Cell Biol*, 27(11), 787-799. <https://doi.org/10.1016/j.tcb.2017.08.009>
- Vogel, F., Bornhovd, C., Neupert, W., & Reichert, A. S. (2006). Dynamic subcompartmentalization of the mitochondrial inner membrane. *J Cell Biol*, 175(2), 237-247. <https://doi.org/10.1083/jcb.200605138>
- Wallin, I. E. (1927). *Symbiogenesis and the Origin of Species*. Рипол Классик.
- Wang, C., Du, W., Su, Q. P., Zhu, M., Feng, P., Li, Y., Zhou, Y., Mi, N., Zhu, Y., Jiang, D., Zhang, S., Zhang, Z., Sun, Y., & Yu, L. (2015). Dynamic tubulation of mitochondria drives mitochondrial network formation. *Cell Res*, 25(10), 1108-1120. <https://doi.org/10.1038/cr.2015.89>
- Wang, F., Zhang, D., Zhang, D., Li, P., & Gao, Y. (2021). Mitochondrial Protein Translation: Emerging Roles and Clinical Significance in Disease. *Front Cell Dev Biol*, 9, 675465. <https://doi.org/10.3389/fcell.2021.675465>
- Wang, H., Lei, M., Hsia, R. C., & Sztalryd, C. (2013). Analysis of lipid droplets in cardiac muscle. *Methods Cell Biol*, 116, 129-149. <https://doi.org/10.1016/B978-0-12-408051-5.00008-5>

- Wang, S., Long, H., Hou, L., Feng, B., Ma, Z., Wu, Y., Zeng, Y., Cai, J., Zhang, D. W., & Zhao, G. (2023). The mitophagy pathway and its implications in human diseases. *Signal Transduct Target Ther*, 8(1), 304. <https://doi.org/10.1038/s41392-023-01503-7>
- Wauer, T., Simicek, M., Schubert, A., & Komander, D. (2015). Mechanism of phospho-ubiquitin-induced PARKIN activation. *Nature*, 524(7565), 370-374. <https://doi.org/10.1038/nature14879>
- Wei, Y., Chiang, W. C., Sumpster, R., Jr., Mishra, P., & Levine, B. (2017). Prohibitin 2 Is an Inner Mitochondrial Membrane Mitophagy Receptor. *Cell*, 168(1-2), 224-238 e210. <https://doi.org/10.1016/j.cell.2016.11.042>
- Wilfling, F., Wang, H., Haas, J. T., Kraemer, N., Gould, T. J., Uchida, A., Cheng, J. X., Graham, M., Christiano, R., Frohlich, F., Liu, X., Buhman, K. K., Coleman, R. A., Bewersdorf, J., Farese, R. V., Jr., & Walther, T. C. (2013). Triacylglycerol synthesis enzymes mediate lipid droplet growth by relocating from the ER to lipid droplets. *Dev Cell*, 24(4), 384-399. <https://doi.org/10.1016/j.devcel.2013.01.013>
- Williams, C. A. (2003). GALACTOSE. In B. Caballero (Ed.), *Encyclopedia of Food Sciences and Nutrition (Second Edition)* (pp. 2843-2846). Academic Press. <https://doi.org/https://doi.org/10.1016/B0-12-227055-X/00544-7>
- Wu, N., Yang, M., Gaur, U., Xu, H., Yao, Y., & Li, D. (2016). Alpha-Ketoglutarate: Physiological Functions and Applications. *Biomol Ther (Seoul)*, 24(1), 1-8. <https://doi.org/10.4062/biomolther.2015.078>
- Wu, W., Tian, W., Hu, Z., Chen, G., Huang, L., Li, W., Zhang, X., Xue, P., Zhou, C., Liu, L., Zhu, Y., Zhang, X., Li, L., Zhang, L., Sui, S., Zhao, B., & Feng, D. (2014). ULK1 translocates to mitochondria and phosphorylates FUNDC1 to regulate mitophagy. *EMBO Rep*, 15(5), 566-575. <https://doi.org/10.1002/embr.201438501>
- Wu, X., & Hammer, J. A. (2021). ZEISS Airyscan: Optimizing Usage for Fast, Gentle, Super-Resolution Imaging. *Methods Mol Biol*, 2304, 111-130. https://doi.org/10.1007/978-1-0716-1402-0_5
- Xiang, G., Yang, L., Long, Q., Chen, K., Tang, H., Wu, Y., Liu, Z., Zhou, Y., Qi, J., Zheng, L., Liu, W., Ying, Z., Fan, W., Shi, H., Li, H., Lin, X., Gao, M., Liu, J., Bao, F., . . . Liu, X. (2017). BNIP3L-dependent mitophagy accounts for mitochondrial clearance during 3 factors-induced somatic cell reprogramming. *Autophagy*, 13(9), 1543-1555. <https://doi.org/10.1080/15548627.2017.1338545>
- Yamano, K., & Youle, R. J. (2013). PINK1 is degraded through the N-end rule pathway. *Autophagy*, 9(11), 1758-1769. <https://doi.org/10.4161/auto.24633>
- Yang, K. C., Ma, X., Liu, H., Murphy, J., Barger, P. M., Mann, D. L., & Diwan, A. (2015). Tumor necrosis factor receptor-associated factor 2 mediates mitochondrial autophagy. *Circ Heart Fail*, 8(1), 175-187. <https://doi.org/10.1161/CIRCHEARTFAILURE.114.001635>
- Yang, M., Fu, J. D., Zou, J., Sridharan, D., Zhao, M. T., Singh, H., Krigman, J., Khan, M., Xin, G., & Sun, N. (2022). Assessment of mitophagy in human iPSC-derived cardiomyocytes. *Autophagy*, 18(10), 2481-2494. <https://doi.org/10.1080/15548627.2022.2037920>
- Yang, Z., & Klionsky, D. J. (2009). An overview of the molecular mechanism of autophagy. *Curr Top Microbiol Immunol*, 335, 1-32. https://doi.org/10.1007/978-3-642-00302-8_1
- Yasuda, M., Han, J. W., Dionne, C. A., Boyd, J. M., & Chinnadurai, G. (1999). BNIP3alpha: a human homolog of mitochondrial proapoptotic protein BNIP3. *Cancer Res*, 59(3), 533-537. <https://www.ncbi.nlm.nih.gov/pubmed/9973195>
- Youle, R. J. (2019). Mitochondria-Striking a balance between host and endosymbiont. *Science*, 365(6454). <https://doi.org/10.1126/science.aaw9855>
- Yu, R., Lendahl, U., Nister, M., & Zhao, J. (2020). Regulation of Mammalian Mitochondrial Dynamics: Opportunities and Challenges. *Front Endocrinol (Lausanne)*, 11, 374. <https://doi.org/10.3389/fendo.2020.00374>
- Yun, J., Puri, R., Yang, H., Lizzio, M. A., Wu, C., Sheng, Z. H., & Guo, M. (2014). MUL1 acts in parallel to the PINK1/parkin pathway in regulating mitofusins and compensates for loss of PINK1/parkin. *Elife*, 3, e01958. <https://doi.org/10.7554/eLife.01958>
- Zachari, M., Gudmundsson, S. R., Li, Z., Manifava, M., Cugliandolo, F., Shah, R., Smith, M., Stronge, J., Karanasios, E., Piunti, C., Kishi-Itakura, C., Vihinen, H., Jokitalo, E., Guan, J. L., Buss, F., Smith, A. M., Walker, S. A., Eskelinen, E. L., & Ktistakis, N. T. (2019). Selective Autophagy

- of Mitochondria on a Ubiquitin-Endoplasmic-Reticulum Platform. *Dev Cell*, 50(5), 627-643 e625. <https://doi.org/10.1016/j.devcel.2019.06.016>
- Zadoorian, A., Du, X., & Yang, H. (2023). Lipid droplet biogenesis and functions in health and disease. *Nat Rev Endocrinol*, 19(8), 443-459. <https://doi.org/10.1038/s41574-023-00845-0>
- Zechner, R., Madeo, F., & Kratky, D. (2017). Cytosolic lipolysis and lipophagy: two sides of the same coin. *Nat Rev Mol Cell Biol*, 18(11), 671-684. <https://doi.org/10.1038/nrm.2017.76>
- Zemirli, N., Morel, E., & Molino, D. (2018). Mitochondrial Dynamics in Basal and Stressful Conditions. *Int J Mol Sci*, 19(2). <https://doi.org/10.3390/ijms19020564>
- Zhang, J., Loyd, M. R., Randall, M. S., Waddell, M. B., Kriwacki, R. W., & Ney, P. A. (2012). A short linear motif in BNIP3L (NIX) mediates mitochondrial clearance in reticulocytes. *Autophagy*, 8(9), 1325-1332. <https://doi.org/10.4161/autophagy.20764>
- Zhang, J., Randall, M. S., Loyd, M. R., Dorsey, F. C., Kundu, M., Cleveland, J. L., & Ney, P. A. (2009). Mitochondrial clearance is regulated by Atg7-dependent and -independent mechanisms during reticulocyte maturation. *Blood*, 114(1), 157-164. <https://doi.org/10.1182/blood-2008-04-151639>
- Zhang, S., Peng, X., Yang, S., Li, X., Huang, M., Wei, S., Liu, J., He, G., Zheng, H., Yang, L., Li, H., & Fan, Q. (2022). The regulation, function, and role of lipophagy, a form of selective autophagy, in metabolic disorders. *Cell Death Dis*, 13(2), 132. <https://doi.org/10.1038/s41419-022-04593-3>
- Zhang, Y., Yao, Y., Qiu, X., Wang, G., Hu, Z., Chen, S., Wu, Z., Yuan, N., Gao, H., Wang, J., Song, H., Girardin, S. E., & Qian, Y. (2019). Listeria hijacks host mitophagy through a novel mitophagy receptor to evade killing. *Nat Immunol*, 20(4), 433-446. <https://doi.org/10.1038/s41590-019-0324-2>
- Zhao, J. F., Rodger, C. E., Allen, G. F. G., Weidlich, S., & Ganley, I. G. (2020). HIF1alpha-dependent mitophagy facilitates cardiomyoblast differentiation. *Cell Stress*, 4(5), 99-113. <https://doi.org/10.15698/cst2020.05.220>
- Zhao, R. Z., Jiang, S., Zhang, L., & Yu, Z. B. (2019). Mitochondrial electron transport chain, ROS generation and uncoupling (Review). *Int J Mol Med*, 44(1), 3-15. <https://doi.org/10.3892/ijmm.2019.4188>
- Zhong, Z., Umemura, A., Sanchez-Lopez, E., Liang, S., Shalpour, S., Wong, J., He, F., Boassa, D., Perkins, G., Ali, S. R., McGeough, M. D., Ellisman, M. H., Seki, E., Gustafsson, A. B., Hoffman, H. M., Diaz-Meco, M. T., Moscat, J., & Karin, M. (2016). NF-kappaB Restricts Inflammasome Activation via Elimination of Damaged Mitochondria. *Cell*, 164(5), 896-910. <https://doi.org/10.1016/j.cell.2015.12.057>
- Zhu, Y., Massen, S., Terenzio, M., Lang, V., Chen-Lindner, S., Eils, R., Novak, I., Dikic, I., Hamacher-Brady, A., & Brady, N. R. (2013). Modulation of serines 17 and 24 in the LC3-interacting region of Bnip3 determines pro-survival mitophagy versus apoptosis. *J Biol Chem*, 288(2), 1099-1113. <https://doi.org/10.1074/jbc.M112.399345>
- Zorova, L. D., Popkov, V. A., Plotnikov, E. Y., Silachev, D. N., Pevzner, I. B., Jankauskas, S. S., Babenko, V. A., Zorov, S. D., Balakireva, A. V., Juhaszova, M., Sollott, S. J., & Zorov, D. B. (2018). Mitochondrial membrane potential. *Anal Biochem*, 552, 50-59. <https://doi.org/10.1016/j.ab.2017.07.009>

Paper I



Autophagy



ISSN: (Print) (Online) Journal homepage: <https://www.tandfonline.com/loi/kaup20>

High-resolution visualization and assessment of basal and OXPPOS-induced mitophagy in H9c2 cardiomyoblasts

Gustav Godtliebsen, Kenneth Bowitz Larsen, Zambarlal Bhujabal, Ida S. Opstad, Mireia Nager, Abhinanda R. Punnakkal, Trine B. Kalstad, Randi Olsen, Trine Lund, Dilip K. Prasad, Krishna Agarwal, Truls Myrmel & Asa Birna Birgisdottir

To cite this article: Gustav Godtliebsen, Kenneth Bowitz Larsen, Zambarlal Bhujabal, Ida S. Opstad, Mireia Nager, Abhinanda R. Punnakkal, Trine B. Kalstad, Randi Olsen, Trine Lund, Dilip K. Prasad, Krishna Agarwal, Truls Myrmel & Asa Birna Birgisdottir (2023) High-resolution visualization and assessment of basal and OXPPOS-induced mitophagy in H9c2 cardiomyoblasts, *Autophagy*, 19:10, 2769-2788, DOI: [10.1080/15548627.2023.2230837](https://doi.org/10.1080/15548627.2023.2230837)

To link to this article: <https://doi.org/10.1080/15548627.2023.2230837>



© 2023 The Author(s). Published by Informa UK Limited, trading as Taylor & Francis Group.



[View supplementary material](#)



Published online: 05 Jul 2023.



[Submit your article to this journal](#)



Article views: 1413




[View related articles](#)



[View Crossmark data](#)

High-resolution visualization and assessment of basal and OXPHOS-induced mitophagy in H9c2 cardiomyoblasts

Gustav Godtliebsen^a, Kenneth Bowitz Larsen^{a,b}, Zambarlal Bhujabal^a, Ida S. Opstad^c, Mireia Nager^d, Abhinanda R. Punnakkal^e, Trine B. Kalstad^d, Randi Olsen^b, Trine Lund^b, Dilip K. Prasad^e, Krishna Agarwal^c, Truls Myrmet^{a,d}, and Asa Birna Birgisdottir 

^aDepartment of Clinical Medicine, UiT-The Arctic University of Norway, Tromsø, Norway; ^bDepartment of Medical Biology, UiT-The Arctic University of Norway, Tromsø, Norway; ^cDepartment of Physics and Technology, UiT-The Arctic University of Norway, Tromsø, Norway; ^dDivision of Cardiothoracic and Respiratory Medicine, UiT-The Arctic University of Norway, Tromsø, Norway; ^eDepartment of Computer Science, UiT-The Arctic University of Norway, Tromsø, Norway

ABSTRACT

Mitochondria are susceptible to damage resulting from their activity as energy providers. Damaged mitochondria can cause harm to the cell and thus mitochondria are subjected to elaborate quality-control mechanisms including elimination via lysosomal degradation in a process termed mitophagy. Basal mitophagy is a house-keeping mechanism fine-tuning the number of mitochondria according to the metabolic state of the cell. However, the molecular mechanisms underlying basal mitophagy remain largely elusive. In this study, we visualized and assessed the level of mitophagy in H9c2 cardiomyoblasts at basal conditions and after OXPHOS induction by galactose adaptation. We used cells with a stable expression of a pH-sensitive fluorescent mitochondrial reporter and applied state-of-the-art imaging techniques and image analysis. Our data showed a significant increase in acidic mitochondria after galactose adaptation. Using a machine-learning approach we also demonstrated increased mitochondrial fragmentation by OXPHOS induction. Furthermore, super-resolution microscopy of live cells enabled capturing of mitochondrial fragments within lysosomes as well as dynamic transfer of mitochondrial contents to lysosomes. Applying correlative light and electron microscopy we revealed the ultrastructure of the acidic mitochondria confirming their proximity to the mitochondrial network, ER and lysosomes. Finally, exploiting siRNA knockdown strategy combined with flux perturbation with lysosomal inhibitors, we demonstrated the importance of both canonical as well as non-canonical autophagy mediators in lysosomal degradation of mitochondria after OXPHOS induction. Taken together, our high-resolution imaging approaches applied on H9c2 cells provide novel insights on mitophagy during physiologically relevant conditions. The implication of redundant underlying mechanisms highlights the fundamental importance of mitophagy.

Abbreviations: ATG: autophagy related; ATG7: autophagy related 7; ATP: adenosine triphosphate; BafA1: bafilomycin A₁; CLEM: correlative light and electron microscopy; EGFP: enhanced green fluorescent protein; MAP1LC3B: microtubule associated protein 1 light chain 3 beta; OXPHOS: oxidative phosphorylation; PepA: pepstatin A; PLA: proximity ligation assay; PRKN: parkin RBR E3 ubiquitin protein ligase; RAB5A: RAB5A, member RAS oncogene family; RAB7A: RAB7A, member RAS oncogene family; RAB9A: RAB9A, member RAS oncogene family; ROS: reactive oxygen species; SIM: structured illumination microscopy; siRNA: short interfering RNA; SYNJ2BP: synaptojanin 2 binding protein; TEM: transmission electron microscopy; TOMM20: translocase of outer mitochondrial membrane 20; ULK1: unc-51 like kinase 1.

ARTICLE HISTORY

Received 9 December 2022
Revised 9 June 2023
Accepted 22 June 2023

KEYWORDS

CLEM; deep learning; lysosomes; mitochondria; quality control; SIM

Introduction

Mitochondria are the main energy producing organelles in eukaryotic cells and are also central in the control of redox homeostasis, Ca²⁺ signaling, iron metabolism, innate immunity and programmed cell death [1–5]. In most cell types, mitochondria are arranged in highly dynamic networks, controlled by constant fusion and fission events [6] driven by mitochondria movements along the cytoskeleton [7]. Events such as cell cycle progression, cellular differentiation, oxidative stress, metabolic perturbation and engagement in

programmed cell death, all lead to significant alterations in the architecture of the mitochondrial network [8].

Mitochondria are dependent on oxygen for energy production in the form of adenosine triphosphate (ATP) through oxidative phosphorylation (OXPHOS). Reactive oxygen species (ROS) are formed as by-products during OXPHOS and thus mitochondria are susceptible to mitochondrial DNA mutations and protein misfolding that can ultimately lead to mitochondrial damage [9]. Damaged mitochondria result in energy-generation defects, the increased production of

CONTACT Asa Birna Birgisdottir  asa.birna.birgisdottir@uit.no 
 Supplemental data for this article can be accessed online at <https://doi.org/10.1080/15548627.2023.2230837>

© 2023 The Author(s). Published by Informa UK Limited, trading as Taylor & Francis Group.

This is an Open Access article distributed under the terms of the Creative Commons Attribution License (<http://creativecommons.org/licenses/by/4.0/>), which permits unrestricted use, distribution, and reproduction in any medium, provided the original work is properly cited. The terms on which this article has been published allow the posting of the Accepted Manuscript in a repository by the author(s) or with their consent.

harmful reactive oxygen species and can trigger programmed cell death when the damage is beyond repair. Hence, mitochondria are subjected to elaborate quality control mechanisms [10]. Damaged mitochondria can be selectively eliminated by one such mechanism, termed mitophagy, dependent on the autophagy machinery [11–13]. Mitophagy is often preceded by fission of damaged mitochondria (or parts of mitochondria) from the mitochondrial network, followed by sequestration by a double-membrane-bound autophagosome and culminates in fusion with a lysosome where the mitochondria are degraded by resident acidic hydrolases. There are multiple signaling pathways that govern autophagosome engulfment of damaged mitochondria [14].

Macroautophagy/autophagy initiation in mammalian cells is driven by the ULK1 (unc-51 like kinase 1) protein kinase complex that phosphorylates and activates key downstream mediators involved in autophagosome formation [15]. Activation and recruitment of the ULK1 complex has been implicated in mitophagy [16–19]. Autophagosome formation involves lipidation of the Atg8 (autophagy-related 8)-family proteins such as MAP1LC3B (microtubule associated protein 1 light chain 3 beta). Here, Atg8-family proteins are conjugated to phosphatidylethanolamine (PE) in the phagophore membrane, representing one of the key molecular signatures of canonical autophagy [20]. Atg8-family protein lipidation is a multistep process driven by the enzymatic activity of core autophagy proteins: the E1-like ATG7 (autophagy related 7), the E2-like ATG3 (autophagy related 3) and the E3-like ATG12–ATG5–ATG16L1 complex [21–23].

Selected cargo such as mitochondria destined for degradation are connected to the forming autophagosome through binding to Atg8-family proteins in a ubiquitin dependent or independent manner [10]. Intriguingly, non-canonical pathways, independent of ATG7 and Atg8-family protein lipidation, have also been described for lysosomal clearance of damaged mitochondria. These include alternative autophagy [24,25], microautophagy involving formation of small mitochondria derived vesicles (MDVs) [26] and degradation through the endo-lysosomal pathway involving the endosomal small GTPase RAB5A (RAB5A, member RAS oncogene family) [27]. Furthermore, non-canonical mitophagy described in mouse cardiomyocytes depends on ULK1 and the small GTPase RAB9A (RAB9A, member RAS oncogene family) [28]. Interestingly, mitochondria and lysosomes can also directly interact through the small GTPase RAB7A (RAB7A, member RAS oncogene family) [29].

The most studied ubiquitin-dependent mitophagy is known as PINK-PRKN-dependent mitophagy, orchestrated by the enzyme 3 (E3) ubiquitin ligase PRKN (parkin RBR E3 ubiquitin protein ligase) and the protein kinase PINK1 (PTEN induced putative kinase 1) [30]. Pioneering work for elucidation of PRKN-mediated mitophagy relied on induction of mitophagy by using cytotoxic agents targeting mitochondria, resulting in membrane potential dissipation of the entire network and loss of most of the mitochondria [31,32]. In contrast, basal mitophagy is considered a house-keeping mechanism where mitochondrial content is fine-tuned depending on the metabolic state of the cell [9,14]. Thus, use of mitochondria depolarizing agents is not

optimal to simulate physiological situations. Notably, the molecular mechanisms governing basal level of mitophagy in cells under physiological conditions remain mostly elusive.

In this work we set out to visualize and assess mitophagy in H9c2 cardiomyoblasts during normal culture conditions and after OXPHOS induction by galactose adaptation. We exploited H9c2 cells expressing pH-sensitive tandem mCherry-enhanced green fluorescent protein (EGFP) fluorescent mitochondrial reporters and applied state-of-the-art imaging methods for a detailed characterization of mitochondrial fragments within acidic compartments. Our results provide novel insights into the dynamics and regulation of lysosomal degradation of mitochondria in physiologically relevant settings.

Results

H9c2 cells with a pH-sensitive fluorescent mitochondrial reporter display induced formation of acidic mitochondria when adapted to galactose

In order to monitor lysosomal degradation of mitochondria in rat cardiac myoblasts (H9c2) we established stable cell lines with constitutive expression of a fluorescent (mCherry-EGFP) tandem-tagged trans-membrane (TM) domain of the outer mitochondrial membrane protein SYNJ2BP/OMP25 (synaptojanin 2 binding protein) [33–35] or tandem tagged full-length TOMM20 (translocase of the outer mitochondrial membrane 20) protein. The mitochondria thus display both green (EGFP) and red (mCherry) fluorescence and appear yellow in merged images of the green and the red channel during fluorescence imaging of the cells. The EGFP fluorescence is quenched at low pH while the mCherry fluorescence is acid stable (Figure 1A) [36]. Therefore, during imaging, mitochondria or parts of mitochondria in acidic compartments (late endosomes or lysosomes) appear as red-only structures in merged images. Under normal culture conditions, red-only dots were easily detected by fluorescence microscopy of stably transfected H9c2 cells, thus enabling monitoring of basal levels of lysosomal acidification of engulfed mitochondria (Figure 1B). In order to investigate the effect of a metabolic shift on mitochondria degradation, the cells were adapted to galactose in glucose-free growth medium for a minimum of 7 days. In this way the cells become mostly dependent on OXPHOS for ATP production [37]. As a control, the cells were kept in normal high glucose containing media for the same time-period and propagated simultaneously. The cells were then fixed and imaged by fluorescence microscopy (Figure 1B). Image analysis software was used to assess the number of cells containing red-only mitochondria as well as the number of red-only dots per cell (Figure S1A). Our data demonstrate that during normal culture conditions approximately 50% of the mCherry-EGFP-SYNJ2BP-TM cells displayed acidic mitochondria (Figure 1C). Interestingly, a significant increase in the number of cells with acidic mitochondria was detected in the galactose-adapted cells (approximately 90%) with an almost a two-fold increase in the number of red-only dots per cell (Figure 1C). Similarly, the TOMM20-mCherry-EGFP H9c2 cells displayed an increase in the number of red-

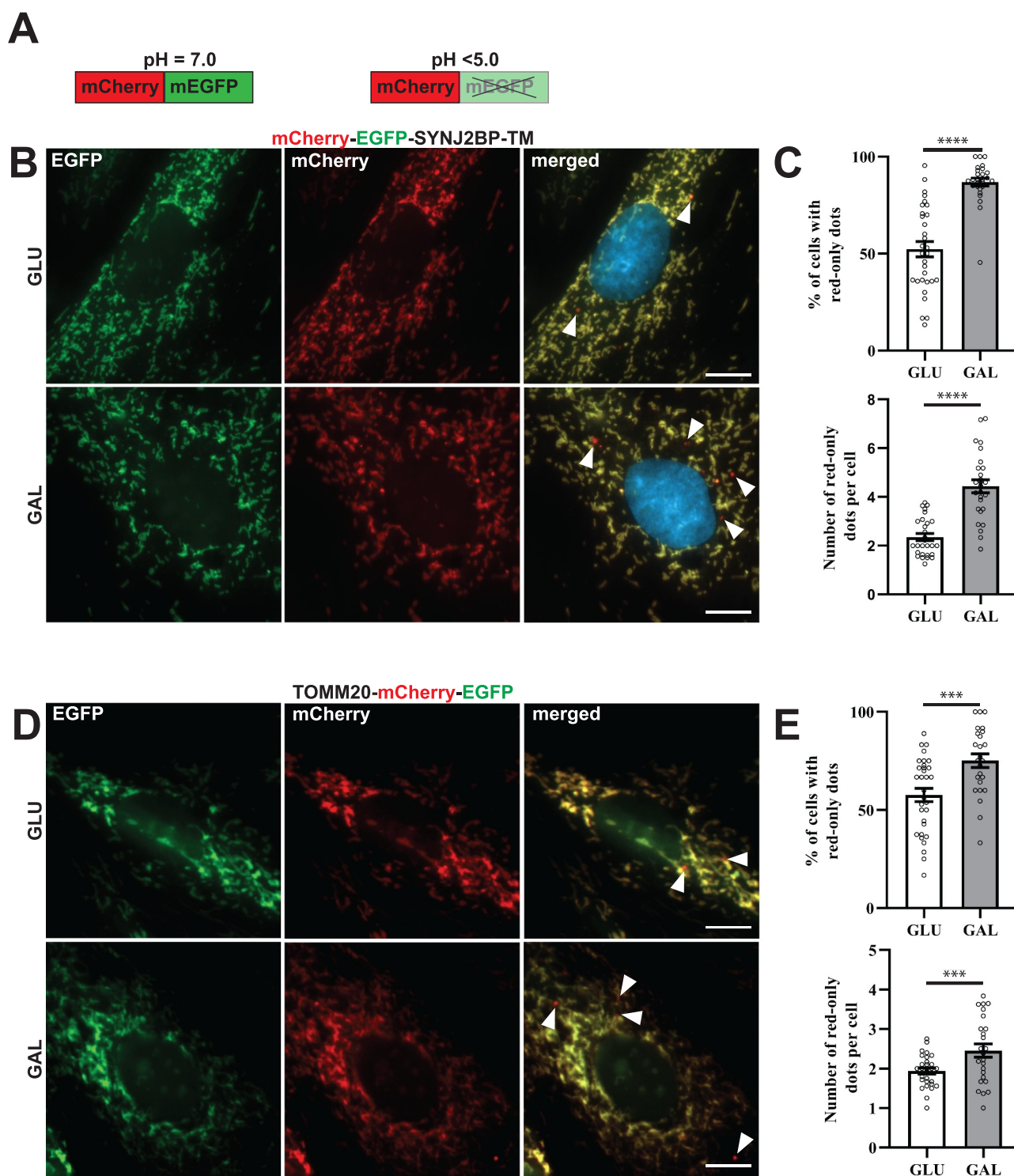


Figure 1. Reporter H9c2 cells display an increase in acidic mitochondria during galactose adaption. (A) An illustration of the pH-sensitive tandem fluorescent reporter mCherry-EGFP at different pH levels (red and green at neutral pH and red-only at acidic pH). (B) Representative widefield fluorescence microscopy images of H9c2 cells with a stable expression of the mCherry-EGFP-SYNJ2BP-TM reporter grown in glucose (GLU) or adapted to galactose (GAL) media. (C) Quantification of the percentage of cells containing red-only dots and quantification of the number of red-only dots per cell in cells with red-only dots in glucose vs galactose media for cells with the mCherry-EGFP-SYNJ2BP-TM reporter. (D) Representative widefield fluorescence microscopy images of H9c2 cells with a stable expression of the TOMM20-mCherry-EGFP reporter grown in glucose (GLU) or adapted to galactose (GAL) media. (E) Quantification of the percentage of cells containing red-only dots and quantification of the number of red-only dots per cell in cells with red only dots in glucose vs galactose media for cells with the TOMM20-mCherry-EGFP reporter. Data presented in (C) and (E) is shown as mean \pm SEM from 3 independent experiments, with more than 100 cells in each condition. The individual datapoints are per frame cell averages.

Note: * $p < 0.05$, ** $p < 0.01$, *** $p < 0.001$ and **** $p < 0.0001$. Scale bar: 10 μ m.

only dots per cell when adapted to galactose (Figure 1D,E). In comparison, 16 h of hypoxia (0.3% O₂), a well-known inducer of mitophagy [38], resulted in an equivalent increase in the number of red-only structures per cell (Figure S1B). Furthermore, using transient transfection of the pH-sensitive mt-Keima probe targeted to the mitochondrial matrix [39,40], we detected a significant increase in acidic mitochondria per cell in galactose adapted H9c2 cells (Figure S1C). To summarize, galactose adaptation of H9c2 cells induced lysosomal engulfment of mitochondria visualized by different pH-sensitive mitochondria targeted probes.

Galactose adaptation of H9c2 cells results in more fragmented mitochondria morphology, elevated mitochondrial respiration and higher susceptibility to mitochondrial damage.

Degradation of mitochondria is commonly preceded by mitochondrial fission or fragmentation [41,42]. We performed computational image analysis of mitochondrial morphology in the tandem-tagged H9c2 cells using machine learning. This enabled classification and quantification of the mitochondria morphology as networks, rods or dots as described previously [43,44]. We used confocal images of fixed mCherry-EGFP-SYNJ2BP-TM H9c2 cells grown under normal culture conditions or adapted to galactose (Figure 2A). Our computational analysis revealed that for both growth conditions, most of the mitochondria were in a network but for the galactose adapted cells the percentage was significantly lower and there were more mitochondria classified as rods and dots (Figure 2B). Furthermore, the average length of rod-shaped mitochondria as well as mitochondrial networks was significantly shorter in the galactose adapted cells (Figure 2C). Thus, our morphology analysis showed more fragmented mitochondria in galactose adapted cells. To demonstrate that galactose adaptation of the cells in fact induces OXPHOS, we characterized mitochondrial function by performing high-resolution respirometry using an Oxygraph-2k (Oroboros Instruments). Our results showed that cells adapted to galactose displayed higher mitochondrial respiration and higher ATP-linked respiration in comparison to cells under normal culture conditions, indicative of induced OXPHOS (Figure 2D). For investigation of the level of mitochondrial ROS production we applied the mitochondria-targeted superoxide indicator MitoSOX Red in H9c2 cells in glucose or adapted to galactose. This indicator gives rise to a fluorescent signal in the presence of mitochondria superoxide [45]. To measure mitochondrial ROS induction, we subjected these cells to antimycin A treatment for 4 h. Live confocal imaging of the cells (Figure S2) and Flow cytometry (Figure 2E) revealed substantially higher mitochondrial ROS production in galactose adapted cells in comparison to cells in glucose after antimycin A treatment. This demonstrates that the cells in galactose have become more dependent on their mitochondria and thus are more susceptible to mitochondrial toxicants [46]. Taken together, these results are consistent with OXPHOS-induced degradation of mitochondria after galactose adaptation as indicated by the increase in red-only structures.

Red-only structures stain positive for markers of the different mitochondrial compartments but are devoid of mitochondrial membrane potential.

To verify targeting of the mCherry-EGFP-SYNJ2BP-TM reporter to the mitochondria in H9c2 cells and to demonstrate that red-only structures contained other mitochondrial markers, we performed immunofluorescence staining with antibodies against the outer mitochondrial membrane proteins TOMM20 and FIS1 (fission, mitochondrial 1) as well as the inner membrane protein ATP5F1A/ATP5A (ATP synthase F1 subunit alpha) and the matrix protein PDHA1 (pyruvate dehydrogenase E1 alpha 1). As expected, our results showed a high degree of colocalization of the tandem-tagged reporter with all the different mitochondrial markers, indicating correct targeting of the reporter to the mitochondria (Figure 3A). In addition, several of the red-only structures stained positive for the markers of the different mitochondrial compartments, confirming the presence of mitochondrial proteins in addition to the reporter in an acidic environment (Figure 3A enlarged). For assessment of mitochondrial membrane potential, we incubated the cells with MitoTracker Deep Red and performed live confocal imaging of the cells. Interestingly, the red-only structures did not stain positive for MitoTracker Deep Red, indicating loss of membrane potential (Figure 3B). In summary, the red-only structures represent fragments of mitochondrial origin that have lost the membrane potential.

Functional lysosomes give rise to red-only structures

To study colocalization of red-only mitochondria and acidic organelles (endo/lysosomes) we utilized LysoTracker Deep Red staining of the mCherry-EGFP-SYNJ2BP-TM H9c2 cells and applied three-dimensional (3D) structured illumination microscopy (SIM) on the cells after fixation. The obtained super-resolution images clearly demonstrated the presence of the reporter on the targeted mitochondrial outer membrane (Figure 4A). Furthermore, our results showed that most of the red-only mitochondria were positive for LysoTracker Deep Red staining, indicating colocalization of red-only mitochondria and lysosomes (Figure 4Ai,ii). To establish that the increased appearance of red-only mitochondria in galactose adapted H9c2 cells was in fact dependent on low pH inside lysosomes (or late endosomes) and that the reporter responded dynamically to lysosomal pH, we subjected the galactose adapted cells to bafilomycin A₁ (BafA1) treatment for 6 h (Figure 4B). BafA1 inhibits the vacuolar type H⁺-ATPase (V-ATPase) and results in pH elevation in the lysosome lumen leading to a subsequent inhibition of resident hydrolases. In addition, BafA1 can impair fusion between autophagosomes and lysosomes [47]. As anticipated, the number of cells with red-only mitochondria as well as the number of these per cell was abolished in the presence of BafA1 (Figure 4C). In contrast, treatment with inhibitors of lysosomal cathepsins, pepstatin A (PepA) and E64d, does not affect acidification of lysosomes but hampers cargo degradation [47]. Indeed, treatment of the H9c2 cells with the cathepsin inhibitors for 6 or 12 h resulted in an increase in the number of cells with red-only mitochondria as well as the abundance of red-only dots per cell, demonstrating the importance of

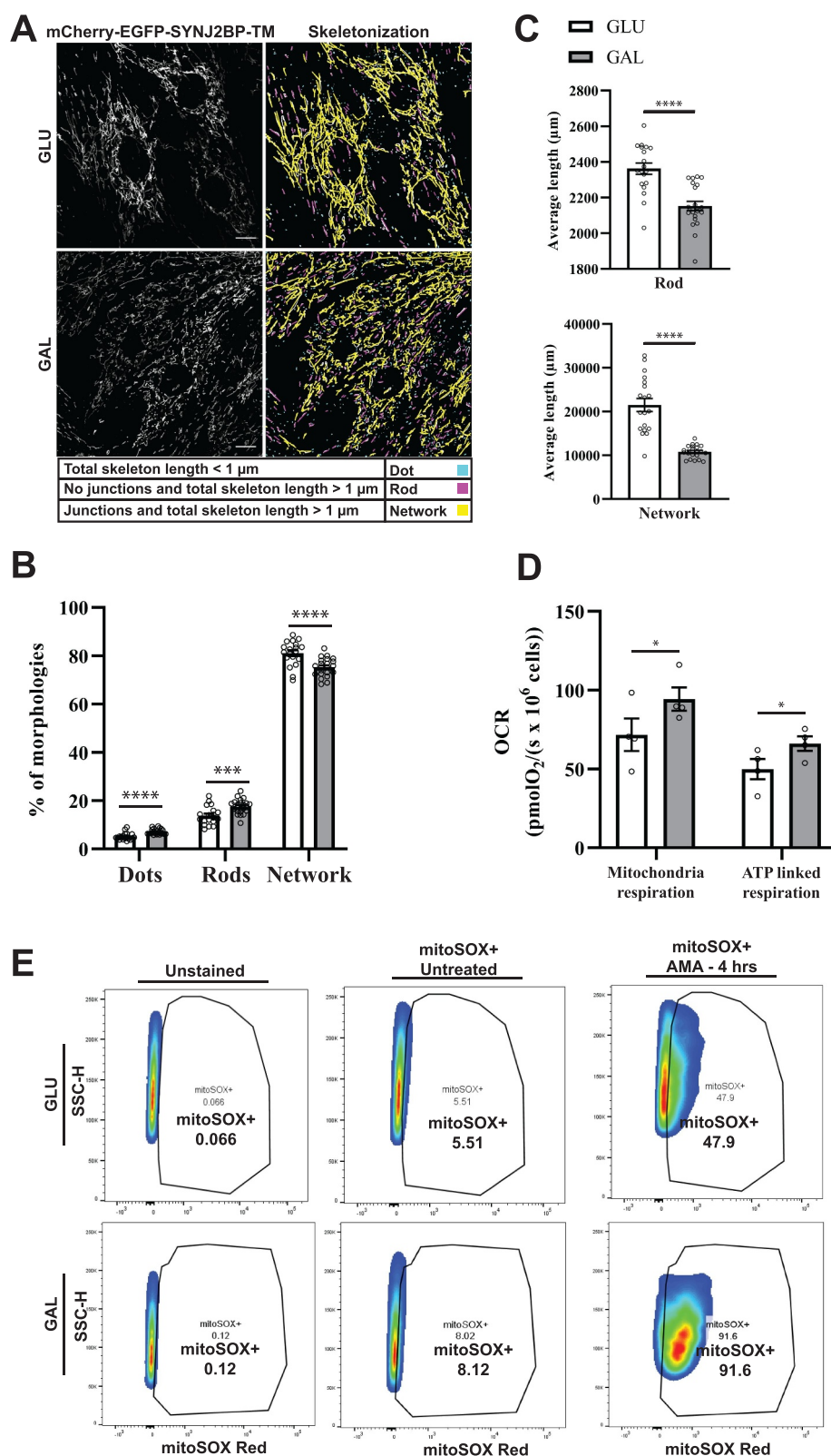


Figure 2. Mitochondria morphology analysis, mitochondrial respiration and ROS measurements indicate more fragmented mitochondria and OXPHOS dependence after galactose adaptation. (A) Morphological analysis of confocal images of cells grown in glucose vs galactose media. A representative skeletonization mask is depicted for each culture condition with the different morphology classes indicated in different colors. Rules for morphology classes are displayed at the bottom. (B) Overview of the distribution of mitochondria morphology classes in percentage for the two different growth conditions. The distribution for glucose vs galactose adaption is 5.16% vs 7.14% for dots, 13.79% vs 17.58% for rods and 81.04% vs 75.28% for network. (C) Quantification of the average length of mitochondria in the rod and network morphology classes for cells grown in glucose vs galactose. (D) High-resolution respirometry performed in an Oxygraph-2k (Oroboros Instruments). Oxygen consumption rate, OCR ($\text{pmolO}_2/\text{s} \times 10^6 \text{ cells}$) of cells grown under normal conditions (high glucose) or adapted to galactose was corrected for residual oxygen consumption (ROX) and normalized to the cell number per ml in the chambers. The values displayed in the graph are from four independent experiments \pm SEM, indicating mitochondrial respiration (basal respiration minus ROX) and ATP-linked respiration (basal respiration minus proton leak), respectively. (E) Flow cytometry analysis of H9c2 cells grown in normal media with glucose or adapted to galactose. The antimycin A (AMA) treated/untreated cells were stained with

lysosomal cathepsins in degradation of red-only dots (Figure 4D). We also demonstrated the same effect of the lysosomal inhibitors in the H9c2 TOMM20-mCherry-EGFP cells (Figure S3). Taken together, these results indicate that functional lysosomes are a prerequisite for the appearance and degradation of acidic mitochondria.

Capturing formation of acidic mitochondria by super-resolution imaging

To visualize the formation of acidic mitochondria we performed three-dimensional (3D) structured illumination microscopy (SIM) of live mCherry-EGFP-SYNJ2BP-TM H9c2 cells during normal culture conditions and in galactose adapted cells after LysoTracker Deep Red staining. Interestingly, in live videos from cells in both growth conditions (Video S1 and S2) we could detect a LysoTracker-positive structure containing a mitochondrial fragment of around 500 nm with both red and green fluorescence, indicating recent engulfment since the EGFP fluorescence was still detectable (Figure 5A,B). We identified these structures in the start of the videos and thus were unable to trace their formation back in time (Figure 5A). The majority of LysoTracker positive structures however did not contain any traces of EGFP fluorescence, possibly reflecting their more “mature” or degradative state. Notably, there is a significant time-delay between capturing the different channels during live 3D SIM imaging resulting in a slightly shifted appearance of the red and the green fluorescence of the same mitochondrial structure (Figure 5A). This makes it challenging to follow the formation of red-only structures in live SIM videos. To overcome this issue, we stained cells with LysoView 650 and used Airyscan FAST imaging to record videos at high temporal and spatial resolution (500 frames, frame time 1.01 s), without time delay between channels (Video S3–S5). As expected, we saw an almost complete overlap between LysoView 650 and red-only dots, confirming their acidic nature. Furthermore, the highly motile red-only dots were observed in close proximity with tubular mitochondria (Figure 6A). The time-lapse imaging revealed the red-only dots engaged in numerous transient contacts with the tubular mitochondria (Figure 6A, 2:34; Figure 6B, 2:19; Figure 6C, 0:24) lasting from less than 30 seconds to several minutes. Following such contacts, a mitochondrion was in some instances seen to alter its shape to become notably pulled toward red-only dots (see mitochondrion in contact with two red-only dots in the enlarged view in Figure 6C; compare timepoints around 1:00 to 2:45 in video S5). Furthermore, we observed several instances of apparent rapid transfer of material between a mitochondrion and a red-only dot (Figure 6C enlarged views from 1:36 to 2:12). Importantly, in such cases EGFP fluorescence was only briefly detectable at the intersection between the structures, suggesting uptake into an acidic

lumen and an almost instant quenching of the EGFP fluorophore. Taken together, by applying 3D SIM and Airyscan FAST live cell imaging we could capture lysosomal engulfment of mitochondrial contents.

CLEM reveals red-only structures as single membrane vesicles containing collapsed mitochondria and lamellar lysosomes

Correlative light and electron microscopy (CLEM) enables the determination of ultrastructural features of fluorescently labeled structures in a cellular context. For this type of high-resolution image analysis of the red-only dots we seeded our tandem-tagged SYNJ2BP-TM H9c2 cells grown under normal conditions or adapted to galactose on gridded dishes and stained the cells with LysoTracker Deep Red prior to fixation. Confocal imaging of the fixed cells and the grid after 4',6-diamidino-2-phenylindole (DAPI) staining allowed us to relocate the coordinates of cells of interest after resin embedding. Serial section ultramicrotomy was performed on selected positions/cells, and the sections were then imaged by transmission electron microscopy (TEM). By overlay of confocal images and TEM images we could identify red-only mitochondria positive for LysoTracker Deep Red as quite electron dense structures with features typical of autophagic vacuoles, with varying size and content in cells under normal conditions (Figure 7A). The ultrastructural characteristics of red-only dots did not seem to depend significantly on their size, since smaller red-only dots showed similar features as larger ones (Figure S4A). In contrast, mitochondria with both EGFP and mCherry fluorescence had a tubular shape and normal cristae (Figure 7A_{vi}). For the galactose adapted cells, the red-only structures were more homogenous and less electron dense (Figure 7B). Of note, when inspecting multiple consecutive sections of the same cells (Figure 7B_{iv-v}), red-only structures were frequently seen in close vicinity (or in contact) with both the tubular mitochondrial network and the ER, as well as with electron-dense structures reminiscent of lysosomes (Figure 7B_{vi}). Serial section imaging revealed the ultrastructure of these red-only/LysoTracker-positive dots as single membrane vesicles surrounding remnants of what appeared to be collapsed mitochondria (no cristae) and an electron dense multilamellar lysosome (Figure 7C). To investigate the ultrastructure of red-only dots in a state of hampered lysosomal turnover, we performed CLEM after treatment with PepA and E64d, on cells grown in both glucose and galactose (Figure S4B and S4C, respectively). As expected, we observed an increased number of red-only dots which appeared heavily aggregated and had an increased electron density after lysosomal inhibition. Our results are consistent with increased lysosomal degradation of mitochondria after galactose

mitoSOX Red and compared with unstained cells as a negative control. During normal culture conditions, antimycin A treatment resulted in approximately 47% mitoSOX Red positive cells, while in galactose 91% of the cells were mitoSOX Red positive. The data depicted represent one of three independent experiments. Data presented in (B) and (C) is shown as mean \pm SEM of 20 fields of view per condition. The individual datapoints are per frame cell averages.

Note: * $p < 0.05$, ** $p < 0.01$, *** $p < 0.001$ and **** $p < 0.0001$. Scale bar: 10 μ m.

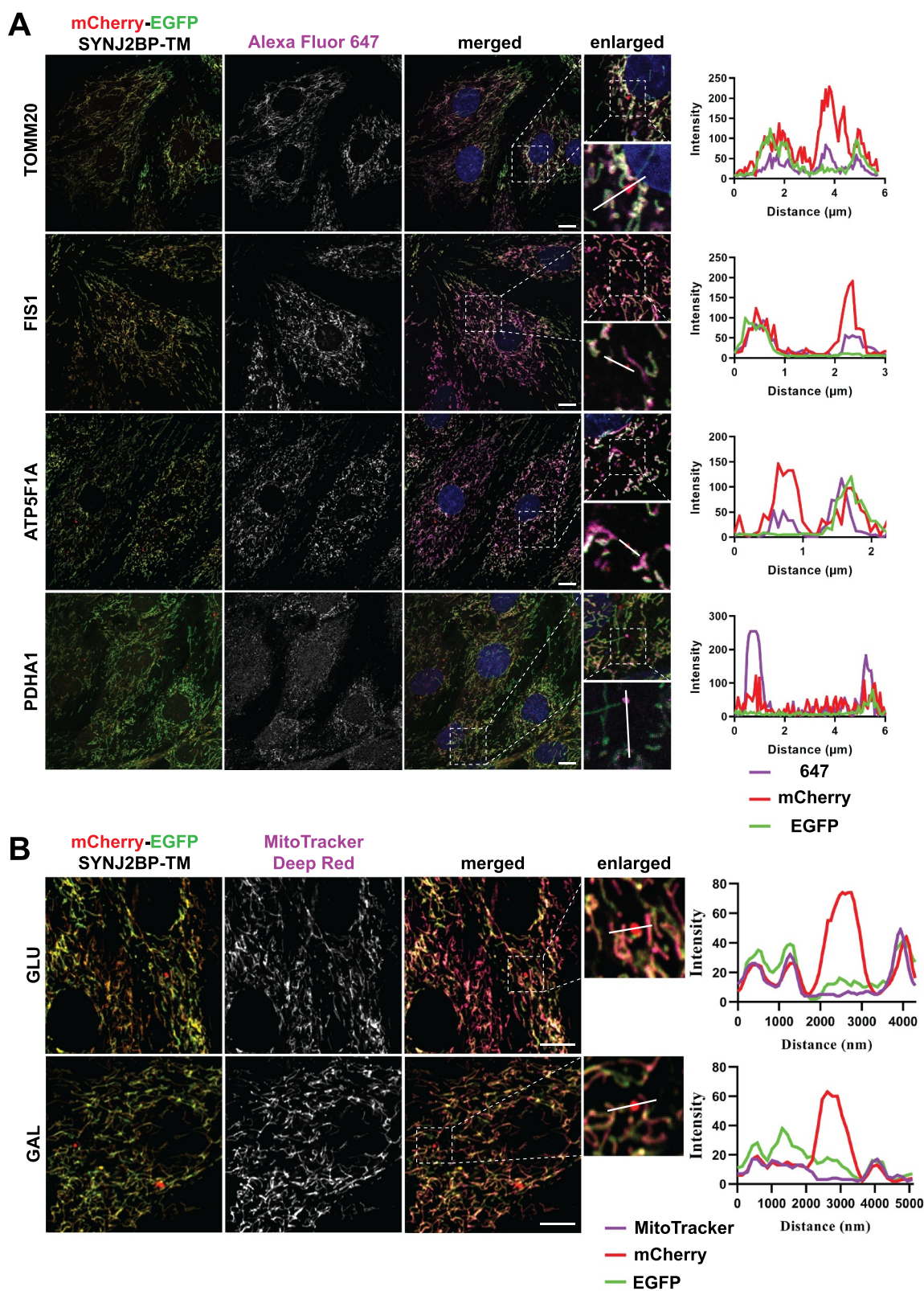


Figure 3. Red-only dots colocalize with mitochondrial markers of different mitochondrial compartments and lack membrane potential. (A) Confocal microscopy images of fixed tandem-tagged (mCherry-EGFP-SYNJ2BP-TM) H9c2 cells demonstrating colocalization of red-only dots with mitochondrial marker proteins of the different mitochondrial compartments; FIS1 and TOMM20 (outer membrane), ATP5F1 A (inner membrane) and PDHA1 (matrix). Region of interest for each marker is presented in a zoomed-in image with a line profile including an enlarged red-only dot displaying the colocalization. (B) Confocal microscopy images of live H9c2 cells with the mCherry-EGFP-SYNJ2BP-TM reporter and MitoTracker Deep Red staining for both glucose and galactose adapted cells. The enlarged region of interest depicts line profiles demonstrating colocalization of MitoTracker Deep Red in mitochondrial networks, but lack of colocalization in red-only dots. Scale bar: 10 µm.

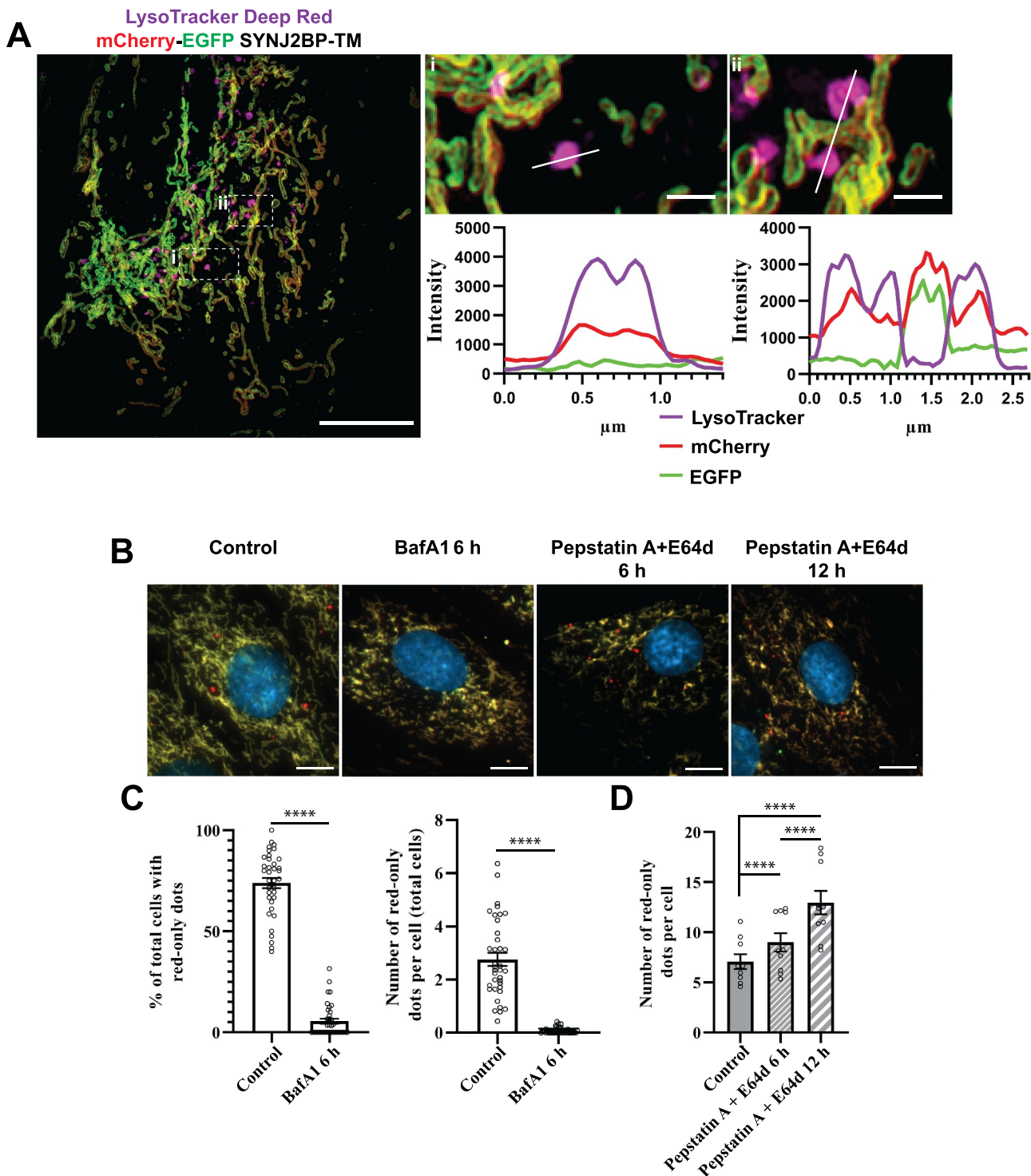


Figure 4. Functional lysosomes are essential for the appearance and removal of red-only dots during galactose adaption. (A) Structured illumination microscopy (SIM) imaging of fixed mCherry-EGFP-SYNJ2BP-TM H9c2 cells showing red-only dots that are positive for LysoTracker DeepRed staining (magenta). Line profiles through the LysoTracker-positive red-only dots in the enlarged boxed regions of interest are depicted, with corresponding numbers between the overview image and enlarged images. (B) Representative images of galactose adapted mCherry-EGFP-SYNJ2BP-TM H9c2 cells during control conditions and after treatment with the lysosomal inhibitors bafilomycin A₁ (BafA1; 200 nM) and pepstatin a (PepA; 10 μg/ml) and E64d (10 μg/ml) for the indicated times. (C) Quantification of the effects of a 6 h treatment of BafA1 on galactose adapted cells with the mCherry-EGFP-SYNJ2BP-TM reporter by assessing the percentage of cells containing red-only dots and number of red-only dots per total cells. (D) Quantification of the effects of a time course treatment of PepA and E64d assessed by number of red-only dots per cell in cells with red-only dots in galactose adapted cells with the mCherry-EGFP-SYNJ2BP-TM reporter. Over 150 cells were analyzed for each condition. The data is presented as mean ± SEM from 3 independent experiments, with more than 100 cells per condition. The individual datapoints are per frame cell averages. NOTE: * $p < 0.05$, ** $p < 0.01$, *** $p < 0.001$ and **** $p < 0.0001$. Scale bars: 10 μm and 1 μm (Ai and Aii).

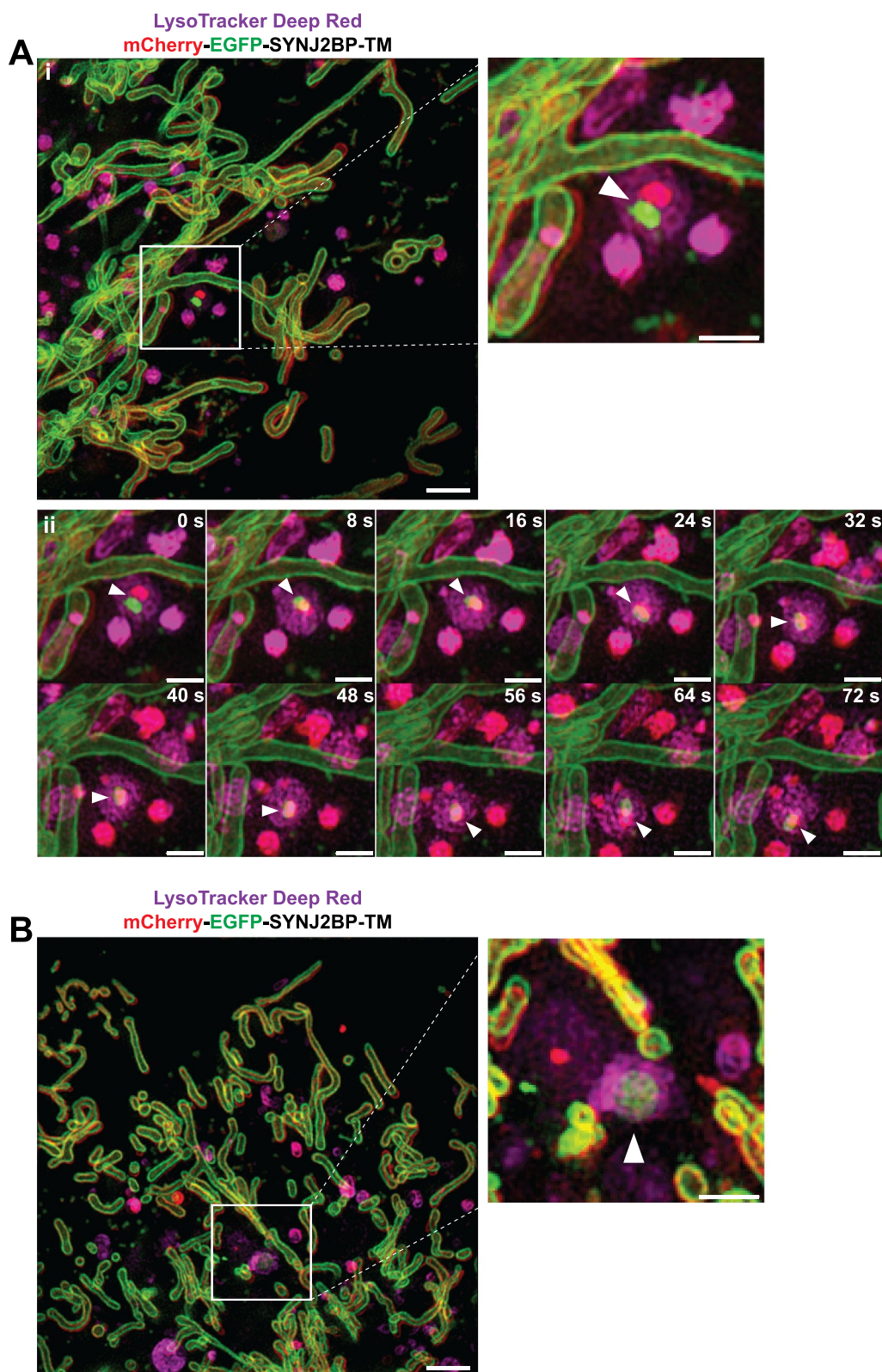


Figure 5. Three-dimensional (3D) structured illumination microscopy (SIM) live cell imaging of mCherry-EGFP-SYNJ2BP-TM H9c2 cells captures mitochondrial fragments within acidic structures. (Ai) A still frame overview image (merged channels) from the start of Video S1 displaying a cell during normal culture conditions after adding the LysoTracker Deep Red dye (100 nM for 40 min). The boxed area indicates a mitochondrial fragment with both EGFP and mCherry fluorescence inside a LysoTracker Deep Red-positive structure. The channels for red and green fluorescence are slightly shifted due to the time-delay between images of the different channels. The region of interest is shown as an enlarged image and the structure is highlighted with an arrowhead. (Aii) A time series of the boxed area in Video S1 following the movement of the lysosome containing the mitochondrial fragment (arrowhead). (B) A still frame overview image (merged channels) from the start of Video S2 displaying a cell after galactose adaptation after adding the LysoTracker Deep Red dye (100 nM for 40 min). The boxed area indicates a mitochondrial fragment with both EGFP and mCherry fluorescence inside a LysoTracker Deep Red-positive structure. The region of interest is shown as an enlarged image with the identified structure highlighted with an arrowhead. Max projection was utilized for all the images. Scale bars: 2 μm (overview images) and 1 μm (the enlarged images and for the time series).

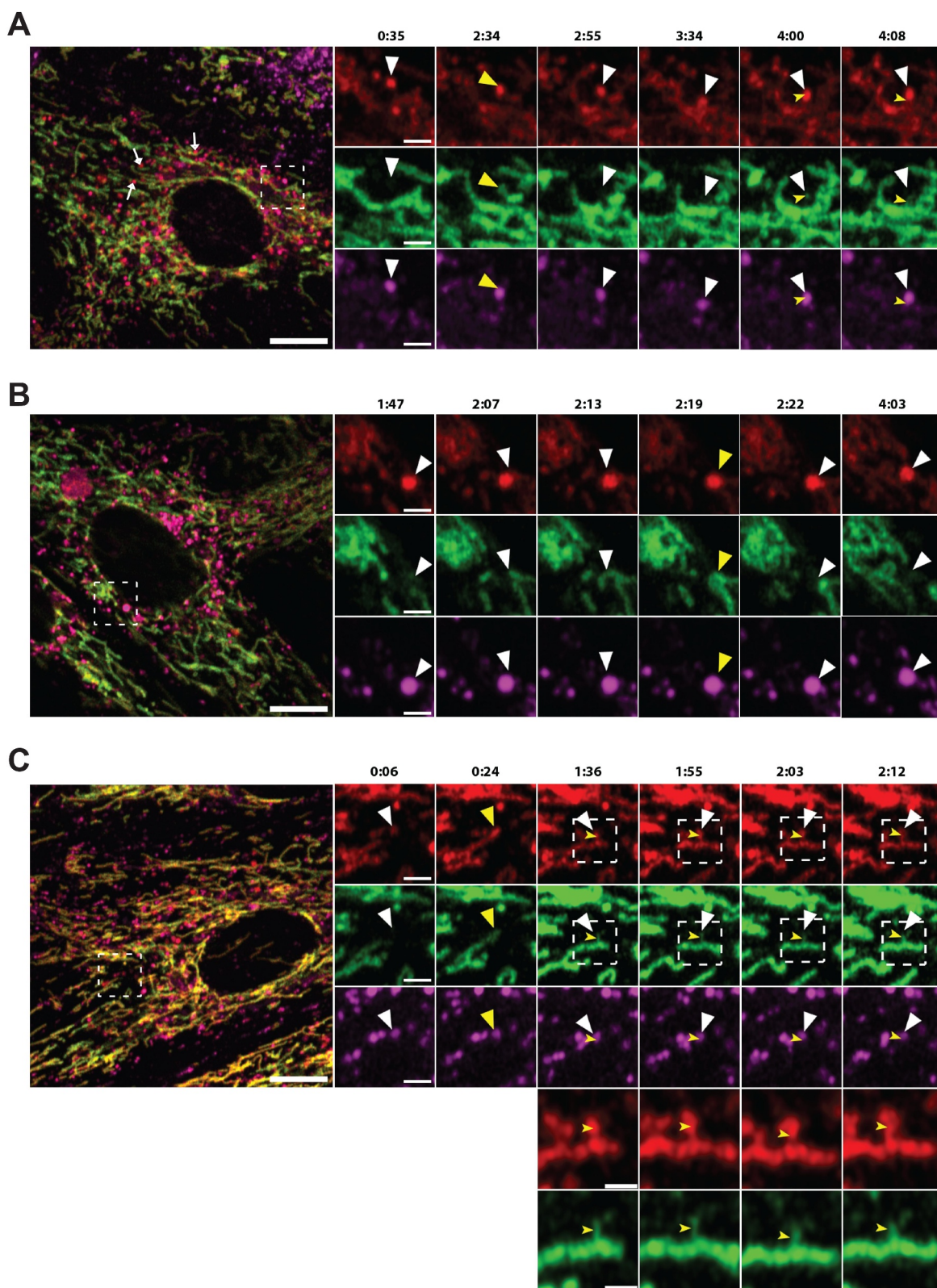


Figure 6. Airyscan FAST imaging of live galactose adapted mCherry-EGFP-SYNJ2B-TM H9c2 cells stained with LysoView 650 reveals transient contact and transfer between the mitochondrial network and red-only dots. (A) Full frame of video S3 at time 0:35 with zoomed-in area indicated (white box) for the selected time points (small panels, right). White arrows in the full frame show examples of red-only dots in close proximity with tubular mitochondria. White arrowheads in the small panels highlight a red-only dot approaching and contacting the mitochondrial network, producing a brief colocalized signal (yellow arrowheads) around time 2:34. At time 2:55, EGFP fluorescence has diminished, and the structure again appears red-only (white arrowheads). In subsequent frames, small protrusions of EGFP fluorescence (notched yellow arrowheads) can be seen upon close inspection to extend from the mitochondrion and into the red-only dot, and then rapidly disappear (see also video S3). (B) Full frame of video S4 at time 1:47 with zoomed-in area indicated (white box) as in (A). White arrowheads indicate a red-only dot approaching the mitochondrial network from time point 2:07. The EGFP signal remains detectable within the red-only dot for a few seconds around time 2:19 (yellow arrowheads) and then disappears around time point 2:22 (see also video S4). (C) Full frame of video S5 at time 0:06 with zoomed-in area indicated (white box) as in (A) and (B). White arrowheads indicate a red-only dot which encounters a tubular mitochondrion from time point 0:24 (yellow arrowheads). In subsequent frames, small protrusions of EGFP fluorescence can be seen to extend into the red-only dots (notched yellow arrowheads at time 1:36, 1:55, 2:03, and 2:12). An enlarged partial view (white boxes) of the mCherry and EGFP channels is shown below each time point. Scale bars: 10 μm (full frames), 2 μm (small panels), and 1 μm (enlarged views).

adaptation and demonstrate the importance of imaging serial sections when characterizing ultrastructural features.

Knockdown of Ulk1, Atg7 or Rab9a, respectively, impacts on OXPPOS induced lysosomal degradation of mitochondria.

In an attempt to elucidate the mechanism(s) driving lysosomal degradation of mitochondria induced by galactose adaptation in H9c2 cells, we performed short interfering RNA (siRNA) knockdown of selected key genes involved in autophagic or endosomal degradation of mitochondria in cardiac cells: *Atg7* (canonical autophagy machinery) [48], *Rab9a* (alternative mitophagy) [28], *Ulk1* (upstream of both ATG7 and RAB9A) [15,28] as well as *Rab5a* (endosomal mitophagy) [27]. We also knocked down *Rab7a*, the small GTPase involved in direct contact between mitochondria and lysosomes [28]. We chose a knockdown strategy with siRNA due to difficulties in generating CRISPR-Cas9 knockouts in H9c2 cells as also previously reported [49]. The cells were subjected to 48 h of siRNA knockdown and grown with or without the lysosomal cathepsin inhibitors PepA and E64d during the final 12 h. After fixation, the cells were analyzed by fluorescence microscopy (Figure 8A). The use of PepA and E64d enabled us to assess perturbation of autophagic flux resulting from siRNA knockdown by quantifying red-only dots (Figure 8B). The knockdown of each protein was verified with western blots of cell lysates from cells adapted to galactose (Figure 8C). The abundance of red-only dots was quantified and compared with cells treated with PepA and E64d. Surprisingly, siRNA knockdown of neither *Ulk1*, *Atg7*, *Rab9a*, *Rab5a* nor *Rab7a* affected the number of red-only dots per cell during steady-state conditions. However, knockdown of *Ulk1*, *Atg7* and *Rab9a* led to an impaired flux, demonstrated by a lack of an increase in red-only dots after PepA and E64d treatment (Figure 8B). This did not apply to siRNA knockdown of *Rab5a* or *Rab7a* where the flux was unaffected. Our data thus show the importance of using lysosomal inhibitors when evaluating the effects of siRNA knockdowns on OXPPOS induced degradation of mitochondria. Prolonging the PepA and E64d treatment from 12 to 24 h did not uncover any further increase in the level of red-only dots (Figure S5A). Likewise, extending the siRNA knock-down to 72 h did not alter mitochondrial protein expression levels (Figure S5B). To further investigate the importance of the canonical autophagy machinery we monitored the presence of the autophagy marker MAP1LC3B on mitochondria and on red-only dots. To this end, we performed a proximity ligation assay (PLA) [50] using anti-MAP1LC3B antibody in combination with anti-PDHA1 antibody. This assay enables the assessment of proximity of the two targeted proteins in situ in fixed cells, giving rise to a fluorescent PLA signal or puncta only when the targeted proteins are within 40 nm of each other. The PLA puncta were localized on mitochondria, both networks and smaller structures, but were not present on red-only dots (Figure 8D). Notably, there was no increase in the number of PLA puncta per cell in galactose adapted cells compared to

cells in normal glucose containing conditions (Figure 8E). This suggests the presence of MAP1LC3B on mitochondria before acidification but also indicates that MAP1LC3B is not the main mediator of enhanced mitochondrial degradation in galactose adapted cells. In conclusion, our data indicate the involvement of both ULK1, ATG7 and RAB9A in lysosomal degradation of mitochondria in H9c2 cells. In contrast, RAB5A and RAB7A do not seem to play a major role.

Discussion

Given the central role of mitochondria in cell homeostasis, maintaining functional mitochondria is crucial. Basal levels of mitophagy have been considered too low for a reliable assessment [47]. Interestingly, use of pH-sensitive mitochondria reporters such as mt-Keima and *mito-QC* reveal a substantial but heterogenous level of basal mitophagy in tissues of mice and flies [51–56] and a detectable level in *C. elegans* and zebrafish [57]. Since the fraction of mitochondria targeted for lysosomal degradation at any given time under normal conditions is likely small compared to the total pool of mitochondria within the cell, such sensitive reporters are crucial to detect the degradation. The *mito-QC* reporter has been used in H9c2 cardiomyoblasts to display induced mitophagy during cell differentiation [49]. We exploited a similar dual color fluorescence-quenching assay based on a mCherry-EGFP outer mitochondrial membrane targeted reporter to detect lysosomal degradation of mitochondria in H9c2 cells. Our quantification of basal mitophagy in H9c2 cells showed a high percentage (around 50%) of cells containing red-only mitochondria. This is substantially higher than reported for e.g., human neuroblastoma SH-SY5Y cells [58] and mouse embryonic fibroblasts [59,60] where less than 20% of the cells display red-only mitochondria. Notably, the number of acidic mitochondrial structures detected per cell (around 3–4) of H9c2 cells with red-only dots was similar as to that reported for SH-SY5Y cells and human retinal pigment epithelial ARPE-19 cells [61]. By employing a metabolic shift to OXPPOS by galactose adaptation we detected a significant increase in both the number of cells containing acidic mitochondria as well as the number of red-only dots per cell. Our results are in line with studies on OXPPOS-induced mitophagy in mouse endothelial fibroblasts (MEFs) [59] as well as in HeLa cells and human primary skeletal muscle myoblasts [62]. In addition, piecemeal mitophagy of specific mitochondrial proteins is OXPPOS induced in HeLa cells [63] and in MEFs [60]. Most likely the induced removal of mitochondria or mitochondrial proteins is due to higher turnover of the mitochondria during elevated activity of the electron transport chain. This would sustain renewal of mitochondria and avoid accumulation of damaged organelles. In support of this, we have previously shown an increased formation of mitochondria derived vesicles in galactose adapted H9c2 cells [35]. Conversely, OXPPOS dependence blocks iron chelator-induced mitophagy in human bone osteosarcoma U2OS cells and SH-SY5Y cells [58] and Carbonyl cyanide 3-chlorophenylhydrazone (CCCP) depolarization-induced mitophagy in neurons and HeLa cells [64–67]. Hence, the

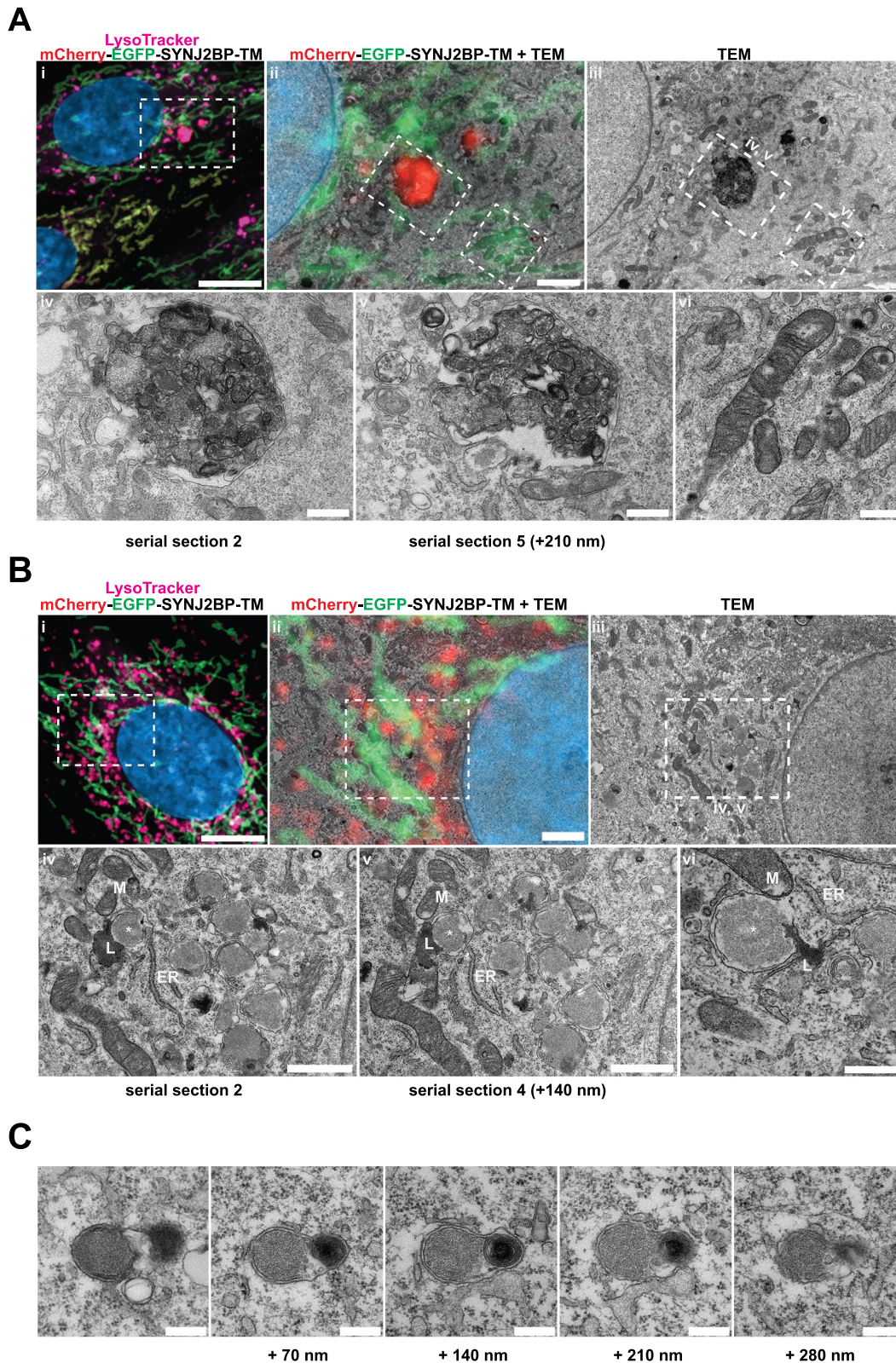


Figure 7. Correlative light and electron microscopy of mCherry-EGFP- SYNJ2BP-TM H9c2 cells reveals the ultrastructure of red-only dots. (A) Red-only dots in cells grown in media containing glucose correspond to autophagic vacuoles with a diverse internal milieu at varying stages of cargo engulfment and maturation (A iv-v). Meanwhile, mitochondria displaying both EGFP and mCherry fluorescence have a normal tubular morphology with distinct inner and outer membranes and intact cristae (A vi). (B) Structures corresponding to red-only dots in galactose adapted cells are more uniform and less electron dense. Imaging of consecutive ultrathin sections (B iv-vi) revealed that these structures are in close proximity (or may be continuous) with membranes of the endoplasmic reticulum (ER) and mitochondria (M). Also note apparent lysosomes (L) at the periphery of red-only structures (*). Scale bars: 10 μm (A i and B i), 2 μm (A ii and B ii), 1 μm (B iv and B v) and 0.5 μm (A iv-vi and B vi). (C) Serial section TEM imaging of a red-only dot shows a single membrane vesicle with apparent remnants of mitochondria and a multilamellar lysosome. Scale bar: 0.3 μm .

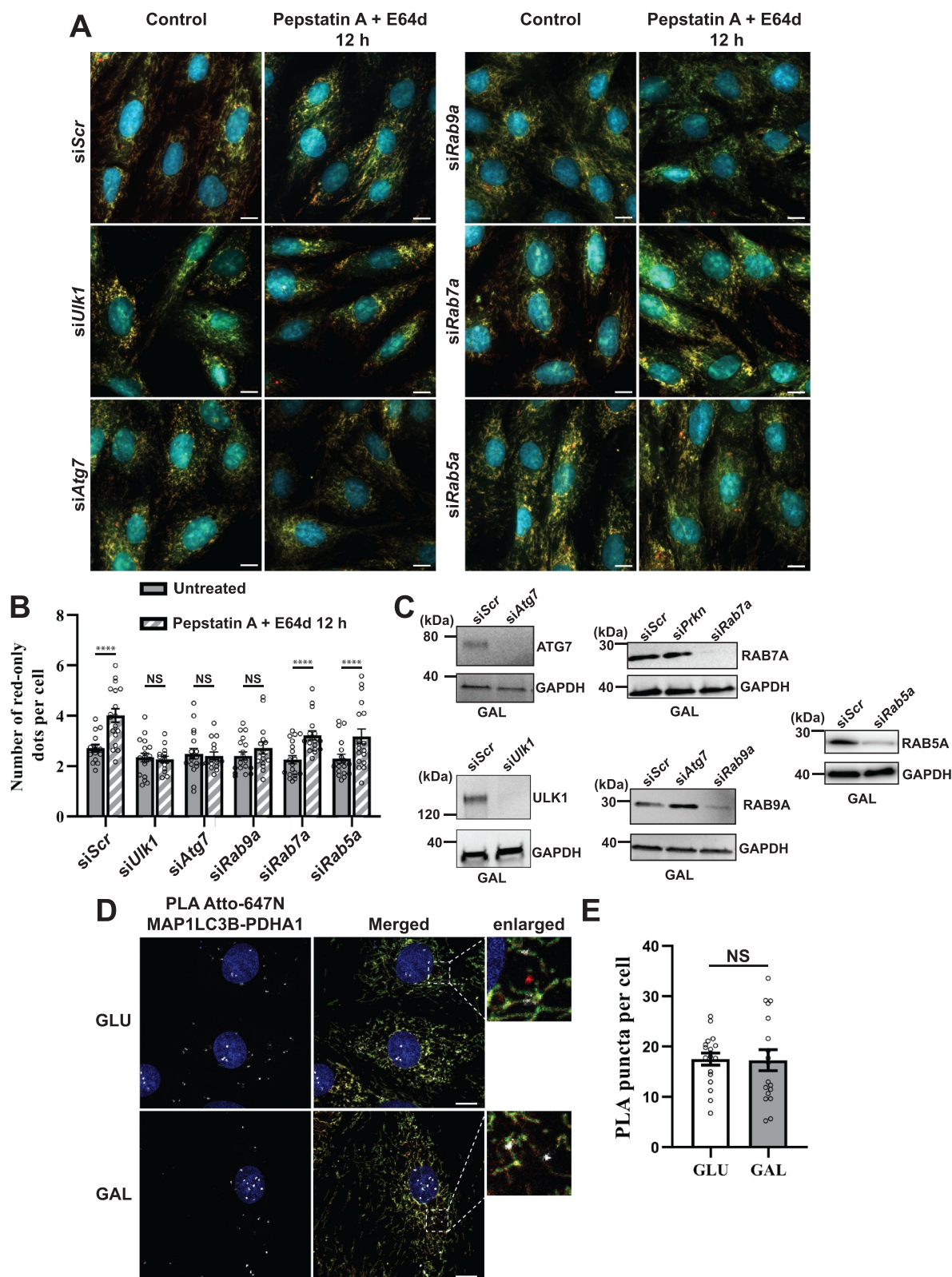


Figure 8. Effect of siRNA knockdowns on mitophagic flux and evaluation of LC3 involvement by proximity ligation assay (PLA). (A) Representative widefield images of mCherry-EGFP- SYNJ2BP-TM H9c2 cells analyzed 48 h after transfection with scrambled siRNA (siScr) or siRNA against *Ulk1*, *Atg7*, *Rab9a*, *Rab7a* or *Rab5a* respectively. (B) Quantification of the effect of 48 h siRNA knockdowns by assessment of number of red-only dots per cell in cells containing red-only dots in control conditions against a 12 h PepA and E64d treatment. The data is presented as mean \pm SEM from 3 independent experiments, with more than 100 cells per condition (total number analyzed per experiment was over 1200 cells). (C) Western blots showing the expression levels of the siRNA targeted proteins in control and siRNA treated cells for verification of successful knockdown. (D) Representative confocal images of detected PLA puncta (white) using anti-MAP1LC3B and anti-PDHA1 antibody during normal (GLU) and galactose (GAL) adapted conditions. The enlarged boxes display the PLA puncta on the mitochondria network and small mitochondrial fragments but their absence on red-only dots. (E) Quantification of the number of PLA puncta per cell in 10 images (with more than 50 cells in total) per condition from two independent experiments. The individual datapoints are per frame cell averages. * $p < 0.05$, ** $p < 0.01$, *** $p < 0.001$ and **** $p < 0.0001$. Scale bar: 10 μ m.

metabolic status of the mitochondria can dictate the level of mitophagy, dependent on the cell type and growth conditions. Interestingly, a recent study suggests that mitophagy itself initiates an increase in mitochondrial biogenesis and oxidative metabolism in induced pluripotent stem cells undergoing endothelial differentiation [68].

Using a deep-learning approach we were able to quantify the morphological change of mitochondria in H9c2 cells, adopting a more fragmented or shorter appearance after the metabolic shift. Mitochondrial fragmentation has also been observed in neonatal cardiomyocytes where the percentage of mitochondria with shorter lengths increases during glucose deprivation by galactose adaptation [28]. Mitochondrial fragmentation is often mediated by peripheral fission which is mechanistically different from mid-zone fission directing mitochondria biogenesis [42]. In green monkey kidney fibroblast-like Cos-7 cells the smaller peripheral fission-derived mitochondria display a length distribution of only 1–2 μm and are mainly subjected to degradation. In addition, the rate of peripheral fissions per cell increases when the Cos-7 cells are grown in glucose-free, galactose containing media [42].

Performing super-resolution live cell imaging on tandem tagged SYNJ2BP-TM H9c2 cells with labeled lysosomes, we were able to monitor highly dynamic interactions between lysosomes and mitochondria. Furthermore, we detected rapid lysosomal engulfment of mitochondrial contents within a few minutes. The rapid formation of these structures could also indicate their rapid degradation and thus influence the numbers of such events detected in snapshots of fixed cells. The potential consequence could therefore be an underestimation of the levels of lysosomal degradation of mitochondria when studying fixed cells and tissue. We are not aware of previous publications demonstrating super-resolution live cell imaging of the formation of acidic mitochondria.

Applying CLEM, we revealed the ultrastructure of red-only mitochondria in the H9c2 cells in steady-state conditions and after a metabolic shift toward OXPHOS. There are only a few studies that have performed CLEM analysis on acidified mitochondria. The ultrastructures of mt-Keima acidic dots analyzed by CLEM in *Drosophila* muscle cells also contain features of multilamellar bodies and are of a comparable size as those detected in the H9c2 cells [55]. In studies performed in mammalian cells, iron depletion with DFP [57,67] or stress induced with propionic acid [69] or CCCP and overexpression of PRKN [70] are used to induce degradation of mitochondria before the CLEM analysis. Thus, to our knowledge, our study is the first to visualize the ultrastructure of acidified mitochondria in mammalian cells cultured under physiologically relevant conditions. Taken together, in view of our results from live cell SIM and Airyscan FAST imaging, the CLEM data presented are consistent with a model where mitochondria are fragmented at (or in close vicinity to) the ER, and rapidly fuse with lysosomes.

There are still many unanswered questions regarding the molecular mechanisms of basal mitophagy. Notably, pH-dependent mitochondrial reporters indicate acidification of tagged mitochondria or parts of mitochondria and thus their presence in acidic late endosomes or lysosomes. However, the

route of the labeled mitochondria toward lysosomes is not revealed by the reporters. We chose siRNA knockdown of *Ulk1*, *Atg7*, *Rab9a* to assess the contribution of both canonical and non-canonical autophagy in lysosomal degradation of mitochondria in the H9c2 cells. Knockdown of neither *Ulk1*, *Atg7* nor *Rab9a* reduced the level of red-only dots in galactose adapted cells. However, these siRNA experiments resulted in hampered mitophagic flux, revealed using lysosomal inhibitors. Therefore, our data indicate the presence of redundant mechanisms for lysosomal degradation of mitochondria in H9c2 cells where both the canonical autophagy machinery and alternative RAB9A mediated mitophagy operate during OXPHOS reliant conditions. In addition, because of the unaffected basal level during all knockdown experiments, other mechanisms such as different types of micromitophagy [26] could be involved and require further investigations.

Our study shows that assessment and visualization of lysosomal degradation of mitochondria at high temporal and spatial resolution is feasible during basal conditions. Our results indicate highly dynamic interactions and transfer of material between mitochondria and lysosomes and give important insights that are valuable for future studies and therapeutic targeting of mitophagy.

Materials and methods

Cell culture

Rat cardiomyoblast H9c2 cells (Sigma-Aldrich, 88092904) were cultured in high-glucose (4.5 g/L) Dulbecco's Modified Eagle Medium (DMEM; Sigma-Aldrich, D5796) with 10% Fetal Bovine Serum (FBS) and 1% streptomycin/penicillin (Sigma-Aldrich, P4333). For glucose deprivation and adaptation to galactose, the cells were grown in DMEM without glucose (Gibco, 11966-025) supplemented with 2 mM L-glutamine (Sigma-Aldrich, G7513) 1 mM sodium pyruvate (Sigma-Aldrich, S8636), 10 mM galactose (Sigma-Aldrich, G5388), 10% fetal bovine serum (Sigma-Aldrich, F7524) and 1% streptomycin-penicillin (Sigma-Aldrich, P4333). The cells were adapted to galactose for at least 7 days before the experiments. Stable H9c2 cells (see below) were grown in the same medium with the addition of 1 $\mu\text{g}/\text{ml}$ of puromycin (InvivoGen, ant-pr-1). For hypoxic conditions, the cells were incubated at 0.3% O_2 for 2, 4, 6 or 16 h. For labeling of lysosomes, the cells were treated with 50 or 100 nM LysoTracker Deep Red (ThermoFisher Scientific, L12492) for 30–40 min or with LysoView 650 (Biotium, 70059). Cells were treated as indicated with 0.2 μM bafilomycin A₁ (BafA1 from *Streptomyces griseus*; Sigma-Aldrich, B1793) or 10 $\mu\text{g}/\text{ml}$ pepstatin A (Sigma-Aldrich, P5318) and 10 $\mu\text{g}/\text{ml}$ E64d (Sigma-Aldrich, E8640). All cell lines were maintained at 37°C and under 5% CO_2 .

Generation of stable mCherry-EGFP-SYNJ2BP-TM and TOMM20-mCherry-EGFP H9c2 cell lines

H9c2 cells with stable expression of tandem tagged (mCherry-EGFP) mitochondria

outer membrane protein SYNJ2BP/OMP25 (synaptojanin 2 binding protein)-transmembrane domain (TM) or tandem-tagged (C terminus) full length TOMM20 protein were generated by retroviral transduction. The mCherry-EGFP-SYNJ2BP-TM construct [32] was amplified with PCR and cloned into the retroviral expression vector pMRXIP with the selection marker puromycin. The vector was made with deletion of GFP-STX17 from the pMRXIP-GFP-STX17 plasmid (Addgene, 45909; Noburo Mizushima lab). Full-length TOMM20 was amplified by PCR using mTagBFP2-TOMM20-N-10 plasmid (Addgene, 55328; Michael Davidson lab) as a template and cloned into the pMRXIP vector with the tandem tag. The plasmids were verified by restriction enzyme digestion and DNA sequencing (Applied Biosystems, 4337455BigDye). The HEK293-Phoenix packaging cell line (ATCC, CRL-3213) was transfected with the pMRXIP-reporter vectors using MetafectenePro (Biontex, T040-1.0). The virus-containing media from transfected HEK293-Phoenix cells was harvested 24, 48 and 72 h post transfection. The harvested media was subsequently filtered through a 0.45- μm filter and then added onto subconfluent H9c2 cells. Hexadimetretribromide-polybrene (Sigma-Aldrich, H9268) was added to a final concentration of 8 $\mu\text{g}/\text{ml}$. The H9c2 cells were incubated with the virus-containing media with polybrene for 6–12 h each time. The transduced H9c2 cells were then selected with 1 $\mu\text{g}/\text{ml}$ of puromycin. Stable expression of mCherry-EGFP-SYNJ2BP-TM or TOMM20-mCherry-EGFP was verified by western blotting and confocal imaging. Furthermore, the cells were sorted by fluorescence activated cell sorting (FACS) to ensure approximately equal expression level of the mitochondrial outer membrane reporter.

High-resolution respirometry

At the day of measurements, the mCherry-EGFP-SYNJ2BP-TM H9c2 cells, grown in glucose or adapted to galactose for 7 to 21 days, were trypsinized, and resuspended in their conditioned medium and counted using Countess II (ThermoFisher Scientific). Respirometry was performed in an Oxygraph-2k system (Oroboros Instruments, Innsbruck, Austria) calibrated to air (gain for oxygen sensor was set to 2) with standard cell culture medium at 37°C. The measurements were repeated in 4 independent experiments. Based on the cell number, a calculated volume of cells was added to the two stirred (750 rpm) chambers aiming to a final concentration of 0.4×10^6 cells/ml. The cell counting was repeated to determine the exact cell concentration in each chamber, and chambers were sealed to obtain a closed system. Analysis of the oxygen concentration in the chambers was performed using DatLab version 5.1.0.20 (Oroboros Instruments, Innsbruck, Austria). Decreasing oxygen concentration in the chambers resembled cellular oxygen consumption. When the oxygen consumption rate, OCR (O_2 flux ($\text{pmolO}_2/\text{s} \cdot \text{ml}$)) reached a steady state level, a measurement was recorded displaying total cellular respiration (basal). Leak respiration was assessed by the addition of oligomycin (Sigma-Aldrich, O4876) in a final concentration of 5 μM . Subsequently, the proton gradient

was released by stepwise titration (0.5 $\mu\text{M}/\text{step}$) of the uncoupler carbonylcyanide-3-chlorophenylhydrazone (CCCP) (Sigma-Aldrich, C2759) until the maximum respiration was achieved (electron transport system capacity, ETS capacity). The addition of 0.5 μM rotenone (Sigma-Aldrich, R8875) an inhibitor of CI and 2.5 μM antimycin A (Sigma-Aldrich, A8674) an inhibitor of CIII blocked mitochondrial respiration completely, resulting in residual oxygen consumption (ROX). The respiration measurement at the different STATES (basal, leak, ETS) were corrected for ROX afterward. Mitochondrial respiration was calculated by subtracting the non-mitochondrial respiration after antimycin A addition from the basal respiration level. ATP linked respiration was derived from subtracting the leak respiration (oligomycin) from the basal level. All respiration data was normalized to the cell count in the chamber. The results were presented as a mean.

Mitochondrial ROS measurements with MitoSox Red

H9c2 cells grown under normal culture conditions or adapted to galactose were treated with 100 nM antimycin A for 4 h or left untreated. After treatment, cells were harvested by trypsinization, washed three times with respective media and then incubated with 1 μM MitoSOX Red (ThermoFisher Scientific, M36008) for 30 min inside the cell incubator in their respective media. The cells were then washed 3 times with HBSS (Gibco, 1402-092) followed by flow cytometry analysis with a LSRFortessa (BD Biosciences). The excitation light used was 488 nm, emission was passed through 556LP filter and detected using a 616/23 nm emission filter. For confocal imaging purposes the cells were seeded in MatTek dishes (MatTek, P35-1.5-14-C) treated with antimycin A and stained with MitoSOX Red as described above, followed by HBSS washing prior to live cell confocal imaging. MitoSOX Red fluorescence was excited using the 514 nm laser and the emitted light was detected between 565–715 nm.

Mitochondrial membrane potential visualization

The mCherry-EGFP-SYNJ2B-TM H9c2 cells grown under normal conditions or adapted to galactose were incubated with MitoTracker Deep Red (ThermoFisher Scientific, M22426) at 100 nM concentration for 30 min. The cells were then given fresh cell culture media and subjected to live Airyscan FAST imaging using the Zeiss LSM 880.

Antibodies

The following primary antibodies were used: anti-GAPDH (Sigma-Aldrich, G9545; 1:5000) anti-TOMM20 (Santa Cruz Biotechnology, SC-11415; 1:500), anti-FIS1 (Proteintech, 10956-1-1ap; 1:100), anti-ATP5F1A/ATP5A (Abcam, Ab14748; 1:200), anti-PDHA1 (Abcam, ab110330; 1:200), anti-ATG7 (Cell Signaling Technology, 8558; 1:1000), anti-RAB9A (Cell Signaling Technology, 5118; 1:1000), anti-ULK1 (Cell Signaling Technology, 8054; 1:1000), anti-RAB5A (Cell Signaling Technology, C8B1; 1:1000), anti-RAB7 (ERP7589; Abcam,

ab137029; 1:1000), anti-LC3B (Sigma-Aldrich, L7543;1:200). Alexa Fluor 647-conjugated goat anti-rabbit and anti-mouse IgG (Invitrogen, A21244 and A32728; 1:500) were used as secondary antibodies.

Immunostaining of fixed cells

For immunofluorescent staining the cells were seeded on #1.5 glass coverslips. At

approximately 80% confluence the cells were subjected to treatment. The cells were then fixed using 4% formaldehyde (ThermoFisher Scientific, J19943.K2) at 37°C for 20 min. The cells were permeabilized with methanol at room temperature for 5 min. The permeabilized cells were blocked with 3% pre-immune goat serum (Sigma-Aldrich, G6767) in phosphate-buffered saline (PBS; Sigma-Aldrich, D8537) for 1 h at room temperature before overnight incubation at 4°C with primary antibodies diluted in PBS with 1% goat serum. Cells were then washed and incubated for 1 h with Alexa Fluor-coupled secondary antibodies diluted 1:500 in PBS supplemented with 1% goat serum. After a final wash in PBS the coverslips were mounted on glass slides using Prolong Glass (Invitrogen, P36980).

RNAi

The short interfering RNAs (siRNAs) used were pre-designed and validated *Silencer*[®]Select siRNAs (Invitrogen, 4390771): siRNA against *Ulk1* (siRNA ID s166350), siRNA against *Atg7* (siRNA ID s161900), siRNA against *Rab9a* (siRNA ID s136762), siRNA against *Rab5a* (siRNA ID s134381), siRNA against *Rab7a* (siRNA ID s131440) and negative control siRNA (Ambion, 4390844). The cells were transfected with siRNA using Lipofectamine RNAiMax Transfection Reagent (Invitrogen, 13778-075) according to the manufacturer's recommendation. After 6 h of incubation the cell media was changed to remove the transfection reagent in order to avoid H9c2 cell death. After 48 or 72 h (two consecutive siRNA transfections) of siRNA knockdown the cells were fixed or harvested for western blot analysis. The cells were fixed with 4% formaldehyde with 0.2% glutaraldehyde (Sigma-Aldrich, G5882). For each coverslip of fixed cells/condition, 10 positions (containing more than 100 cells in total) were selected and imaged as a Z-stack on a Cell Discoverer7 widefield microscope (Carl Zeiss Microscopy). Quantification of red-only dots was performed using the IMARIS imaging analysis software (see below).

NaveniFlex Proximity Ligation Assay (PLA)

The PLA assay was performed according to Navinci's recommendations using NaveniFlex MR In Situ Detection kit (Navinci, NF.100.2) and all incubations were performed in a humidity chamber. Briefly, cells were seeded on coverslips and grown until around 80% confluency. The cells were fixed using 4% PFA at 37°C for 20 min and permeabilized with 100% methanol at room temperature for 5 min. The coverslips were then washed two times in PBS, blocked with Blocking solution (Navinci, NF.1.100.01) for 30 min at 37°C and then incubated with two primary antibodies (derived from mouse

and rabbit, respectively) diluted in primary antibody diluent (Navinci, NF.1.100.02) overnight at 4°C. As a negative control one coverslip was incubated in Antibody diluent with only one primary antibody. The coverslips were washed and then incubated with the PLA probes corresponding to the primary antibodies using Navenibody M1 (Navinci, NF.1.100.004,) and Navenibody R2 (Navinci, NF.1.100.05) in Navenibody Diluent (Navinci, NF.1.100.03) for 1 h at 37°C. Then, the coverslips were washed and subsequently incubated for DNA ligation with enzyme A (Navinci, NF.2.100.09) in buffer A (Navinci, NF.2.100.08) and enzyme B (Navinci, NF.2.100.11) in buffer B (Navinci, NF.2.100.10) for 1 hour and 30 min, respectively at 37°C. The coverslips were washed and finally incubated with enzyme C (Navinci, NF.2.100.15), a DNA polymerase, diluted in amplification buffer C Atto 647N (Navinci, NF.2.100.14) for 90 min at 37°C protected from light. Finally, the coverslips were stained with DAPI, washed, and then mounted on glass slides using Prolong Glass antifade mountant media. The fluorescent PLA signal and DAPI was detected using LSM800 confocal microscope (Carl Zeiss Microscopy) equipped with a 40X NA1.2 water immersion objective. Images were acquired as 3-slice Z-stacks. A minimum of 10 positions per coverslip of fixed cells (containing over 50 cells in total) were imaged per condition in two independent experiments. Quantification of PLA puncta was performed on the images using the IMARIS image analysis software.

Western blot analysis of total H9c2 cell lysates

Cells were lysed by scraping in 2X sodium dodecyl sulfate (SDS) buffer (100 mM Tris-HCl, pH 6.8, 20% glycerol, 4% SDS) with 1× Complete Mini EDTA-Free Protease Inhibitor Cocktail (Roche, 11697498001) and boiling for 5 min. Total protein content of cell extracts was determined using a Bicinchoninic Acid (BCA) Kit (ThermoFisher Scientific, 23227). Total protein lysates (15 µg) were run on Mini-Protean TGX 4–20% gradient gels (Bio-Rad, 456–1093) and transferred onto Invitrolon[™] PVDF membranes (Invitrogen, LC2005). Transfer was visualized with Ponceau staining and the membrane was blocked with 5% nonfat dry milk in TBST (20 mM Tris pH 7.5, 150 mM NaCl, 0.1% Tween 20 [P1379, Sigma-Aldrich]). The membrane was incubated with primary antibody overnight at 4°C followed by 1 h incubation at room temperature with horseradish peroxidase (HRP)-conjugated secondary antibody; BD Pharmingen HRP Goat Anti-Mouse Ig (BD Biosciences, 554002) or HRP-conjugated Affinipure Goat Anti-Rabbit IgG (H+L) (Proteintech, SA00001–2). Signal detection was performed with a western blotting chemiluminescent reagent (Sigma-Aldrich, CPS3500) and an iBright Imaging System (ThermoFisher Scientific).

Widefield and confocal imaging of fixed cells

For imaging, Celldiscoverer7, LSM800 and LSM880 (all systems Carl Zeiss Microscopy) were used. For all images taken with the Celldiscoverer7 a Plan-Apochromat 50× objective with an NA of 1.2 was used. The images were acquired as

z-stacks. The LSM800 was used with a Plan-Apochromat 63× oil (M27) objective with an NA of 1.4 for verification of colocalization of red-only dots and mitochondrial proteins. The Plan-Apochromat 40× water objective with an NA of 1.2 was used for imaging PLA puncta, which were acquired as z-stacks. For the LSM880 the images were acquired either with a Plan-Apochromat 63× oil objective with an NA of 1.4 or a C-Apochromat 40× water objective with an NA of 1.2. The LSM880 was used for bright field and fluorescence imaging in CLEM experiments to image cells of interest and to map the relevant grid coordinate for correlation with TEM images.

Three-dimensional (3D) structured illumination microscopy (SIM) imaging of fixed and live cells cells.

The mCherry-EGFP-SYNJAB-TM H9c2 cells were seeded on MatTek dishes (MatTek Corporation, P35G-1.5-14-C) and imaged when they reached approximately 80% confluency. For labeling of lysosomes, the cells were treated with 100 nM LysoTracker Deep Red (ThermoFisher Scientific, L12492) for 40 min. After labeling, the cells were fixed with 4% formaldehyde and 0.2% glutaraldehyde or the media was replaced with fresh cell-culture media right before live imaging. The fixed cells were washed in PBS and imaged in PBS. For live cell imaging the cells were imaged in their growth medium at 37°C with atmospheric gas levels. The images were acquired using a DeltaVision OMX V4 Blaze imaging system (GE Healthcare) equipped with a 60X 1.42NA oil-immersion objective (Olympus), three sCMOS cameras, and 405, 488, 568, and 642 nm lasers for excitation. The vendor-specified optical resolution of the 3DSIM system is 110–160 nm laterally, and 340–380 nm axially, depending on the color channel. Super-resolution 3D images were obtained by 3DSIM reconstructions using the manufacturer-supplied softWoRx program (GE Healthcare). The SIM figure panels and AVI movies (maximum intensity z-projected and bleach corrected image sequenced using the exponential fit option) were assembled using Fiji [71].

Airyscan FAST imaging of live cells after lysosome labeling with LysoView 650

Live mCherry-EGFP-SYNJ2B-TM H9c2 cells grown in MatTek dishes were stained with LysoView 650 (Biotium, 70059) for 30 min and imaged using the Airyscan FAST mode of the LSM880, utilizing line-wise switching between tracks to avoid time delay between channels. Cells were maintained in a humidified stage-top incubator at 37°C and 5% CO₂ during imaging. Timelapse series (500 frames in total) were recorded using a 40× NA1.2 water immersion objective lens and a zoom factor of 4.0, with optimized scan settings for subsequent Airyscan processing (50 nm pixel size). The pixel dwell time was 0.73 μs, resulting in an individual frame time of 1.01 s. Laser excitation at 488 nm, 561 nm and 633 nm was used for EGFP, mCherry, and LysoView 650, respectively. The resulting

raw files were processed using automatic settings (strength 6.0) in ZEN ver. 2.3 (Carl Zeiss Microscopy).

Correlative-light and electron microscopy (CLEM)

Cells were grown on gridded #1.5 glass coverslips in 35-mm dishes (P35G-1.5-14-CGRD, MatTek). The cells were incubated with 50 nM LysoTracker Deep Red for 30 min before fixation with 4% formaldehyde and 0.5% glutaraldehyde in PHEM buffer, pH 6.9 (60 mM PIPES, 25 mM HEPES, 10 mM EGTA, 2 mM MgCl₂). The cells were stained with DAPI and washed twice with PBS. After confocal imaging, the cells were processed for TEM using 0.05% malachite green (Sigma-Aldrich, 101398), 1% osmium tetroxide (Electron Microscopy Sciences, 19110)/0.8% K₃Fe(CN)₆ (Sigma-Aldrich, 702587), 1% tannic acid (Electron Microscopy Sciences, 21700), and 1% uranyl acetate (Electron Microscopy Sciences, 22400), followed by stepwise ethanol dehydration and embedding in epoxy resin (Agar, R1043). All processing steps were carried out using a microwave processor (Pelco BioWave, Ted Pella, Inc.). Finally, the resin was polymerized at 60° C for 48 h. After polymerization, the relevant dish coordinates were relocated and trimmed using a glass knife on an UC6 ultramicrotome (Leica Microsystems). Ultrathin sections (70 nm) were cut using a 35° ultra-knife (Diatome) and collected on slot grids. Sections were imaged using a HT7800 transmission electron microscope (Hitachi High-Tech) at 100 kV using a Xarosa CMOS camera and Radius ver. 2.0 (EMSYS). Preliminary image correlation of confocal images and TEM images was performed at the microscope using MirrorCLEM ver. 2.0.3 (Astron, Inc.). Final correlation was performed using the ec-CLEM plugin [72] in Icy ver. 2.4.2.0 [73] using DAPI, LysoTracker Deep Red, and tubular EGFP/mCherry-positive mitochondria as registration landmarks.

Image analysis.

Fluorescence images were analyzed using Imaris ver. 9.6.1 (Bitplane). Images were converted from the .zen file format used by ZEISS microscopes into the .ims file format used by Imaris by the Imaris file converter. No preprocessing was performed. For the quantification of red-only mitochondria the Imaris XTension Channel Arithmetics was used in conjunction with an adapted Batch Processing XTension to create a new third image channel containing only areas where the mCherry signal was 50% higher than the EGFP signal. The Spots function was then

utilized to mark the mCherry signal and the DAPI-stained nuclei of all cells in the image, excluding those within 1 μm of the edge of the image. Each image was then manually inspected to remove artifacts. The Spots function was also utilized for the quantification of PLA puncta.

Machine learning classification of mitochondria morphology

Classification of mitochondria was performed on the segmentation results obtained from the deep learning-based

segmentation model that is trained on a simulated dataset [43]. The training dataset consists of thousands of images that are simulated by one, mimicking the geometrical shapes of mitochondria, and two, computationally modeling the process of image formation in a microscope. The simulated dataset is curated to closely match the microscope parameters of the data to be analyzed. The steps of segmentation began with the input confocal fluorescence images (EGFP-channel) that were cropped to sizes suitable for the deep learning-based segmentation model. The results from the segmentation model were then stitched back together to the original sizes of the images. The morphological classification of the individual mitochondria was done based on their branch lengths. For this, the segmentation results were first skeletonized using the Skan library [74] and the branch lengths of individual mitochondria were calculated for each experimental group. To prevent noisy segmentations from being included in the analysis, entries with branch lengths less than the resolution limit of the microscope were excluded. The rules for classifying mitochondria into the morphological classes of dots, rods, and networks were as follows; any mitochondria less than 1 μm in length was classified as a dot, those having lengths greater than 1 μm were further subdivided into rods, if they did not have junctions in their skeleton, and networks if they had at least one junction. The morphology classification was normalized per image frame for 19 or 22 images from each condition, glucose or galactose adapted cells respectively.

Statistical analysis

The quantification data acquired using the IMARIS software underwent statistical analysis.

For the percentage of cells that contained red-only dots we approximated the proportions with normal distributions and thereafter we performed a two-tailed Z-test. For the average number of red-only dots per cell we assumed that these averages followed normal distributions so that a two-tailed Z-test could be utilized for the large sample sizes. The same was assumed for analysis of average number of PLA puncta per cell and for the morphological analysis. For the morphological analysis the statistical analysis was performed on a per frame basis. For the mitochondrial respiration data two-tailed paired t-tests were performed. Multiple comparison correction was performed with Bonferroni correction. Datasets subjected to quantitative and statistical analysis were from a minimum of three independent experiments, each independent experiment contained minimum 100 cells per condition analyzed. The exception was the dataset for PLA puncta quantification that was derived from two independent experiments and the morphological classification which had a dataset made from a single independent experiment. The PLA dataset contained minimum 50 cells per condition analyzed for each independent experiment, while the morphological classification was based on a single qualitative dataset of approximately 20 frames with representative cells from each condition. The data in graphs is represented as the mean \pm SEM, individual datapoints are

per frame averages. Statistical significance in the form of p-value is shown as * $p < 0.05$, ** $p < 0.01$, *** $p < 0.001$ and **** $p < 0.0001$.

Acknowledgements

We thank professor Terje Johansen (University of Tromsø–The Arctic University of Norway) for access to reagents for constructing stable cell lines. We acknowledge professor Balpreet S. Ahluwalia and Dr. Deanna Wolfson (University of Tromsø–The Arctic University of Norway) for facilitating SIM imaging. We thank the Advanced Microscopy Core-Facility (University of Tromsø–The Arctic University of Norway) for use of instruments and assistance.

Disclosure statement

No potential conflict of interest was reported by the author(s).

Funding

The work was supported by the Helse Nord RHF [HNF1449-19]; Horizon 2020 Framework Programme [grant agreement No 964800]; Universitetet i Tromsø [VirtualStain; project number 2061348].

ORCID

Asa Birna Birgisdottir  <http://orcid.org/0000-0003-1080-3619>

Data availability statement

The 3D SIM data that support the findings of this study are openly available in *Opstad, IS. et al, 2021, "3DSIM data of mitochondria in the cardiomyoblast cell-line H9c2 adapted to either glucose or galactose", at <https://doi.org/10.18710/PDCLAS>, DataverseNO, V2*

References

- [1] Zorov DB, Juhaszova M, Sollott SJ. Mitochondrial reactive oxygen species (ROS) and ROS-induced ROS release. *Physiol Rev.* 2014 Jul;94(3):909–950. Pubmed PMID: 24987008. doi: [10.1152/physrev.00026.2013](https://doi.org/10.1152/physrev.00026.2013)
- [2] Pathak T, Trebak M. Mitochondrial Ca^{2+} signaling. *Pharmacol Ther.* 2018 Dec;192:112–123. Pubmed PMID: 30036491. doi: [10.1016/j.pharmthera.2018.07.001](https://doi.org/10.1016/j.pharmthera.2018.07.001)
- [3] Dietz JV, Fox JL, Khalimonchuk O. Down the Iron path: mitochondrial Iron Homeostasis and Beyond. *Cells.* 2021 Aug 25;10(9):2198. Pubmed PMID: 34571846. doi: [10.3390/cells10092198](https://doi.org/10.3390/cells10092198)
- [4] Sandhir R, Halder A, Sunkaria A. Mitochondria as a centrally positioned hub in the innate immune response. *Biochim Biophys Acta Mol Basis Dis.* 2017 May;1863(5):1090–1097. Pubmed PMID: 27794419. doi: [10.1016/j.bbadis.2016.10.020](https://doi.org/10.1016/j.bbadis.2016.10.020)
- [5] Bock FJ, Tait SWG. Mitochondria as multifaceted regulators of cell death. *Nat Rev Mol Cell Biol.* 2020 Feb;21(2):85–100. Pubmed PMID: 31636403. doi: [10.1038/s41580-019-0173-8](https://doi.org/10.1038/s41580-019-0173-8)
- [6] Youle RJ, van der Bliek AM. Mitochondrial fission, fusion, and stress. *Science.* 2012 Aug 31;337(6098):1062–1065. Pubmed PMID: 22936770. doi: [10.1126/science.1219855](https://doi.org/10.1126/science.1219855)
- [7] Kruppa AJ, Buss F. Motor proteins at the mitochondria-cytoskeleton interface. *J Cell Sci.* 2021 Apr 1;134(7):jcs226084. Pubmed PMID: 33912943. doi: [10.1242/jcs.226084](https://doi.org/10.1242/jcs.226084)
- [8] Yapa NMB, Lisnyak V, Reljic B, et al. Mitochondrial dynamics in health and disease. *FEBS Lett.* 2021 Apr;595(8):1184–1204. Pubmed PMID: 33742459. doi: [10.1002/1873-3468.14077](https://doi.org/10.1002/1873-3468.14077)
- [9] Montava-Garriga L, Ganley IG. Outstanding questions in mitophagy: what we do and do not know. *J Mol Biol.* 2020 Jan 3;432

- (1):206–230. Pubmed PMID: 31299243. doi: [10.1016/j.jmb.2019.06.032](https://doi.org/10.1016/j.jmb.2019.06.032)
- [10] Ng MYW, Wai T, Simonsen A. Quality control of the mitochondrion. *Developmental Cell*. 2021 Apr 5;56(7):881–905. Pubmed PMID: 33662258. doi: [10.1016/j.devcel.2021.02.009](https://doi.org/10.1016/j.devcel.2021.02.009)
- [11] Lemasters JJ. Selective mitochondrial autophagy, or mitophagy, as a targeted defense against oxidative stress, mitochondrial dysfunction, and aging. *Rejuvenation Res*. 2005;8(1):3–5. SpringSpring. doi: [10.1089/rej.2005.8.3](https://doi.org/10.1089/rej.2005.8.3)
- [12] Kim I, Rodriguez-Enriquez S, Lemasters JJ. Selective degradation of mitochondria by mitophagy. *Arch Biochem Biophys*. 2007 Jun 15;462(2):245–253. Pubmed PMID: 17475204. doi: [10.1016/j.abb.2007.03.034](https://doi.org/10.1016/j.abb.2007.03.034)
- [13] Youle RJ, Narendra DP. Mechanisms of mitophagy. *Nat Rev Mol Cell Biol*. 2011 Jan;12(1):9–14. Pubmed PMID: 21179058. doi: [10.1038/nrm3028](https://doi.org/10.1038/nrm3028)
- [14] Palikaras K, Lionaki E, Tavernarakis N. Mechanisms of mitophagy in cellular homeostasis, physiology and pathology. *Nat Cell Biol*. 2018 Sep;20(9):1013–1022. Pubmed PMID: 30154567. doi: [10.1038/s41556-018-0176-2](https://doi.org/10.1038/s41556-018-0176-2)
- [15] Zachari M, Ganley IG, Lane JD, et al. The mammalian ULK1 complex and autophagy initiation. *Essays Biochem*. 2017 Dec 12;61(6):585–596. Pubmed PMID: 29233870. doi: [10.1042/EBC20170021](https://doi.org/10.1042/EBC20170021)
- [16] Egan DF, Shackelford DB, Mihaylova MM, et al. Phosphorylation of ULK1 (hATG1) by AMP-activated protein kinase connects energy sensing to mitophagy. *Science*. 2011 Jan 28;331(6016):456–461. Pubmed PMID: 21205641. doi: [10.1126/science.1196371](https://doi.org/10.1126/science.1196371)
- [17] Wu W, Tian W, Hu Z, et al. ULK1 translocates to mitochondria and phosphorylates FUNDC1 to regulate mitophagy. *EMBO Rep*. 2014 May;15(5):566–575. Pubmed PMID: 24671035. doi: [10.1002/embr.201438501](https://doi.org/10.1002/embr.201438501)
- [18] Laker RC, Drake JC, Wilson RJ, et al. Ampk phosphorylation of Ulk1 is required for targeting of mitochondria to lysosomes in exercise-induced mitophagy. *Nat Commun*. 2017 Sep 15;8(1):548. Pubmed PMID: 28916822. doi: [10.1038/s41467-017-00520-9](https://doi.org/10.1038/s41467-017-00520-9)
- [19] Murakawa T, Okamoto K, Omiya S, et al. A mammalian mitophagy receptor, Bcl2-L-13, recruits the ULK1 complex to induce mitophagy. *Cell Rep*. 2019 Jan 8;26(2):338–345. Pubmed PMID: 30625316. doi: [10.1016/j.celrep.2018.12.050](https://doi.org/10.1016/j.celrep.2018.12.050)
- [20] Martens S, Fracchiolla D. Activation and targeting of ATG8 protein lipidation. *Cell Discov*. 2020 May 5;6(1):23. Pubmed PMID: 32377373. doi: [10.1038/s41421-020-0155-1](https://doi.org/10.1038/s41421-020-0155-1)
- [21] Tanida I, Mizushima N, Kiyooka M, et al. Apg7p/Cvt2p: a novel protein-activating enzyme essential for autophagy. *Mol Biol Cell*. 1999 May;10(5):1367–1379. Pubmed PMID: 10233150. doi: [10.1091/mbc.10.5.1367](https://doi.org/10.1091/mbc.10.5.1367)
- [22] Tanida I, Tanida-Miyake E, Ueno T, et al. The human homolog of *Saccharomyces cerevisiae* Apg7p is a Protein-activating enzyme for multiple substrates including human Apg12p, GATE-16, GABARAP, and MAP-LC3. *J Biol Chem*. 2001 Jan 19;276(3):1701–1706. Pubmed PMID: 11096062. doi: [10.1074/jbc.C000752200](https://doi.org/10.1074/jbc.C000752200)
- [23] Komatsu M, Tanida I, Ueno T, et al. The C-terminal region of an Apg7p/Cvt2p is required for homodimerization and is essential for its E1 activity and E1-E2 complex formation. *J Biol Chem*. 2001 Mar 30;276(13):9846–9854. Pubmed PMID: 11139573. doi: [10.1074/jbc.M007737200](https://doi.org/10.1074/jbc.M007737200)
- [24] Honda S, Arakawa S, Nishida Y, et al. Ulk1-mediated Atg5-independent macroautophagy mediates elimination of mitochondria from embryonic reticulocytes. *Nat Commun*. 2014 Jun 4;5(1):4004. Pubmed PMID: 24895007. doi: [10.1038/ncomms5004](https://doi.org/10.1038/ncomms5004)
- [25] Hirota Y, Yamashita S, Kurihara Y, et al. Mitophagy is primarily due to alternative autophagy and requires the MAPK1 and MAPK14 signaling pathways. *Autophagy*. 2015;11(2):332–343. Pubmed PMID: 25831013. doi: [10.1080/15548627.2015.1023047](https://doi.org/10.1080/15548627.2015.1023047)
- [26] Wang L, Klionsky DJ, Shen HM. The emerging mechanisms and functions of microautophagy. *Nat Rev Mol Cell Biol*. 2022 Sep 12;24(3):186–203. Pubmed PMID: 36097284. doi: [10.1038/s41580-022-00529-z](https://doi.org/10.1038/s41580-022-00529-z)
- [27] Hammerling BC, Najor RH, Cortez MQ, et al. A Rab5 endosomal pathway mediates Parkin-dependent mitochondrial clearance. *Nat Commun*. 2017 Jan 30;8(1):14050. Pubmed PMID: 28134239. doi: [10.1038/ncomms14050](https://doi.org/10.1038/ncomms14050)
- [28] Saito T, Nah J, Oka SI, et al. An alternative mitophagy pathway mediated by Rab9 protects the heart against ischemia. *J Clin Invest*. 2019 Feb 1;129(2):802–819. Pubmed PMID: 30511961. doi: [10.1172/JCI122035](https://doi.org/10.1172/JCI122035)
- [29] Wong YC, Ysselstein D, Krainc D. Mitochondria-lysosome contacts regulate mitochondrial fission via RAB7 GTP hydrolysis. *Nature*. 2018;554(7692):382–386. Feb 15 Pubmed PMID: 29364868 doi: [10.1038/nature25486](https://doi.org/10.1038/nature25486)
- [30] McWilliams TG, Muqit MM. PINK1 and Parkin: emerging themes in mitochondrial homeostasis. *Curr Opin Cell Biol*. 2017 Apr;45:83–91. Pubmed PMID: 28437683. doi: [10.1016/j.ceb.2017.03.013](https://doi.org/10.1016/j.ceb.2017.03.013)
- [31] Narendra D, Tanaka A, Suen DF, et al. Parkin is recruited selectively to impaired mitochondria and promotes their autophagy. *J Cell Bio*. 2008 Dec 1;183(5):795–803. Pubmed PMID: 19029340. doi: [10.1083/jcb.200809125](https://doi.org/10.1083/jcb.200809125)
- [32] Narendra DP, Jin SM, Tanaka A, et al. PINK1 is selectively stabilized on impaired mitochondria to activate Parkin. *PLoS Biol*. 2010 Jan 26;8(1):e1000298. Pubmed PMID: 20126261. doi: [10.1371/journal.pbio.1000298](https://doi.org/10.1371/journal.pbio.1000298)
- [33] Wang Y, Serricchio M, Jauregui M, et al. Deubiquitinating enzymes regulate PARK2-mediated mitophagy. *Autophagy*. 2015 Apr 3;11(4):595–606. Pubmed PMID: 25915564. doi: [10.1080/15548627.2015.1034408](https://doi.org/10.1080/15548627.2015.1034408)
- [34] Bhujabal Z, Birgisdottir ÅB, Sjøttem E, et al. FKBP8 recruits LC3A to mediate Parkin-independent mitophagy. *EMBO Rep*. 2017 Jun;18(6):947–961. Pubmed PMID: 28381481. doi: [10.15252/embr.201643147](https://doi.org/10.15252/embr.201643147)
- [35] Opstad IS, Godtliebsen G, Ahluwalia BS, et al. Mitochondrial dynamics and quantification of mitochondria-derived vesicles in cardiomyoblasts using structured illumination microscopy. *J Biophoto*. 2022 Feb;15(2):e202100305. Pubmed PMID: 34766731. doi: [10.1002/jbio.202100305](https://doi.org/10.1002/jbio.202100305)
- [36] Shaner NC, Steinbach PA, Tsien RY. A guide to choosing fluorescent proteins. *Nat Methods*. 2005 Dec;2(12):905–909. Pubmed PMID: 16299475. doi: [10.1038/nmeth819](https://doi.org/10.1038/nmeth819)
- [37] Dott W, Mistry P, Wright J, et al. Modulation of mitochondrial bioenergetics in a skeletal muscle cell line model of mitochondrial toxicity. *Redox Biol*. 2014. Jan 10;2:224–233. Pubmed PMID: 24494197. doi: [10.1016/j.redox.2013.12.028](https://doi.org/10.1016/j.redox.2013.12.028)
- [38] Wu H, Chen Q. Hypoxia activation of mitophagy and its role in disease pathogenesis. *Antioxid Redox Signal*. 2015 Apr 20;22(12):1032–1046. Pubmed PMID: 25526784. doi: [10.1089/ars.2014.6204](https://doi.org/10.1089/ars.2014.6204)
- [39] Katayama H, Kogure T, Mizushima N, et al. A sensitive and quantitative technique for detecting autophagic events based on lysosomal delivery. *Chem Biol*. 2011 Aug 26;18(8):1042–1052. Pubmed PMID: 21867919. doi: [10.1016/j.chembiol.2011.05.013](https://doi.org/10.1016/j.chembiol.2011.05.013)
- [40] Sun N, Malide D, Liu J, et al. A fluorescence-based imaging method to measure in vitro and in vivo mitophagy using mt-Keima. *Nat Protoc*. 2017 Aug;12(8):1576–1587. Pubmed PMID: 28703790. doi: [10.1038/nprot.2017.060](https://doi.org/10.1038/nprot.2017.060)
- [41] Twig G, Elorza A, Molina AJ, et al. Fission and selective fusion govern mitochondrial segregation and elimination by autophagy. *Embo J*. 2008 Jan 23;27(2):433–446. Pubmed PMID: 18200046. doi: [10.1038/sj.emboj.7601963](https://doi.org/10.1038/sj.emboj.7601963)
- [42] Kleele T, Rey T, Winter J, et al. Distinct fission signatures predict mitochondrial degradation or biogenesis. *Nature*. 2021 May;593(7859):435–439. Pubmed PMID: 33953403. doi: [10.1038/s41586-021-03510-6](https://doi.org/10.1038/s41586-021-03510-6)
- [43] Sekh AA, Opstad IS, Godtliebsen G, et al. Physics-based machine learning for subcellular segmentation in living cells. *Nat Mach Intell*. 2021;3(12):1071–1080. doi: [10.1038/s42256-021-00420-0](https://doi.org/10.1038/s42256-021-00420-0)

- [44] Punnakkal AR, Godtliebsen G, Somani A, et al. Analyzing mitochondrial morphology through simulation supervised learning. *J Vis Exp.* 2023 Mar 3;(193). Pubmed PMID: 36939264. doi: [10.3791/64880-v](https://doi.org/10.3791/64880-v)
- [45] Mukhopadhyay P, Rajesh M, Haskó G, et al. Simultaneous detection of apoptosis and mitochondrial superoxide production in live cells by flow cytometry and confocal microscopy. *Nat Protoc.* 2007;2(9):2295–2301. Pubmed PMID: 17853886. doi: [10.1038/nprot.2007.327](https://doi.org/10.1038/nprot.2007.327)
- [46] Marroquin LD, Hynes J, Dykens JA, et al. Circumventing the Crabtree effect: replacing media glucose with galactose increases susceptibility of HepG2 cells to mitochondrial toxicants. *Toxicol Sci.* 2007 Jun;97(2):539–547. Pubmed PMID: 17361016. doi: [10.1093/toxsci/kfm052](https://doi.org/10.1093/toxsci/kfm052)
- [47] Klionsky DJ, Abdel-Aziz AK, Abdelfatah S, et al. Guidelines for the use and interpretation of assays for monitoring autophagy (4th edition)¹. *Autophagy.* 2021 Jan;17(1):1–382. Pubmed PMID: 33634751. doi: [10.1080/15548627.2020.1797280](https://doi.org/10.1080/15548627.2020.1797280)
- [48] Collier JJ, Suomi F, Oláhová M, et al. Emerging roles of ATG7 in human health and disease. *EMBO Mol Med.* 2021 Dec 7;13(12):e14824. Pubmed PMID: 34725936. doi: [10.15252/emmm.202114824](https://doi.org/10.15252/emmm.202114824)
- [49] Zhao JF, Rodger CE, Allen GFG, et al. HIF1 α -dependent mitophagy facilitates cardiomyoblast differentiation. *Cell Stress.* 2020 Mar 4;4(5):99–113. Pubmed PMID: 32420530. doi: [10.15698/cst2020.05.220](https://doi.org/10.15698/cst2020.05.220)
- [50] Söderberg O, Gullberg M, Jarvius M, et al. Direct observation of individual endogenous protein complexes in situ by proximity ligation. *Nat Methods.* 2006 Dec;3(12):995–1000. Pubmed PMID: 17072308. doi: [10.1038/nmeth947](https://doi.org/10.1038/nmeth947)
- [51] Sun N, Yun J, Liu J, et al. Measuring in vivo mitophagy. *Molecular Cell.* 2015 Nov 19;60(4):685–696. Pubmed PMID: 26549682. doi: [10.1016/j.molcel.2015.10.009](https://doi.org/10.1016/j.molcel.2015.10.009)
- [52] McWilliams TG, Prescott AR, Allen GF, et al. Mito-QC illuminates mitophagy and mitochondrial architecture in vivo. *J Cell Bio.* 2016 Aug 1;214(3):333–345. Pubmed PMID: 27458135. doi: [10.1083/jcb.201603039](https://doi.org/10.1083/jcb.201603039)
- [53] McWilliams TG, Prescott AR, Montava-Garriga L, et al. Basal mitophagy occurs independently of PINK1 in mouse tissues of high metabolic demand. *Cell Metab.* 2018 Feb 6;27(2):439–449.e5. Pubmed PMID: 29337137. doi: [10.1016/j.cmet.2017.12.008](https://doi.org/10.1016/j.cmet.2017.12.008)
- [54] Lee JJ, Sanchez-Martinez A, Martinez Zarate A, et al. Basal mitophagy is widespread in *Drosophila* but minimally affected by loss of Pink1 or parkin. *J Cell Bio.* 2018 May 7;217(5):1613–1622. Pubmed PMID: 29500189. doi: [10.1083/jcb.201801044](https://doi.org/10.1083/jcb.201801044)
- [55] Cornelissen T, Vilain S, Vints K, et al. Deficiency of parkin and PINK1 impairs age-dependent mitophagy in *Drosophila*. *Elife.* 2018 May 29;7:e35878. Pubmed PMID: 29809156. doi: [10.7554/eLife.35878](https://doi.org/10.7554/eLife.35878)
- [56] Singh F, Prescott AR, Rosewell P, et al. Pharmacological rescue of impaired mitophagy in Parkinson's disease-related LRRK2 G2019S knock-in mice. *Elife.* 2021 Aug 3;10:e67604. Pubmed PMID: 34340748. doi: [10.7554/eLife.67604](https://doi.org/10.7554/eLife.67604)
- [57] Munson MJ, Mathai BJ, Ng MYW, et al. GAK and PRKCD are positive regulators of PRKN-independent mitophagy. *Nat Commun.* 2021 Oct 20;12(1):6101. Pubmed PMID: 34671015. doi: [10.1038/s41467-021-26331-7](https://doi.org/10.1038/s41467-021-26331-7)
- [58] Allen GF, Toth R, James J, et al. Loss of iron triggers PINK1/Parkin-independent mitophagy. *EMBO Rep.* 2013 Dec;14(12):1127–1135. Pubmed PMID: 24176932. doi: [10.1038/embor.2013.168](https://doi.org/10.1038/embor.2013.168)
- [59] Rojansky R, Cha MY, Chan DC. Elimination of paternal mitochondria in mouse embryos occurs through autophagic degradation dependent on PARKIN and MUL1. *Elife.* 2016 Nov 17;5:e17896. Pubmed PMID: 27852436. doi: [10.7554/eLife.17896](https://doi.org/10.7554/eLife.17896)
- [60] Abudu YP, Shrestha BK, Zhang W, et al. SAMM50 acts with p62 in piecemeal basal- and OXPHOS-induced mitophagy of SAM and MICOS components. *J Cell Bio.* 2021 Aug 2;220(8):e202009092. Pubmed PMID: 34037656. doi: [10.1083/jcb.202009092](https://doi.org/10.1083/jcb.202009092)
- [61] Montava-Garriga L, Singh F, Ball G, et al. Semi-automated quantitation of mitophagy in cells and tissues. *Mech Ageing Dev.* 2020 Jan;185:111196. Pubmed PMID: 31843465. doi: [10.1016/j.mad.2019.111196](https://doi.org/10.1016/j.mad.2019.111196)
- [62] Melsner S, Chatelain EH, Lavie J, et al. Rheb regulates mitophagy induced by mitochondrial energetic status. *Cell Metab.* 2013 May 7;17(5):719–730. Pubmed PMID: 23602449. doi: [10.1016/j.cmet.2013.03.014](https://doi.org/10.1016/j.cmet.2013.03.014)
- [63] Guerroué F L, Eck F, Jung J, et al. Autophagosomal content profiling reveals an LC3C-Dependent piecemeal mitophagy pathway. *Mol Cell.* 2017 Nov 16;68(4):786–796.e6. Pubmed PMID: 29149599. doi: [10.1016/j.molcel.2017.10.029](https://doi.org/10.1016/j.molcel.2017.10.029)
- [64] Van Laar VS, Arnold B, Cassidy SJ, et al. Bioenergetics of neurons inhibit the translocation response of Parkin following rapid mitochondrial depolarization. *Hum Mol Genet.* 2011 Mar 1;20(5):927–940. Pubmed PMID: 21147754. doi: [10.1093/hmg/ddq531](https://doi.org/10.1093/hmg/ddq531)
- [65] MacVicar TD, Lane JD. Impaired OMA1-dependent cleavage of OPA1 and reduced DRP1 fission activity combine to prevent mitophagy in cells that are dependent on oxidative phosphorylation. *J Cell Sci.* 2014 May 15;127(Pt 10):2313–2325. Pubmed PMID: 24634514. doi: [10.1242/jcs.144337](https://doi.org/10.1242/jcs.144337)
- [66] Lee S, Zhang C, Liu X. Role of glucose metabolism and ATP in maintaining PINK1 levels during Parkin-mediated mitochondrial damage responses. *J Biol Chem.* 2015 Jan 9;290(2):904–917. Pubmed PMID: 25404737. doi: [10.1074/jbc.M114.606798](https://doi.org/10.1074/jbc.M114.606798)
- [67] Zhen Y, Spangenberg H, Munson MJ, et al. ESCRT-mediated phagophore sealing during mitophagy. *Autophagy.* 2020 May;16(5):826–841. Pubmed PMID: 31366282. doi: [10.1080/15548627.2019.1639301](https://doi.org/10.1080/15548627.2019.1639301)
- [68] Krantz S, Kim YM, Srivastava S, et al. Mitophagy mediates metabolic reprogramming of induced pluripotent stem cells undergoing endothelial differentiation. *J Biol Chem.* 2021 Dec;297(6):101410. Pubmed PMID: 34785214. doi: [10.1016/j.jbc.2021.101410](https://doi.org/10.1016/j.jbc.2021.101410)
- [69] Jung M, Choi H, Kim J, et al. Correlative light and transmission electron microscopy showed details of mitophagy by mitochondria quality control in propionic acid treated SH-SY5Y cell. *Materials.* 2020 Sep 29;13(19):4336. Pubmed PMID: 33003589. doi: [10.3390/ma13194336](https://doi.org/10.3390/ma13194336)
- [70] Li H, Doric Z, Berthet A, et al. Longitudinal tracking of neuronal mitochondria delineates PINK1/Parkin-dependent mechanisms of mitochondrial recycling and degradation. *Sci Adv.* 2021 Aug 6;7(32):eabf6580. Pubmed PMID: 34362731. doi: [10.1126/sciadv.abf6580](https://doi.org/10.1126/sciadv.abf6580)
- [71] Schindelin J, Arganda-Carreras I, Frise E, et al. Fiji: an open-source platform for biological-image analysis. *Nat Methods.* 2012 Jun 28;9(7):676–682. Pubmed PMID: 22743772. doi: [10.1038/nmeth.2019](https://doi.org/10.1038/nmeth.2019)
- [72] Paul-Gilloteaux P, Heiligenstein X, Belle M, et al. Ec-CLEM: flexible multidimensional registration software for correlative microscopies. *Nat Methods.* 2017 Jan 31;14(2):102–103. Pubmed PMID: 28139674. doi: [10.1038/nmeth.4170](https://doi.org/10.1038/nmeth.4170)
- [73] de Chaumont F, Dallongeville S, Chenouard N, et al. Icy: an open bioimage informatics platform for extended reproducible research. *Nat Methods.* 2012 Jun 28;9(7):690–696. Pubmed PMID: 22743774. doi: [10.1038/nmeth.2075](https://doi.org/10.1038/nmeth.2075)
- [74] Nunez-Iglesias J, Blanch AJ, Looker O, et al. A new Python library to analyse skeleton images confirms malaria parasite remodelling of the red blood cell membrane skeleton. *PeerJ.* 2018 Feb 15;6:e4312. Pubmed PMID: 29472997. doi: [10.7717/peerj.4312](https://doi.org/10.7717/peerj.4312)

Supplementary Materials

High-resolution visualization and assessment of basal and OXPHOS-induced mitophagy in H9c2 cardiomyoblasts

Gustav Godtliebsen, Kenneth B. Larsen, Zambarlal Bhujabal, Ida S. Opstad, Mireia Nager, Abhinanda R. Punnakkal, Trine B. Kalstad, Randi Olsen, Trine Lund, Dilip K. Prasad, Krishna Agarwal, Truls Myrmel and Asa B. Birgisdottir*

***Corresponding author:**

Asa B. Birgisdottir, e-mail: aasa.birna.birgisdottir@uit.no

This file includes:

Figures S1-S5 with legends

Short description of Videos S1-S5

Materials and Methods description for mt-Keima mitophagy analysis

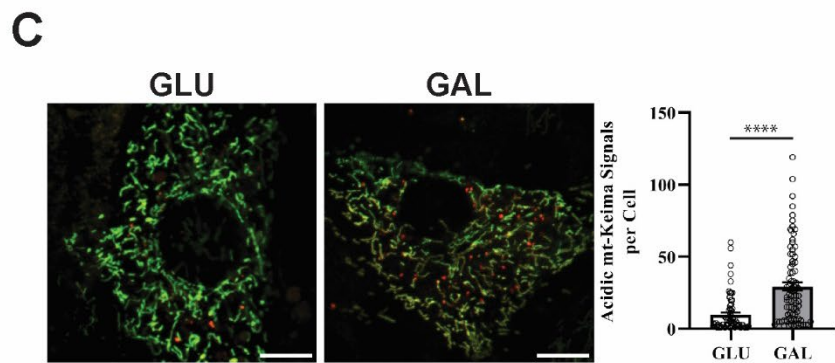
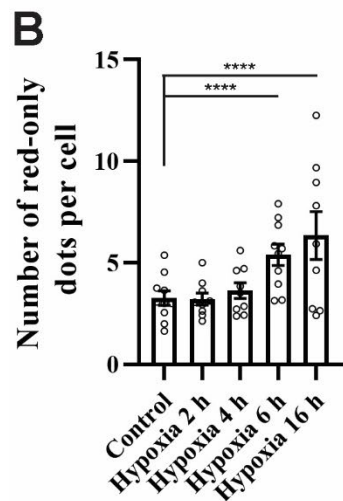
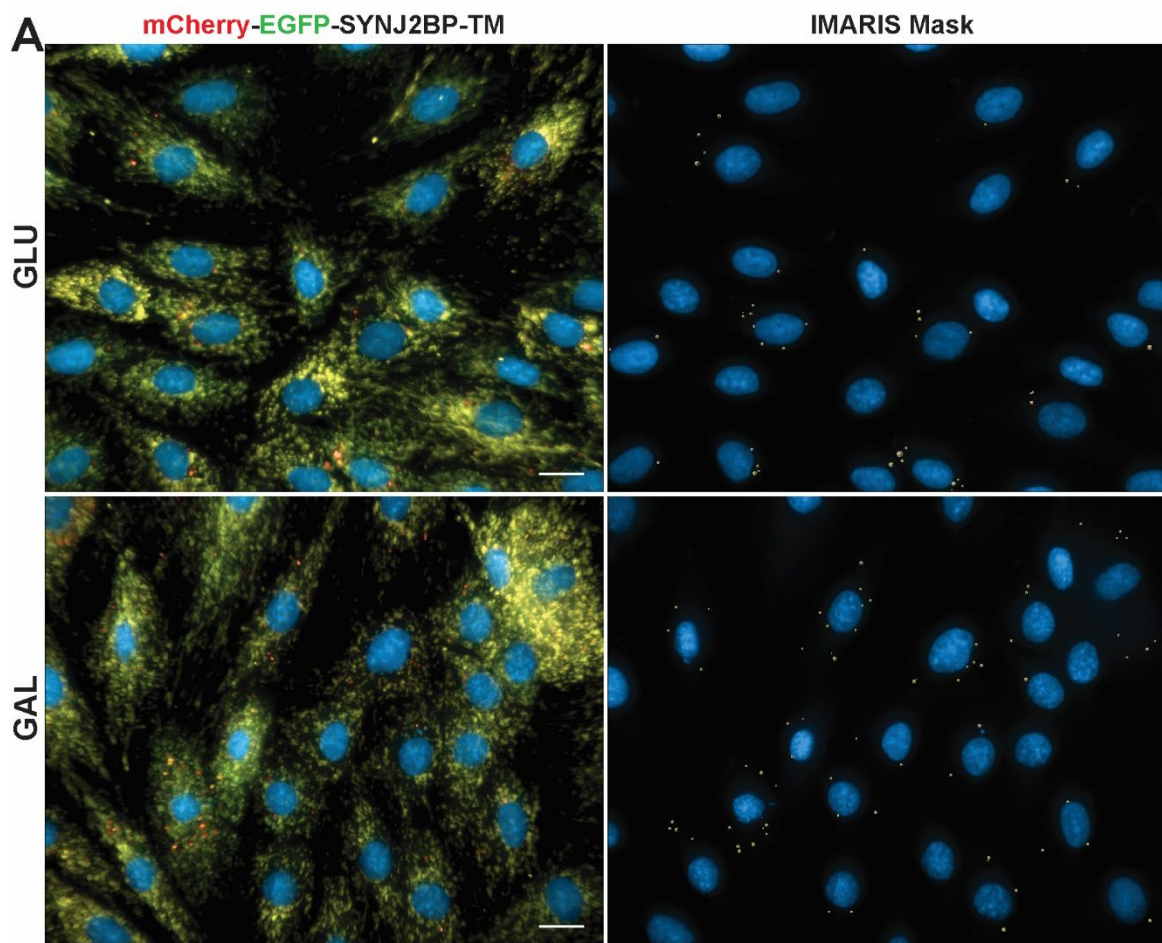


Figure S1. Detection of red-only dots applying the IMARIS image analysis software, evaluation of hypoxia time-course and mt-Keima as a model for mitophagy monitoring. (A) Representative widefield fluorescence microscopy images of H9c2 cells with a stable expression of mCherry-EGFP-SYNJ2BP-TM grown in normal glucose (GLU) conditions or adapted to galactose (GAL) media. The red-only dots identified and counted in each image

employing the IMARIS software are depicted as an IMARIS mask. Nuclear DAPI staining was used for quantification of the number of cells per image. Scale bar: 20 μm . **(B)** The mCherry-EGFP-SYNJ2BP-TM cells were incubated under hypoxic (0.3 % O_2) conditions for 2, 4, 6 or 16 h in normal media. As a control the cells were kept under normoxic conditions. Quantification of the number of red-only dots per cell in cells containing red-only dots during hypoxia. Results in graphs are shown as mean \pm SEM of 10 fields of view containing number of cell (n), $n \geq 200$, for each condition. **(C)** Representative images of mt-Keima transfected H9c2 cells in glucose media vs galactose adapted. The graph indicates the number of acidic mt-Keima signals per cell during the high glucose and galactose adapted condition. Scale bar: 10 μm . The individual datapoints are per frame averages for all graphs. * $p < 0.05$, ** $p < 0.01$, *** $p < 0.001$ and **** $p < 0.0001$.

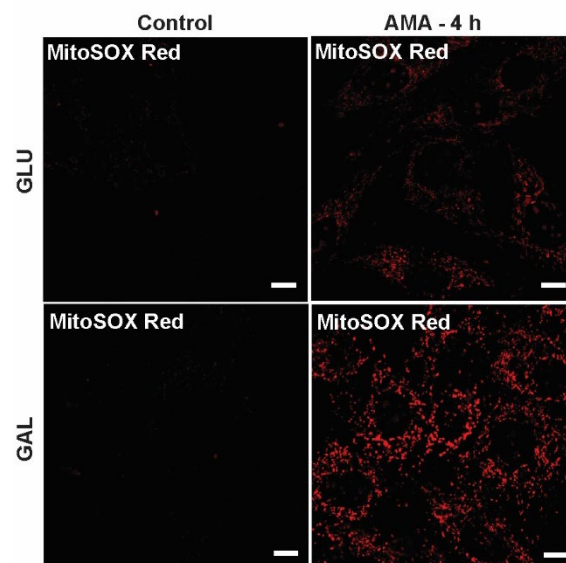


Figure S2. MitoSOX Red live cell imaging. Glucose or galactose adapted H9c2 cells were untreated or treated with 100 nM antimycin A (AMA) for 4 h, stained with MitoSOX Red and washed with HBSS. The MitoSOX superoxide indicator displayed higher intensity after AMA treatment compared to controls and was notably stronger in the galactose-adapted cells. Scale bar:10 μ m.

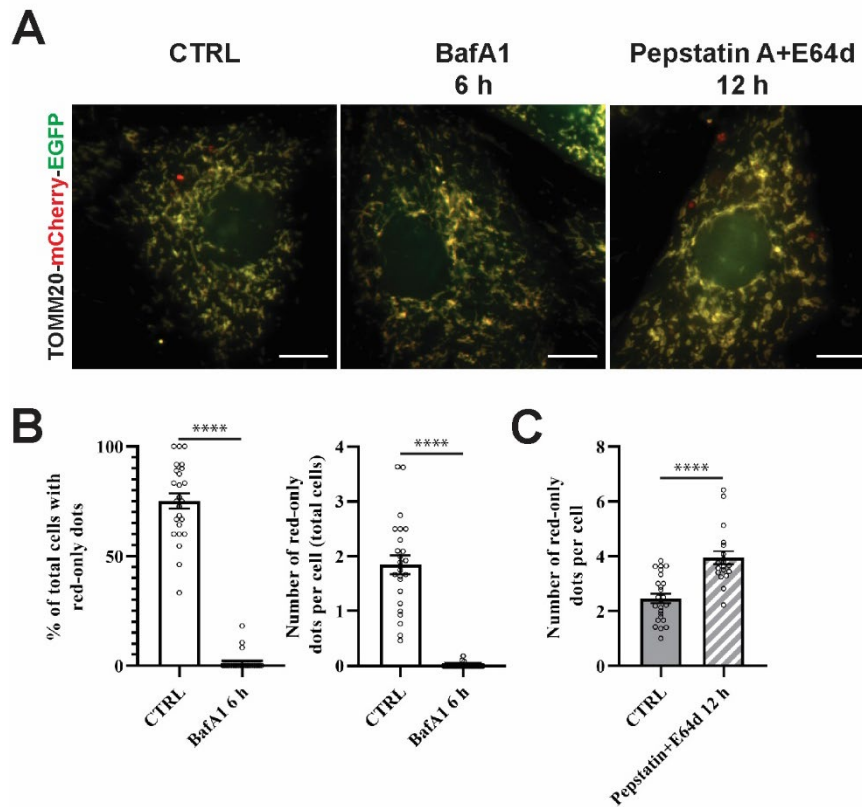


Figure S3. Evaluation of lysosomal inhibitors on the appearance and removal of red-only dots during galactose adaption. **(A)** Representative images of galactose adapted TOMM20-mCherry-EGFP H9c2 cells during control conditions and after treatment with the lysosomal inhibitors bafilomycin A₁ (BafA1, 200 nM) or pepstatin A (10 µg/ml) and E64d (10 µg/ml), respectively for the indicated times. **(B)** Quantification of the effects of a 6-h treatment of BafA1 on galactose-adapted cells with the TOMM20-mCherry-EGFP reporter by assessing the percentage of cells containing red-only dots and number of red-only dots per total cells. **(C)** Quantification of the effects of a time course treatment of pepstatin A and E64d assessed by number of red-only dots per cell in cells with red only dots in galactose adapted cells with the TOMM20-mCherry-EGFP reporter. Data presented in **(B)** and **(C)** are shown as mean ± SEM from 3 independent experiments, with more than 100 cells per condition in each experiment. The individual datapoints are per frame averages. * p<0.05, ** p<0.01, *** p<0.001 and **** p<0.0001. Scale bar: 10 µm.

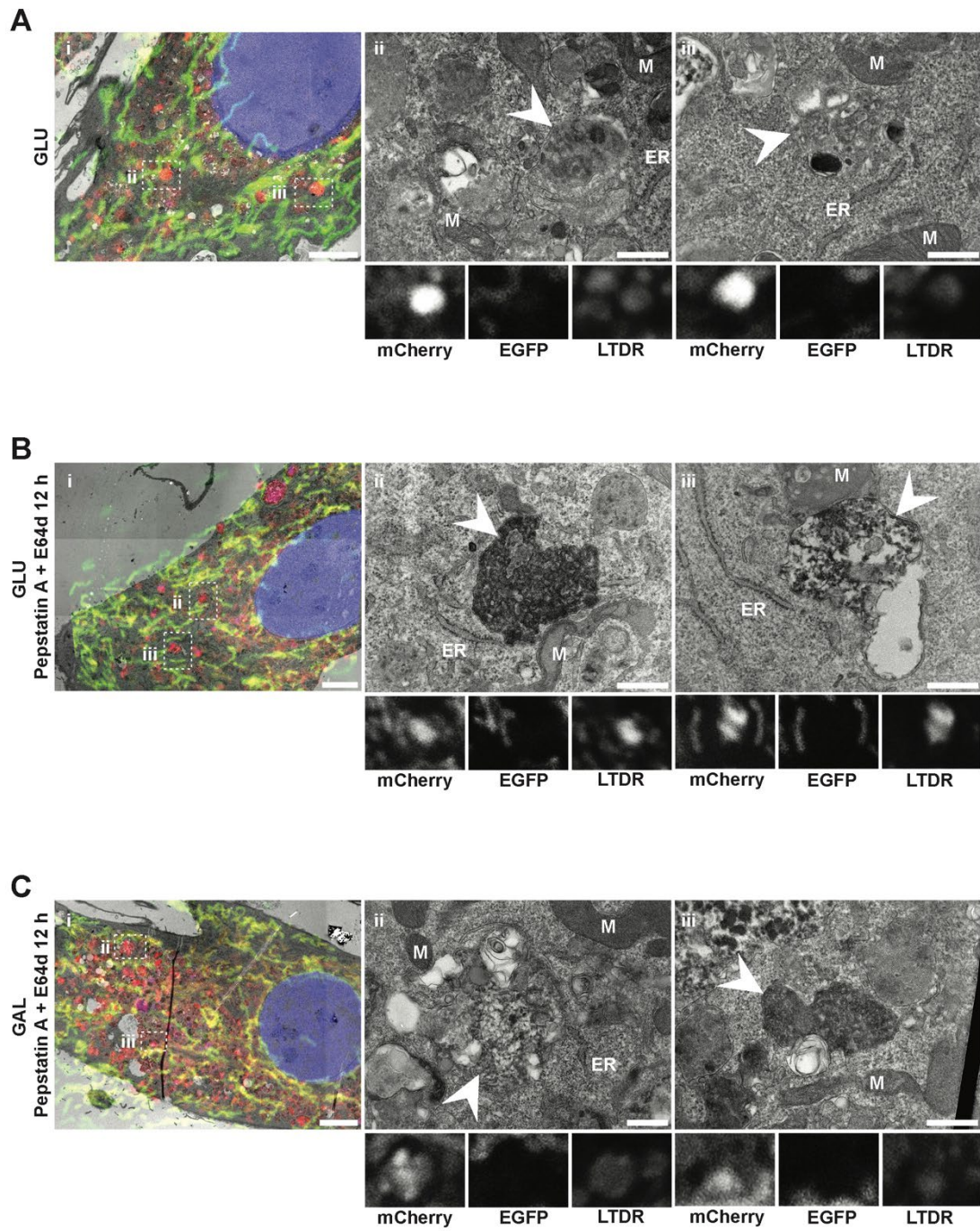


Figure S4. Correlative light and electron microscopy of mCherry-EGFP-SYNJ2BP-TM cells grown in glucose or grown in either glucose or galactose and treated with PepA and E64D. (A)

In cells grown in glucose, small red-only dots (0.5–1 μm in diameter) do not show a significant difference in ultrastructure when compared to larger red-only dots (Fig. 7A). As for their larger counterparts, small red-only dots (arrowheads in Aii and Aiii) are found in close vicinity to tubular mitochondria and ER membranes and contain a diverse mix of engulfed material. Scale bars: 5 μm (Ai) and 500 nm (Aii and Aiii). Individual fluorescence channels corresponding to the TEM fields shown in Aii and Aiii are displayed below each panel. **(B)** and **(C)** In cells treated with PepA and E64D, red-only dots (arrowheads in Bii, Biii, Cii, and Ciii) are also found in the vicinity of tubular mitochondria and ER membranes. However, we observed a clear increase in electron density and overall aggregation of engulfed material within structures corresponding to red-only dots after inhibition of lysosomal turnover. Scale bars: 5 μm (Bi and Ci) and 500 nm (Bii, Biii, Cii, and Ciii). Individual fluorescence channels corresponding to each TEM field are shown below each panel as in (A).

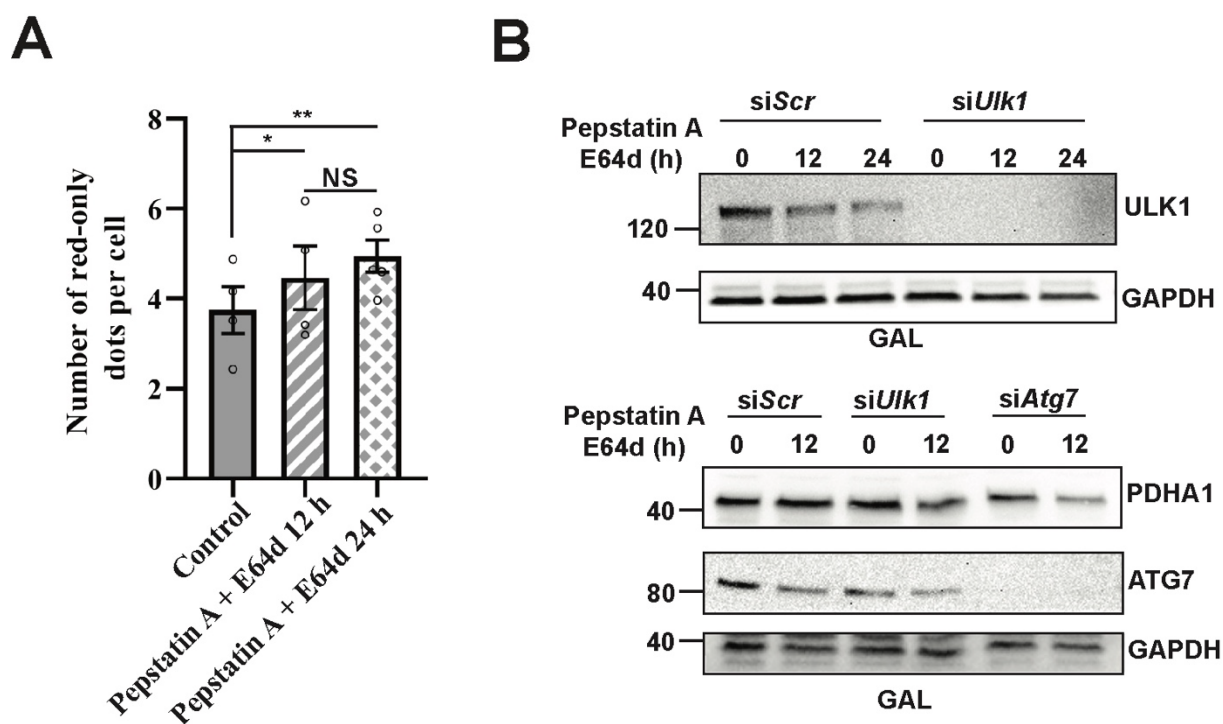


Figure S5. Assessment of extended treatments with pepstatin A and E64d for 12 and 24 h. **(A)** Quantification of the effects of a time course treatment of pepstatin A and E64d assessed by number of red-only dots per cell in cells with red only dots in galactose adapted cells with the mCherry-EGFP-SYNJ2BP-TM reporter. Over 100 cells were analyzed for each condition. The individual datapoints are per frame averages. **(B)** Western blot verification of the siRNA mediated knock down of the proteins ULK1 and ATG7, with indicated time of the pepstatin A and E64d treatment. * $p < 0.05$, ** $p < 0.01$, *** $p < 0.001$ and **** $p < 0.0001$.

Video S1. 3D SIM live cell video corresponding to the images shown in main Figure 5A (file name from data repository: 20210511_H9c2-dTag_GLU_LTDR100nm-40m_1520_sim256_10sTL_017_SIR_ALX_PRJ). Please note that the channels are colored here with mCherry as green, EGFP as blue, and LysoTracker Deep Red as red.

Video S2. 3D SIM live cell video corresponding to the images shown in main Figure 5B (file name from data repository: 20210511_H9c2-dTag_GAL_LTDR100nm-40m_1520_sim256_005_SIR_ALX_PRJ). Please note that the channels are colored here with mCherry as green, EGFP as blue, and LysoTracker Deep Red as red.

Video S3. Airyscan FAST live cell video corresponding to the images shown in main Figure 6A. mCherry (top left), EGFP (top right), and LysoView 650 (bottom left) panels are shown individually, while the merged panel (bottom right) shows mCherry and EGFP overlaid.

Video S4. Airyscan FAST live cell video corresponding to the images shown in main Figure 6B. Individual channels and the merged panel are as described for Video S3.

Video S5. Airyscan FAST live cell video corresponding to the images shown in main Figure 6C. Individual channels and the merged panel are as described for Video S3 and S4.

Supplemental Materials and Methods




Assessment of mitophagy in H9c2 cells using mt-Keima

For assessment of mitophagy with a matrix targeted pH-dependent probe, we transiently transfected H9c2 cells grown under normal conditions (high glucose) or adapted to galactose with mt-Keima plasmid mKeima-Red-Mito-7 (Addgene, 56018; Michael Davidson lab) using Neon Transfection System (ThermoFischer Scientific, MPK10096). The cells were analyzed 48 h post transfection by confocal microscopy. The fluorescence of mt-Keima was imaged in two channels via two sequential excitations (405 nm, green; 561 nm, red) and using a 570 to 695 nm emission range. Representative confocal images were processed manually. Calculation of mitophagy based on acidic mt-Keima signal was performed using the Zeiss ZEN software.

Paper II

RESEARCH ARTICLE

Mitochondrial dynamics and quantification of mitochondria-derived vesicles in cardiomyoblasts using structured illumination microscopy

Ida S. Opstad^{1*}  | Gustav Godtliebsen² | Balpreet Singh Ahluwalia^{1,3}  |
Truls Myrnes^{2,4} | Krishna Agarwal¹  | Åsa Birna Birgisdottir^{2,4} 

¹Department of Physics and Technology, UiT – The Arctic University of Norway, Tromsø, Norway

²Department of Clinical Medicine, UiT – The Arctic University of Norway, Tromsø, Norway

³Department of Clinical Science, Intervention and Technology, Karolinska Institute, Stockholm, Sweden

⁴Division of Cardiothoracic and Respiratory Medicine, University Hospital of North Norway, Tromsø, Norway

*Correspondence

Ida S. Opstad, Department of Physics and Technology, UiT – The Arctic University of Norway, Tromsø, Norway.
Email: ida.s.opstad@uit.no

Present address

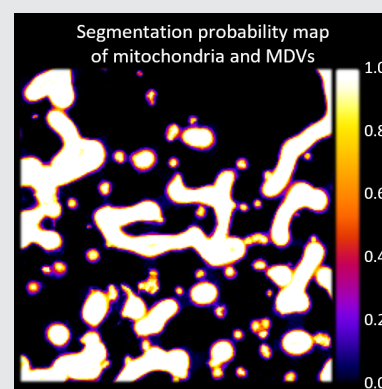
Ida S. Opstad, Balpreet Singh Ahluwalia and Krishna Agarwal, Institutt for fysikk og teknologi, UiT Norges Arktiske Universitet, Teknologibygget, Tromsø, Norway

Funding information

Helse Nord RHF, Grant/Award Number: HNF1449-19; Universitetet i Tromsø, Grant/Award Number: Tematiske satsinger (Virtual Stain)

Abstract

Mitochondria are essential energy-providing organelles of particular importance in energy-demanding tissue such as the heart. The production of mitochondria-derived vesicles (MDVs) is a cellular mechanism by which cells ensure a healthy pool of mitochondria. These vesicles are small and fast-moving objects not easily captured by imaging. In this work, we have tested the ability of the optical super-resolution technique 3DSIM to capture high-resolution images of MDVs. We optimized the imaging conditions both for high-speed video microscopy and fixed-cell imaging and analysis. From the 3DSIM videos, we observed an abundance of MDVs and many dynamic mitochondrial tubules. The density of MDVs in cells was compared for cells under normal growth conditions and cells during metabolic perturbation. Our results indicate a higher abundance of MDVs in H9c2 cells during glucose deprivation compared with cells under normal growth conditions. Furthermore, the results reveal a large untapped potential of 3DSIM in MDV research.



KEYWORDS

3DSIM, cardiomyoblasts, MDVs, mitochondria, mitochondria tubules, mitochondria-derived vesicles, three-dimensional structured illumination microscopy, Trainable Weka Segmentation

1 | INTRODUCTION

Mitochondria are the energy providing organelles in cells and produce energy in the form of adenosine

triphosphate (ATP). Mitochondria are comprised of four major compartments: the outer mitochondrial membrane, the inter-membrane space, the inner mitochondrial membrane with invaginations termed cristae and

This is an open access article under the terms of the Creative Commons Attribution License, which permits use, distribution and reproduction in any medium, provided the original work is properly cited.

© 2021 The Authors. *Journal of Biophotonics* published by Wiley-VCH GmbH.

the matrix. In most cell types, mitochondria are arranged in highly dynamic networks controlled by frequent mitochondrial fusion and fission (division) events driven by mitochondria movements on the cytoskeleton [1]. Damaged mitochondria result in energy-generation defects, increased production of harmful reactive oxygen species (ROS) and show a greater tendency to trigger programmed cell death [2]. Hence, in order to ensure a healthy pool of mitochondria, cells employ different mitochondria quality control mechanisms [3] to maintain normal cell function.

Mitochondria-derived vesicles (MDVs) act in mitochondria quality control. These are small (70–150 nm in diameter), single or double-membrane vesicles that arise through budding from the mitochondria and are induced under stress conditions [4]. MDV populations have previously been defined and classified as translocase of the outer mitochondria membrane 20 (TOMM 20, outer membrane) positive or pyruvate dehydrogenase (PDH, matrix protein) positive [4]. However, several other mitochondria resident proteins (matrix or inner membrane-associated) have been identified on MDVs [5–7] indicating their heterogeneous nature.

The MDVs' size and dynamic nature pose a challenge for conducting imaging studies (particularly for live imaging) of their formation and trafficking. Elucidation of their significance for mitochondria homeostasis as well as cell function in general is important, especially in high-energy demanding cardiac cells.

Previously, the formation and dynamics of TOMM 20 positive MDVs in Vero cells were observed at a rate of 10 frames per second using an ultrafast spinning disk super-resolution microscope developed as a high-speed alternative to SIM [8]. However, the high speed comes at a cost of compromised optical sectioning ability and poorer signal-to-noise ratio (SNR). Furthermore, no quantification of the vesicles was conducted in this work.

The acquisition of images at high enough resolution and contrast to allow MDVs to be visualizable by eye is a significant challenge, but not the only hurdle in gathering knowledge about MDVs. Other significant challenges are the appropriate labeling for super-resolution microscopy (e.g., bright, photostable and specific fluorescent markers) and the quantification of these small and (in living cells) dynamic structures. Using traditional hard thresholding methods for MDV quantification is challenging because of the vesicles' low signal compared with the noise level and the presence of image reconstruction artifacts.

In this work, we investigated the capabilities of three-dimensional structured illumination microscopy (3DSIM) for visualizing and quantifying MDVs in live and fixed H9c2 cardiomyoblasts with a stable expression of a

fluorescent transmembrane domain of the outer mitochondria membrane protein 25 (OMP25) [9]. The technique requires the acquisition of 120 modulated images per 1 μm image volume per color channel and, hence, is not as fast as spinning disk microscopy, but benefits from three-dimensional resolution doubling compared with conventional microscopy. Using 3DSIM, we optimized the acquisition conditions for high-speed and up to 100 time-points super-resolution volumetric imaging. To quantify and compare the number of fluorescently-tagged OMP25 MDVs produced under normal (GLU) and glucose-deprived (galactose adapted, GAL) growth conditions, we applied Trainable Weka Segmentation (TWS). Replacing glucose in the growth media with galactose forces cells in culture to become more oxidative and has been shown to facilitate stress-induced MDV production [10, 11].

2 | METHODS

2.1 | Cell-culture and sample preparation

The rat cardiomyoblast cell-line H9c2 (cells derived from embryonic heart tissue; Sigma Aldrich) was genetically modified using a retrovirus to achieve a stable expression of tandem tagged (mCherry-EGFP) mitochondrial outer membrane protein 25 (OMP25)-transmembrane domain (TM). A uniform expression of fluorescence intensity in the cells was achieved through flow cytometry sorting. The stable H9c2 cells were cultured in high glucose (4.5 g/L) Dulbecco's Modified Eagle Medium (DMEM; [D5796, Sigma-Aldrich]) with 10% FBS, 1% streptomycin/penicillin and 1 $\mu\text{g}/\text{mL}$ of puromycin (InvivoGen). For glucose deprivation and adaptation to galactose, the cells were grown in DMEM without glucose (11966-025, Gibco) supplemented with 2 mM L-glutamine, 1 mM sodium pyruvate, 10 mM galactose, 10% FBS, 1% streptomycin/penicillin and 1 $\mu\text{g}/\text{mL}$ of puromycin (InvivoGen). The cells were adapted to galactose for a minimum of 7 days before experiments. The cells were seeded on MatTek dishes (P35G-1.5-14-C, MatTek Corporation) and imaged when they reached approximately 80% confluency.

2.1.1 | Cell fixation

The cells were fixed using either 4% paraformaldehyde (PFA) or 4% PFA + 0.2% glutaraldehyde (GA) in phosphate-buffered saline (PBS, preheated to 37°C) for 30 minutes at room temperature. The samples were then washed and re-immersed in PBS before imaging.

2.1.2 | Imaging conditions

The living cells were imaged in their usual growth media at 37°C with atmospheric gas levels. The fixed samples were imaged at either room temperature or 37°C.

2.2 | Microscope

The images were acquired using a DeltaVision OMX V4 Blaze imaging system (GE Healthcare) equipped with a $\times 60$ 1.42 NA oil-immersion objective (Olympus), three sCMOS cameras and 405, 488, 568 and 642 nm lasers for excitation. The vendor-specified optical resolution of the 3DSIM system is 110–160 nm laterally and 340–380 nm axially, depending on color channel. To surpass the diffraction limit, this SIM set-up uses sinusoidal illumination patterns and acquires 120 images per 1 μm z-stack thickness (three illumination angles times five phase shifts times 8 planes/ μm thickness) per color channel. Super-resolution 3DSIM images are then obtained via image processing using the manufacturer-supplied SoftWoRx program.

2.2.1 | Optimization of imaging speed and differences between fixed cell and live-cell image data

To maximize the system imaging speed for as accurate as possible detection of fast-moving MDVs in living cells, the following differences were implemented compared with for fixed cell imaging:

The camera mode was changed from “Medium” low-noise sCMOS readout rate (95 MHz, rolling shutter) to “Fast” readout (286 MHz, global shutter), increasing the camera read noise by about 33% (from 1.5 e to 2 e), while reducing possible motion-induced image artifacts (presuming a larger effect for fast-moving objects).

The camera read area was reduced to 1/4 from the normal for SIM field-of-view (FOV, used for the fixed samples) of 512×512 pixels ($41 \times 41 \mu\text{m}^2$) to 256×256 pixels ($20.5 \times 20.5 \mu\text{m}^2$)

The selection of image volume was done sparingly with careful selection of the lower and upper cell boundaries. For the live imaging (with smaller FOVs), volumes avoiding the thicker cell area close to the nucleus allowed for a higher volumetric frame rate without losing significant parts of the mitochondria and MDVs moving axially during video acquisition. This reduced the stack size (and acquisition time) up to three times, from about 3 μm to 1–2 μm . Stack sizes down to 1.0 μm were acquired, but

here in some cases, mitochondria appear to move out of the acquired volume axially, indicating a too sparingly chosen image volume. For the larger images used for the fixed-cells, the cell nuclear region was included, resulting in stack sizes of instead 3–3.5 μm to cover the entire cell volume of the captured area.

The camera exposure time was changed by a factor of four, from 20 ms (fixed samples) to 5 ms for the live samples (both with 10% transmission of 0.10 W lasers, not including the loss in the optical path of at least 50%). This was the shortest exposure time that could be used without too severely compromising the SIM reconstruction quality or at a significantly increased rate of photobleaching (especially relevant for time-lapse studies).

Under these conditions (employed for the data of Figure 1), the live acquisition of a 2.0 μm thick volume (single channel) took 1.50 s. Volumes of 1.0 μm thickness took down to 1.16 s. In comparison, the fixed cell 3DSIM images (512×512 pixels and 3.0 μm thickness) had an acquisition time of 12.0 s. Taken together, *the 3DSIM image acquisition time was reduced up to 10 times* compared with the fixed cell (and normally employed) acquisition parameters.

2.3 | Image processing

2.3.1 | Image reconstruction and channel registration

Image deconvolution and 3DSIM reconstructions were completed using the manufacturer-supplied SoftWoRx program (GE Healthcare). Image registration (color channel alignment) was also performed in the same program using experimentally measured calibration values compensating for minor lateral and axial shifts, rotation and magnification differences between cameras. The pixel area of the 3DSIM images is 1/4 of the acquired raw data ($40 \text{ nm} \times 40 \text{ nm}$ after SIM reconstruction vs. $80 \text{ nm} \times 80 \text{ nm}$ for raw data). The processed 3D images were then maximum intensity z-projected as a final step.

2.3.2 | Image analysis and processing

Image analysis and processing beyond the preprocessing described above was done using Fiji/ImageJ [12]. The mitochondria vesicle segmentation and quantification were done with help of TWS, a machine learning tool for pixel classification in microscopy images [13].

The TWS training was conducted for two manually annotated classes (background and mitochondria) using

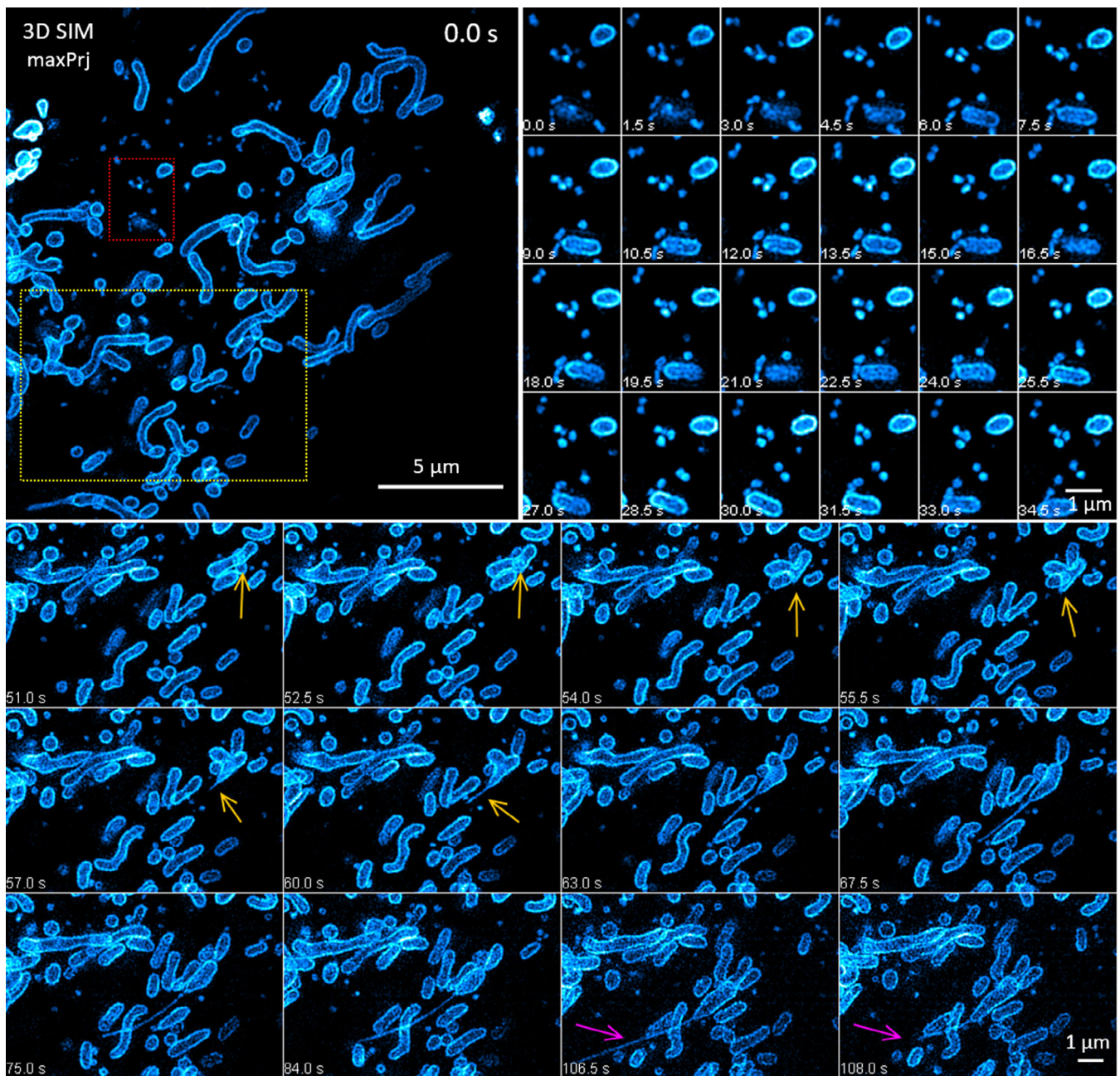


FIGURE 1 Fast 3DSIM time-lapse of MDVs and dynamic mitochondrial tubules in H9c2 cells (outer mitochondrial membrane, EGFP) cultivated in galactose medium. A part of the vesicle dynamics denoted by the small red box is shown on the left. Here, the vesicles in the upper left part of the panels are seen to interact dynamically with each other, while the vesicles and nanorods toward the bottom of the frames are interacting with a much larger mitochondrion (0–25.5 s). In the bottom row panels, the MDVs appear to both fuse and bud-off from the lower mitochondrion (27–34.5 s). The yellow box is shown in the bottom montage for selected subsequent time-points. The yellow arrows show the formation of a tubule, while the magenta arrows indicate the rapid retraction (several micrometers in 1.5 s) of the same tubule about 10 s later. The shown time-sequence has been intensity corrected for photobleaching (exponential fit). The full time-lapse is available as Movie S1

FastRandomForest and all other default options. The supervised training of the classifier was done using one maximum intensity projected 3DSIM image of fixed (4% PFA + 0.2% GA) cells from the GAL conditions with both clearly visible MDVs and SIM reconstruction

artifacts (the annotation was done by a SIM expert). SIM artifacts were added to the background class of the training set to avoid these intensity patterns to be classified as mitochondria (or MDVs). The classifier was then applied to both the live and fixed samples from both pools (GAL

and GLU). Probability maps were generated and the segmentation threshold was chosen at 0.80 after manual inspection and comparison with the raw data of both live and fixed samples.

A couple of outliers where the learned classifier did not achieve satisfactory results were removed from the dataset before quantification. These are shown and discussed in Figure S1.

3 | RESULTS AND DISCUSSION

3.1 | 3DSIM of MDVs and dynamic mitochondrial tubules

The optimized acquisition conditions for high-speed and lowest possible laser illumination intensity—while still achieving good 3DSIM reconstruction—enabled capturing videos of the delicate and fast-moving OMP25-TM positive MDVs in H9c2 cells at volumetric super-resolution for up to 100 time-points. A part of such a time-lapse is shown in Figure 1, with the large top panel showing an overview of the volumetric super-resolution image. The full time-lapse (maximum intensity z-projected 3DSIM images) is provided in Movie S1. The highest volumetric imaging speed achieved was 1.5 s for image volumes of $20.5 \times 20.5 \times 2.0 \mu\text{m}^3$. Higher imaging speeds could be achieved for even smaller volumes, but then greatly reducing the likelihood of capturing interesting biological events in a subcellular context.

In addition to an abundance of MDVs, several rapidly extending and retracting tubules derived from the mitochondrial outer membrane were observed in cells cultivated under both GLU and GAL conditions. An example of a rapidly extending and retracting tubule over a time span of about a minute is shown and indicated by arrows in the lower part of Figure 1. At its longest, this tubule extended to about $5 \mu\text{m}$ away from the mitochondrion from which it formed, and with a width of about 120 nm (FWHM of the tubule in the maxPrj 3DSIM image), corresponding to the lateral SIM resolution (GFP channel). The actual width of the tubule could be much narrower, but that is not measurable using this imaging technique. For the retracting tubule pointed out by the arrow in magenta color (106.5–108 s), the retraction appears to be occurring at a speed of several micrometers per second.

Such dynamic mitochondrial tubulation has previously been detected by SIM imaging in normal rat kidney cells (NRK) as well as in several other cell lines [14]. Recently, dynamic mitochondrial tubules were studied in COS-7 cell-line where they were shown to mediate transportation of mitochondrial DNA between different mitochondria [15]. However, mitochondrial tubulation has

previously not been demonstrated in H9c2 cardiomyoblasts. Interestingly, mitochondrial tubules have similarities to nanotunnels formed between mitochondria in cardiomyocytes [16]. In Movies S2 and (magnified view) S3, some of the tubules fuse with other mitochondria to form a temporary membrane bridge between two different mitochondria. A tubule can then subsequently detach from the originating mitochondria and remain attached to the recipient mitochondria. Interestingly, also the budding of a fragment was detected from a retracting tubule. A magnified view of this phenomenon is provided in Movie S4. Our measurements of the speed of these tubules are within the range of velocities measured for the tubules in COS-7 cells [17].

Next, we present a simple but effective semi-automatic analysis pipeline to quantify and compare the number of MDVs in cultured H9c2 cells under different conditions.

3.2 | Quantification of vesicles in live and fixed cells

Two different strategies were employed to quantify and compare the number of MDVs between H9c2 cells cultivated under either GLU or GAL conditions: Either live-cell imaging using small imaging volumes ($840.5 \mu\text{m}^3$) or fixed-cell conditions using six times larger volumes ($5043 \mu\text{m}^3$). The two different strategies entail different advantages and limitations. For the live-cell imaging strategy, we ensure that no vesicles are lost or destroyed during fixation. On the other hand, due to the unwanted effect of motion artifacts in the SIM images, only small volumes were acquired, reducing throughput for statistical inferences. For the fixed-cell case, we risk no motion-related artifacts such that larger volumes and better statistics (per imaging time) can be inferred. Also, the nature of fixed samples allows for an easier comparison of different conditions without risking effects from possible time delays between and during imaging experiments. On the downside, the process of fixation can alter the biology we wish to study, and it can be hard to assess how this compares to the live-cell condition.

Two different protocols for chemical preservation of the cells were tested: either fixation using 4% PFA in PBS or 4% PFA + 0.2% GA in PBS. The results are shown in Figure 2, where a comparison with mitochondria in living cells is used as reference (Figure 1A). As shown in Figure 2B, using PFA only for fixation led to unsatisfactory preservation of the mitochondrial morphology at SIM resolution. Trying to segment MDVs from these images led to a high portion of false positives, where fragmented mitochondria—seemingly part of a continuous

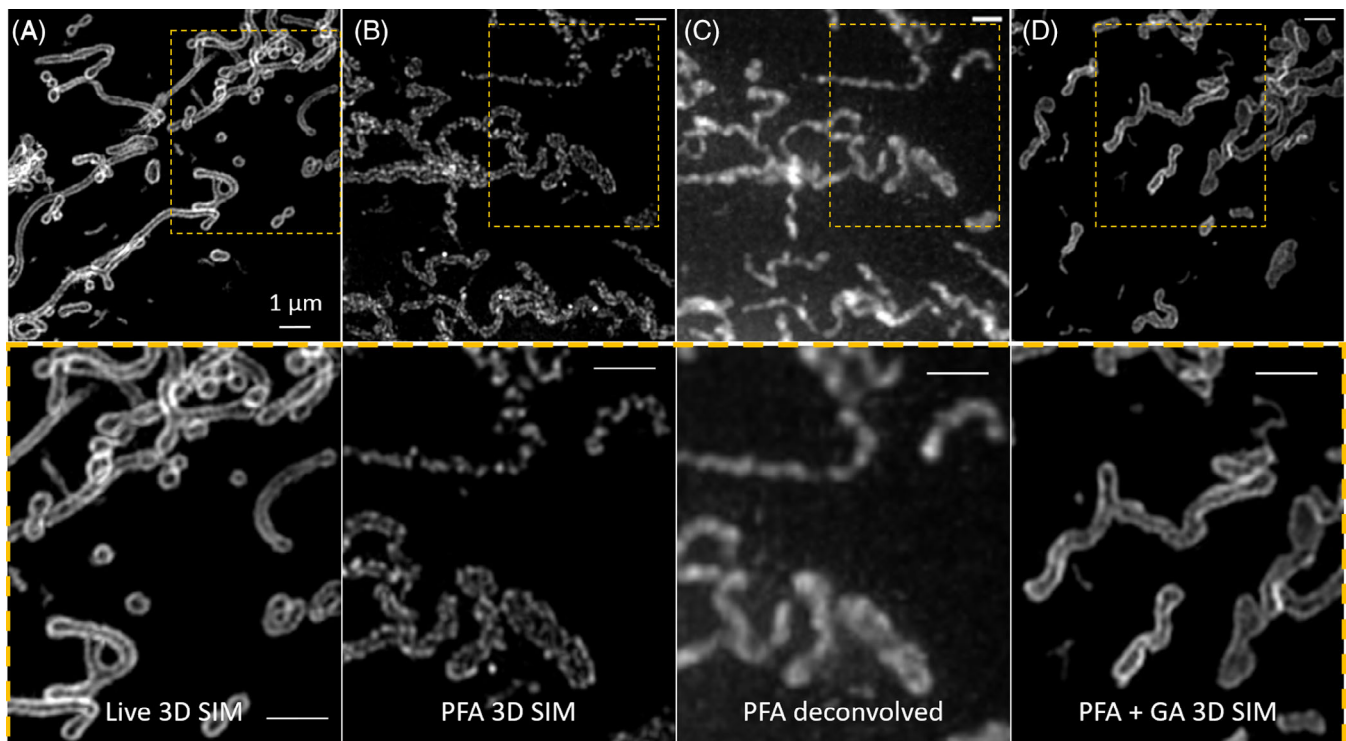


FIGURE 2 Comparison of live and fixed mitochondrial morphologies. The regions indicated in the upper panels A–D are displayed magnified below. Fixation using paraformaldehyde (PFA) only (panels B and C) causes fragmentation and disruption of the mitochondrial network as observed for living samples (panel A) hindering reliable MDV quantification. This effect is difficult to notice at conventional resolution (deconvolved image, panel C). Applying a fixation solution additionally containing glutaraldehyde (GA) preserves the live mitochondrial morphology much better and can be used for quantifying MDVs in fixed samples (panel D). The images are maxPrj 3DSIM images of H9c2 cells from the normal cultivation condition (GLU). Scale bars: 1 μm

structure before chemical fixation—would be counted as many additional MDVs not actually present. At conventional optical resolution (like the deconvolved image example in Figure 2C), this effect is much harder to notice and may be unimportant for some types of quantification of mitochondria. However, the analysis of MDVs—which are smaller than the resolution limit—requires the use of super-resolution techniques like 3DSIM for accurate quantification, together with a more potent fixation method than PFA alone. Preservation using both PFA and GA (Figure 2D) gave satisfactory results, resembling the live-cell imaging results even at SIM resolution (compare panels A and D of Figure 2) and showing MDVs unlikely to appear from fixation-induced mitochondrial fragmentation. A different challenge concerning GA fixed samples is the added background signal from GA autofluorescence. We noted additional artifacts in the SIM images likely resulting from this origin.

To overcome the challenges of MDV quantification in the presence of both SIM reconstruction artifacts (often of similar size and intensity level as the MDVs) and comparatively large and bright mitochondria, we employed TWS for MDV segmentation prior to quantification.

The pixelwise TWS classifier was trained using supervised learning on two classes: Background and Mitochondria. The annotated regions used for training the classifier together with the rest of the particle quantification workflow are shown in Figure 3.

To reduce the impact of SIM artifacts, lower axial resolution and to facilitate the assessment of classifier performance, only maxPrj 3DSIM images were used both for training and MDV quantification. The main loss of information from this simplification is that the MDVs located directly above or below the mitochondria are not counted. Since the images are 10–20 times larger laterally than axially, and the volume thickness only constitute about five resolution units laterally (for 2 μm stacks) versus 170 resolution units in either lateral dimension (for 20.2 μm images), we considered this a valid simplification only improving the accuracy of the particular analysis.

The training conducted on a fixed GLU cell (with visible SIM artifacts relegated to the background class) showed good transfer learning to both GAL and live-cell images (of smaller size). The manually assessed segmentation results were found satisfactory for all except two cases (discarded from the MDV quantification) of the

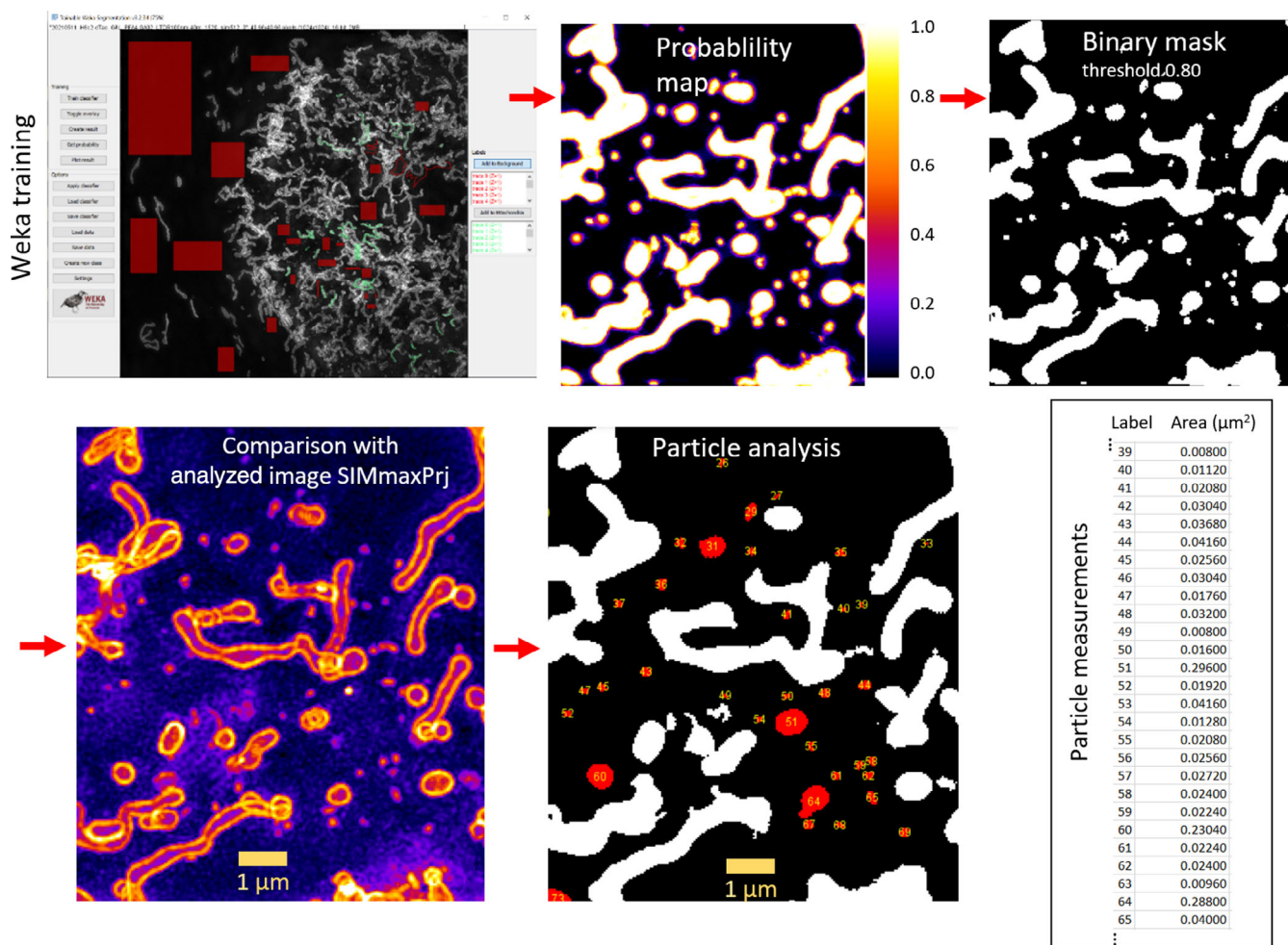


FIGURE 3 Segmentation of mitochondria for MDV quantification was done in ImageJ/Fiji using TWS. First, a maximum intensity z-projected (maxPrj) 3DSIM image was annotated with regions from the two classes *background* (including SIM artifacts) and *mitochondria*. Then the classifier was trained and applied to the remaining data of both live and fixed cells from both the GAL and GLU growth conditions. A probability map was chosen as output and a threshold of 0.80 was chosen as a binary mask for the mitochondria class. This was chosen after visual inspection and comparison with the SIM images to yield a satisfactory segmentation. The MDVs were measured from the binary images using Analyze Particles in ImageJ, excluding particles with a circularity <0.7 or not falling within the area range 0.0032 to $0.30 \mu\text{m}^2$

TABLE 1 The number of MDVs measured per image, area and volume for GLU and GAL samples under both fixed and live imaging conditions

Sample condition	GLU		GAL	
	Live	Fixed	Live	Fixed
MDV/image	60 ± 26	127 ± 48	70 ± 31	223 ± 59
MDV/ μm^2	0.14	0.076	0.17	0.13
MDV/ μm^3	0.071	0.025	0.083	0.044

fixed-cell images that appeared particularly challenging due to two reasons:

1. Two different cells with distinct mitochondria morphology and brightness in the same image.
2. Dominating SIM reconstruction artifacts obscuring the actual cellular details.

Both of these fail cases are displayed in Figure S1.

The MDV quantification results are summarized in Table 1. Both the live- and fixed-cell imaging strategies yielded a higher vesicle number for cells under the GAL condition than under the GLU condition.

Quantification of MDVs in H9c2 cells has previously been conducted using confocal images of fixed cells with

immunofluorescent staining of TOMM20 and PDH mitochondria markers after galactose adaptation [11] or during normal (glucose) growth conditions [18]. The numbers of MDVs per cell obtained in these studies (10–30 MDVs per cell) are significantly lower than the numbers obtained here (the numbers per image cover less than one cell). Furthermore, a comparison of the number of MDVs in H9c2 cells under these different growth conditions was not investigated earlier.

The high standard deviations in Table 1 indicate that the particular state of individual cells also has a large impact on the number of MDVs, beyond growth conditions. Although the fixed images are of six times larger volumes (four times larger area), the number of MDVs was only 2.1 and 3.2 times higher (for GAL and GLU, respectively). The reason for this is can be a combination of several factors:

1. The inclusion of sparser parts of the samples with few or no MDVs, that is, especially the nuclear region and volumes completely outside of the cells.
2. The effect of z-projection is larger in the case of fixed samples as larger z-stacks were used for these. In effect, a larger portion of the vesicles could be invisible straight above or below brighter mitochondria.
3. Vesicles could be lost or destroyed during fixation and the subsequent sample washing steps.

Especially when considering volumetric cell densities of MDVs, the smaller image volumes (with carefully chosen volumetric boundaries) are likely to provide a more accurate estimate of the actual vesicle density inside cells, as the non-cell containing sample parts can be more accurately excluded. The cell boundaries could alternatively be determined with help of a membrane marker. However, due to the added cellular stress, experimental and analytical complexity associated with this membrane labeling, we instead used the distribution of mitochondria as a rough guide for cell boundaries.

4 | CONCLUSIONS

We have in this work explored the capability of 3DSIM for the challenging study of MDVs in living and fixed H9c2 cardiomyoblasts with a stable expression of a fluorescent mitochondria marker. The optimized high-speed imaging conditions enabled following mitochondria and MDVs at volumetric super-resolution for up to 80 time-points, each $20.5 \times 20.5 \times 2 \mu\text{m}^3$ volume with about 1.5 s acquisition time. In addition to a large number of MDVs, a multitude of rapidly extending and retracting mitochondrial tubules were observed for cells cultivated

under both normal and galactose-adapted conditions. Interestingly, these nanotubules could be involved in the formation of MDVs.

Two different cell fixation approaches of the mitochondria for the purpose of MDV quantification were tested: 4% PFA and 4% PFA + 0.2% GA. Only the latter one was found suitable for the quantification of MDVs, as the PFA-only fixation led to the fragmentation of mitochondria and a misleadingly high number of MDVs.

Segmentation using the TWS machine learning tool provided satisfactory segmentation of mitochondria for the quantification of MDVs when the images contained mitochondria of single cells—and not of mitochondria of vastly different morphology and brightness as often the case in different adjacent cells—and for moderate SIM reconstruction artifacts. The SIM artifacts were largely successfully trained to be classified as part of the background class.

MDVs were quantified from TWS segmented images for both live and fixed conditions and their abundance was compared in normal and galactose-adapted cultivation conditions. Although varying largely within each group, the number of MDVs was on average found to be larger for the galactose-adapted condition than for the normal glucose-containing growth condition. This has previously not been demonstrated for H9c2 cells. Notably, COS-7 cell-line adapted to galactose did not display an increase in the number of MDVs compared with cells in glucose when exploiting confocal images of fixed and immunolabeled cells for MDV quantification [10]. The use of H9c2 cells with stable expression of a fluorescent mitochondria outer membrane marker and the application of super-resolution imaging display the advantage of our approach for both more accurate MDV detection and quantification.

Future work will involve MDV quantification of larger SIM image datasets from different growth conditions. In addition, analyzing the dynamics of MDVs will enable us to better assess their origin, fate, overall cellular function and, ultimately, their importance for the cardiovascular system [19].

ACKNOWLEDGMENTS

The assistance provided by Dr Zambarlal Bhujabal with creating the stable double-tag cell-line was greatly appreciated. Funding was provided by the Helse Nord RHF (Helse Nord RHF; grant number HNF1449-19) and UiT-The Arctic University of Norway “Tematiske satsinger” (VirtualStain; project number 2061348).

CONFLICT OF INTEREST

The authors declare no conflicts of interest.

AUTHOR CONTRIBUTIONS

Åsa Birna Birgisdottir: Conceived the idea, provided expertise on cardiac cell biology, prepared a manuscript draft and conducted extensive review of relevant literature. **Ida S. Opstad:** Conducted the imaging experiments, data analysis, prepared a manuscript draft, image data archiving and prepared the figures and videos. **Gustav Godtlielsen:** Constructed the stable double-tag cell-line, cultivated the cells and advised on H9c2 sample preparation for microscopy. **Truls Myrmel:** Provided funding which enabled the project and experiments. **Krishna Agarwal:** Provided funding which enabled the project and experiments. **Balpreet Singh Ahluwalia:** Provided funding which enabled the project and experiments. All authors reviewed and commented on the manuscript.

DATA AVAILABILITY STATEMENT

The data that support the findings of this study are available from the UiT Open Research Data repository [19]. All image data (not only for the images shown) from these sets of experiments are provided as a community resource for, e.g., the further development of 3DSIM reconstruction algorithms, machine learning tools for bio-image analysis, and mitochondria research.

ORCID

Ida S. Opstad  <https://orcid.org/0000-0003-4462-4600>

Balpreet Singh Ahluwalia  <https://orcid.org/0000-0001-7841-6952>

Krishna Agarwal  <https://orcid.org/0000-0001-6968-578X>

Åsa Birna Birgisdottir  <https://orcid.org/0000-0003-1080-3619>

REFERENCES

- [1] H.-M. Ni, J. A. Williams, W.-X. Ding, *Redox Biol.* **2015**, *4*, 6.
- [2] D. A. Brown, J. B. Perry, M. E. Allen, H. N. Sabbah, B. L. Stauffer, S. R. Shaikh, J. G. F. Cleland, W. S. Colucci, J. Butler, A. A. Voors, S. D. Anker, B. Pitt, B. Pieske, G. Filippatos, S. J. Greene, M. Gheorghiadu, *Nat. Rev. Cardiol.* **2017**, *14*(4), 238.
- [3] S. Pickles, P. Vigié, R. J. Youle, *Curr. Biol.* **2018**, *28*(4), R170.
- [4] A. Sugiura, G.-L. McLelland, E. A. Fon, H. M. McBride, *EMBO J.* **2014**, *33*(19), 2142.
- [5] D. Matheoud, A. Sugiura, A. Bellemare-Pelletier, A. Laplante, C. Rondeau, M. Chemali, A. Fazel, J. J. Bergeron, L.-E. Trudeau, Y. Burelle, E. Gagnon, M. B. HM, M. Desjardins, *Cell* **2016**, *166*(2), 314.

- [6] B. H. Abuaita, T. L. Schultz, M. X. O'Riordan, *Cell Host Microbe* **2018**, *24*(5), 625.
- [7] K. Todkar, L. Chikhi, V. Desjardins, F. El-Mortada, G. Pépin, M. Germain, *Nat. Commun.* **2021**, *12*(1), 1.
- [8] S. Hayashi, Y. Okada, *Mol. Biol. Cell* **2015**, *26*(9), 1743.
- [9] Y. Wang, M. Serricchio, M. Jauregui, R. Shanbhag, T. Stoltz, C. T. di Paolo, P. K. Kim, G. A. McQuibban, *Autophagy* **2015**, *11*(4), 595.
- [10] V. Soubannier, G.-L. McLelland, R. Zunino, E. Braschi, P. Rippstein, E. A. Fon, H. M. McBride, *Curr. Biol.* **2012**, *22*(2), 135.
- [11] V. J. J. Cadete, S. Deschênes, A. Cuillerier, F. Brisebois, A. Sugiura, A. Vincent, D. Turnbull, M. Picard, H. M. McBride, Y. Burelle, *J. Physiol.* **2016**, *594*(18), 5343.
- [12] J. Schindelin, I. Arganda-Carreras, E. Frise, V. Kaynig, M. Longair, T. Pietzsch, S. Preibisch, C. Rueden, S. Saalfeld, B. Schmid, J. Y. Tinevez, D. J. White, V. Hartenstein, K. Eliceiri, P. Tomancak, A. Cardona, *Nat. Methods* **2012**, *9*(7), 676.
- [13] I. Arganda-Carreras, V. Kaynig, C. Rueden, K. W. Eliceiri, J. Schindelin, A. Cardona, H. S. Seung, *Bioinformatics* **2017**, *33*(15), 2424.
- [14] C. Wang, D. Wanqing, Q. P. Su, M. Zhu, P. Feng, Y. Li, Y. Zhou, N. Mi, Y. Zhu, D. Jiang, S. Zhang, Z. Zhang, Y. Sun, L. Yu, *Cell Res.* **2015**, *25*(10), 1108.
- [15] J. Qin, Y. Guo, B. Xue, P. Shi, C. Yang, Q. P. Su, H. Hao, S. Zhao, C. Wu, L. Yu, D. Li, Y. Sun, *Nat. Commun.* **2020**, *11*(1), 1.
- [16] X. Huang, L. Sun, S. Ji, T. Zhao, W. Zhang, J. Xu, J. Zhang, Y. Wang, X. Wang, C. Franzini-Armstrong, M. Zheng, H. Cheng, *Proc. Natl. Acad. Sci. U. S. A.* **2013**, *110*(8), 2846.
- [17] T. Zhao, H. Hao, Z. Wang, Y. Liang, K. Feng, M. He, Y. Xue, P. R. Bianco, Y. Sun, B. Yao, M. Lei, *Biomed. Opt. Express* **2021**, *12*(6), 3474.
- [18] B. Li, H. Zhao, Y. Wu, Z. Yu, J. Zhang, G. Yang, Q. Yan, J. Li, T. Li, L. Liu, *Front. Cell Dev. Biol.* **2020**, *8*, 214.
- [19] I. S. Opstad, 3D SIM data of mitochondria in the cardiomyoblast cell-line H9c2 adapted to either glucose or galactose, **2021**.

SUPPORTING INFORMATION

Additional supporting information may be found in the online version of the article at the publisher's website.

How to cite this article: I. S. Opstad, G. Godtlielsen, B. S. Ahluwalia, T. Myrmel, K. Agarwal, Å. B. Birgisdottir, *J. Biophotonics* **2022**, *15*(2), e202100305. <https://doi.org/10.1002/jbpo.202100305>

Paper III

